Constraining the mechanisms of aeolian bedform formation on Mars through a global morphometric survey

David Alegre Vaz[1], Simone Silvestro[2], Matthew Chojnacki[3], and David C.A. Silva[4]

[1]Centre for Earth and Space Research of the University of Coimbra
[2]INAF
[3]Planetary Science Institute
[4]Centre for Earth and Space Research of the University of Coimbra

December 13, 2022

Abstract

Aeolian processes on Mars form a distinct class of meter-scale ripples, whose mechanisms of formation are debated. We present a global morphometric survey of bedforms on Mars, adding relevant observational constraints to the ongoing debate. We show that the bedforms located in the Tharsis region form a distinct group, not akin to the large dark-toned ripples which cover dune fields elsewhere on the planet. The relation between wavelength and atmospheric density derived from the new data is consistent with the predictions of a wind-drag mechanism, favoring the model that uses a saltation saturation length. Regardless of the mechanism that limits the size of bedforms, these results confirm the existence of a robust relationship between the wavelength of large ripples and atmospheric density (ripples spacings increases with decreasing atmospheric density). This provides further support to the interpretation of paleoatmospheric conditions on Mars through the analysis of its aeolian sedimentary record.

Constraining the mechanisms of aeolian bedform formation on Mars through a global morphometric survey

David A. Vaz[1], Simone Silvestro[2,3], Matthew Chojnacki[4] and David C. A. Silva[1]

[1] Centre for Earth and Space Research of the University of Coimbra, Observatório Geofísico e Astronómico da Universidade de Coimbra, Coimbra, Portugal.

[2] INAF Osservatorio Astronomico di Capodimonte, Napoli, Italia.

[3] SETI Institute, Carl Sagan Center, Mountain View, CA, USA.

[4] Planetary Science Institute, Lakewood, CO, USA.

Corresponding author: David Vaz (davidvaz@uc.pt)

Key Points:

- We present a global morphometric survey of aeolian bedforms on Mars and assess the mechanisms that may control their size
- Bedforms within the high elevation Tharsis region form a distinct group, attributed here to different sediment and transport conditions
- We confirm the existence of a robust relation between wavelength and atmospheric density, which is consistent with a fluid-drag mechanism

Abstract

Aeolian processes on Mars form a distinct class of meter-scale ripples, whose mechanisms of formation are debated. We present a global morphometric survey of bedforms on Mars, adding relevant observational constraints to the ongoing debate. We show that the bedforms located in the Tharsis region form a distinct group, not akin to the large dark-toned ripples which cover dune fields elsewhere on the planet. The relation between wavelength and atmospheric density derived from the new data is consistent with the predictions of a wind-drag mechanism, favoring the model that uses a saltation saturation length. Regardless of the mechanism that limits the size of bedforms, these results confirm the existence of a robust relationship between the wavelength of large ripples and atmospheric density (ripples spacings increases with decreasing atmospheric density). This provides further support to the interpretation of paleoatmospheric conditions on Mars through the analysis of its aeolian sedimentary record.

Plain Language Summary

The winds that shape the surface of Mars form two distinct scales of aeolian ripples, which coexist and evolve over martian dunes. The larger ripples (with spacing between crests between 1-5 m) are enigmatic, as the mechanisms that control their equilibrium size are not fully understood. In this study we provide new observational data, which we use to assess different models that predict a dependence of bedform wavelength with atmospheric density. This new dataset shows that there are more than one population of meter-scale bedforms, with the ones located around the Tharsis volcanos being significantly different from the ones that cover dark dunes. We found a good agreement with the predictions of the wind-drag model, suggesting that the size of the large ripples is controlled by an aerodynamic mechanism. Most importantly, we confirm the existence of a global relation between wavelength and atmospheric density (ripples spacings increases with decreasing atmospheric density). This provides further support to the interpretation of paleoatmospheric conditions on Mars, as this relation can be applied to infer past atmospheric densities from the sedimentary record.

1 Introduction

Martian dark dunes are covered by large ripple-like bedforms which are actively migrating under present-day atmospheric conditions (Bridges et al., 2012; Silvestro et al., 2010). These are metric-scale bedforms (~1-5 m spacing between crests, ~5-40 cm high) which can have symmetrical or asymmetrical profiles and sinuous or straight crests. On terrestrial aeolian environments with well-sorted sediments there are no obvious analogue bedforms in terms of scale, morphometry and dynamics (Lapotre et al., 2018; Silvestro et al., 2016; Vaz et al., 2017). Most notably, the meter-scale bedform are overlaid by centimeter-scale ripples, similar in scale and dynamics to impact ripples (Bridges et al., 2012; Lapotre et al., 2016; Weitz et al., 2018). The coexistence to these two different scales of bedforms raised several questions. Namely, why do we have two scales of ripples on Mars and what are the mechanisms that control their sizes?

To explain orbital and ground-based observations of widespread aeolian activity (Baker et al., 2022; Bridges et al., 2012; Silvestro et al., 2010, 2013) transient low-flux transport regimes, that occur between impact threshold and fluid threshold speeds, were invoked (Andreotti et al., 2021; Baker et al., 2018; Lapotre et al., 2018; Sullivan & Kok, 2017; Swann et al., 2020). Recent in situ observations by the Curiosity rover at Gale crater demonstrate that intermittent saltation is taking place, contributing to the migration of centimeter-scale ripples (Baker et al., 2022; Sullivan et al., 2022). In addition, wind tunnel experiments suggest that the size of impact ripples does not vary significantly with atmospheric density, maintaining their characteristic centimeter scale even in the low density conditions that exist on the surface of Mars (Andreotti et al., 2021). Therefore, all evidence shows that the size of centimeter scale ripples on Mars is controlled by the same impact-splash mechanism that produces terrestrial aeolian impact ripples.

In contrast, two hypotheses have been proposed to explain the origin of the meter-scale ripples. They have been interpreted: a) as arising from a hydrodynamic instability i.e., they are analogous to fluid drag ripples typically found on terrestrial subaqueous environments (Duran Vinent et al., 2019; Lapotre et al., 2016, 2021); or b) as forming from the same impact-splash mechanism as terrestrial aeolian ripples (Sullivan et al., 2020; Sullivan & Kok, 2017). In the first hypothesis, the equilibrium wavelength of the large ripples is limited by a hydrodynamic anomaly (Duran Vinent et al., 2019; Lapotre et al., 2016), while in the second case ripple height (and consequently their wavelength) is controlled by the wind dynamic pressure at the bedforms crests, which is lower on Mars and would allow the growth of the bedforms (Sullivan et al., 2020). Lapotre et al. (2016, 2021) argued that there is a clear wavelength gap between the two types of bedforms, inferring that two different mechanisms are limiting the size of the bedforms (impact-splash for the centimeter-scale ripples and fluid-drag for the meter-scale bedforms). In contrast, Sullivan et al. (2022) reported a continuum distribution of superimposed ripple wavelengths observed by the Curiosity rover at the "Sands of Forvie" sand sheet. They also reported the existence of granulometric segregation between the troughs and crests of large ripples (the same was reported in other areas by Gough et al., 2021) with coarser grains preferentially located on the crests of the larger bedforms. They interpreted these two characteristics as evidence that the meter-scale ripples are impact ripples rather than fluid-drag bedforms.

An important aspect of the debate about the mechanism that sets the size of large ripples is the near-inverse relation observed between wavelength and atmospheric density at a global scale. This relation was initially hinted at by Lorenz et al. (2014) for the bedforms located across the high elevation Tharsis region, while Lapotre et al. (2016) extended the number of surveyed areas, focusing on sites where dark dunes are present. Based on this compilation, Lapotre et al. (2016) argued that the observed decrease in ripple wavelength with increasing atmospheric density is consistent with a fluid-drag origin. A view not shared by Lorenz (2020), which highlighted the different gradient of the model predictions and observational data (see Fig. 2 in Lorenz, 2020). Lapotre et al. (2021) revisited the same dataset proposing that when a saltation saturation length formulation is adopted (Duran Vinent et al., 2019), the fluid-drag mechanism provides a better fit to the data, particularly to the bedforms analyzed outside Tharsis.

Drag ripples wavelength scales according to $\lambda \approx \frac{\left(\frac{\mu}{\rho_f}\right)^{2/3} D^{1/6}}{(Rg)^{1/6} u_*^{1/3}}$ (Lapotre et al., 2017), where μ is the dynamic viscosity, ρ_f is the fluid density, D is grain diameter, g is the gravity acceleration and R is the submerged reduced density of the sediment ($\frac{\rho_s - \rho_f}{\rho_f}$). This relation predicts that bedform wavelength is strongly dependent on $\rho_f^{-2/3}$. The mechanisms that set the wavelength of impact ripples are less understood. Wind tunnel experiments show that the saturation wavelength on well sorted sediments increases linearly with friction velocity (Andreotti et al., 2006; Cheng et al., 2018; Rasmussen et al., 2015), and is thought to be limited by the height of the ripples (Bagnold, 1954; Manukyan & Prigozhin, 2009). Yet, in less well sorted sediments coarser particles form an armor layer on the crests, causing ripples to increase in height and consequently in wavelength (Sharp, 1963). Sullivan et al. (2020) argue that the wind dynamic pressure $WDP = \frac{1}{2}\rho_f u^2$ (u is the wind velocity) controls ripples height, with higher dynamic pressures removing particles from the crests and precluding the growth of the bedforms. Therefore, higher WDP should generate smaller ripples. In this case, if we assume a constant wind velocity the wavelength of impact ripples scales with $1/\rho_f$. Note that this assumption (constant wind speed at a global scale) may be problematic, as according to the equation WDP may be relatively more influenced by wind velocity than by density variations, which is the only factor addressed in previous studies as well as in this work. Nevertheless, both theories suggest an increase in wavelength when atmospheric density decreases.

Other questions not entirely settled in previous studies regard the nature of the bedforms located in the Tharsis region. Lapotre et al. (2016) noticed the morphologic and albedo differences between the dark-toned ripples covering dunes and Tharsis bedforms. Nevertheless, they merged the two datasets to fit their wind-drag model, while in later works Tharsis and non-Tharsis bedforms were analyzed separately (Lapotre et al., 2021; Lorenz, 2020).

Here we focus on these unresolved issues, reviewing and expanding the observational dataset, analyzing the consistency of measurements, and testing the models that predict the size of large ripples on Mars as a function of atmospheric density.

2 Data and methodology

We use High-Resolution Imaging Science Experiment (HiRISE) images (0.25-0.5 m/pix, McEwen et al., 2007) to perform a global scale mapping and wavelength survey of aeolian bedforms. Our survey cover the same 25 areas located in the Tharsis regions and analyzed by Lorenz et al. (2014), as well as the 11 areas reported in Lapotre et al. (2016) (Fig. 1). Furthermore, we expand the elevation coverage including 39 new areas where meter-scale bedforms are present covering dark-toned dunes (Supporting information S1 - section 1, Fig. S1 and Table S1).

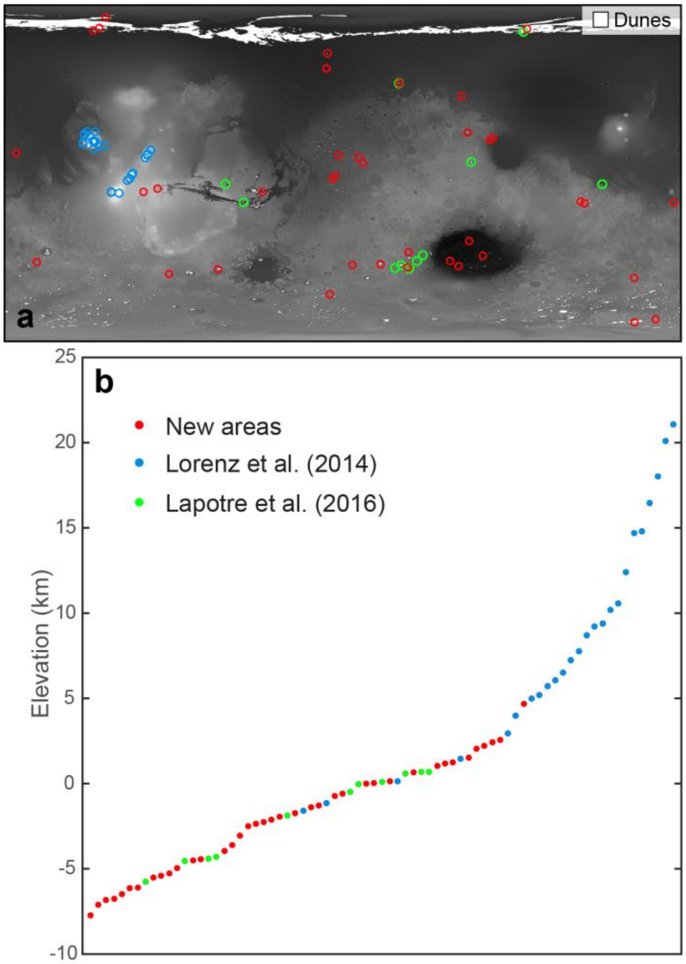

Figure 1. Location (a) and elevation distribution (b) of the 75 sites surveyed in this study. We analyzed the same 25 areas of Lorenz et al. (2014) as well as the 11 dark-tone dune sites previously analyzed by Lapotre et al. (2016). Our survey improves the spatial coverage, extends the range of surveyed elevations and provides a more continuous elevation sampling. A global dune catalog (Fenton, 2020; Hayward et al., 2014) is shown overlaying MOLA elevation data.

Previous surveys relied on the discrete manual measurements of crest-to-crest distances in randomly selected points (Lapotre et al., 2016; Lorenz et al., 2014). Here we applied a set of image processing and machine learning techniques which allow the mass automatic mapping of bedforms and the accurate measurement of their wavelengths (Fig. 2). We adapted the 2D Fast Fourier Transform approach introduced by Voulgaris and Morin (2008), implementing a multiscale scheme coupled with neural networks. This method allows the mapping and characterization of large ripples and transverse aeolian ridges (TARs) in a wide range of spatial scales and surface settings. See Supporting information S1 - section 2 for a in depth description of the method.

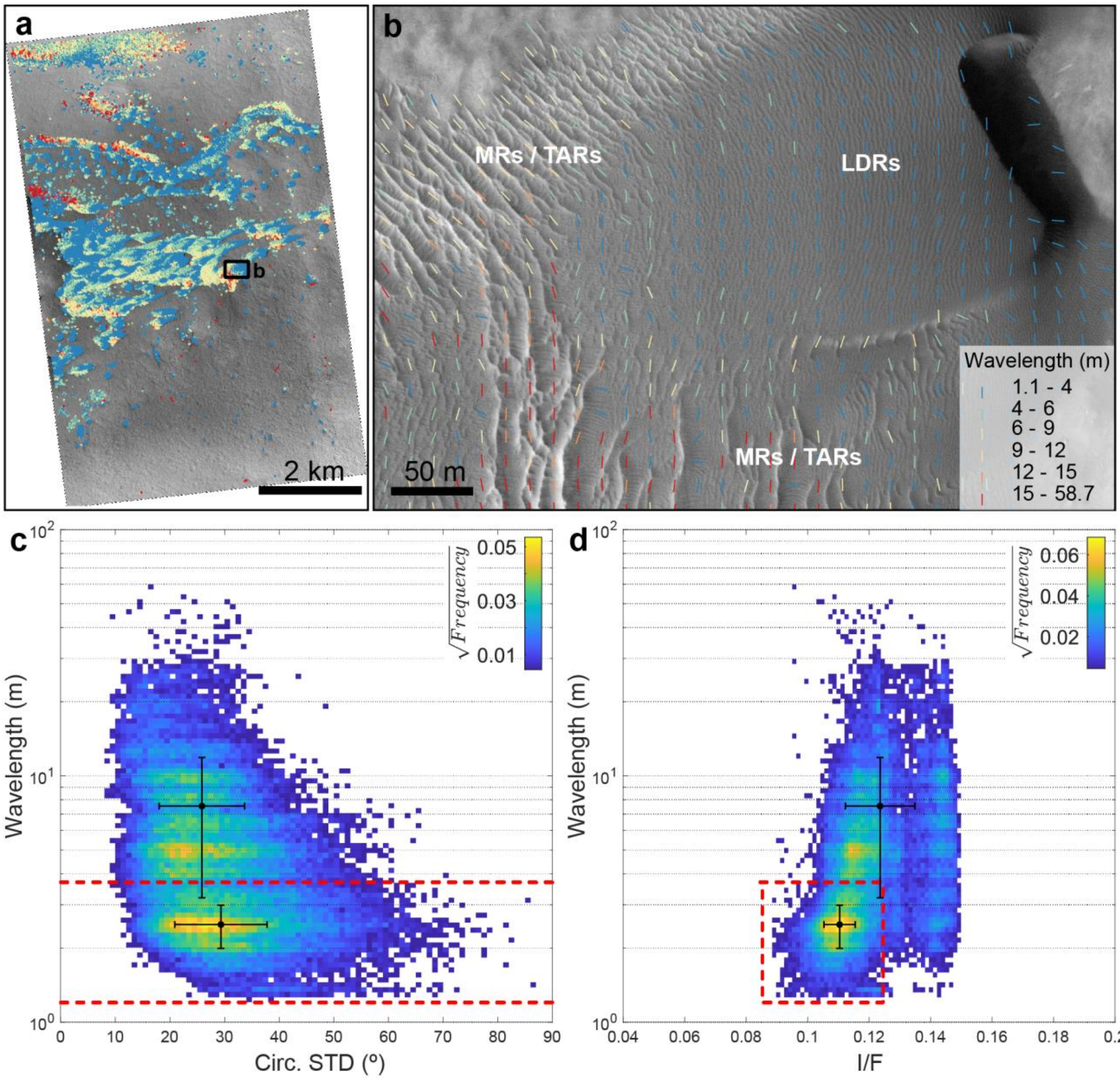

Figure 2. Wavelength survey of aeolian bedforms on Lyot crater (ESP_055318_2290, area 26 in Table S1). a) The applied method allows the full mapping and wavelength characterization of aeolian bedforms. b) Detailed view of the wavelength and trend of the mapped bedforms: large dark-toned ripples (LDRs) cover a barchan dune and have a spacing between crests of less than 4 m; megaripples (MRs) and transverse aeolian ridges (TARs) present higher albedos, higher wavelengths and are overlaid by the dune darker sediments. c and d) 2D histograms showing the

distribution of wavelength, circular standard deviation and albedo (I/F), a square root stretch is used to highlight secondary peaks. Red dashed lines correspond to the wavelength and albedo thresholds used to segment two bedform classes. The black dots and lines represent the computed averages and 1σ intervals.

Previous studies analyzed the relation between the average wavelength and atmospheric density at the surface, focusing on large ripples and TARs. To comply with this framework, we segment the mapped bedforms in two classes: a) large dark-toned ripples and b) a second class that comprises megaripples and TARs. Wavelength and relative grain size were proposed to be key parameters to discriminate different types of aeolian bedforms on Mars (Day & Zimbelman, 2021). We use albedo as a proxy for grain size, as it is usually assumed to be related to dust coating and/or to the presence of coarser particles (Sullivan et al., 2020). We examine the wavelength and albedo distributions using 2D histograms and we define threshold values that allow the partition of the mapping results, so that summary statistics can be computed for each class (see Supporting information S1 - section 3 for examples and Supporting information S2 for global results).

To evaluate the mechanisms that set the size of large ripples on Mars we test which model best describes the wavelength vs. atmospheric density relation observed in our dataset. We tested three models (refer to Supporting information S1 - section 5 for details): a) the wind-drag model of Lapotre et al. (2016), where the saturation length scale is approximated as that of fluvial bedload, b) a modified version of the same scaling, which instead uses a saturation length scale for aeolian saltation (Duran Vinent et al., 2019; Lapotre et al., 2021), and c) a generic inverse linear dependence between wavelength and atmospheric density (as proposed by Lorenz et al., 2014). We fit power laws and linear models to facilitate the comparison between our measurements and the models' predictions.

4 Results and discussion

Bedforms spaced between 1 to 100 m were mapped over a total area of ~2200 km^2 (Supporting information S2). The applied method correctly identifies the location of bedforms (93.7% of overall accuracy) and robustly measures their wavelength (we estimate a confidence interval of ±12%, Supporting information S1 - section 2). When comparing our data with previous surveys, we found a good agreement with large ripple measurements reported by Lapotre et al. (2016), which on average differ by 4%. Yet, the averages for the larger bedforms (megaripples and TARs) reported in the same study are severely underestimated by 84%, which we attribute to a possible under sampling. To assess the wavelength of these larger bedforms Lapotre et al. (2016) collected on average of 46 wavelength measurements on each site. This number of randomly located measurements may not be enough to characterize these populations, as they cover a small percentage of the mapped areas and form scattered patches of bedforms with variable wavelengths.

Our results for the Tharsis sites (which represent ~2/3 of the data analyzed in previous studies) show that Lorenz et al. (2014) values are systematically underestimated: on average they are 73% lower than the values obtained in this study (Fig. S10 and S11; Supporting information S1 - section 4). Indeed, some cited measurements there (e.g., 0.5-1.1 m) are dubious at best given HiRISE resolution (0.25 m/pix). The causes for this large disparity are less clear, nevertheless we note that in this case the measurement locations were not randomized, and that in some of the areas the spatial distribution of the bedforms is not uniform. These two factors may complicate the obtention of representative values from a few tens of scattered measurements.

Other potential sources of uncertainty are the elevation values reported for each site, which are used to derive the atmospheric pressure. We sampled the MOLA elevations at the centroid point of the largest bedform patch mapped in each area. However, previous works do not refer the sampling scheme or location where elevation values were collected. Therefore, in areas where the HiRISE footprints cover regions with higher elevation gradients (mainly in the Tharsis region) we can have elevation differences between our values and previous surveys of more than 2 km. This happens in four of the areas analyzed by Lorenz et al. (2014) (Fig. S11b).

We found several lines of evidence which support that Tharsis bedforms form a distinct population, apart from the large dark-toned ripples found elsewhere on Mars: a) as noted by Lapotre et al. (2021), we found that Tharsis bedforms have higher albedos (Fig. S12); b) we found that they have distinct thermal inertia (Putzig and Mellon, 2007) and dust cover index signatures (Ruff and Christensen, 2002), denoting lower thermal inertias (possibly associated with finer materials) and higher dust content/coverage (Fig. S13); c) as noted by others, Tharsis bedforms form unique patterns (Fig. S14) such as honeycomb or reticulate patterns (Bridges et al., 2010; Lorenz et al., 2014); and d) are in most cases associated with extensive mantling units, while large ripples outside Tharsis are typically found overlaying dark dunes (see Supporting information S1

- section 5 for details). These distinctive characteristics suggest that the two sets of bedforms should be considered separately when evaluating bedform-formation mechanisms.

The compiled data confirms the existence of a decrease of wavelength with increasing atmospheric density for the large dark-toned ripples (Fig. 3). Only five areas (~7%) deviate from this general tendency (Supporting information S1 - section 5 and Fig. S15), corresponding to cases where: a) sand sheets occupy a significant percentage of the mapped areas, suggesting the presence of coarse and/or poorly sorted sediments; and b) where dust devil tracks are visible covering the bedforms, suggesting limited migration/activity. These outliers are not included in the fits done to evaluate the proposed models, but their existence highlights two points: the accuracy and consistency of the measurements and the need to select comparable dune settings, as differences in grain size and sorting influence the wavelength of the bedforms.

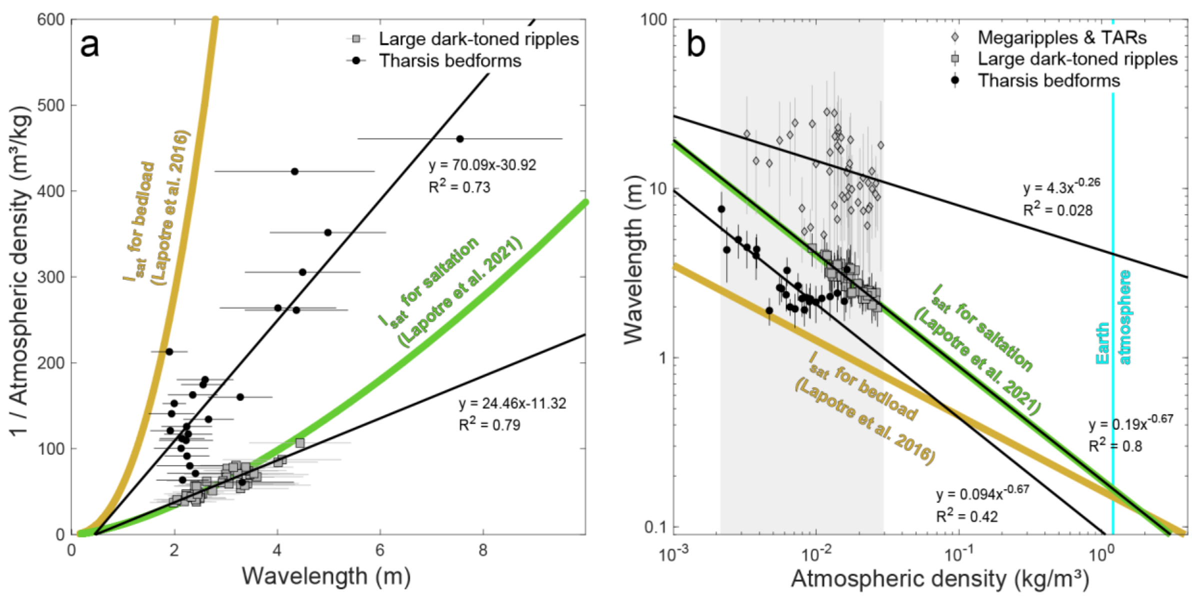

Figure 3. Relation between bedforms wavelength and Martian atmospheric density. The same data is shown in two different plots: a) highlighting the linear inverse relation proposed by Lorenz et al. (2014) and b) comparing with the models proposed by Lapotre et al. (2016; 2021), the gray area represents the maximum range of atmospheric densities on Mars while the cyan line represents the density of Earth's atmosphere. Black lines represent the best fitted models for each dataset, computed using the average wavelengths for each site (linear models in a) and power laws in b); the R^2 values in b) were computed in the log space). The golden line represents Lapotre et al. (2016) empirical relationship where transport saturation length is taken as that of fluvial bedload,

while the green line corresponds to a transport saturation length for aeolian saltation (Lapotre et al., 2021). A similar plot that includes the datasets used in previous studies is shown in Fig. S19.

The model obtained by fitting previous datasets which takes into account the bedload transport saturation length (Lapotre et al., 2016) predicts significantly lower wavelengths and a different scaling to the one we derived from our dataset. Conversely, our data for the dark-toned large ripples overlaps the predictions of the wind-drag model that uses the saltation transport saturation length, with a best fitted power law with ~2/3 scaling.

Tharsis data presents higher scattering, particularly for lower wavelengths where data points seem to converge towards the dark-toned ripple dataset. Due to the discrepancies found between our results and those of Lorenz et al. (2014), we note that the Tharsis data compiled in this study does not overlap or follow a similar scaling to the wind-drag model that considers a bedload transport saturation length (Fig. 3 and S19). Instead, the best fitted power law (R^2=0.42) has the same scaling (~2/3) of the model that uses the saltation transport saturation length.

The compiled data suggests that the mechanism that limits the size of large ripples on Mars is dependent on the atmospheric density. Overall, we observe that all our data are bounded by the two saturation length scaling laws, supporting the hypothesis that the equilibrium size of large martian ripples is controlled by an aerodynamic mechanism. The scaling laws for saturation length arise from idealized representations of transport in unimodal sediments. As previously discussed, the grain size distribution of the sediments on the Tharsis bedforms is probably more complex, which may contribute to the observed differences between Tharsis and non-Tharsis bedforms.

Even so, in accordance with previous studies (Lorenz, 2020; Lorenz et al., 2014) we notice that linear functions (which imply that $\lambda \propto 1/\rho_f$) also provide robust fits to the data (R^2=0.79 and 0.73 for the dark large ripples and Tharsis bedforms, respectively). In the case of the large ripples, both inverse and power law functions explain ~80% of the variance. This means that, strictly from a numeric point of view, we cannot discriminate what is the best model to fit the data. As previously mentioned, to fully test the impact ripple hypothesis we would need to consider the wind velocities at each site, something that could be done using climate model predictions.

Finally, the wavelengths of the larger bedforms (megaripples and TARs) present a large dispersion (Fig. 3B), not showing an obvious relation with any of the scaling laws. Linear or power law models do not produce a meaningful fit to the data (R^2=0.03). This suggests that at a global scale these bedforms do not form a homogeneous set and are probably not representative of the same boundary conditions (i.e., they likely formed with different grain size distributions, or under differing atmospheric conditions). Nonetheless, we cannot exclude the possibility that including TARs and megaripples in a same class may be flawed, especially since different degrees of mobility under present day winds have been described for the two sets of bedforms (Chojnacki et al., 2021; Silvestro et al., 2020).

For the dark-toned large ripples the degree of agreement between the global measurements and the predictions of the scaling relationship of Lapotre et al. (2021) (where saturation length is taken as that of aeolian saltation) is remarkable. Particularly if we consider that we are using a "static" average atmospheric density, which is merely a function of elevation and does not consider regional and seasonal atmospheric density variations. On the other hand, we cannot exclude that the density may just be one of the factors influencing the bedforms dimensions. As suggested by Lorenz (2020), wind speed at a global scale may increase with elevation creating a more complex interplay between density, wind speed and resulting bedform size.

5 Conclusions

This survey provides improved measurements to evaluate the mechanisms that set the size of bedform on Mars. We show that previous works used biased measurements, particularly for the bedforms located in the Tharsis region. We investigated the uniqueness of the bedforms located in this region, concluding that these bedforms form a distinct population and should be analyzed separately from the more common dark-toned large ripples that cover dunes outside Tharsis.

Our survey covers a larger range of elevations than previous works, and for the first time provides full wavelength mapping of extensive regions. Overall, our results are consistent with the predictions of the "wind-drag" hypothesis, favoring the model that considers a saltation transport saturation length. Still, the compiled morphometric data is not enough to refute the impact ripple hypothesis, as that would probably require the integration of variable wind velocities for each site.

The compiled dataset corroborates the existence of a robust relation between the wavelength of large dark-toned ripples and atmospheric density. Therefore, this new survey complements and helps to validate the main concept introduced in Lapotre et al. (2016): that paleoatmospheric density can be inferred for Mars by looking at the aeolian sedimentary record, providing an important tool to probe the evolution of the planet's environment.

Acknowledgments

This research was supported by CITEUC (UID/Multi/00611/2021&POCI-01- 0145-FEDER-006922) and by FCT grant CEECIND/02981/2017. M. C. and S.S. were funded by NASA Mars Data Analysis Program Grant 80NSSC20K1066. We thank the Laboratory for Advanced Computing at University of Coimbra for providing computing resources.

We acknowledge the valuable comments and suggestions made by Mathieu Lapotre and two anonymous reviewers to an earlier version of this work. We thank Rob Sullivan for insights on the morphodynamics of impact ripples.

Open Research

HiRISE images used in this work are publicly available at the Planetary Data System (https://hirise-pds.lpl.arizona.edu/PDS/) where details can be obtained at McEwen et al. (2007). The morphometric database compiled in this study is available at https://doi.org/10.6084/m9.figshare.21064657.

References

Andreotti, B, Claudin, P., & Pouliquen, O. (2006). Aeolian sand ripples: Experimental study of fully developed states. *Physical Review Letters*, *96*(2). https://doi.org/Doi 10.1103/Physrevlett.96.028001

Andreotti, Bruno, Claudin, P., Iversen, J. J., Merrison, J. P., & Rasmussen, K. R. (2021). A lower-than-expected saltation threshold at Martian pressure and below. *Proceedings of the National Academy of Sciences of the United States of America*, *118*(5). https://doi.org/10.1073/pnas.2012386118

Bagnold, R. A. (1954). *The Physics of Blown Sand and Desert Dunes* (2nd ed.). New York: Dover Publications, INC.

Baker, M. M., Lapotre, M. G. A., Minitti, M. E., Newman, C. E., Sullivan, R., Weitz, C. M., et al. (2018). The Bagnold Dunes in Southern Summer: Active Sediment Transport on Mars Observed by the Curiosity Rover. *Geophysical Research Letters*, *45*(17), 8853–8863. https://doi.org/10.1029/2018GL079040

Baker, M. M., Newman, C. E., Sullivan, R., Minitti, M. E., Edgett, K. S., Fey, D., et al. (2022). Diurnal Variability in Aeolian Sediment Transport at Gale Crater, Mars. *Journal of Geophysical Research: Planets*, *127*(2), 1–27. https://doi.org/10.1029/2020JE006734

Bridges, N. T., Banks, M. E., Beyer, R. A., Chuang, F. C., Noe Dobrea, E. Z., Herkenhoff, K. E., et al. (2010). Aeolian bedforms, yardangs, and indurated surfaces in the Tharsis Montes as seen by the HiRISE Camera: Evidence for dust aggregates. *Icarus*, *205*(1), 165–182. https://doi.org/10.1016/j.icarus.2009.05.017

Bridges, N. T., Ayoub, F., Avouac, J.-P., Leprince, S., Lucas, a, & Mattson, S. (2012). Earth-like sand fluxes on Mars. *Nature*, *485*(7398), 339–42. https://doi.org/10.1038/nature11022

Cheng, H., Liu, C., Li, J., Liu, B., Zheng, Z., Zou, X., et al. (2018). Experimental study of aeolian sand ripples in a wind tunnel. *Earth Surface Processes and Landforms*, *43*(1), 312–321. https://doi.org/10.1002/esp.4246

Chojnacki, M., Vaz, D. A., Silvestro, S., & Silva, D. C. A. (2021). Widespread Megaripple Activity Across the North Polar Ergs of Mars. *Journal of Geophysical Research: Planets*, 1–19. https://doi.org/10.1029/2021je006970

Day, M., & Zimbelman, J. R. (2021). Ripples, megaripples, and TARs, Oh, My! Recommendations regarding Mars aeolian bedform terminology. *Icarus*, *369*, 114647. https://doi.org/10.1016/j.icarus.2021.114647

Duran Vinent, O., Andreotti, B., Claudin, P., & Winter, C. (2019). A unified model of ripples and dunes in water and planetary environments. *Nature Geoscience*, *12*(5), 345–350. https://doi.org/10.1038/s41561-019-0336-4

Fenton, L. K. (2020). Updating the global inventory of dune fields on mars and identification of many small dune fields. *Icarus*, *352*(May), 114018. https://doi.org/10.1016/j.icarus.2020.114018

Foroutan, M., & Zimbelman, J. R. (2017). Semi-automatic mapping of linear-trending bedforms using 'Self-Organizing Maps' algorithm. *Geomorphology*, *293*(May), 156–166. https://doi.org/10.1016/j.geomorph.2017.05.016

Gonzalez, R. C., Woods, R. E., & Eddins, S. L. (2004). *Digital Image processing using MATLAB*. Upper Saddle River, NJ: Pearson/Prentice Hall.

Gough, T. R., Hugenholtz, C. H., & Barchyn, T. E. (2021). Re-Evaluation of Large Martian Ripples in Gale Crater: Granulometric Evidence for an Impact Mechanism and Terrestrial Analogues. *Journal of Geophysical Research: Planets*, *126*(12). https://doi.org/10.1029/2021JE007011

Hayward, R. K., Fenton, L. K., & Titus, T. N. (2014). Mars Global Digital Dune Database (MGD3): Global dune distribution and wind pattern observations. *Icarus*, *230*, 38–46. https://doi.org/10.1016/j.icarus.2013.04.011

Kok, J. F. (2010). An improved parameterization of wind-blown sand flux on Mars that includes the effect of hysteresis. *Geophysical Research Letters*, *37*(12), 1–6. https://doi.org/10.1029/2010GL043646

Lapotre, M. G. A., Ewing, R. C., Lamb, M. P., Fischer, W. W., Grotzinger, J. P., Rubin, D. M., et al. (2016). Large wind ripples on Mars: A record of atmospheric evolution. *Science*, *353*(6294), 55–58. https://doi.org/10.1126/science.aaf3206

Lapotre, M. G. A., Ewing, R. C., Weitz, C. M., Lewis, K. W., Lamb, M. P., Ehlmann, B. L., & Rubin, D. M. (2018). Morphologic Diversity of Martian Ripples: Implications for Large-Ripple Formation. *Geophysical Research Letters*, *45*(19), 10,229-10,239. https://doi.org/10.1029/2018GL079029

Lapotre, Mathieu G.A., Lamb, M. P., & McElroy, B. (2017). What sets the size of current ripples? *Geology*, *45*(3), G38598.1. https://doi.org/10.1130/G38598.1

Lapotre, Mathieu G.A., Ewing, R. C., & Lamb, M. P. (2021). An Evolving Understanding of Enigmatic Large Ripples on Mars. *Journal of Geophysical Research: Planets*, *126*(2), 1–8. https://doi.org/10.1029/2020JE006729

Lorenz, R. D. (2020). Martian Ripples Making a Splash. *Journal of Geophysical Research: Planets*, *125*(10), 12–15. https://doi.org/10.1029/2020JE006658

Lorenz, R. D., Bridges, N. T., Rosenthal, A. A., & Donkor, E. (2014). Elevation dependence of bedform wavelength on Tharsis Montes, Mars: Atmospheric density as a controlling parameter. *Icarus*, *230*, 77–80. https://doi.org/10.1016/j.icarus.2013.10.026

Manukyan, E., & Prigozhin, L. (2009). Formation of aeolian ripples and sand sorting. *Physical Review E - Statistical, Nonlinear, and Soft Matter Physics*, *79*(3).

https://doi.org/10.1103/PhysRevE.79.031303
McEwen, A. S., Eliason, E. M., Bergstrom, J. W., Bridges, N. T., Hansen, C. J., Delamere, W. A., et al. (2007). Mars Reconnaissance Orbiter's High Resolution Imaging Science Experiment (HiRISE). *Journal of Geophysical Research-Planets*, *112*(E5). https://doi.org/Doi 10.1029/2005je002605
Moller, M. F. (1993). A Scaled Conjugate-Gradient Algorithm for Fast Supervised Learning. *Neural Networks*, *6*(4), 525–533. https://doi.org/Doi 10.1016/S0893-6080(05)80056-5
Putzig, N. E., & Mellon, M. T. (2007). Apparent thermal inertia and the surface heterogeneity of Mars. *Icarus*, *191*(1), 68–94. https://doi.org/10.1016/j.icarus.2007.05.013
Rasmussen, K. R., Valance, A., & Merrison, J. (2015). Laboratory studies of aeolian sediment transport processes on planetary surfaces. *Geomorphology*, *244*, 74–94. https://doi.org/10.1016/j.geomorph.2015.03.041
Ruff, S. W., & Christensen, P. R. (2002). Bright and dark regions on Mars: Particle size and mineralogical characteristics based on thermal emission spectrometer data. *Journal of Geophysical Research E: Planets*, *107*(12), 1–22. https://doi.org/10.1029/2001je001580
Sharp, R. P. (1963). Wind Ripples. *Journal of Geology*, *71*(5), 617–636. Retrieved from http://www.jstor.org/stable/30061128
Silvestro, S., Fenton, L. K., Vaz, D. A., Bridges, N. T., & Ori, G. G. (2010). Ripple migration and dune activity on Mars: Evidence for dynamic wind processes. *Geophysical Research Letters*, *37*(20), L20203. https://doi.org/Doi 10.1029/2010gl044743
Silvestro, S., Vaz, D. A., Ewing, R. C., Rossi, A. P., Fenton, L. K., Michaels, T. I., et al. (2013). Pervasive aeolian activity along rover Curiosity's traverse in Gale Crater, Mars. *Geology*, *41*(4), 483–486. https://doi.org/Doi 10.1130/G34162.1
Silvestro, S., Vaz, D. A., Yizhaq, H., & Esposito, F. (2016). Dune-like dynamic of Martian Aeolian large ripples. *Geophysical Research Letters*, *43*(16), 8384–8389. https://doi.org/10.1002/2016GL070014
Silvestro, S., Chojnacki, M., Vaz, D. A., Cardinale, M., Yizhaq, H., & Esposito, F. (2020). Megaripple Migration on Mars. *Journal of Geophysical Research: Planets*, *125*(8). https://doi.org/10.1029/2020JE006446
Smith, D. E., Zuber, M. T., Solomon, S. C., Phillips, R. J., Head, J. W., Garvin, J. B., et al. (1999). The Global Topography of Mars and Implications for Surface Evolution, *284*(May),

1495–1503.

Soille, P. (2002). *Morphological Image Analysis - Principles and Applications*. Berlin: Springer-Verlag.

Sullivan, R., & Kok, J. F. (2017). Aeolian saltation on Mars at low wind speeds. *Journal of Geophysical Research: Planets*, *122*(10), 2111–2143. https://doi.org/10.1002/2017JE005275

Sullivan, R., Kok, J. F., Katra, I., & Yizhaq, H. (2020). A Broad Continuum of Aeolian Impact Ripple Morphologies on Mars is Enabled by Low Wind Dynamic Pressures. *Journal of Geophysical Research: Planets*, *125*(10), 1–39. https://doi.org/10.1029/2020je006485

Sullivan, R., Baker, M., Newman, C., Turner, M., Schieber, J., Weitz, C., et al. (2022). The Aeolian Environment in Glen Torridon, Gale Crater, Mars. *Journal of Geophysical Research: Planets*, *127*(8), 1–39. https://doi.org/10.1029/2021JE007174

Swann, C., Sherman, D. J., & Ewing, R. C. (2020). Experimentally Derived Thresholds for Windblown Sand on Mars. *Geophysical Research Letters*, *47*(3), 1–10. https://doi.org/10.1029/2019GL084484

Taubman, D. S., & Marcellin, M. W. (2002). JPEG2000: Standard for interactive imaging. *Proceedings of the IEEE*, *90*(8), 1336–1357. https://doi.org/10.1109/JPROC.2002.800725

Vaz, D. A., & Silvestro, S. (2014). Mapping and characterization of small-scale aeolian structures on Mars: An example from the MSL landing site in Gale Crater. *Icarus*, *230*, 151–161.

Vaz, D. A., Sarmento, P. T. K., Barata, M. T., Fenton, L. K., & Michaels, T. I. (2015). Object-based Dune Analysis: Automated dune mapping and pattern characterization for Ganges Chasma and Gale crater, Mars. *Geomorphology*, *250*, 128–139. https://doi.org/10.1016/j.geomorph.2015.08.021

Vaz, D. A., Silvestro, S., Sarmento, P. T. K., & Cardinale, M. (2017). Migrating meter-scale bedforms on Martian dark dunes: Are terrestrial aeolian ripples good analogues? *Aeolian Research*, *26*, 101–116. https://doi.org/10.1016/j.aeolia.2016.08.003

Voulgaris, G., & Morin, J. P. (2008). A long-term real time sea bed morphology evolution system in the South Atlantic Bight. *Proceedings of the Ieee/Oes/Cmtc Ninth Working Conference on Current Measurement Technology*, 71–79.

Weitz, C. M., Sullivan, R. J., Lapotre, M. G. A., Rowland, S. K., Grant, J. A., Baker, M., &

Yingst, R. A. (2018). Sand Grain Sizes and Shapes in Eolian Bedforms at Gale Crater, Mars. *Geophysical Research Letters*, *45*(18), 9471–9479. https://doi.org/10.1029/2018GL078972

Withers, P., & Smith, M. D. (2006). Atmospheric entry profiles from the Mars Exploration Rovers Spirit and Opportunity. *Icarus*, *185*(1), 133–142. https://doi.org/10.1016/j.icarus.2006.06.013

Constraining the mechanisms of aeolian bedform formation on Mars through a global morphometric survey

David A. Vaz[1], Simone Silvestro[2,3], Matthew Chojnacki[4] and David C. A. Silva[1]

[1] Centre for Earth and Space Research of the University of Coimbra, Observatório Geofísico e Astronómico da Universidade de Coimbra, Coimbra, Portugal.

[2] INAF Osservatorio Astronomico di Capodimonte, Napoli, Italia.

[3] SETI Institute, Carl Sagan Center, Mountain View, CA, USA.

[4] Planetary Science Institute, Lakewood, CO, USA.

Corresponding author: David Vaz (davidvaz@uc.pt)

Key Points:

- We present a global morphometric survey of aeolian bedforms on Mars and assess the mechanisms that may control their size
- Bedforms within the high elevation Tharsis region form a distinct group, attributed here to different sediment and transport conditions
- We confirm the existence of a robust relation between wavelength and atmospheric density, which is consistent with a fluid-drag mechanism

Abstract

Aeolian processes on Mars form a distinct class of meter-scale ripples, whose mechanisms of formation are debated. We present a global morphometric survey of bedforms on Mars, adding relevant observational constraints to the ongoing debate. We show that the bedforms located in the Tharsis region form a distinct group, not akin to the large dark-toned ripples which cover dune fields elsewhere on the planet. The relation between wavelength and atmospheric density derived from the new data is consistent with the predictions of a wind-drag mechanism, favoring the model that uses a saltation saturation length. Regardless of the mechanism that limits the size of bedforms, these results confirm the existence of a robust relationship between the wavelength of large ripples and atmospheric density (ripples spacings increases with decreasing atmospheric density). This provides further support to the interpretation of paleoatmospheric conditions on Mars through the analysis of its aeolian sedimentary record.

Plain Language Summary

The winds that shape the surface of Mars form two distinct scales of aeolian ripples, which coexist and evolve over martian dunes. The larger ripples (with spacing between crests between 1-5 m) are enigmatic, as the mechanisms that control their equilibrium size are not fully understood. In this study we provide new observational data, which we use to assess different models that predict a dependence of bedform wavelength with atmospheric density. This new dataset shows that there are more than one population of meter-scale bedforms, with the ones located around the Tharsis volcanos being significantly different from the ones that cover dark dunes. We found a good agreement with the predictions of the wind-drag model, suggesting that the size of the large ripples is controlled by an aerodynamic mechanism. Most importantly, we confirm the existence of a global relation between wavelength and atmospheric density (ripples spacings increases with decreasing atmospheric density). This provides further support to the interpretation of paleoatmospheric conditions on Mars, as this relation can be applied to infer past atmospheric densities from the sedimentary record.

1 Introduction

Martian dark dunes are covered by large ripple-like bedforms which are actively migrating under present-day atmospheric conditions (Bridges et al., 2012; Silvestro et al., 2010). These are metric-scale bedforms (~1-5 m spacing between crests, ~5-40 cm high) which can have symmetrical or asymmetrical profiles and sinuous or straight crests. On terrestrial aeolian environments with well-sorted sediments there are no obvious analogue bedforms in terms of scale, morphometry and dynamics (Lapotre et al., 2018; Silvestro et al., 2016; Vaz et al., 2017). Most notably, the meter-scale bedform are overlaid by centimeter-scale ripples, similar in scale and dynamics to impact ripples (Bridges et al., 2012; Lapotre et al., 2016; Weitz et al., 2018). The coexistence to these two different scales of bedforms raised several questions. Namely, why do we have two scales of ripples on Mars and what are the mechanisms that control their sizes?

To explain orbital and ground-based observations of widespread aeolian activity (Baker et al., 2022; Bridges et al., 2012; Silvestro et al., 2010, 2013) transient low-flux transport regimes, that occur between impact threshold and fluid threshold speeds, were invoked (Andreotti et al., 2021; Baker et al., 2018; Lapotre et al., 2018; Sullivan & Kok, 2017; Swann et al., 2020). Recent in situ observations by the Curiosity rover at Gale crater demonstrate that intermittent saltation is taking place, contributing to the migration of centimeter-scale ripples (Baker et al., 2022; Sullivan et al., 2022). In addition, wind tunnel experiments suggest that the size of impact ripples does not vary significantly with atmospheric density, maintaining their characteristic centimeter scale even in the low density conditions that exist on the surface of Mars (Andreotti et al., 2021). Therefore, all evidence shows that the size of centimeter scale ripples on Mars is controlled by the same impact-splash mechanism that produces terrestrial aeolian impact ripples.

In contrast, two hypotheses have been proposed to explain the origin of the meter-scale ripples. They have been interpreted: a) as arising from a hydrodynamic instability i.e., they are analogous to fluid drag ripples typically found on terrestrial subaqueous environments (Duran Vinent et al., 2019; Lapotre et al., 2016, 2021); or b) as forming from the same impact-splash mechanism as terrestrial aeolian ripples (Sullivan et al., 2020; Sullivan & Kok, 2017). In the first hypothesis, the equilibrium wavelength of the large ripples is limited by a hydrodynamic anomaly (Duran Vinent et al., 2019; Lapotre et al., 2016), while in the second case ripple height (and consequently their wavelength) is controlled by the wind dynamic pressure at the bedforms crests, which is lower on Mars and would allow the growth of the bedforms (Sullivan et al., 2020). Lapotre et al. (2016, 2021) argued that there is a clear wavelength gap between the two types of bedforms, inferring that two different mechanisms are limiting the size of the bedforms (impact-splash for the centimeter-scale ripples and fluid-drag for the meter-scale bedforms). In contrast, Sullivan et al. (2022) reported a continuum distribution of superimposed ripple wavelengths observed by the Curiosity rover at the "Sands of Forvie" sand sheet. They also reported the existence of granulometric segregation between the troughs and crests of large ripples (the same was reported in other areas by Gough et al., 2021) with coarser grains preferentially located on the crests of the larger bedforms. They interpreted these two characteristics as evidence that the meter-scale ripples are impact ripples rather than fluid-drag bedforms.

An important aspect of the debate about the mechanism that sets the size of large ripples is the near-inverse relation observed between wavelength and atmospheric density at a global scale. This relation was initially hinted at by Lorenz et al. (2014) for the bedforms located across the high elevation Tharsis region, while Lapotre et al. (2016) extended the number of surveyed areas, focusing on sites where dark dunes are present. Based on this compilation, Lapotre et al. (2016) argued that the observed decrease in ripple wavelength with increasing atmospheric density is consistent with a fluid-drag origin. A view not shared by Lorenz (2020), which highlighted the different gradient of the model predictions and observational data (see Fig. 2 in Lorenz, 2020). Lapotre et al. (2021) revisited the same dataset proposing that when a saltation saturation length formulation is adopted (Duran Vinent et al., 2019), the fluid-drag mechanism provides a better fit to the data, particularly to the bedforms analyzed outside Tharsis.

Drag ripples wavelength scales according to $\lambda \approx \frac{\left(\frac{\mu}{\rho_f}\right)^{2/3} D^{1/6}}{(Rg)^{1/6} u_*^{1/3}}$ (Lapotre et al., 2017), where μ is the dynamic viscosity, ρ_f is the fluid density, D is grain diameter, g is the gravity acceleration and R is the submerged reduced density of the sediment ($\frac{\rho_s - \rho_f}{\rho_f}$). This relation predicts that bedform wavelength is strongly dependent on $\rho_f^{-2/3}$. The mechanisms that set the wavelength of impact ripples are less understood. Wind tunnel experiments show that the saturation wavelength on well sorted sediments increases linearly with friction velocity (Andreotti et al., 2006; Cheng et al., 2018; Rasmussen et al., 2015), and is thought to be limited by the height of the ripples (Bagnold, 1954; Manukyan & Prigozhin, 2009). Yet, in less well sorted sediments coarser particles form an armor layer on the crests, causing ripples to increase in height and consequently in wavelength (Sharp, 1963). Sullivan et al. (2020) argue that the wind dynamic pressure $WDP = \frac{1}{2}\rho_f u^2$ (u is the wind velocity) controls ripples height, with higher dynamic pressures removing particles from the crests and precluding the growth of the bedforms. Therefore, higher WDP should generate smaller ripples. In this case, if we assume a constant wind velocity the wavelength of impact ripples scales with $1/\rho_f$. Note that this assumption (constant wind speed at a global scale) may be problematic, as according to the equation WDP may be relatively more influenced by wind velocity than by density variations, which is the only factor addressed in previous studies as well as in this work. Nevertheless, both theories suggest an increase in wavelength when atmospheric density decreases.

Other questions not entirely settled in previous studies regard the nature of the bedforms located in the Tharsis region. Lapotre et al. (2016) noticed the morphologic and albedo differences between the dark-toned ripples covering dunes and Tharsis bedforms. Nevertheless, they merged the two datasets to fit their wind-drag model, while in later works Tharsis and non-Tharsis bedforms were analyzed separately (Lapotre et al., 2021; Lorenz, 2020).

Here we focus on these unresolved issues, reviewing and expanding the observational dataset, analyzing the consistency of measurements, and testing the models that predict the size of large ripples on Mars as a function of atmospheric density.

2 Data and methodology

We use High-Resolution Imaging Science Experiment (HiRISE) images (0.25-0.5 m/pix, McEwen et al., 2007) to perform a global scale mapping and wavelength survey of aeolian bedforms. Our survey cover the same 25 areas located in the Tharsis regions and analyzed by Lorenz et al. (2014), as well as the 11 areas reported in Lapotre et al. (2016) (Fig. 1). Furthermore, we expand the elevation coverage including 39 new areas where meter-scale bedforms are present covering dark-toned dunes (Supporting information S1 - section 1, Fig. S1 and Table S1).

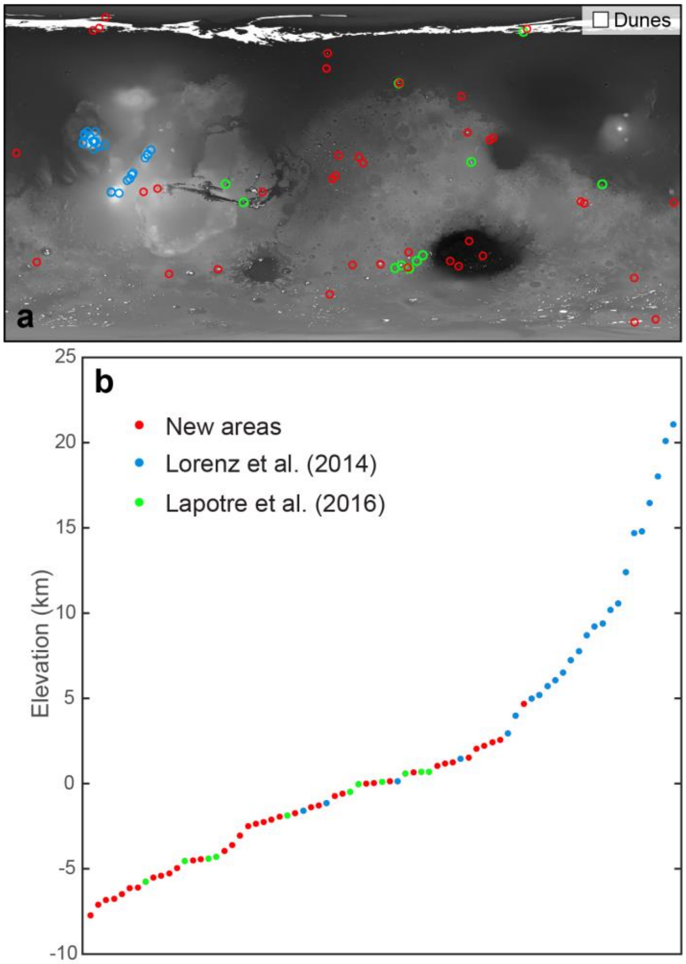

Figure 1. Location (a) and elevation distribution (b) of the 75 sites surveyed in this study. We analyzed the same 25 areas of Lorenz et al. (2014) as well as the 11 dark-tone dune sites previously analyzed by Lapotre et al. (2016). Our survey improves the spatial coverage, extends the range of surveyed elevations and provides a more continuous elevation sampling. A global dune catalog (Fenton, 2020; Hayward et al., 2014) is shown overlaying MOLA elevation data.

Previous surveys relied on the discrete manual measurements of crest-to-crest distances in randomly selected points (Lapotre et al., 2016; Lorenz et al., 2014). Here we applied a set of image processing and machine learning techniques which allow the mass automatic mapping of bedforms and the accurate measurement of their wavelengths (Fig. 2). We adapted the 2D Fast Fourier Transform approach introduced by Voulgaris and Morin (2008), implementing a multiscale scheme coupled with neural networks. This method allows the mapping and characterization of large ripples and transverse aeolian ridges (TARs) in a wide range of spatial scales and surface settings. See Supporting information S1 - section 2 for a in depth description of the method.

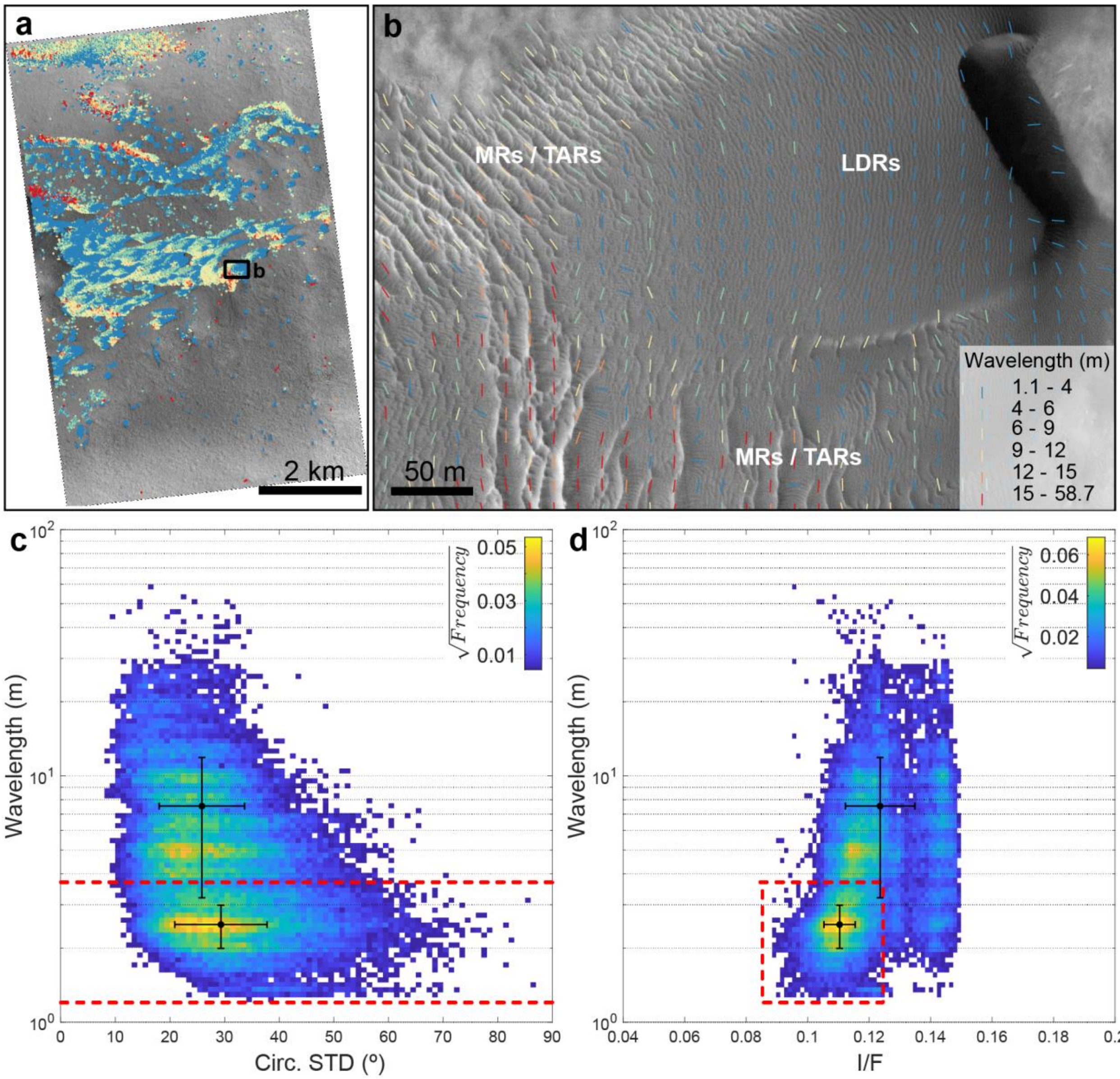

Figure 2. Wavelength survey of aeolian bedforms on Lyot crater (ESP_055318_2290, area 26 in Table S1). a) The applied method allows the full mapping and wavelength characterization of aeolian bedforms. b) Detailed view of the wavelength and trend of the mapped bedforms: large dark-toned ripples (LDRs) cover a barchan dune and have a spacing between crests of less than 4 m; megaripples (MRs) and transverse aeolian ridges (TARs) present higher albedos, higher wavelengths and are overlaid by the dune darker sediments. c and d) 2D histograms showing the

distribution of wavelength, circular standard deviation and albedo (I/F), a square root stretch is used to highlight secondary peaks. Red dashed lines correspond to the wavelength and albedo thresholds used to segment two bedform classes. The black dots and lines represent the computed averages and 1σ intervals.

Previous studies analyzed the relation between the average wavelength and atmospheric density at the surface, focusing on large ripples and TARs. To comply with this framework, we segment the mapped bedforms in two classes: a) large dark-toned ripples and b) a second class that comprises megaripples and TARs. Wavelength and relative grain size were proposed to be key parameters to discriminate different types of aeolian bedforms on Mars (Day & Zimbelman, 2021). We use albedo as a proxy for grain size, as it is usually assumed to be related to dust coating and/or to the presence of coarser particles (Sullivan et al., 2020). We examine the wavelength and albedo distributions using 2D histograms and we define threshold values that allow the partition of the mapping results, so that summary statistics can be computed for each class (see Supporting information S1 - section 3 for examples and Supporting information S2 for global results).

To evaluate the mechanisms that set the size of large ripples on Mars we test which model best describes the wavelength vs. atmospheric density relation observed in our dataset. We tested three models (refer to Supporting information S1 - section 5 for details): a) the wind-drag model of Lapotre et al. (2016), where the saturation length scale is approximated as that of fluvial bedload, b) a modified version of the same scaling, which instead uses a saturation length scale for aeolian saltation (Duran Vinent et al., 2019; Lapotre et al., 2021), and c) a generic inverse linear dependence between wavelength and atmospheric density (as proposed by Lorenz et al., 2014). We fit power laws and linear models to facilitate the comparison between our measurements and the models' predictions.

4 Results and discussion

Bedforms spaced between 1 to 100 m were mapped over a total area of ~2200 km^2 (Supporting information S2). The applied method correctly identifies the location of bedforms (93.7% of overall accuracy) and robustly measures their wavelength (we estimate a confidence interval of ±12%, Supporting information S1 - section 2). When comparing our data with previous surveys, we found a good agreement with large ripple measurements reported by Lapotre et al. (2016), which on average differ by 4%. Yet, the averages for the larger bedforms (megaripples and TARs) reported in the same study are severely underestimated by 84%, which we attribute to a possible under sampling. To assess the wavelength of these larger bedforms Lapotre et al. (2016) collected on average of 46 wavelength measurements on each site. This number of randomly located measurements may not be enough to characterize these populations, as they cover a small percentage of the mapped areas and form scattered patches of bedforms with variable wavelengths.

Our results for the Tharsis sites (which represent ~2/3 of the data analyzed in previous studies) show that Lorenz et al. (2014) values are systematically underestimated: on average they are 73% lower than the values obtained in this study (Fig. S10 and S11; Supporting information S1 - section 4). Indeed, some cited measurements there (e.g., 0.5-1.1 m) are dubious at best given HiRISE resolution (0.25 m/pix). The causes for this large disparity are less clear, nevertheless we note that in this case the measurement locations were not randomized, and that in some of the areas the spatial distribution of the bedforms is not uniform. These two factors may complicate the obtention of representative values from a few tens of scattered measurements.

Other potential sources of uncertainty are the elevation values reported for each site, which are used to derive the atmospheric pressure. We sampled the MOLA elevations at the centroid point of the largest bedform patch mapped in each area. However, previous works do not refer the sampling scheme or location where elevation values were collected. Therefore, in areas where the HiRISE footprints cover regions with higher elevation gradients (mainly in the Tharsis region) we can have elevation differences between our values and previous surveys of more than 2 km. This happens in four of the areas analyzed by Lorenz et al. (2014) (Fig. S11b).

We found several lines of evidence which support that Tharsis bedforms form a distinct population, apart from the large dark-toned ripples found elsewhere on Mars: a) as noted by Lapotre et al. (2021), we found that Tharsis bedforms have higher albedos (Fig. S12); b) we found that they have distinct thermal inertia (Putzig and Mellon, 2007) and dust cover index signatures (Ruff and Christensen, 2002), denoting lower thermal inertias (possibly associated with finer materials) and higher dust content/coverage (Fig. S13); c) as noted by others, Tharsis bedforms form unique patterns (Fig. S14) such as honeycomb or reticulate patterns (Bridges et al., 2010; Lorenz et al., 2014); and d) are in most cases associated with extensive mantling units, while large ripples outside Tharsis are typically found overlaying dark dunes (see Supporting information S1

- section 5 for details). These distinctive characteristics suggest that the two sets of bedforms should be considered separately when evaluating bedform-formation mechanisms.

The compiled data confirms the existence of a decrease of wavelength with increasing atmospheric density for the large dark-toned ripples (Fig. 3). Only five areas (~7%) deviate from this general tendency (Supporting information S1 - section 5 and Fig. S15), corresponding to cases where: a) sand sheets occupy a significant percentage of the mapped areas, suggesting the presence of coarse and/or poorly sorted sediments; and b) where dust devil tracks are visible covering the bedforms, suggesting limited migration/activity. These outliers are not included in the fits done to evaluate the proposed models, but their existence highlights two points: the accuracy and consistency of the measurements and the need to select comparable dune settings, as differences in grain size and sorting influence the wavelength of the bedforms.

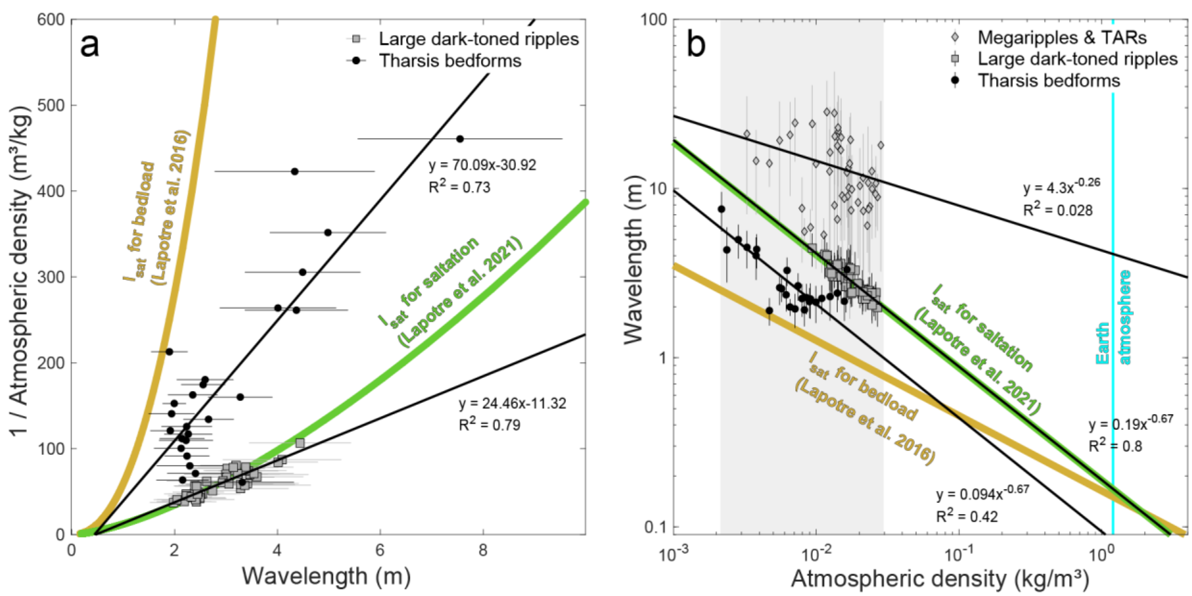

Figure 3. Relation between bedforms wavelength and Martian atmospheric density. The same data is shown in two different plots: a) highlighting the linear inverse relation proposed by Lorenz et al. (2014) and b) comparing with the models proposed by Lapotre et al. (2016; 2021), the gray area represents the maximum range of atmospheric densities on Mars while the cyan line represents the density of Earth's atmosphere. Black lines represent the best fitted models for each dataset, computed using the average wavelengths for each site (linear models in a) and power laws in b); the R^2 values in b) were computed in the log space). The golden line represents Lapotre et al. (2016) empirical relationship where transport saturation length is taken as that of fluvial bedload,

while the green line corresponds to a transport saturation length for aeolian saltation (Lapotre et al., 2021). A similar plot that includes the datasets used in previous studies is shown in Fig. S19.

The model obtained by fitting previous datasets which takes into account the bedload transport saturation length (Lapotre et al., 2016) predicts significantly lower wavelengths and a different scaling to the one we derived from our dataset. Conversely, our data for the dark-toned large ripples overlaps the predictions of the wind-drag model that uses the saltation transport saturation length, with a best fitted power law with ~2/3 scaling.

Tharsis data presents higher scattering, particularly for lower wavelengths where data points seem to converge towards the dark-toned ripple dataset. Due to the discrepancies found between our results and those of Lorenz et al. (2014), we note that the Tharsis data compiled in this study does not overlap or follow a similar scaling to the wind-drag model that considers a bedload transport saturation length (Fig. 3 and S19). Instead, the best fitted power law (R^2=0.42) has the same scaling (~2/3) of the model that uses the saltation transport saturation length.

The compiled data suggests that the mechanism that limits the size of large ripples on Mars is dependent on the atmospheric density. Overall, we observe that all our data are bounded by the two saturation length scaling laws, supporting the hypothesis that the equilibrium size of large martian ripples is controlled by an aerodynamic mechanism. The scaling laws for saturation length arise from idealized representations of transport in unimodal sediments. As previously discussed, the grain size distribution of the sediments on the Tharsis bedforms is probably more complex, which may contribute to the observed differences between Tharsis and non-Tharsis bedforms.

Even so, in accordance with previous studies (Lorenz, 2020; Lorenz et al., 2014) we notice that linear functions (which imply that $\lambda \propto 1/\rho_f$) also provide robust fits to the data (R^2=0.79 and 0.73 for the dark large ripples and Tharsis bedforms, respectively). In the case of the large ripples, both inverse and power law functions explain ~80% of the variance. This means that, strictly from a numeric point of view, we cannot discriminate what is the best model to fit the data. As previously mentioned, to fully test the impact ripple hypothesis we would need to consider the wind velocities at each site, something that could be done using climate model predictions.

Finally, the wavelengths of the larger bedforms (megaripples and TARs) present a large dispersion (Fig. 3B), not showing an obvious relation with any of the scaling laws. Linear or power law models do not produce a meaningful fit to the data (R^2=0.03). This suggests that at a global scale these bedforms do not form a homogeneous set and are probably not representative of the same boundary conditions (i.e., they likely formed with different grain size distributions, or under differing atmospheric conditions). Nonetheless, we cannot exclude the possibility that including TARs and megaripples in a same class may be flawed, especially since different degrees of mobility under present day winds have been described for the two sets of bedforms (Chojnacki et al., 2021; Silvestro et al., 2020).

For the dark-toned large ripples the degree of agreement between the global measurements and the predictions of the scaling relationship of Lapotre et al. (2021) (where saturation length is taken as that of aeolian saltation) is remarkable. Particularly if we consider that we are using a "static" average atmospheric density, which is merely a function of elevation and does not consider regional and seasonal atmospheric density variations. On the other hand, we cannot exclude that the density may just be one of the factors influencing the bedforms dimensions. As suggested by Lorenz (2020), wind speed at a global scale may increase with elevation creating a more complex interplay between density, wind speed and resulting bedform size.

5 Conclusions

This survey provides improved measurements to evaluate the mechanisms that set the size of bedform on Mars. We show that previous works used biased measurements, particularly for the bedforms located in the Tharsis region. We investigated the uniqueness of the bedforms located in this region, concluding that these bedforms form a distinct population and should be analyzed separately from the more common dark-toned large ripples that cover dunes outside Tharsis.

Our survey covers a larger range of elevations than previous works, and for the first time provides full wavelength mapping of extensive regions. Overall, our results are consistent with the predictions of the "wind-drag" hypothesis, favoring the model that considers a saltation transport saturation length. Still, the compiled morphometric data is not enough to refute the impact ripple hypothesis, as that would probably require the integration of variable wind velocities for each site.

The compiled dataset corroborates the existence of a robust relation between the wavelength of large dark-toned ripples and atmospheric density. Therefore, this new survey complements and helps to validate the main concept introduced in Lapotre et al. (2016): that paleoatmospheric density can be inferred for Mars by looking at the aeolian sedimentary record, providing an important tool to probe the evolution of the planet's environment.

Acknowledgments

This research was supported by CITEUC (UID/Multi/00611/2021&POCI-01- 0145-FEDER-006922) and by FCT grant CEECIND/02981/2017. M. C. and S.S. were funded by NASA Mars Data Analysis Program Grant 80NSSC20K1066. We thank the Laboratory for Advanced Computing at University of Coimbra for providing computing resources.

We acknowledge the valuable comments and suggestions made by Mathieu Lapotre and two anonymous reviewers to an earlier version of this work. We thank Rob Sullivan for insights on the morphodynamics of impact ripples.

Open Research

HiRISE images used in this work are publicly available at the Planetary Data System (https://hirise-pds.lpl.arizona.edu/PDS/) where details can be obtained at McEwen et al. (2007). The morphometric database compiled in this study is available at https://doi.org/10.6084/m9.figshare.21064657.

References

Andreotti, B, Claudin, P., & Pouliquen, O. (2006). Aeolian sand ripples: Experimental study of fully developed states. *Physical Review Letters*, *96*(2). https://doi.org/Doi 10.1103/Physrevlett.96.028001

Andreotti, Bruno, Claudin, P., Iversen, J. J., Merrison, J. P., & Rasmussen, K. R. (2021). A lower-than-expected saltation threshold at Martian pressure and below. *Proceedings of the National Academy of Sciences of the United States of America*, *118*(5). https://doi.org/10.1073/pnas.2012386118

Bagnold, R. A. (1954). *The Physics of Blown Sand and Desert Dunes* (2nd ed.). New York: Dover Publications, INC.

Baker, M. M., Lapotre, M. G. A., Minitti, M. E., Newman, C. E., Sullivan, R., Weitz, C. M., et al. (2018). The Bagnold Dunes in Southern Summer: Active Sediment Transport on Mars Observed by the Curiosity Rover. *Geophysical Research Letters*, *45*(17), 8853–8863. https://doi.org/10.1029/2018GL079040

Baker, M. M., Newman, C. E., Sullivan, R., Minitti, M. E., Edgett, K. S., Fey, D., et al. (2022). Diurnal Variability in Aeolian Sediment Transport at Gale Crater, Mars. *Journal of Geophysical Research: Planets*, *127*(2), 1–27. https://doi.org/10.1029/2020JE006734

Bridges, N. T., Banks, M. E., Beyer, R. A., Chuang, F. C., Noe Dobrea, E. Z., Herkenhoff, K. E., et al. (2010). Aeolian bedforms, yardangs, and indurated surfaces in the Tharsis Montes as seen by the HiRISE Camera: Evidence for dust aggregates. *Icarus*, *205*(1), 165–182. https://doi.org/10.1016/j.icarus.2009.05.017

Bridges, N. T., Ayoub, F., Avouac, J.-P., Leprince, S., Lucas, a, & Mattson, S. (2012). Earth-like sand fluxes on Mars. *Nature*, *485*(7398), 339–42. https://doi.org/10.1038/nature11022

Cheng, H., Liu, C., Li, J., Liu, B., Zheng, Z., Zou, X., et al. (2018). Experimental study of aeolian sand ripples in a wind tunnel. *Earth Surface Processes and Landforms*, *43*(1), 312–321. https://doi.org/10.1002/esp.4246

Chojnacki, M., Vaz, D. A., Silvestro, S., & Silva, D. C. A. (2021). Widespread Megaripple Activity Across the North Polar Ergs of Mars. *Journal of Geophysical Research: Planets*, 1–19. https://doi.org/10.1029/2021je006970

Day, M., & Zimbelman, J. R. (2021). Ripples, megaripples, and TARs, Oh, My! Recommendations regarding Mars aeolian bedform terminology. *Icarus*, *369*, 114647. https://doi.org/10.1016/j.icarus.2021.114647

Duran Vinent, O., Andreotti, B., Claudin, P., & Winter, C. (2019). A unified model of ripples and dunes in water and planetary environments. *Nature Geoscience*, *12*(5), 345–350. https://doi.org/10.1038/s41561-019-0336-4

Fenton, L. K. (2020). Updating the global inventory of dune fields on mars and identification of many small dune fields. *Icarus*, *352*(May), 114018. https://doi.org/10.1016/j.icarus.2020.114018

Foroutan, M., & Zimbelman, J. R. (2017). Semi-automatic mapping of linear-trending bedforms using ‘Self-Organizing Maps’ algorithm. *Geomorphology*, *293*(May), 156–166. https://doi.org/10.1016/j.geomorph.2017.05.016

Gonzalez, R. C., Woods, R. E., & Eddins, S. L. (2004). *Digital Image processing using MATLAB*. Upper Saddle River, NJ: Pearson/Prentice Hall.

Gough, T. R., Hugenholtz, C. H., & Barchyn, T. E. (2021). Re-Evaluation of Large Martian Ripples in Gale Crater: Granulometric Evidence for an Impact Mechanism and Terrestrial Analogues. *Journal of Geophysical Research: Planets*, *126*(12). https://doi.org/10.1029/2021JE007011

Hayward, R. K., Fenton, L. K., & Titus, T. N. (2014). Mars Global Digital Dune Database (MGD3): Global dune distribution and wind pattern observations. *Icarus*, *230*, 38–46. https://doi.org/10.1016/j.icarus.2013.04.011

Kok, J. F. (2010). An improved parameterization of wind-blown sand flux on Mars that includes the effect of hysteresis. *Geophysical Research Letters*, *37*(12), 1–6. https://doi.org/10.1029/2010GL043646

Lapotre, M. G. A., Ewing, R. C., Lamb, M. P., Fischer, W. W., Grotzinger, J. P., Rubin, D. M., et al. (2016). Large wind ripples on Mars: A record of atmospheric evolution. *Science*, *353*(6294), 55–58. https://doi.org/10.1126/science.aaf3206

Lapotre, M. G. A., Ewing, R. C., Weitz, C. M., Lewis, K. W., Lamb, M. P., Ehlmann, B. L., & Rubin, D. M. (2018). Morphologic Diversity of Martian Ripples: Implications for Large-Ripple Formation. *Geophysical Research Letters*, *45*(19), 10,229-10,239. https://doi.org/10.1029/2018GL079029

Lapotre, Mathieu G.A., Lamb, M. P., & McElroy, B. (2017). What sets the size of current ripples? *Geology*, *45*(3), G38598.1. https://doi.org/10.1130/G38598.1

Lapotre, Mathieu G.A., Ewing, R. C., & Lamb, M. P. (2021). An Evolving Understanding of Enigmatic Large Ripples on Mars. *Journal of Geophysical Research: Planets*, *126*(2), 1–8. https://doi.org/10.1029/2020JE006729

Lorenz, R. D. (2020). Martian Ripples Making a Splash. *Journal of Geophysical Research: Planets*, *125*(10), 12–15. https://doi.org/10.1029/2020JE006658

Lorenz, R. D., Bridges, N. T., Rosenthal, A. A., & Donkor, E. (2014). Elevation dependence of bedform wavelength on Tharsis Montes, Mars: Atmospheric density as a controlling parameter. *Icarus*, *230*, 77–80. https://doi.org/10.1016/j.icarus.2013.10.026

Manukyan, E., & Prigozhin, L. (2009). Formation of aeolian ripples and sand sorting. *Physical Review E - Statistical, Nonlinear, and Soft Matter Physics*, *79*(3).

https://doi.org/10.1103/PhysRevE.79.031303

McEwen, A. S., Eliason, E. M., Bergstrom, J. W., Bridges, N. T., Hansen, C. J., Delamere, W. A., et al. (2007). Mars Reconnaissance Orbiter's High Resolution Imaging Science Experiment (HiRISE). *Journal of Geophysical Research-Planets*, *112*(E5). https://doi.org/Doi 10.1029/2005je002605

Moller, M. F. (1993). A Scaled Conjugate-Gradient Algorithm for Fast Supervised Learning. *Neural Networks*, *6*(4), 525–533. https://doi.org/Doi 10.1016/S0893-6080(05)80056-5

Putzig, N. E., & Mellon, M. T. (2007). Apparent thermal inertia and the surface heterogeneity of Mars. *Icarus*, *191*(1), 68–94. https://doi.org/10.1016/j.icarus.2007.05.013

Rasmussen, K. R., Valance, A., & Merrison, J. (2015). Laboratory studies of aeolian sediment transport processes on planetary surfaces. *Geomorphology*, *244*, 74–94. https://doi.org/10.1016/j.geomorph.2015.03.041

Ruff, S. W., & Christensen, P. R. (2002). Bright and dark regions on Mars: Particle size and mineralogical characteristics based on thermal emission spectrometer data. *Journal of Geophysical Research E: Planets*, *107*(12), 1–22. https://doi.org/10.1029/2001je001580

Sharp, R. P. (1963). Wind Ripples. *Journal of Geology*, *71*(5), 617–636. Retrieved from http://www.jstor.org/stable/30061128

Silvestro, S., Fenton, L. K., Vaz, D. A., Bridges, N. T., & Ori, G. G. (2010). Ripple migration and dune activity on Mars: Evidence for dynamic wind processes. *Geophysical Research Letters*, *37*(20), L20203. https://doi.org/Doi 10.1029/2010gl044743

Silvestro, S., Vaz, D. A., Ewing, R. C., Rossi, A. P., Fenton, L. K., Michaels, T. I., et al. (2013). Pervasive aeolian activity along rover Curiosity's traverse in Gale Crater, Mars. *Geology*, *41*(4), 483–486. https://doi.org/Doi 10.1130/G34162.1

Silvestro, S., Vaz, D. A., Yizhaq, H., & Esposito, F. (2016). Dune-like dynamic of Martian Aeolian large ripples. *Geophysical Research Letters*, *43*(16), 8384–8389. https://doi.org/10.1002/2016GL070014

Silvestro, S., Chojnacki, M., Vaz, D. A., Cardinale, M., Yizhaq, H., & Esposito, F. (2020). Megaripple Migration on Mars. *Journal of Geophysical Research: Planets*, *125*(8). https://doi.org/10.1029/2020JE006446

Smith, D. E., Zuber, M. T., Solomon, S. C., Phillips, R. J., Head, J. W., Garvin, J. B., et al. (1999). The Global Topography of Mars and Implications for Surface Evolution, *284*(May), 1495–1503.

Soille, P. (2002). *Morphological Image Analysis - Principles and Applications*. Berlin: Springer-Verlag.

Sullivan, R., & Kok, J. F. (2017). Aeolian saltation on Mars at low wind speeds. *Journal of Geophysical Research: Planets*, *122*(10), 2111–2143. https://doi.org/10.1002/2017JE005275

Sullivan, R., Kok, J. F., Katra, I., & Yizhaq, H. (2020). A Broad Continuum of Aeolian Impact Ripple Morphologies on Mars is Enabled by Low Wind Dynamic Pressures. *Journal of Geophysical Research: Planets*, *125*(10), 1–39. https://doi.org/10.1029/2020je006485

Sullivan, R., Baker, M., Newman, C., Turner, M., Schieber, J., Weitz, C., et al. (2022). The Aeolian Environment in Glen Torridon, Gale Crater, Mars. *Journal of Geophysical Research: Planets*, *127*(8), 1–39. https://doi.org/10.1029/2021JE007174

Swann, C., Sherman, D. J., & Ewing, R. C. (2020). Experimentally Derived Thresholds for Windblown Sand on Mars. *Geophysical Research Letters*, *47*(3), 1–10. https://doi.org/10.1029/2019GL084484

Taubman, D. S., & Marcellin, M. W. (2002). JPEG2000: Standard for interactive imaging. *Proceedings of the IEEE*, *90*(8), 1336–1357. https://doi.org/10.1109/JPROC.2002.800725

Vaz, D. A., & Silvestro, S. (2014). Mapping and characterization of small-scale aeolian structures on Mars: An example from the MSL landing site in Gale Crater. *Icarus*, *230*, 151–161.

Vaz, D. A., Sarmento, P. T. K., Barata, M. T., Fenton, L. K., & Michaels, T. I. (2015). Object-based Dune Analysis: Automated dune mapping and pattern characterization for Ganges Chasma and Gale crater, Mars. *Geomorphology*, *250*, 128–139. https://doi.org/10.1016/j.geomorph.2015.08.021

Vaz, D. A., Silvestro, S., Sarmento, P. T. K., & Cardinale, M. (2017). Migrating meter-scale bedforms on Martian dark dunes: Are terrestrial aeolian ripples good analogues? *Aeolian Research*, *26*, 101–116. https://doi.org/10.1016/j.aeolia.2016.08.003

Voulgaris, G., & Morin, J. P. (2008). A long-term real time sea bed morphology evolution system in the South Atlantic Bight. *Proceedings of the Ieee/Oes/Cmtc Ninth Working Conference on Current Measurement Technology*, 71–79.

Weitz, C. M., Sullivan, R. J., Lapotre, M. G. A., Rowland, S. K., Grant, J. A., Baker, M., &

Yingst, R. A. (2018). Sand Grain Sizes and Shapes in Eolian Bedforms at Gale Crater, Mars. *Geophysical Research Letters*, *45*(18), 9471–9479. https://doi.org/10.1029/2018GL078972

Withers, P., & Smith, M. D. (2006). Atmospheric entry profiles from the Mars Exploration Rovers Spirit and Opportunity. *Icarus*, *185*(1), 133–142. https://doi.org/10.1016/j.icarus.2006.06.013

AGU PUBLICATIONS

Geophysical Research Letters

Supporting Information for

Constraining the mechanisms of aeolian bedform formation on Mars through a global morphometric survey: Supporting information S1

David A. Vaz[1], Simone Silvestro[2,3], Matthew Chojnacki[4] and David C. A. Silva[1]

[1]Centre for Earth and Space Research of the University of Coimbra, Observatório Geofísico e Astronómico da Universidade de Coimbra, Coimbra, Portugal.

[2]INAF Osservatorio Astronomico di Capodimonte, Napoli, Italia.

[3]SETI Institute, Carl Sagan Center, Mountain View, CA, USA.

[4]Planetary Science Institute, Lakewood, CO, USA.

Contents of this file

Introduction

This file includes a detailed explanation of the applied methods, auxiliary data, supplementary figures and tables.

Text S1.

1. DATA AND GLOBAL BEFORM SURVEYS

To investigate the relation between atmospheric pressure (as function of elevation) and the wavelength of Martian large ripples we analyze a total of 75 HiRISE images (Table S1), some of which were previously surveyed by other authors. Namely, the first 11 areas are the same reported by Lapotre et al. (2016), while the last 25 areas are the same analyzed by Lorenz et al. (2014) in the Tharsis region. We provide a complete mapping of the HiRISE images, extending the elevation coverage (Fig. S1b) and filling the gaps of previous works.

The new areas were selected based on the presence of dark-toned dunes or sand sheets which are covered by large ripples. Besides the Tharsis cluster that corresponds to the Lorenz et al. (2014) dataset, the selected areas are scattered across Mars surface (Fig. S1a). We primarily use full resolution HiRISE data (0.25 m/pix), although 0.5 m/pix images were used in five areas (this coarser spatial resolution is still enough to identify and map large ripples).

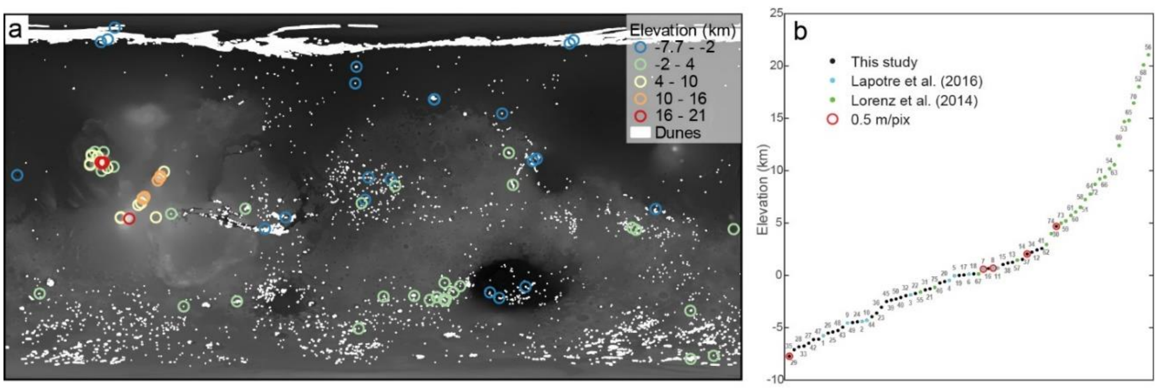

Fig. S1 – Global map and elevation distribution of the study areas. a) Location of the study areas, the global distribution of dune fields is shown in white (Fenton, 2020; Hayward et al., 2013). b) Elevations of the mapped areas, the different colors highlight the areas which were analyzed in previous studies (Lapotre et al., 2016; Lorenz et al., 2014); the numbers next to each dot correspond to the IDs in Table 1; areas where lower resolution 50 cm/pixel data were used are also noted. In this study we extend the sampled elevation range and provide more continuous coverage.

Table S1 – List of surveyed areas, including their location and spatial resolution. A full record of the information compiled in this study can be found at https://doi.org/10.6084/m9.figshare.21064657.

Area ID	Image	Spatial resolution (m/pix)	Location	Previous studies
1	ESP_027864_2295_RED	0.25	Acidalia Mensa	Lapotre et al. 2016
2	ESP_018854_1755_RED	0.25	Gale crater	Lapotre et al. 2016
3	ESP_034909_1755_RED	0.25	Juventae Chasma	Lapotre et al. 2016
4	ESP_025042_1375_RED	0.25	SE of Yaonis Regio	Lapotre et al. 2016
5	ESP_011421_1300_RED	0.25	Hellespontus	Lapotre et al. 2016
6	ESP_041987_1340_RED	0.25	Proctor crater	Lapotre et al. 2016
7	ESP_011909_1320_RED	0.50	SE of Proctor crater	Lapotre et al. 2016
8	ESP_024502_1305_RED	0.50	SW of Proctor crater	Lapotre et al. 2016
9	PSP_001970_1655_RED	0.25	Coprates Chasma	Lapotre et al. 2016
10	ESP_018011_2565_RED	0.25	North Polar erg	Lapotre et al. 2016
11	ESP_039955_1875_RED	0.25	S of Nili Patera	Lapotre et al. 2016
12	ESP_013790_1035_RED	0.25	Planum Australe	
13	ESP_049439_1165_RED	0.25	Sisyphi Planum	
14	ESP_023913_1275_RED	0.25	Thaumasia	
15	ESP_021509_1325_RED	0.25	Kaiser Crater	
16	ESP_048154_1255_RED	0.25	S Eridania	
17	ESP_022320_1335_RED	0.25	Terra Sirenum	
18	ESP_022422_1300_RED	0.25	Ogygis Undae	
19	ESP_032941_1310_RED	0.25	Noachis Terra	
20	ESP_019570_1390_RED	0.25	North of Rabe Crater	
21	PSP_009758_2030_RED	0.25	Baldet Crater	
22	ESP_037082_1870_RED	0.25	S Arabia Terra	
23	ESP_018500_2000_RED	0.25	Crater NE of Jezero	
24	ESP_045307_2580_RED	0.25	Mare Boreum	
25	PSP_010413_1920_RED	0.25	Pettit Crater	
26	ESP_055318_2290_RED	0.25	Lyot Crater	
27	ESP_037201_2450_RED	0.25	Lomonosov Crater	
28	ESP_024237_1315_RED	0.25	Hellas Planitia	
29	ESP_022668_1340_RED	0.25	Hellas Planitia	
30	ESP_028410_1710_RED	0.50	Noctis Labyrinthus	
31	ESP_034274_1780_RED	0.25	Meridiani Planum	
32	PSP_001513_1655_RED	0.25	Gusev Crater	
33	ESP_025054_1370_RED	0.25	Hellas Planitia	
34	ESP_017610_1730_RED	0.25	Noctis Labyrinthus	
35	PSP_008097_1450_RED	0.50	Hellas Basin	
36	ESP_028856_1710_RED	0.25	Ganges Chasma	
37	ESP_022151_1660_RED	0.50	Crater West of Herschel	
38	PSP_002860_1650_RED	0.25	Herschel Crater	
39	ESP_035948_1900_RED	0.25	Arabia Terra	
40	ESP_043742_1800_RED	0.25	Meridiani Planum	
41	ESP_040058_1020_RED	0.25	Ultima Lingula	
42	ESP_062177_2370_RED	0.25	Kunowsky Crater	
43	ESP_062168_2585_RED	0.25	Mare Boreum	

44	ESP_063282_2225_RED	0.25	Renaudot Crater	
45	ESP_057799_1910_RED	0.25	Arabia Terra	
46	ESP_058788_1320_RED	0.25	Asimov Crater	
47	PSP_009721_2370_RED	0.25	Kunowsky Crater	
48	ESP_017426_2570_RED	0.25	Scandia Cavi	
49	ESP_018427_2640_RED	0.25	Mare Boreum	
50	ESP_061119_1990_RED	0.25	North of Jezero Crater	
51	PSP_005387_1935_RED	0.25	Ascraeus Mons	Lorenz et al. 2014
52	PSP_005032_1985_RED	0.25	Olympus Mons	Lorenz et al. 2014
53	PSP_006811_1910_RED	0.25	Ascraeus Mons	Lorenz et al. 2014
54	PSP_002249_1805_RED	0.25	Pavonis Mons	Lorenz et al. 2014
55	ESP_011928_2025_RED	0.25	NW of Olympus Mons	Lorenz et al. 2014
56	PSP_008460_1980_RED	0.25	Olympus Mons	Lorenz et al. 2014
57	PSP_005546_1960_RED	0.25	E of Olympus Mons	Lorenz et al. 2014
58	ESP_013655_1710_RED	0.25	Arsia Mons	Lorenz et al. 2014
59	PSP_005441_1970_RED	0.25	Olympus Mons	Lorenz et al. 2014
60	ESP_012310_1715_RED	0.25	Arsia Mons	Lorenz et al. 2014
61	PSP_002118_2015_RED	0.25	Olympus Mons	Lorenz et al. 2014
62	PSP_003476_1940_RED	0.25	Olympus Mons	Lorenz et al. 2014
63	PSP_001642_1895_RED	0.25	Ascraeus Mons	Lorenz et al. 2014
64	PSP_005783_1775_RED	0.25	Pavonis Mons	Lorenz et al. 2014
65	PSP_004754_1915_RED	0.25	Ascraeus Mons	Lorenz et al. 2014
66	PSP_004109_2010_RED	0.25	Olympus Mons	Lorenz et al. 2014
67	ESP_013998_2035_RED	0.25	Olympus Mons	Lorenz et al. 2014
68	PSP_005111_1985_RED	0.25	Olympus Mons	Lorenz et al. 2014
69	PSP_005084_1810_RED	0.25	Pavonis Mons	Lorenz et al. 2014
70	PSP_008341_1705_RED	0.25	Arsia Mons	Lorenz et al. 2014
71	PSP_010780_1805_RED	0.25	Pavonis Mons	Lorenz et al. 2014
72	PSP_010213_1785_RED	0.25	Pavonis Mons	Lorenz et al. 2014
73	PSP_005322_1955_RED	0.25	Olympus Mons	Lorenz et al. 2014
74	PSP_008803_1980_RED	0.25	Olympus Mons	Lorenz et al. 2014
75	ESP_014341_2035_RED	0.25	Olympus Mons	Lorenz et al. 2014

2. RIPPLE PATTERN MAPPING AND WAVELENGTH SURVEY

Different methods have been proposed to automatically map aeolian bedforms from HiRISE images. Previous studies mapped bedform crests, producing a set of polylines that can be used to assess bedform trends and lengths (Foroutan & Zimbelman, 2017; Vaz & Silvestro, 2014). These outputs can be used to study bedforms' spatial variations and patterns, however when applied at a dune field scale they generate a large set of crestlines, requiring subsequent spatial integration/generalization (Vaz et al., 2017). Furthermore, given the high number of ripples that can be present on one image, the size of the output datasets may be of the same order of magnitude of the image itself (a few gigabits), which complicates the study of these bedforms at a global level.

Here we address these limitations by applying a new approach to Mars data for detection and quantification of bedform metrics, namely wavelength. We adapted the 2D Fast Fourier Transform (2D FFT) approach described by Voulgaris and Morin (2008) to study seabed bedforms, implementing a multiscale search scheme that allows the identification and characterization of large ripples and TARs (Transverse Aeolian Ridge) at different spatial scales. Figure S2 illustrates the adopted procedure.

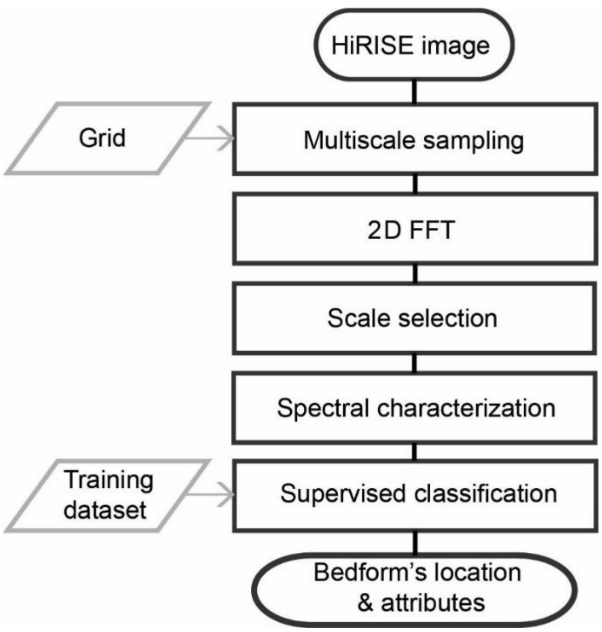

Fig. S2 - Flowchart with the main processing steps used to map and characterize large ripples and TARs using HiRISE images. See text for details.

Multiscale sampling

The technique we use to map the location of the bedforms and extract precise wavelength measurements begins with the creation of a regular grid which overlaps the HiRISE scene. A grid spacing of 15 m is used, so that we guarantee that each grid note includes several large ripples crests (~3 m spacing between crests). We then sample the image content around the grid nodes, with different spatial resolutions and window sizes (Fig. S3a). HiRISE images are stored in JP2000 image file format, therefore we take advantage of the wavelet-based compression algorithm that is used in this format (Taubman & Marcellin, 2002) to sample the image at different scales (Fig. S3c-f). A dyadic sampling scheme is implemented, where the spatial resolution (r_s) at each scale/reduction level (L) is given as a function of the images' spatial resolution (r_i):

$$r_s = r_i * 2^L \qquad \text{(Eq. 1)}$$

This implies that the extent of the sampled area and the examined wavelength at each scale also increases proportionally to 2^L, while the dimensions of the sampled areas are constant. For instance, when L=0 the band-pass filter that is later applied in the spectral domain preserves wavelengths in the range 1-5 m, while when L=1 the range is 2-10 m (Fig. S3g-j). The only required input is the maximum wavelength of analysis, which is derived from a preliminary inspection of the image and that corresponds to the estimated maximum TAR spacing. This parameter is used to define the maximum L, controlling the maximum scale of analysis.

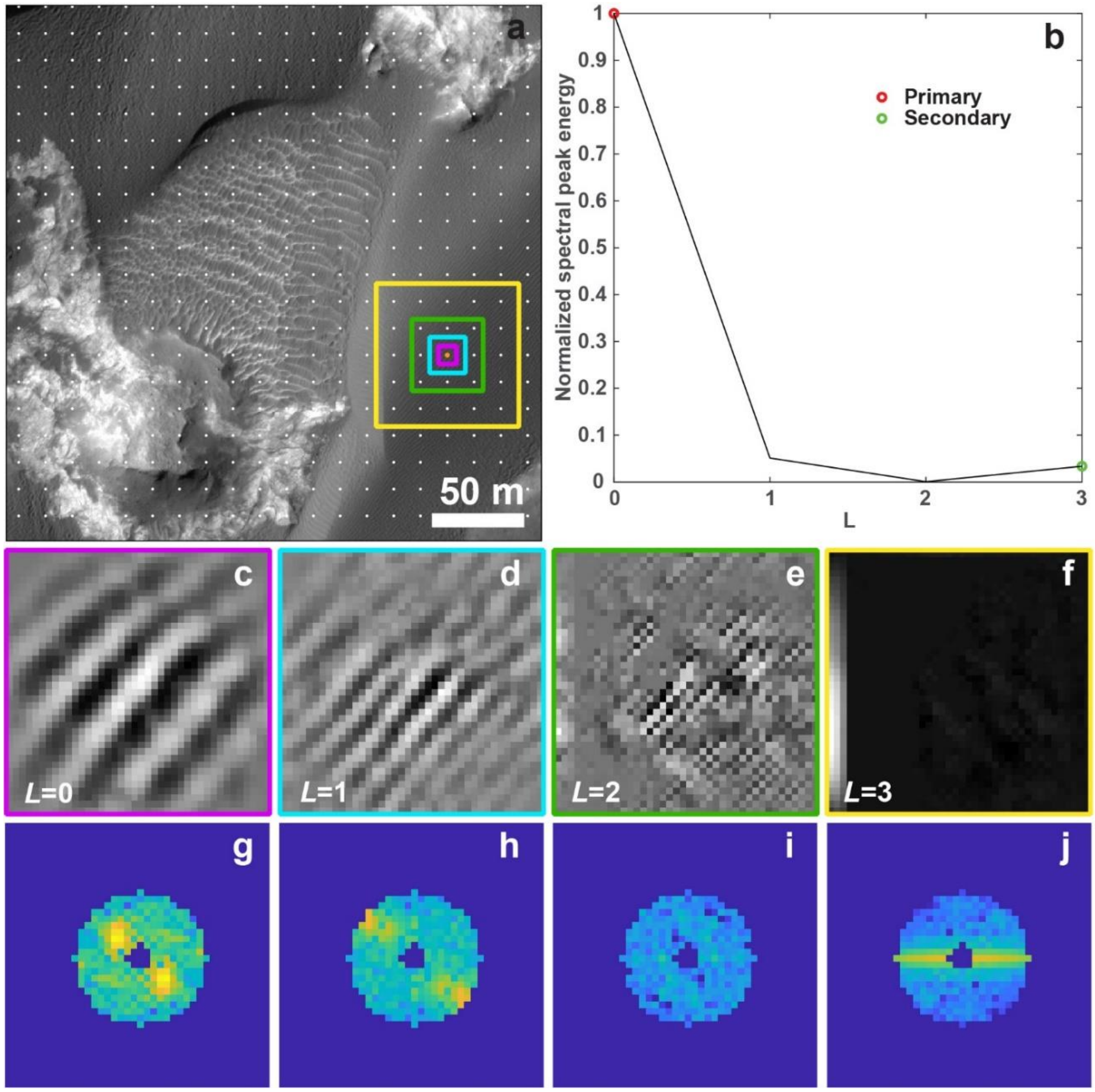

Fig. S3 – Example of the adopted sampling scheme and scale selection procedure (Area 2: ESP_018854_1755_RED). a) A grid with 15 m spacing is created and for each node the image is sampled at different spatial resolutions and extents (the colored outlines correspond to the extent of the sampled areas for each *L*, c-f). b) normalized peak energy (derived from g-j), the identification of the primary and secondary local maxima allows the selection of the best scales of analysis, i.e. the ones with more relevant and sharpest content. c-f) sampled datasets which include the filtering pre-processing described in the following section, note the smoother appearance of the corner areas created by the imposed circular taper function. Large ripples with straight crests are discernible when $0 \leq L \leq 2$, while for *L*=3 the albedo variation due to dune topography is the only recognizable feature. g-j) shifted 2D FFT spectra (values were stretched with a log transformation) for each *L*, a band pass filter is used to subset the target wavelengths at each scale. At *L=0* a strong peak is present, denoting the preferential trend and periodicity of the large ripples. The maximum energy at each scale is used to select the best scale/s of analysis (b).

2D FFT analysis and scale selection

The objective of the described sampling scheme is to implement the spectral characterization (which provides the characterization of the bedforms, for instance their trend and wavelength) in the most suitable scale of analysis, the same way as a mapper would use different zoom levels (i.e. different scales of analysis) to map ripples or larger TARs. To remove long wavelength components (e.g. created by dune topography) and increase the image contrast we subtract top-hat and bottom-hat (Soille, 2002) filtered versions of the input areas (a circular structuring element with radius 8 is used). To reduce the artifacts caused by the non-isotropic sampling (the sampled areas have square shapes) we multiply the matrix by a circular taper function (computed as the normalized Euclidean distance to the central pixel). Figures S3c-f show the results of these operations, which prepare the data for the subsequent spectral analysis.

A 2D spectrum is computed for each filtered area/scale using the FFT. A band-pass filter is applied in the spectral domain, which subsets the analyzed wavelength range on each scale. The same scaling function described in Eq. 1 is used to define the target wavelength ranges, starting at a range of 1-5 m for L=0 (Fig. S3g-j). Power spectrums (the square of the transform magnitudes; Gonzalez et al., 2004) are computed and the spectral peak energies (S_L) are collected for each scale (Voulgaris & Morin, 2008). This is the parameter used to choose the most relevant scale (i.e. the scale with the sharpest periodic features), which is found by identifying the local maxima of the peak spectral energy across scales (Fig. S3b). In certain situations, different sets of bedforms with different trends and wavelengths overlap in the same areas, which translates in the existence of a secondary maxima. If present, the two local maxima are recorded, while if only one is present the secondary scale is set as $argmax(S_L)-1$. No secondary maxima is derived when $argmax(S_L)$ is one.

Spectral and textural characterization

The objective of this processing step is twofold: 1) measure the trend and wavelength of the bedforms, and 2) assemble a sparse set of descriptors that summarize image proprieties and textures, to be used in the following classification step. Table S1 lists the computed parameters and detail how they were computed while Fig. S4 show some examples. The same descriptors are computed for the two selected scales and stored in a database. We adopted the same approach described by Voulgaris and Morin (2008) to measure the wavelength and the trend of the bedforms. Additionally, we apply a kernel-based technique to analyze the circular distribution derived from the spectral analysis in order to parameterize bimodal circular distributions (Vaz et al., 2015), which is of relevance since the trend of large ripples may not be unidirectional.

Table S2 – List of parameters compiled for the identified primary and secondary scales.

Description	Descriptors	Details	References
Selected scale/reduction level	L (Fig. S4b)	See previous section for details	
Normalized peak energy	S_L	e.g., Fig. S3b	
Azimuth	Trend of the spectral peak	Sub-pixel interpolation using the neighborhood of the maximum peak	(Voulgaris & Morin, 2008)
Wavelength	Wavelength of the spectral peak (Fig. S4e)	Sub-pixel interpolation using the neighborhood of the maximum peak	(Voulgaris & Morin, 2008)
Average trend and wavelength	Mean vector trend, circular standard deviation (Fig. S4d), circular skewness and kurtosis. Wavelength weighted average and standard deviation.	Spectral energies are used as weighting factor.	
Directional modes	Trend of the primary and secondary modes. Primary mode kernel frequency (Fig. S4f) and kernel frequency ratio.	Spectral energies are used as weighting factor and a kernel window of 20º is used to create the circular kernel function (see Vaz et al., 2015 for details).	(Vaz et al., 2015)
Spectral proprieties	Maximum peak energy. Peak and quality indices (Fig. S4c).	Provide textural context and can be regarded as proxies for bedform/image sharpness	(Voulgaris & Morin, 2008)
Lambert albedo	Lambert albedo (I/F) average and standard deviation	Computed using the scaling factors and offsets obtained from the HiRISE label files	

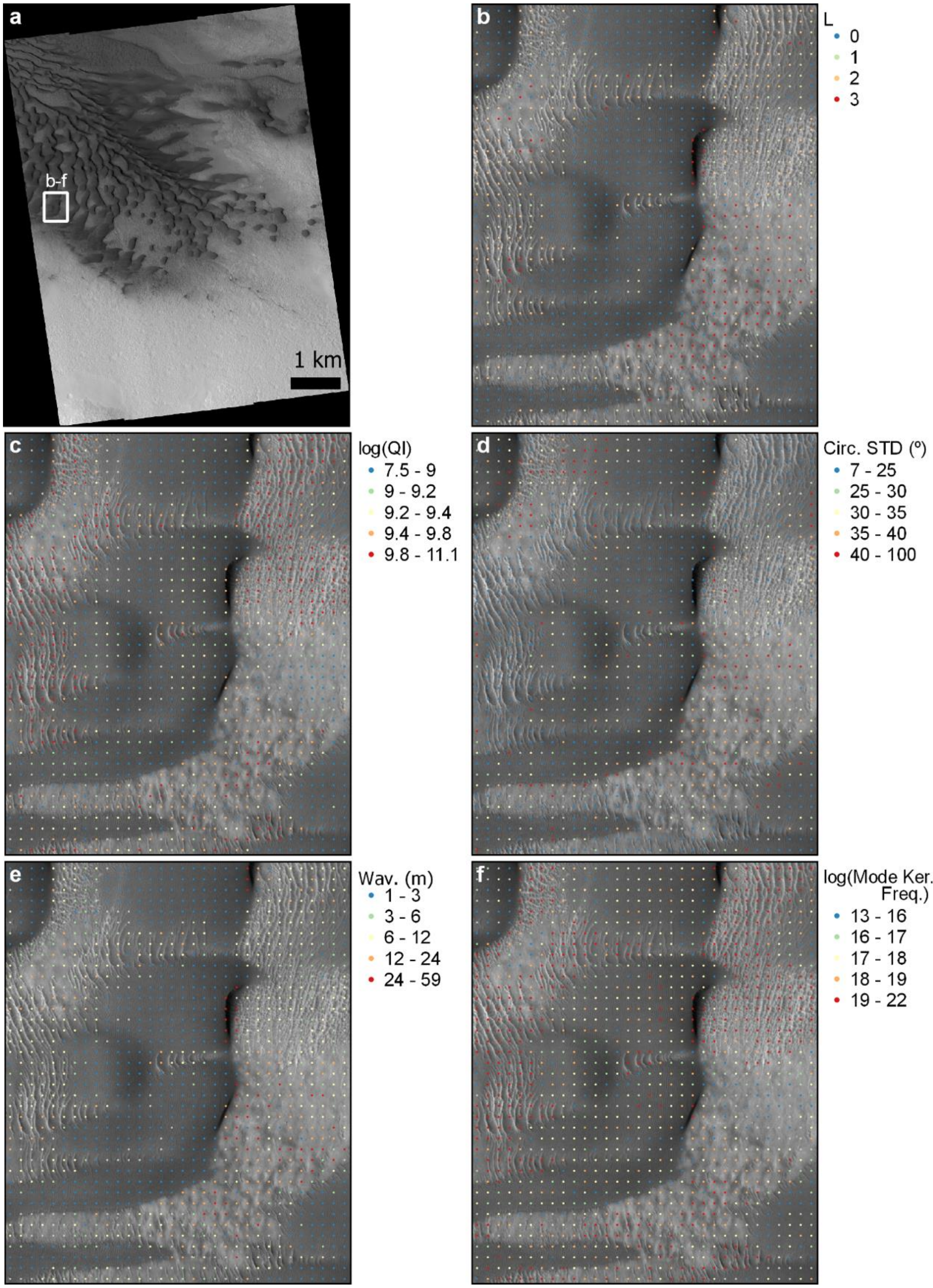

Fig. S4 – Examples of pattern descriptors used in the classification process (see Table S2 for details and Fig. S5 for the classification outputs). a) HiRISE image (Area 1: ESP_027864_2295_RED). b) Selected primary scale. c) Quality index (stretched using a log scaling). d) Circular standard deviation. e) Spectral peak wavelength. f) Kernel frequency of the main mode (stretched using a log scaling).

Supervised classification

Bedforms are typically scattered covering different types of surfaces (e.g. bedrock, regolith), and do not usually form a continuous patch. Therefore, we need to discriminate two classes: targeted bedforms (large ripples, megaripples and TARs) and bedrock (including slipfaces and other long-wavelength or shadowed terrains). To achieve this, we implemented a supervised classification using artificial neural networks (ANN). We use a feedforward ANN architecture with one input, one hidden (38 nodes) and one output layer (two nodes). We use hyperbolic tangent transfer functions and conjugate gradient backpropagation (Moller, 1993) to train the networks.

All the fields listed in Table S2 that correspond to azimuthal information are excluded from the classification procedure (using them would result in directional bias). The remaining parameters for the primary and secondary scales are normalized (min-max normalization) to serve as inputs to the ANN classifier. The training datasets were digitized for each area using QGIS and a random partition (train, test, and validation datasets) is performed. Fig. S5 show examples of training data and output final classification.

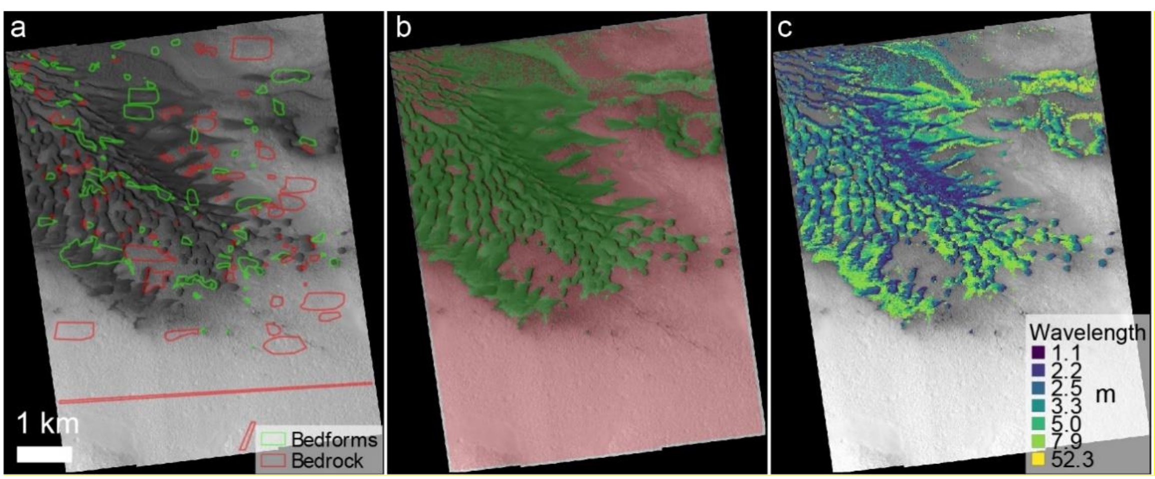

Fig. S5 - Classification process overview. a) Labeled training data (Area 1: ESP_027864_2295_RED). b) Output classification (accuracy of 96.6%). c) Measured bedform wavelength.

Accuracy Assessment

To assess the performance of the described technique we need to evaluate two types of accuracies: 1) classification accuracy: how well can we identify and map bedforms?; and 2) wavelength accuracy: can we retrieve accurate wavelength measurements?

The first question is addressed by creating confusion matrices and computing the overall accuracy and kappa index to evaluate the classification results. Overall, the training data corresponds to 7.5% of total mapped area, with a prevalence (percentage of bedform class in the training dataset) of 59%. The overall classification accuracy is 93.7% (kappa index of 0.87) which demonstrates the excellent performance of the proposed technique (Table S3).

Table S3 – Accuracy of the supervised classification with two classes: bedforms (large ripples and TARs) and bedrock (other non-bedforms features). Overall accuracy ranges from 0 to 100%, with 100% denoting a perfect classification. Kappa index range from 0 to 1, where 0 corresponds to a random non-agreement case. Prevalence is the percentage of training data that correspond to the positive case (bedform class), ideally if should be ~50%. N is the number of mapped grid nodes. The training dataset corresponds to 7.5% of the total mapped area.

Area ID	Accuracy (%)	Kappa index	Prevalence (%)	N	Train %
1	96.6	0.93	58.1	20923	10.0
2	98.0	0.87	90.7	56423	15.9
3	97.8	0.93	19.6	19659	7.3
4	92.5	0.83	66.2	28902	14.6
5	92.3	0.84	63.8	39844	10.7
6	88.0	0.73	68.6	29173	17.3
7	94.3	0.86	28.1	14635	3.7
8	96.1	0.91	66.3	60308	20.0
9	93.4	0.81	79.6	52435	16.7
10	96.0	0.91	68.5	9534	2.6
11	93.4	0.87	47.5	21168	6.8
12	94.1	0.86	71.4	16189	3.0
13	94.5	0.87	30.8	6779	5.8
14	90.2	0.80	50.7	13724	14.2
15	94.7	0.87	29.0	15132	5.1
16	92.9	0.85	60.1	11059	5.2
17	99.2	0.95	91.4	29229	13.2
18	91.3	0.81	37.1	31141	11.6
19	94.8	0.90	44.6	31954	15.5
20	90.2	0.80	43.3	46403	22.8
21	95.0	0.84	17.0	17445	3.3
22	88.7	0.76	33.0	14769	8.5
23	98.0	0.96	46.2	19334	6.1
24	96.1	0.92	63.7	23035	5.7
25	94.8	0.88	67.0	39433	9.7
26	98.1	0.96	66.5	22238	9.5
27	94.8	0.89	57.4	8663	1.7

28	94.4	0.89	44.3	11122	5.2
29	89.9	0.70	17.4	15666	7.6
30	94.1	0.52	91.8	45895	6.0
31	97.0	0.94	45.5	13917	3.9
32	92.3	0.72	81.5	28053	5.2
33	87.8	0.75	54.9	27698	8.5
34	95.3	0.89	71.0	13885	6.0
35	85.3	0.71	47.6	77548	12.9
36	92.6	0.76	83.1	15699	7.0
37	93.5	0.87	45.7	13657	12.0
38	90.4	0.80	35.9	11340	3.2
39	95.3	0.91	47.0	23407	8.4
40	97.3	0.95	53.2	38685	14.1
41	94.6	0.88	67.4	4484	3.0
42	92.1	0.84	55.3	18859	7.8
43	98.7	0.96	18.5	14804	7.1
44	93.1	0.83	27.2	17261	9.8
45	96.5	0.90	78.6	19742	16.3
46	93.3	0.75	86.4	31039	11.6
47	92.0	0.82	65.4	31130	7.8
48	93.9	0.87	37.1	43224	11.8
49	94.5	0.88	64.4	52921	7.3
50	95.2	0.90	64.4	20660	9.2
51	91.8	0.72	81.2	32572	6.8
52	96.4	0.8	12.9	4926	1.4
53	90.4	0.8	34.8	11924	4.3
54	96.2	0.9	17.2	4521	3.6
55	93.7	0.7	84.4	14067	6.6
56	99.5	0.8	1.4	13800	5.8
57	90.3	0.8	59.2	41672	10.4
58	98.9	1.0	16.4	28720	26.1
59	90.6	0.8	70.4	15438	3.3
60	97.7	0.9	81.0	25090	6.8
61	90.5	0.8	70.8	16495	6.1
62	89.4	0.8	67.3	11844	2.5
63	97.8	0.9	27.9	10764	3.1
64	98.0	0.9	17.0	5810	3.4
65	90.8	0.8	38.0	36124	10.8
66	98.2	1.0	36.6	5438	2.1
67	92.6	0.5	92.8	49404	15.9
68	89.1	0.8	56.1	5046	0.9
69	99.1	1.0	75.5	21921	4.4
70	98.0	0.9	15.1	11501	5.4
71	99.3	0.7	1.2	8536	2.9

72	96.7	0.8	10.0	3379	1.4
73	97.6	0.8	90.9	32621	8.1
74	91.1	0.7	19.4	18819	3.7
75	93.4	0.8	77.7	46119	10.9
Total	93.71	0.87	58.8	1766778	7.45

To evaluate the accuracy of the wavelength measurements we use hillshade images of synthetic bedforms' topography, modelled with a superellipse function (Eq. 2). Transverse bedform topography is modelled with n=0.4 and h= λ /10 (h represents the maximum height of the bedforms and corresponds to 1/10 of the wavelength λ). The length of the bedforms is assumed to scale with wavelength (λ*50) and is controlled with a longitudinal taper, obtained with n=4 and h=1.

$$|x|^n + \left|\frac{y}{h}\right|^n = 1 \qquad \text{(Eq. 2)}$$

Random azimuths allow to test the directional precision of the adopted technique. Fig. S6a-c shows examples of the test datasets, displaying periodic bedform-like features with different trend and spacing. In Fig. S6d we evaluate our measurements (peak and average) for a wide range of wavelengths. Peak wavelengths provide the most accurate predictions (average error of 3% and trend accuracy below 1^{o}, Table S4) and present narrower uncertainty bars. Additionally, we demonstrate the stability of the sampling and scale selection schemes, with a regular progression of L with increasing wavelength (Fig. S6d).

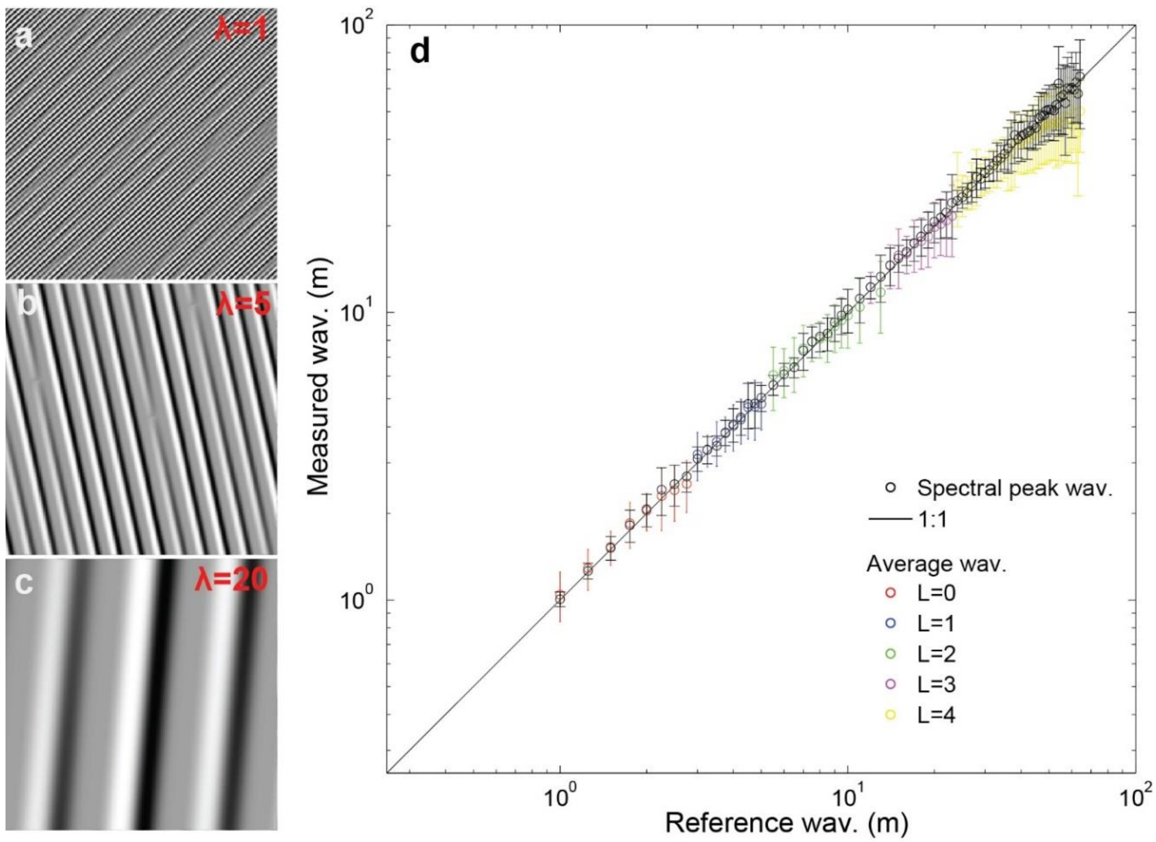

Fig. S6 – Wavelength accuracy assessment using synthetic hillshade views of periodic bedform-like patterns. a-c) Examples of the datasets created using random trends (λ corresponds to the crest spacing in meters). d) Measured vs. modelled wavelength, the black line corresponds to a perfect agreement case while two different wavelength estimates are shown: the spectral peak wavelength which produces more accurate results across all scales of analysis and with smaller uncertainty bars, and the average wavelength with larger uncertainty bars. The different scales of analysis (*L*) are depicted in different colors, note the congruent sequency of selected scales when wavelength increases.

Table S4 – Wavelength percentual error and azimuth error computed using synthetic datasets (Fig. S6). We estimate wavelength errors of 3% and trend errors of less than 1º.

Measurement type	Wavelength percent error (average±STD %)	Azimuth error (average ±STD º)
Spectral peak	2.7±2.3	-0.1±0.8
Spectral average	6.4±6.9	-0.01±0.6

Finally, a total of 978 reference wavelength measurements were compiled in QGIS (e.g. Fig. S7a) and compared with our results. Fig. S7b highlights the linear response of the mapping algorithm for a large range of values. We compute an average percentual difference of -0.7±11.9% (Table S5), which demonstrates that the obtained results are not biased and that differences are within a standard deviation interval of ±12%. Besides this detailed local assessment, section 4 presents a global comparison with previously published measurements.

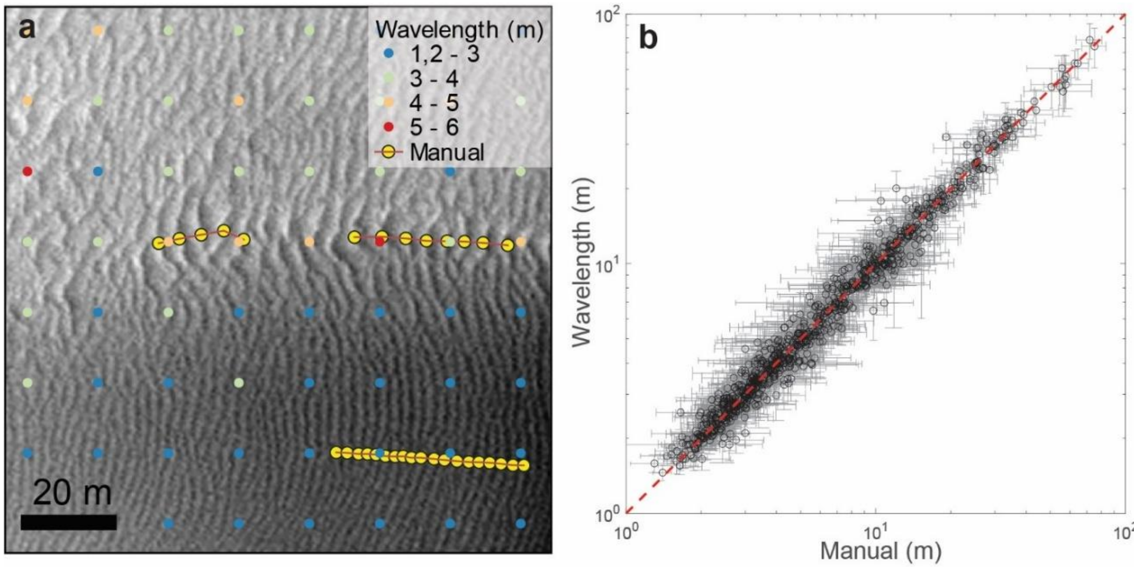

Fig. S7 – Comparison of wavelength measurements. a) Example of reference wavelength measurements obtained by mapping successive bedform crests (yellow dots), the peak wavelength obtained automatically is also shown. b) automated wavelength estimates vs. manually derived measurements (manual estimates were averaged and integrated into the sampling grid using a 7.5 m spatial buffer), the red line corresponds to a 1:1 ratio.

Table S5 – Wavelength was compared for five different areas, including one with coarser spatial resolution. Overall, we estimate that the obtained wavelengths are comparable to manually derived measurements within a ±12% confidence interval.

Area ID	Percent difference (average±STD %)	N	Spatial resolution (m/pix)
1	-0.8±11.6	331	0.25
2	-1.7±14.4	181	0.25
3	-0.6±12.5	192	0.25
4	0.7±9	111	0.25
8	-0.1±10.1	163	0.5
All	-0.7±11.9	978	

3. BEDFORM POPULATION SEGMENTATION AND SUMMARY STATISTICS

Two main characteristics are commonly used to discriminate and classify Martian aeolian bedforms from remote sensing imagery: wavelength and albedo (Day & Zimbelman, 2021). We use an exploratory and iterative approach to set threshold values for these two parameters. This allows a quantitative and more objective segmentation of the bedform types. To the purpose of this work, we discriminate two classes: large ripples and megaripples & TARs. We create 2D kernel density histograms using the mapped bedform's wavelength (e.g. Fig. S5c), HiRISE Lambertian albedo (I/F) and circular standard deviation (here used as a proxy to crest straightness). These plots are inspected for each area, and putative wavelength and albedo thresholds are selected (Fig. S8e, f). These values are then tested/visualized in QGIS and iteratively adjusted (Fig. S8b-d). In most cases this is a straightforward process, since large ripples cover extensive areas, thus forming clear maxima corresponding to meter-scale wavelengths and low albedos. Fig. S8 shows how the threshold values identified in the histograms correspond to clear pattern changes in map view. Supporting information S2 includes the histograms and global map views for all the mapped areas.

In this work we focus on a first order segmentation, collapsing the data into two classes. Yet, in some areas the plots also highlight the presence of second order sub-populations, which may be attributed to the effect of dune topography and/or granulometric differences (for instance between putative megaripples and TARs, Fig. S9). A finer analysis and clustering are thus possible, although it is out of the scope of this paper.

Summary statistics (wavelength mean and standard deviation) are computed for the two classes and constitute the basis of the following analysis. To help to identify outliers and evaluate possible relations between dune morphology and large ripples morphometry, we identified the type of dunes in the areas mapped outside Tharsis (Fig. S15), as that region lacks dark dunes. Most areas present more than one dune type, therefore we used a dual classification scheme, visually identifying a primary and secondary dune types. Primary class corresponds to the type of dune most abundant, in terms of relative area.

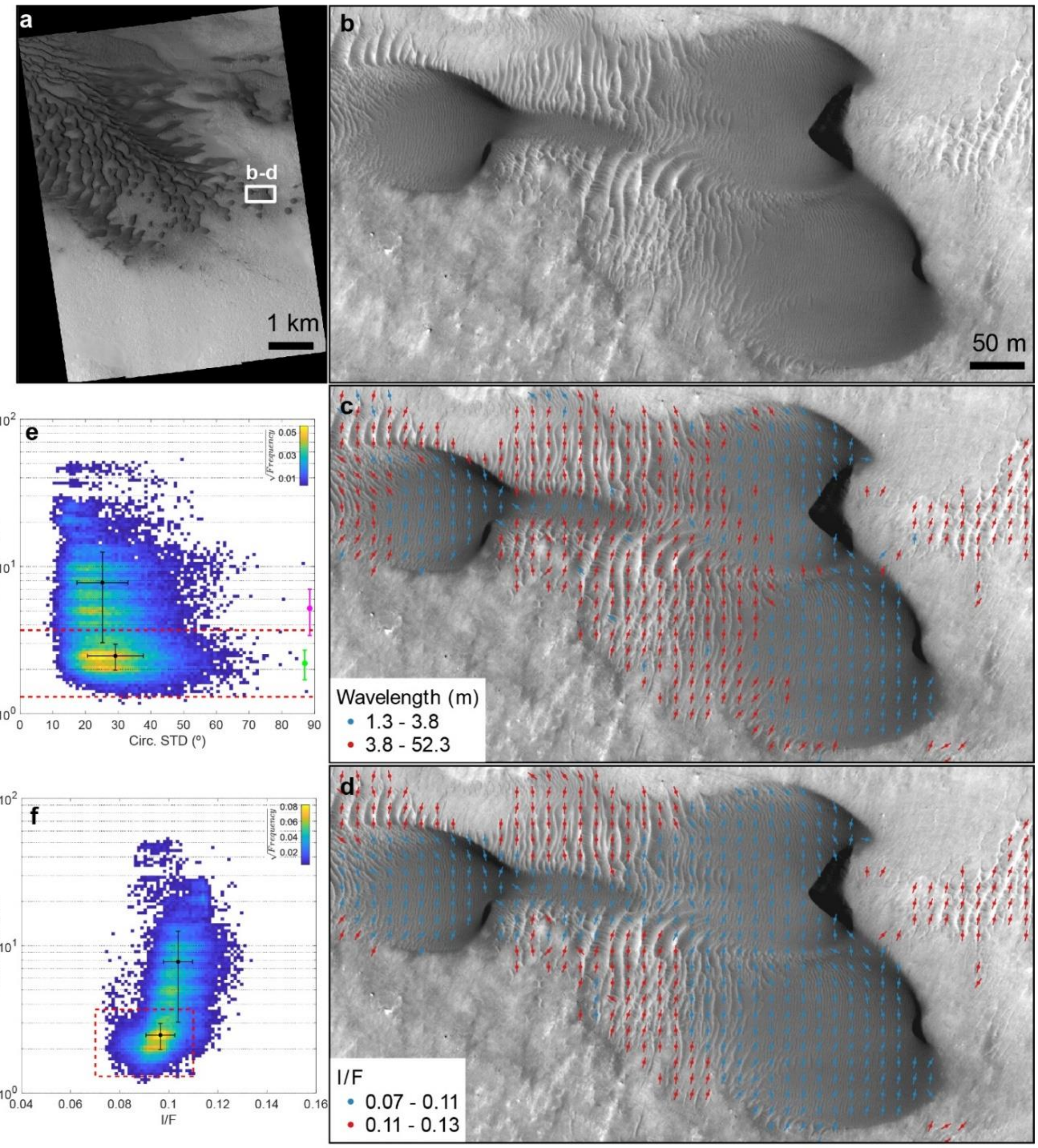

Fig. S8 – Bedform segmentation using wavelength and albedo threshold values derived from 2D histograms. a, b) HiRISE image (Area 1: ESP_027864_2295_RED). c) map view of the two classes defined using a wavelength threshold range of 1.3-3.8 m (large ripples) and >3.8 m (megaripples & TARs); these values correspond to the red dashed lines in (e); the trend of the mapped bedforms is also shown. d) map view of the two classes defined using an albedo threshold range of 0.07-0.11 (large ripples) and >0.11 (megaripples & TARs); these values correspond to the vertical red dashed lines in (f); the trend of the mapped bedforms is also shown. e) 2D histogram relating bedforms' wavelength and circular standard deviation (to improve readability the frequencies were scaled with a square root function), the defined threshold values are depicted as red dashed lines (figure (c) provides a map view), note the main maxima corresponding to a wavelength of ~2.5 m; the black dots and variation intervals correspond to the averages and standard deviations computed for the segmented classes; the green (large ripples) and magenta (TARs) dots located near the right edge of the plot correspond to the summary statistics of Lapotre et al. (2016). f) 2D histogram relating bedforms' wavelength and albedo (frequencies were scaled with a square root function), the defined threshold values are depicted

as a red square (figures (c, d) provide map views of the two parameters); the black dots and intervals correspond to the computed averages and standard deviations.**

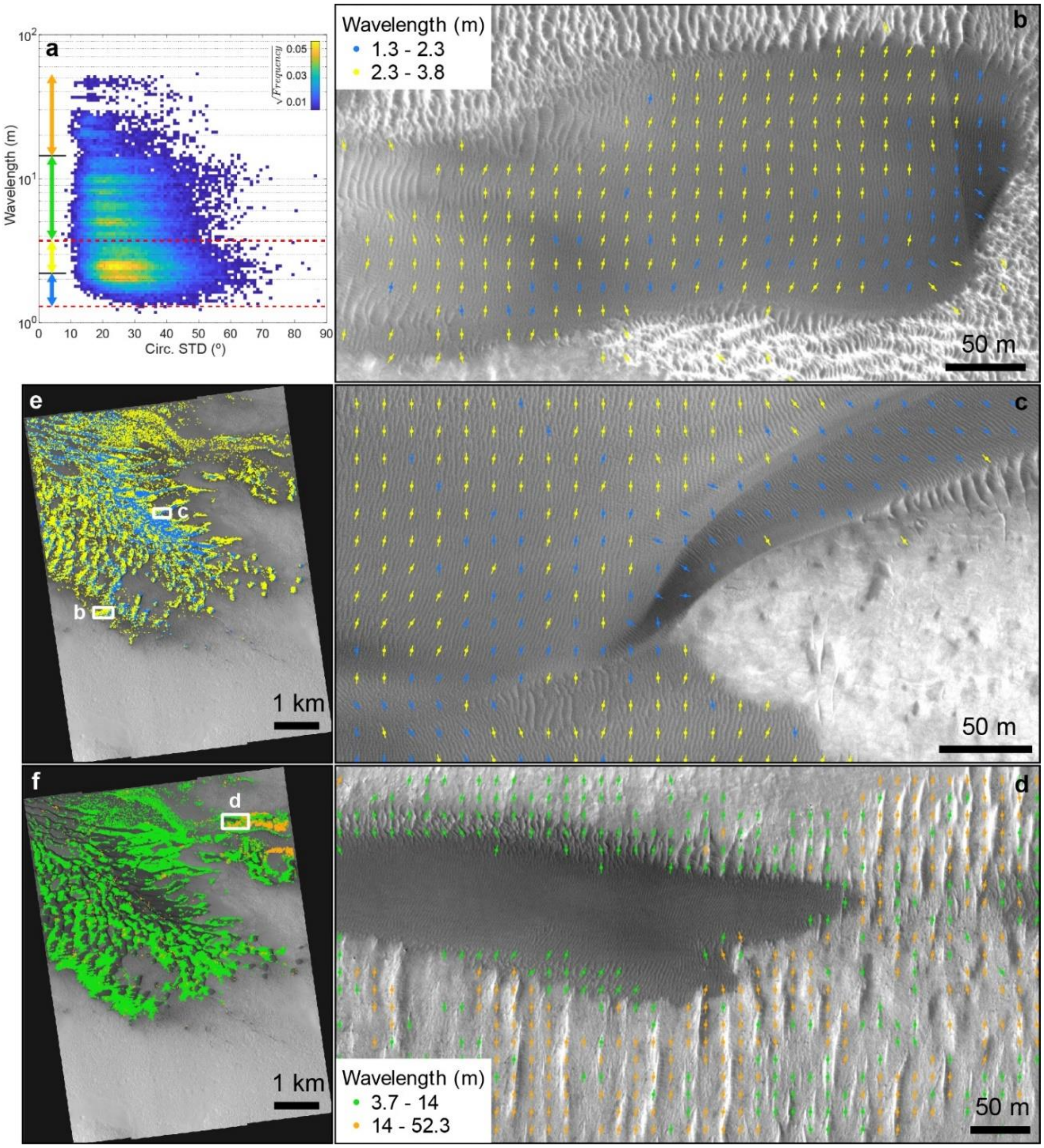

**Fig. S9 - To establish direct comparisons with previous studies only a first order bedform segmentation is discussed in this work (Fig. S8), nevertheless this example illustrates the possibility to pursuit more detailed studies in the future. a) 2D histogram showing the wavelength intervals that produce the partition shown in the map views, the first order wavelength thresholds correspond to the red dashed lines while the colored double arrows identify the wavelength intervals shown in the map views. b, c, e) possible secondary partition of the large meter-scale ripples, bedforms with less than 2.3 m appear clustered in the center of the dune field (e) and occur in the downwind sections of some dunes (b, c). d, f) possible megaripples are widespread (f), have wavelengths between 3.7 and 14 m, are located in the

lower sections of the dunes and appear in continuity with large ripples (d), while TARs have larger wavelengths and are mainly located in the NE corner of the mapped area (f).

4. COMPARISON WITH PUBLISHED MEASUREMENTS

In this section we compare our results with the ones obtained by Lapotre et al. (2016) and Lorenz et al. (2014) for a total of 11 and 25 areas, respectively (Table S6). The average large ripples wavelengths computed in this study are inline with the values reported by Lapotre et al. (2016) (Fig. S10a). On average, we estimate a percentual difference of 4±10% with a maximum difference of 21% for Area 2 (Table S6). If we also consider the standard deviation intervals, we conclude that the two sets of measurements are very similar, presenting overlapping distributions (Fig. S10a and Table S6). The case of the larger bedforms seems to be different, with an average percentual difference of 84±83% and a maximum of 236%. Even if we have overlapping distributions in four areas (Fig. S10b, note how in some cases the standard deviation intervals intersect the 1:1 line), half of Lapotre et al. (2016) areas clearly show an underestimation of the larger bedforms' wavelengths (data points and standard deviations below the 1:1 curve, Fig. S10b).

In summary, our wavelength estimates for the large ripples are consistent with the measurements made by Lapotre et al. (2016). We found that for most of the areas the averages differ by less than 10%, approximately the same confidence interval derived from the comparison made with manually derived measurements in this work (±12% confidence interval, Table S5). To understand the larger discrepancies associated with the larger bedforms, one must question if the sampling used by Lapotre et al. (2016) was enough to characterize these populations. Focusing in the two areas with larger differences (Areas 6 and 8), Lapotre et al. (2016) collected 36 and 40 measurements for TARs and 136 and 98 for large ripples. These were randomly sampled across the HiRISE scenes. Yet, our complete mapping reveals that TARs only cover a small fraction of the mapped areas (38 and 20% respectively), in addition TARs tend to form disperse sets of bedforms with variable wavelengths. Therefore, we hypothesize that a more complete sampling would be needed to characterize these populations and that this is the main reason for the observed wavelength disparities.

Lorenz et al. (2014) values are consistently underestimated when compare with our measurements (Fig. S10a). On average, their values differ by 73±106% with a maximum percentual difference of 563% (Area 55, Table S6). In this specific area, Lorenz et al. (2014) reported an average wavelength of 0.5 m, which is a questionable estimate since it only corresponds to two pixels. This was noted in Lapotre et al. (2021), which replace this value by an estimated wavelength of ~1 m (see their Fig. 2). In each area Lorenz et al. (2014) sampled approximately 40 sets of bedforms, divided by four selected sub-areas. Among other possible causes (e.g. non-random sampling), also in this case we hypothesize that under sampling may have contributed to the measured differences. Bedforms in the Tharsis region do not form unambiguous dune fields or sand sheets, and most of the times they are scattered or preferentially located in depressions. This non-uniform spatial distribution may further complicate the obtention of representative wavelength samples from a few tens of measurements. In section 5 we argue that Tharsis bedforms represent a different type of bedforms and that merging the two datasets is not appropriate. In any case, from the validation presented in section 2 and from the comparison with Lapotre et al. (2016) results we determine that wavelengths derived with our method are robust, which means Lorenz et al. (2014) results denote a systematic underestimation (Fig. S11a).

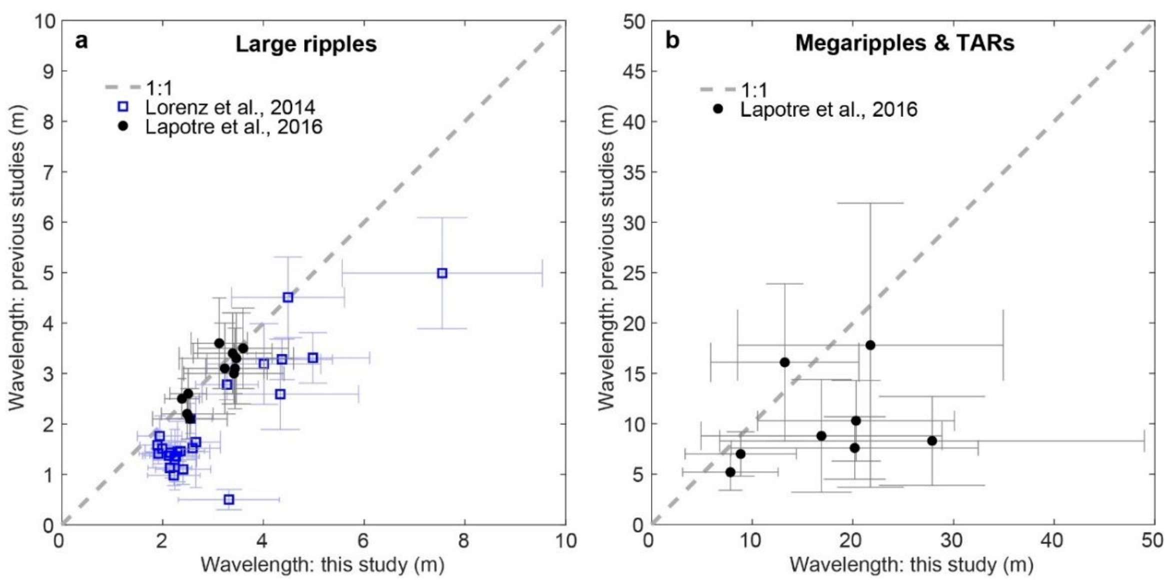

Fig. S10 – Comparison of wavelength measurements. a) Large ripples, there is a good agreement with Lapotre et al. (2016) values and error bars always overlap the 1:1 (perfect agreement) line; when compared with our data, Lorenz et al. (2014) measurements are clearly underestimated. b) In the case of the larger bedforms, half of Lapotre et al. (2016) values are comparable to our data, while the other half seems to be relatively underestimated.

Previous works used MOLA elevations to compute atmospheric density, so this is also a variable we try to verify and compare. The elevations presented in this work are automatically extracted from the MOLA MEGDR (Mission Experiment Gridded Data Records), which represent elevations above the areoid with a spatial resolution of 463 m/pixel (Smith et al., 1999). The spatial centroids of the largest bedform patches mapped in each area are used as sampling points. Lorenz et al. (2014) mentions that their elevation data was derived from MOLA data, however they do not provide any other detail (e.g. specific sampling locations, reference datum or methods used to collect the elevation values). In their supplementary materials, Lapotre et al. (2016) mentions that Lorenz's data "were measured with respect to the Mars Reconnaissance Orbiter reference ellipsoid" and that for this reasons they have corrected the data to be consistent with the areoid datum used in their survey. We applied the same correction, converting Lorenz's (2014) elevations to orthographic heights.

We found a good agreement with Lapotre et al. (2016) elevations (Fig. S11b), the only exception is Area 3, which has an elevation difference of ~700 m. In this specific case, elevations inside the mapped area can vary by ~ 1000 m, therefore the mentioned discrepancy can be attributed to the different sampling location.

We found significant differences between the elevations computed in this work and part of the elevations reported in Lorenz et al. (2014). In four areas differences can range between 2 and 3 km (Fig. S11b). Also in this case, differences are likely caused by a different sampling location. The Tharsis region extreme topography result in large elevation variations across the HiRISE image footprints. In some cases, maximum elevation differences of ~4 km are possible, depending where in the image footprint the MOLA data is sampled.

We conclude that relevant elevation differences may exist between studies. These are due to the uncertain location of the sampling points and produce higher disparities for the studied areas located in the Tharsis region. We implicitly use the location of the mapped bedforms to define the sampling points, thus we adopt a more consistent and robust methodology which reduces the uncertainty in the measurement of this variable.

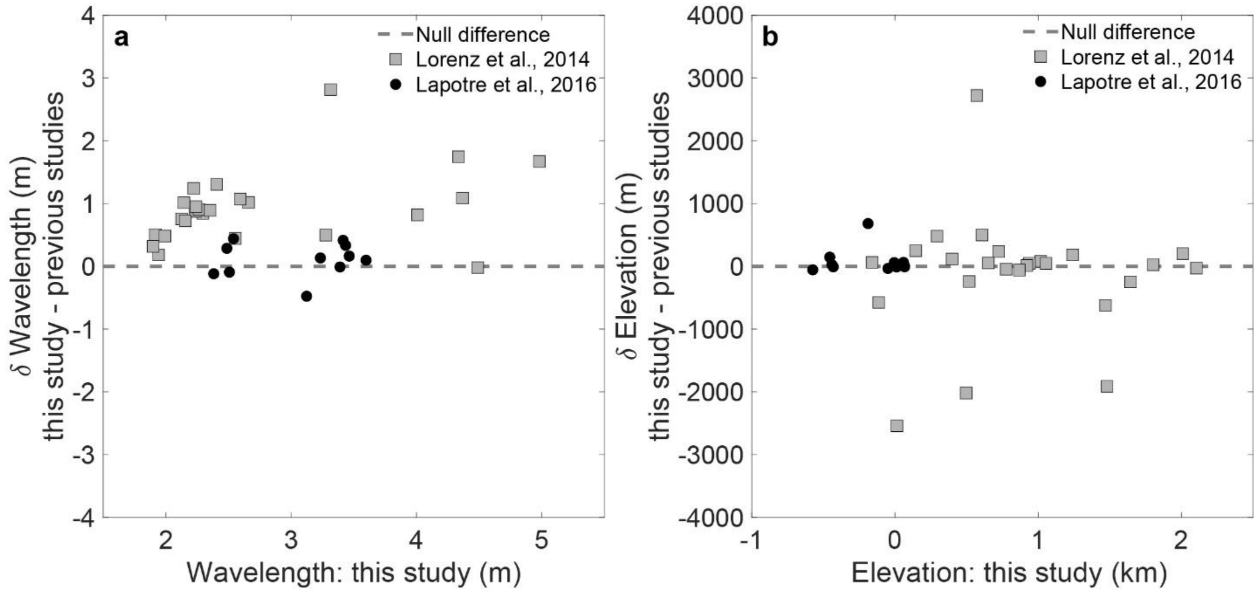

Fig. S11 – Differences in large ripples' average wavelength and elevation. a) Wavelength differences between our measurements and Lapotre et al. (2016) are small and cluster around 0 m, while Lorenz et al. (2014) dataset presents higher discrepancies and are consistently bellow the values obtained in this study. b) Lapotre et al. (2016) elevation values are consistent with our work, except for Area 3 which has an elevation difference of ~700 m, yet this is understandable since inside the mapped area elevations can vary by ~ 1000 m; the differences with Lorenz et al. (2014) measurements are more relevant, with elevation differences that can reach 3 km, which is justified by the fact that high slope areas in the Tharsis region (e.g. Olympus Mons basal scarp) can produce large topographic differences (we measured elevation ranges up to 4 km) even inside the relatively small footprint of an HiRISE image.

Table S6 – Comparison of wavelength summary statistics, the first 11 areas correspond to the areas analyzed by Lapotre et al. (2016) while area IDs above 51 correspond to the 25 areas studied in Lorenz et al. (2014). Summary statistics (average and standard deviation) are reported, and percentual errors were computed according to: 100*($Wav_{\text{this study}}$ – $Wav_{\text{other studies}}$) / $Wav_{\text{other studies}}$.

	Large ripples		TARs & megaripples		Percentual differences	
Area ID	Wav. avg. ± STD (m)	Wav. avg. ± STD (Lapotre, 2016 / Lorenz, 2014)	Wav. avg. ± STD (m)	Wav. avg. ± STD (Lapotre, 2016 / Lorenz, 2014)	LRs % difference	TARs % difference
1	2.5 ± 0.5	2.2 ± 0.5	7.8 ± 4.8	5.2 ± 1.8	13.0	50.7
2	2.5 ± 0.7	2.1 ± 0.6	8.9 ± 5.5	7 ± 2.2	20.9	26.5
3	3.4 ± 1	3 ± 0.6	13.2 ± 7.4	16.1 ± 7.8	13.8	-17.8
4	3.6 ± 0.9	3.5 ± 0.8	16.9 ± 12	8.8 ± 5.6	2.8	91.8
5	3.5 ± 1.1	3.3 ± 0.9	21.7 ± 13.2	17.8 ± 14.1	5.0	22.2
6	3.2 ± 0.8	3.1 ± 0.9	20.2 ± 12.3	7.6 ± 3.1	4.3	165.6
7	3.4 ± 0.6	3.1 ± 0.8	20.3 ± 9.8	10.3 ± 4	10.8	97.3
8	3.1 ± 0.6	3.6 ± 0.9	27.9 ± 21.1	8.3 ± 4.4	-13.2	235.8
9	2.5 ± 0.4	2.6 ± 0.5	7.4 ± 4.1		-3.6	
10	2.4 ± 0.3	2.5 ± 0.4	9.6 ± 7		-4.7	

11	3.4 ± 0.8	3.4 ± 0.8	13 ± 7.7	-0.3
51	2.7 ± 0.5	1.6 ± 0.9	7.4 ± 4.7	62.1
52	5 ± 1.1	3.3 ± 0.5		50.5
53	4.4 ± 1	3.3 ± 0.4	13.1 ± 9.9	33.1
54	2.6 ± 0.4	2.1 ± 0.3	6 ± 1.2	21.0
55	3.3 ± 1	0.5 ± 0.2	12.4 ± 5.7	563.0
56	7.5 ± 2	5 ± 1.1	17.8 ± 2.1	51.3
57	2.3 ± 0.6	1.5 ± 0.6	16.3 ± 14	58.3
58	2.2 ± 0.5	1.4 ± 0.2	7.6 ± 4	64.3
59	2.1 ± 0.4	1.1 ± 0.2	5.1 ± 3.7	89.7
60	1.9 ± 0.4	1.4 ± 0.2	5.6 ± 1.1	35.8
61	2.3 ± 0.5	1.4 ± 0.2	5 ± 1.3	66.5
62	2.2 ± 0.4	1.3 ± 0.6	4.1 ± 0.9	73.7
63	2.6 ± 0.5	1.5 ± 0.2	19.2 ± 13.4	70.6
64	1.9 ± 0.4	1.8 ± 0.4	24.4 ± 10	10.3
65	4 ± 1.1	3.2 ± 0.8	14.6 ± 7.5	25.7
66	2.4 ± 0.5	1.5 ± 0.2	4.3 ± 0.6	61.1
67	2.4 ± 0.5	1.1 ± 0.3	6.6 ± 4.2	118.7
68	4.3 ± 1.6	2.6 ± 0.7	10.5 ± 1.2	67.4
69	1.9 ± 0.4	1.6 ± 0.3	14.1 ± 3.9	20.1
70	4.5 ± 1.1	4.5 ± 0.8	21 ± 14	-0.5
71	3.3 ± 0.6	2.8 ± 0.3	8.7 ± 1.8	17.9
72	2 ± 0.2	1.5 ± 0.1	20.7 ± 11.7	32.0
73	2.2 ± 0.5	1 ± 0.2	5.9 ± 1.7	126.7
74	2.1 ± 0.5	1.4 ± 0.3	14 ± 10.6	55.2
75	2.2 ± 0.5	1.4 ± 0.2	8.7 ± 3.8	50.7

5. EXPLORATORY DATA ANALYSIS AND OUTLIER IDENTIFICATION

We note that Lapotre et al. (2016) merged their dataset with the one derived by Lorenz et al. (2014), and evaluated the model predictions using both datasets. In contrast, a segmentation of the two datasets and the fit of different models was later preferred (Lapotre et al., 2021; Lorenz, 2020). Therefore, the first question we address here is: can we integrate the measurements made in the Tharsis region with others made elsewhere on Mars, or do they constitute different sets of bedforms? To answer this question, we evaluate if there is a unique and continuous distribution of wavelength and albedo. Then we briefly discuss the morphological differences and overall setting and significance of the two sets of bedforms.

In Fig. S12 we compare the wavelength and albedo distributions of the large ripples mapped in the Tharsis region (the same 25 areas of Lorenz et al., 2014) and elsewhere on Mars. The wavelength of Tharsis' bedforms is more variable, on average form more sinuous patterns (i.e. with higher circular standard deviation, Fig. S12a and c) and most importantly, they present higher HiRISE albedos (Fig. S12b and d). This clearly different albedo signature is further corroborated by plotting the thermal inertias (Putzig and Mellon, 2007) and dust cover index (Ruff & Christensen, 2002) for the mapped areas (Fig. S13). This data shows that the Tharsis bedforms form a distinct population, with lower thermal inertia (possibly denoting finer materials), higher dust coverage/content and morphologies that possess a higher degree of directional variability (the fine "reticulate" texture of the bedforms in this region was previously discussed by Bridges et al., 2010).

The morphology of some of the Tharsis bedforms is also distinctive and variable (e.g. Fig. S14), forming honeycomb patterns or appearing in association with longitudinal spurs/erosive features (Bridges et al., 2010; Lorenz et al., 2014). Tharsis bedforms usually overlay bedrock, forming in some cases extensive mantling units. In contrast, meter-scale bedforms surveyed outside Tharsis typically cover larger scale bedforms (i.e. dark dunes).

The new global survey we present confirms the uniqueness of the bedforms located in the Tharsis region. Tharsis' bedforms were studied in detail by Bridges et al. (2010), proposing that they were formed by saltation of dust aggregates, which in some cases may have produced indurated bedforms. This suggests that major differences in granulometry, density and transport susceptibility exist. Therefore, to test/fit wavelength predictive models Tharsis and non-Tharsis bedforms should be treated separately, as they represent two distinct populations.

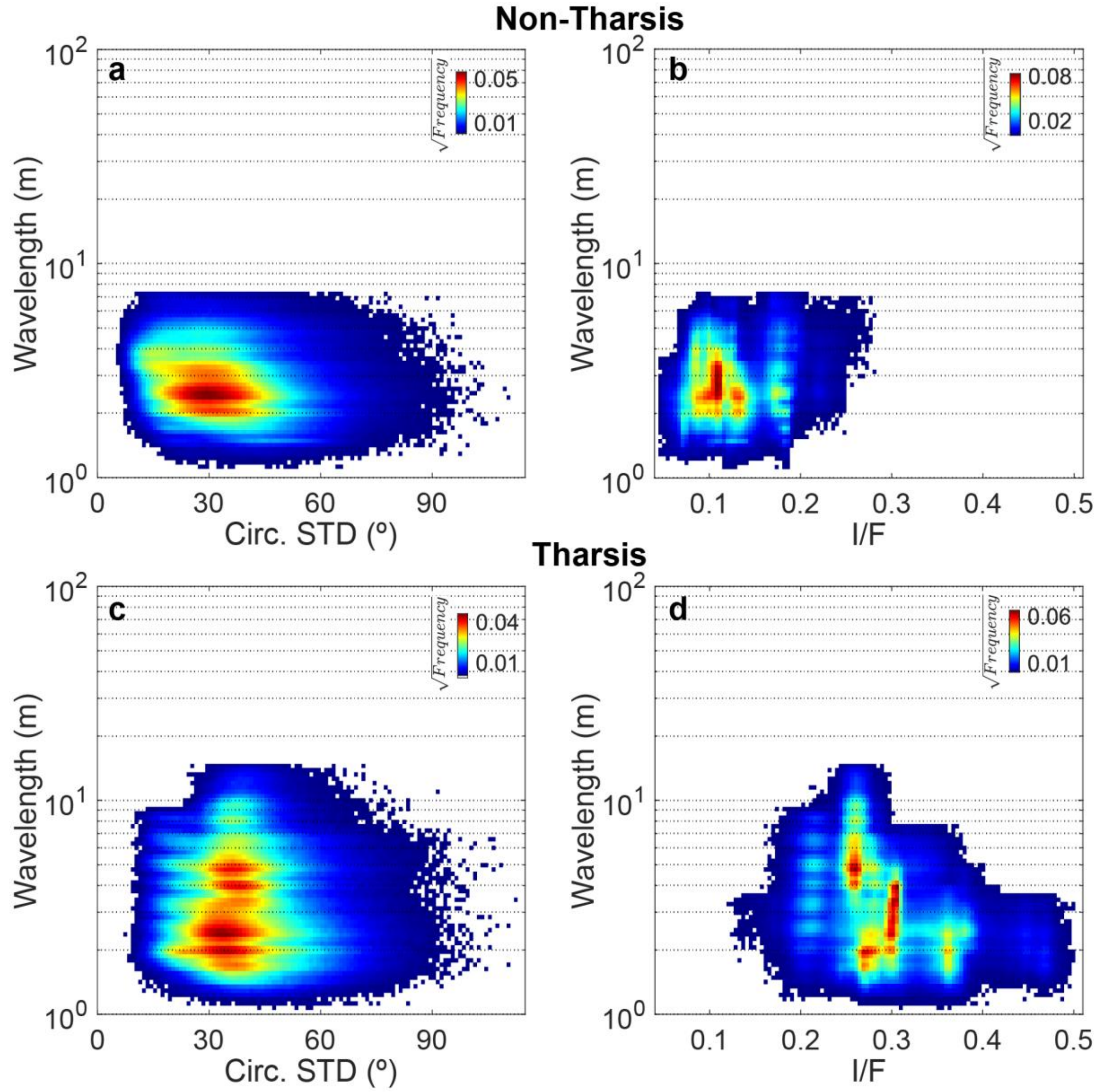

Fig. S12 – 2D histograms of the dark-toned large bedforms mapped in the Tharsis region (c, b) and elsewhere on Mars (a, b). Bedforms in Tharsis show a larger dispersion of wavelengths (clustering at ~2.5 m outside Tharsis and ranging from 1.5-5 m in Tharsis), form patterns with larger trend variations (median circular distributions of ~30º vs. 30-45º) and consistently present higher albedos (<0.25 vs. >0.2).

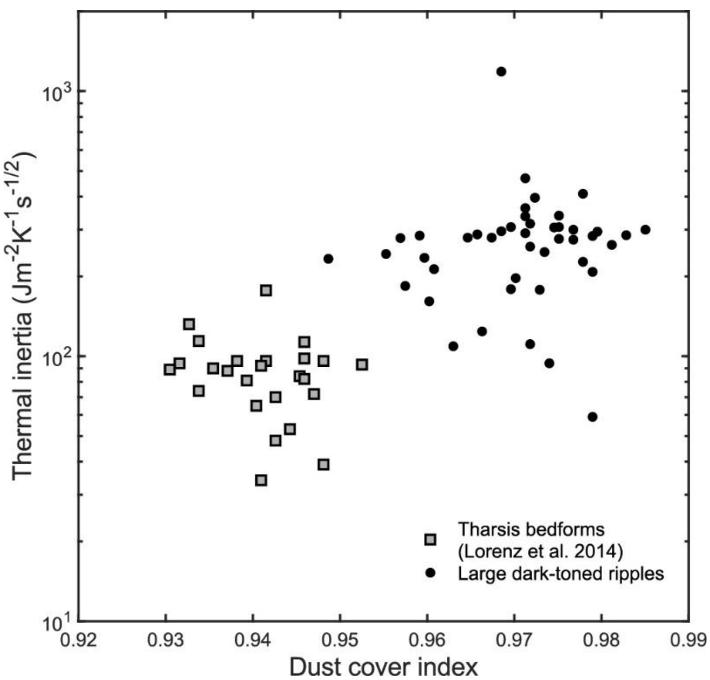

Fig. S13 – Nightside TES thermal inertia (Putzig & Mellon, 2007) **vs. dust cover index** (Ruff & Christensen, 2002) **for all mapped areas. Tharsis areas form a distinct cluster, characterized by lower thermal inertias and lower dust cover index (lower index values are indicative of dust covering, while higher values correspond to dust free areas). This demonstrates that the Tharsis bedforms form a different population, in terms of thermophysical proprieties and dust coverage/content.**

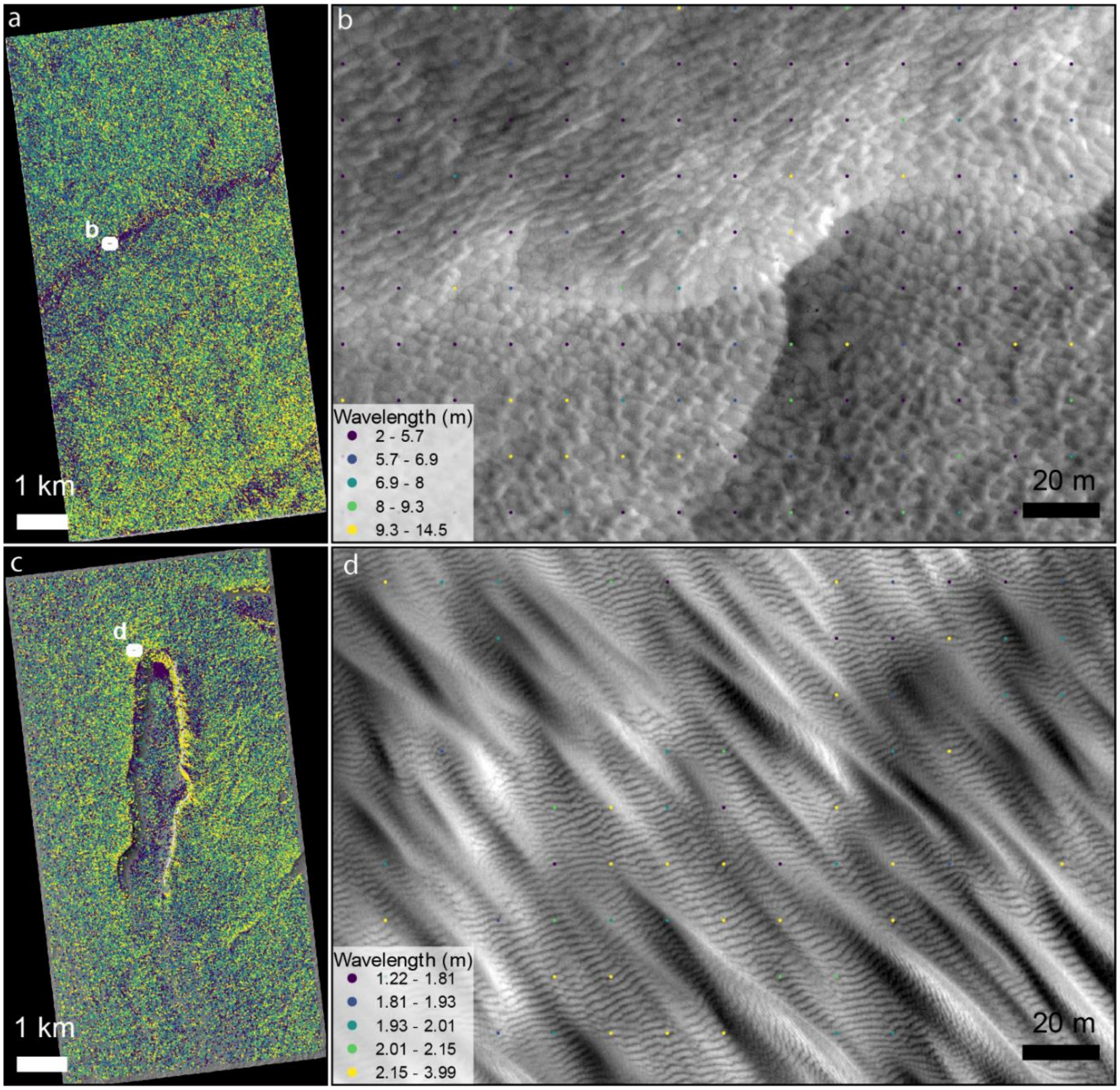

Fig. S14 – Different bedform morphologies in the Tharsis region. a, b) Example of honeycomb shaped bedforms forming a continuous covering unit that encompass all the area (Area 56, PSP_008460_1980). c, d) Transverse linear bedforms that overlay what appear to be erosive longitudinal troughs; also, in this case the bedforms are pervasive, covering almost completely the region and forming a mantling unit that seems to be controlled by the bedrock's main topographic features (Area 72, PSP_010213_1785).

Another point we address here regards the uniformity of the dataset collected outside Tharsis, does our survey include areas which may not be representative of the global trend, i.e. do we have and can we identify possible outliers?

A linear direct relation is evident between average wavelength and elevation (Fig. S15), although a few points do not seem to follow the same trend (the five labelled points in the plot correspond to the outliers we discuss here). Coincidently, we notice that these five areas have a common attribute: a significant part of the meter-scale bedforms in those areas are located on sand sheets and/or dome dunes.

A closer inspection further revealed other factors that may condition the average measurements for these areas. Namely, in Area 16 (Fig. S16) we have a mixture of two sets of bedforms, one covering barchans and other covering a sand sheet area. The later set presents lower wavelengths which contribute to lower the average wavelength plotted in Fig. S15, producing a noticeable underestimation. Large ripples in Area 34 (Fig. S17) cover low-lying dome dunes or small sand patches located in depressions. This may justify why this area does not follow the same generic trend, as these topographic settings may shelter bedforms and influence their wavelength. Moreover, the assumption of well sorted sediments may not apply in this case, since substantial lag materials may be present in this sediment starved environment. We also note that large ripples in some of the areas identified as outliers are overprinted by dust devil tracks (Fig. S18). This may denote low or even null migration of the bedforms, since the presence of dust devil tracks implies cycles of dust deposition and removal.

To summarize, five areas stand out as outliers, which we associate with cases where sediments may be coarser and poorly sorted, and where active aeolian processes may not be in equilibrium with current day atmospheric conditions. These areas were removed from the subsequent analysis and model fits.

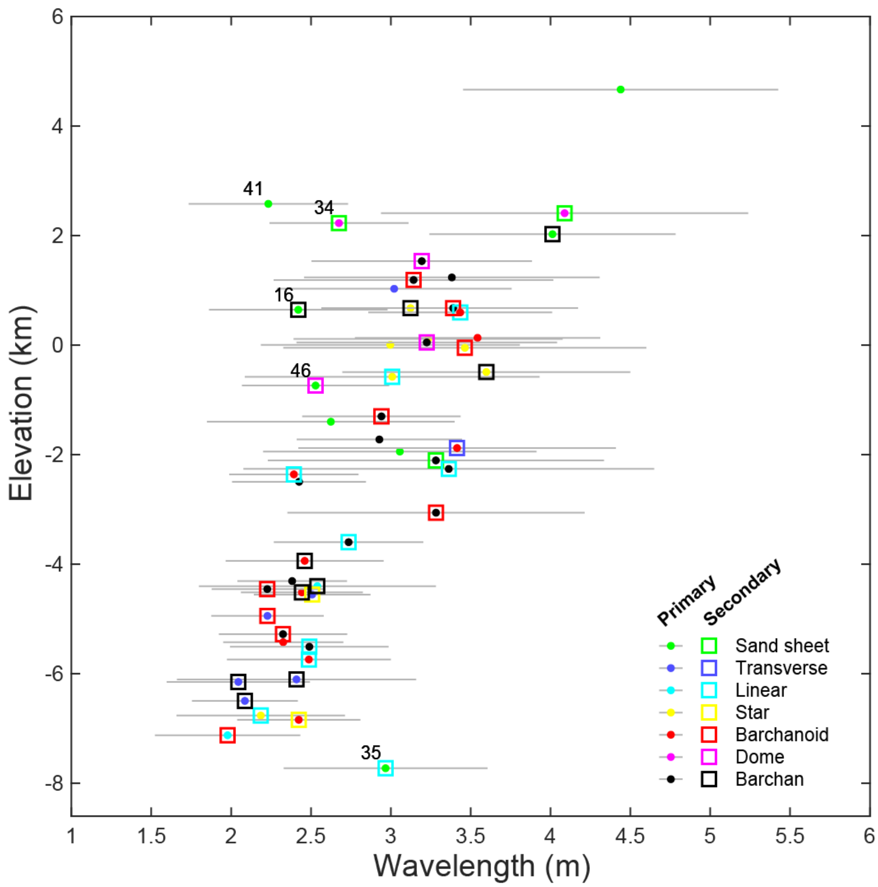

Fig. S15 – Average wavelength vs. elevation for the 50 areas located outside Tharsis, gray lines correspond to 1σ intervals. The color code represents the type of dune morphology present in the mapped areas, when more than one type is present, we assign a primary (covering higher area) and secondary class. The five labeled sites correspond to the outliers discussed in this section.

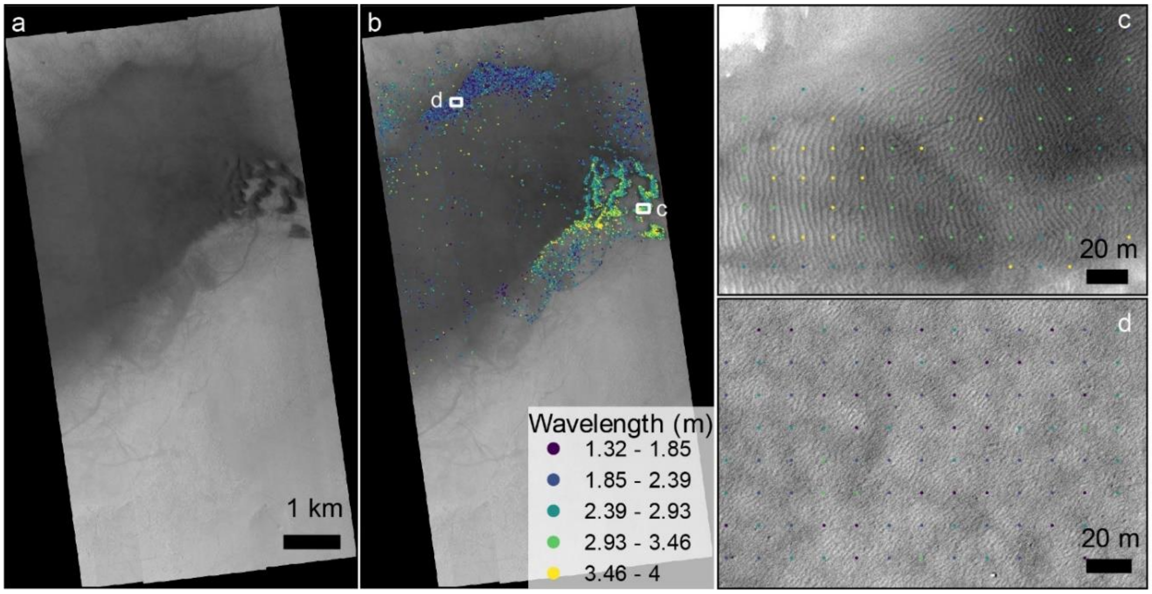

Fig. S16 – Example of a possible outlier where barchans transition to an extensive sand sheet (Area 16). a, b) Wavelength measurements overlaid in the HiRISE image, note the lower wavelengths in the sand sheet (northern section) when compared to the barchans (eastern section). c) Bedforms that cover the barchans, note the presence of dust devil tracks and the higher wavelengths of the ripples. d) Bedforms on the sand sheet present lower wavelengths, therefore the average value for this area merges two different sets of bedforms, with the sand sheet contributing to decreasing the overall wavelength estimate (Fig. S15).

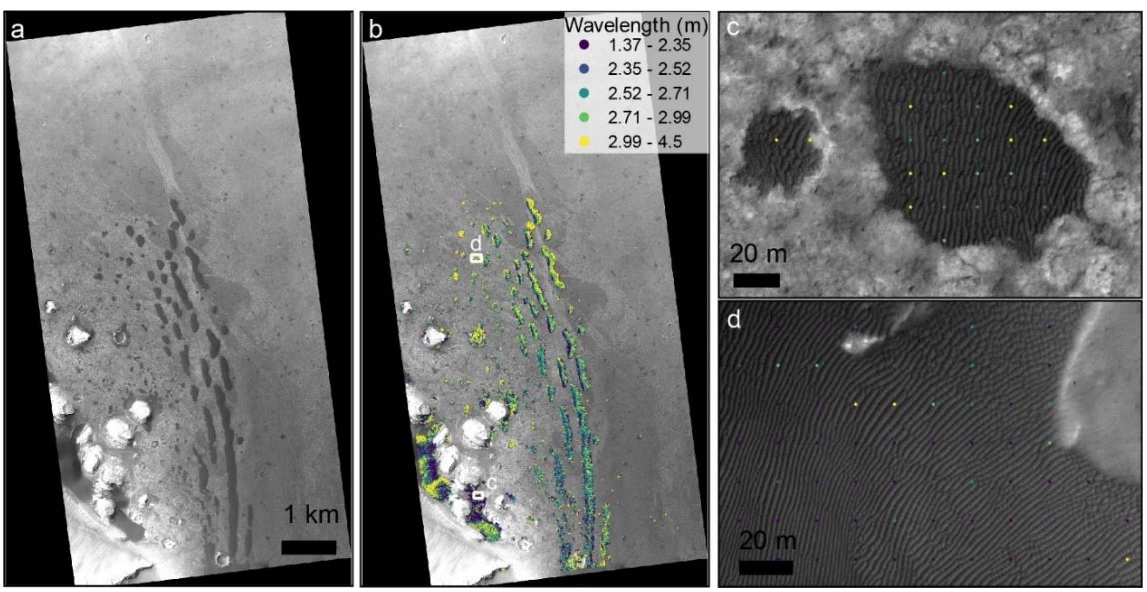

Fig. S17 – Area 34 large ripples cover low-lying dome dunes and sand sheets (ESP_017610_1730), typically located in depressions. We hypothesize that the bedforms in this area may be enriched in coarser/lag materials and that the specific topographic setting may also influence their wavelength. a, b) Wavelength measurements overlaid in the HiRISE image. c, d) large ripples located in crater depressions or other topographic lows.

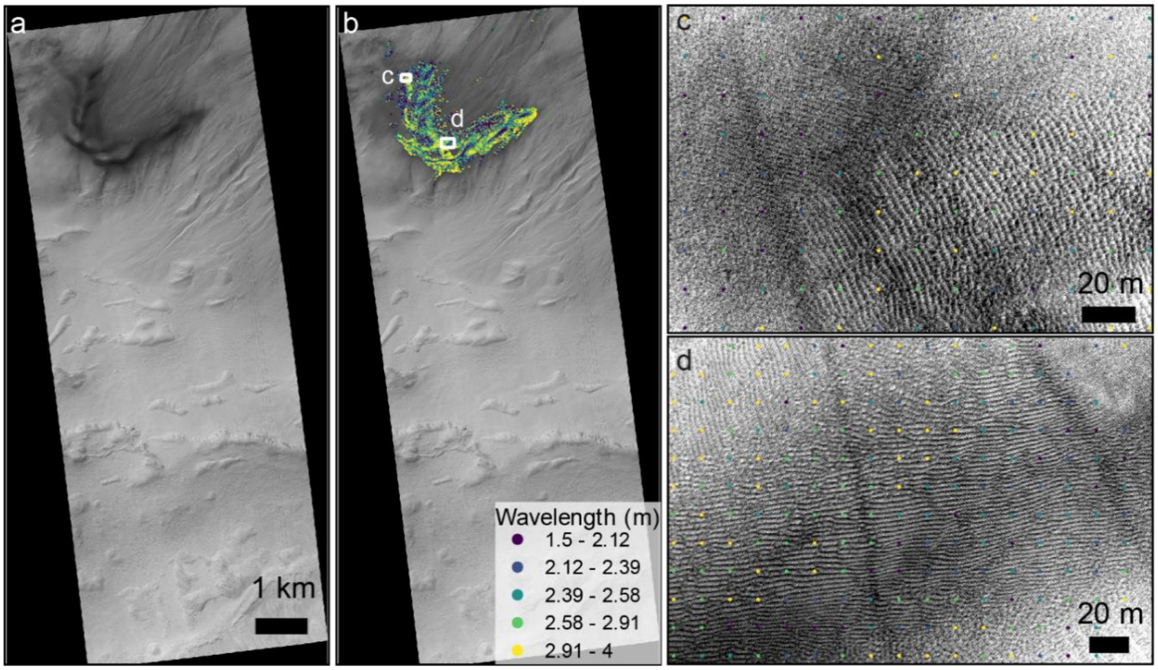

Fig. S18 – Dust devil tracks overlay large ripples in Area 46 (ESP_058788_1320), which implies dust deposition and removal cycles as well as reduced bedform migration. a, b) Wavelength measurements overlaid in the HiRISE image. c, d) Examples of dust devil tracks overlapping the large ripples.

6. WAVELENGTH VS. ATMOSPFERIC DENSITY SCALING: MODELS AND FITS

Here we implemented the same model described in Lapotre et al. (2016), where wind shear velocity (u_*) is set to be equal to the impact threshold shear velocity (u_t) predicted by Kok (2010) model (Table S7 summarizes the models input parameters). Atmospheric density is computed as a function of elevation using the ideal gas law:

$$\boldsymbol{\rho_f(z)} = \frac{M_{CO_2}}{r}\frac{p(z)}{T(z)} \qquad \text{(Eq. 3),}$$

where M_{CO2} is the molar mass of carbon dioxide, r is the ideal gas constant and $p(z)$ is the atmospheric pressure computed from MOLA elevations (section 4) using the relation derived from the atmospheric descent profiles of the Mars Exploration Rovers missions (Withers & Smith, 2006). We assume an isothermal atmosphere with a temperature (T) of 227 K, while kinematic viscosity (v) at elevation z is computed through:

$$\boldsymbol{v(z)} = \frac{\mu}{\rho_f(z)} \qquad \text{(Eq. 4),}$$

where μ is a constant dynamic viscosity (Table S7).

Based on a fit made to flume experiments and Martian morphometric data, drag ripples' wavelength was predicted to vary according to:

$$\boldsymbol{\lambda = 2777\frac{\nu^{2/3}D^{1/6}}{(Rg)^{1/6}u_*^{1/3}}} \qquad \text{(Eq. 5)}$$

where D is grain diameter, g is the gravity acceleration on Mars and R is the submerged reduced density of the sediment ($R = \frac{\rho_s - \rho_f}{\rho_f}$) (Lapotre et al., 2016). This is essentially the same relation later generalized in Lapotre et al. (2017), and is considered to be representative of bedload saturation length (Duran Vinent et al., 2019; Lapotre et al., 2021).

Lapotre et al. (2021) adapted the same framework, considering a saltation saturation length $l_{sat} = \frac{\rho_s u_t^2}{g(\rho_s - \rho_f)}$, which is used to predict bedform wavelength through $\lambda = \frac{\lambda^* \nu}{u_*}$, where λ^* is a dimensionless wavelength: $\lambda^* \approx 600\left(\frac{l_{sat}u_*}{\nu}\right)^{1/3}$ (Lapotre et al., 2021).

In Fig. 3 and S19 we compare our wavelength measurements with the predictions of both models, and we fit power laws and linear models (as proposed by Lorenz et al., 2014) to our datasets.

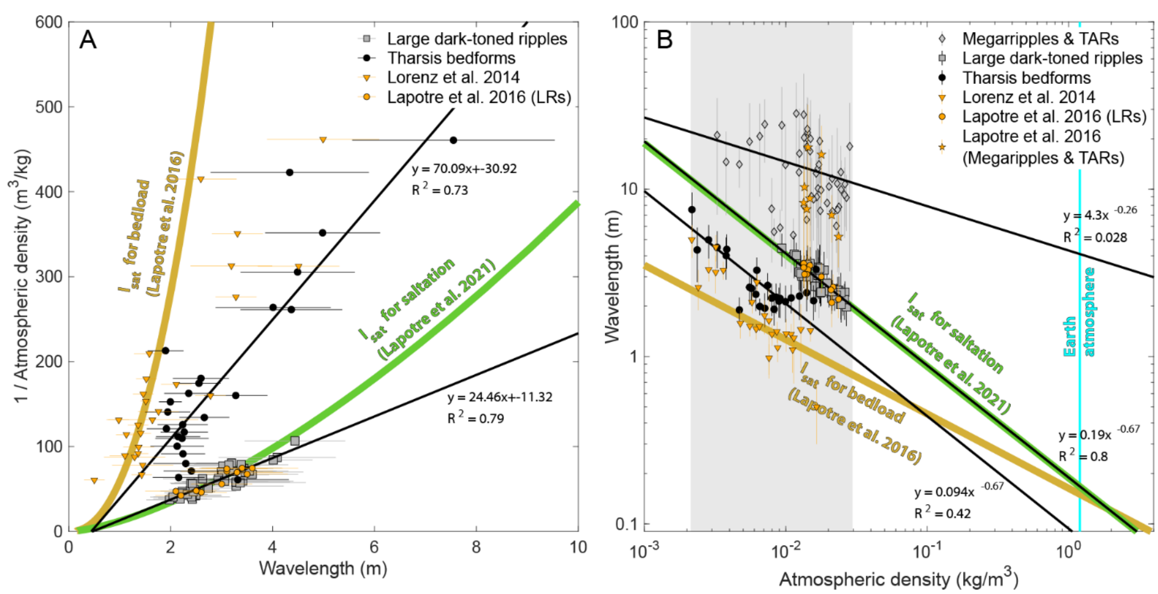

Fig. S20 – Previous surveys and relation between bedforms wavelength and Martian atmospheric density. This is the same plot shown in Fig. 3, where we added the dataset compiled by Lapotre et al. (2016), which includes Lorenz et al. (2014) data for the Tharsis region. We see that a large fraction of this data (corresponding to the Tharsis region bedforms) overlaps the fluid-drag predictions with a bedload saturation length formulation (golden line), while our dataset for these same areas presents higher wavelengths, with the data points located between the two models' predictions. Like in our dataset, the existence of two different clusters is noticeable in the previous compilation, as well as an

overlap of the large ripples datasets with the fluid-drag model predictions when saltation saturation length is considered (green line). The gray area represents the maximum range of atmospheric densities on Mars while the cyan line represents the density of Earth's atmosphere. Black lines represent the best fitted models for the datasets compiled in this study and were computed using the average values for each site (linear models in A and power laws in B; the R^2 values in B were computed in the log space).

Table S7 – Model input parameters.

Variables	Description	Values
M_{CO2}	CO_2 molar mass	44.01 g/mol
r	Ideal gas constant	8.314 $JK^{-1}mol^{-1}$
T	Temperature	227 K
g	Mars gravity acceleration	3.78 m/s^2
σ_s	Grain density (basalt)	2900 kg/m^3
D	Grain diameter	200 µm
µ	Dynamic viscosity	$10.8x10^{-6}$ Pa.s

Geophysical Research Letters

Supporting Information for

Constraining the mechanisms of aeolian bedform formation on Mars through a global morphometric survey: Supporting information S2

David A. Vaz[1], Simone Silvestro[2,3], Matthew Chojnacki[4] and David C. A. Silva[1]

[1]Centre for Earth and Space Research of the University of Coimbra, Observatório Geofísico e Astronómico da Universidade de Coimbra, Coimbra, Portugal.

[2]INAF Osservatorio Astronomico di Capodimonte, Napoli, Italia.

[3]SETI Institute, Carl Sagan Center, Mountain View, CA, USA.

[4]Planetary Science Institute, Lakewood, CO, USA.

Contents of this file

In this file we present the maps and histograms used to discriminate bedform populations. A common layout was adopted for the 75 areas, the first 11 areas are the same surveyed by Lapotre et al. (2016), while areas 51-75 correspond to the Tharsis regions analyzed by Lorenz et al. (2014).

The 2D kernel density histograms located in the first row display the distributions of wavelength, circular standard deviation and albedo (I/F), a square root stretch is used to highlight secondary maxima. Red dashed lines correspond to the wavelength and albedo thresholds used to segment the two bedform classes: large dark-toned ripples and megaripples & TARs. Computed averages and standard deviation intervals are shown in black, while wavelength averages from previous studies are shown in the right side of the first plot (green: large dark-toned ripples; magenta: TARs; cyan: Tharsis bedforms). In the middle row we show the HiRISE image (left) and the wavelength map (right). The lower-left map displays the albedo variations, and the lower-right map displays the classified bedform type.

Area 1

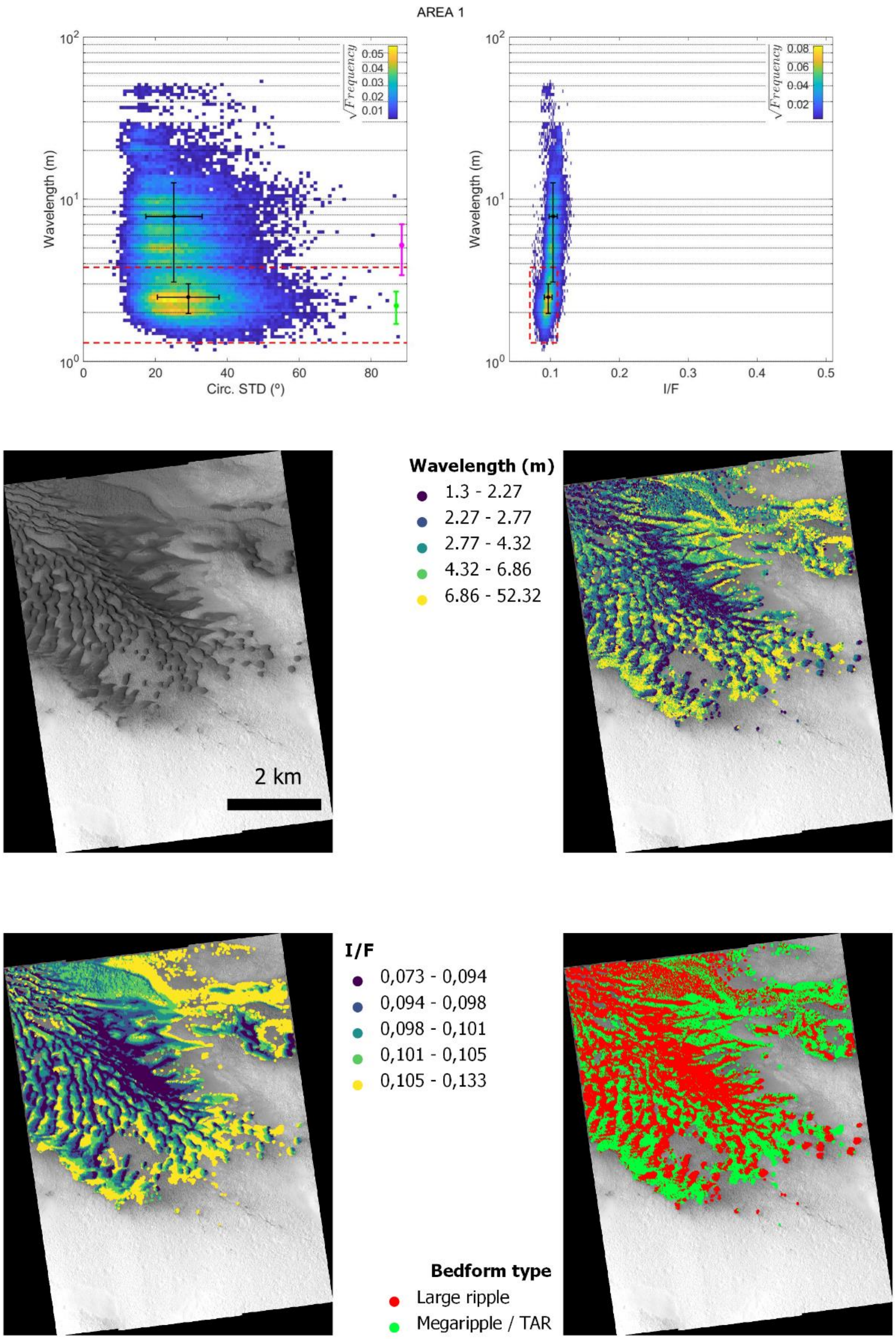
AREA 1
Wavelength (m)
Circ. STD (º)
I/F
√Frequency
Wavelength (m)
1.3 - 2.27
2.27 - 2.77
2.77 - 4.32
4.32 - 6.86
6.86 - 52.32
2 km
I/F
0,073 - 0,094
0,094 - 0,098
0,098 - 0,101
0,101 - 0,105
0,105 - 0,133
Bedform type
Large ripple
Megaripple / TAR

Area 2

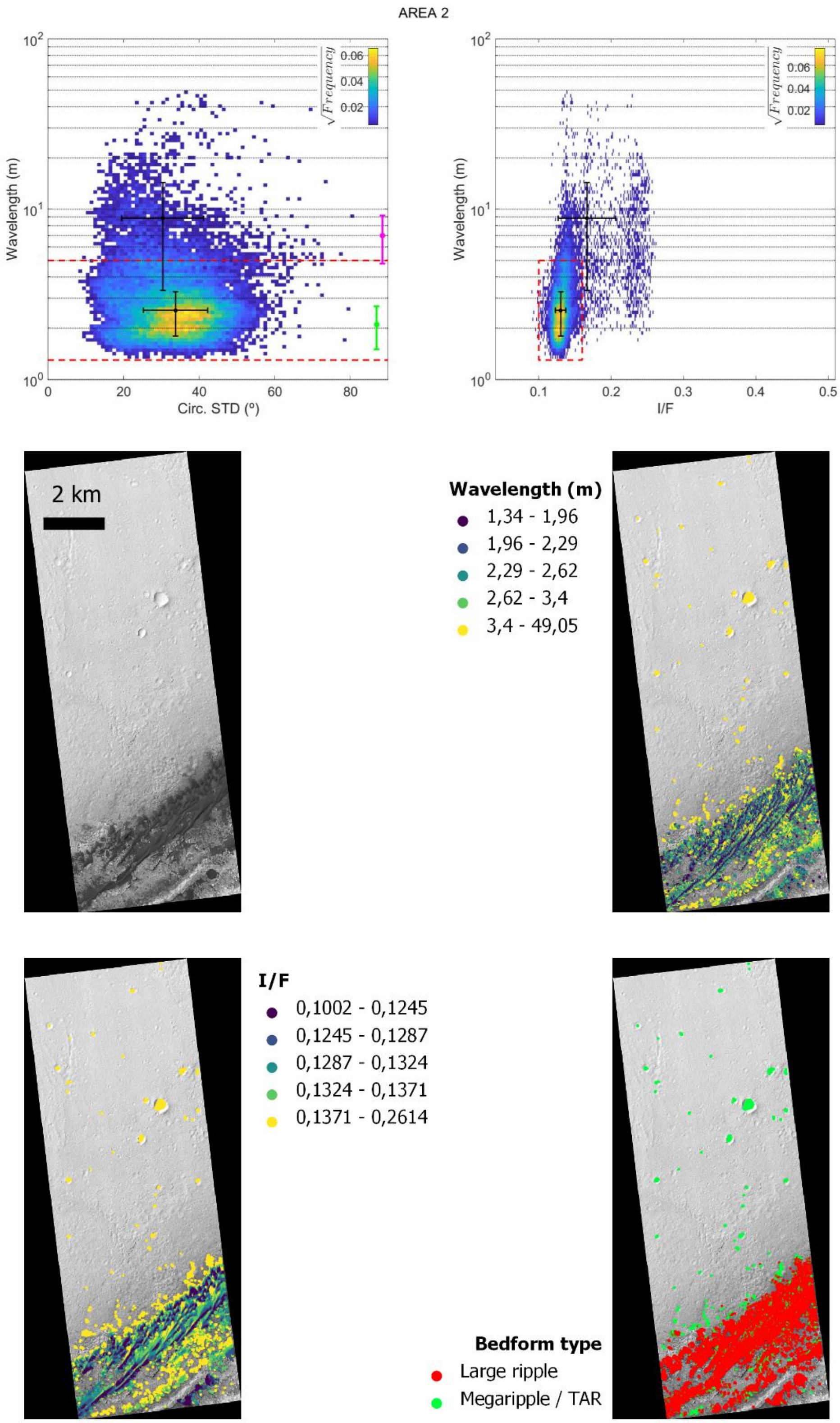

AREA 2
Wavelength (m)
Circ. STD (º)
I/F
√Frequency
0.06
0.04
0.02
2 km
Wavelength (m)
1,34 - 1,96
1,96 - 2,29
2,29 - 2,62
2,62 - 3,4
3,4 - 49,05
I/F
0,1002 - 0,1245
0,1245 - 0,1287
0,1287 - 0,1324
0,1324 - 0,1371
0,1371 - 0,2614
Bedform type
Large ripple
Megaripple / TAR

Area 3

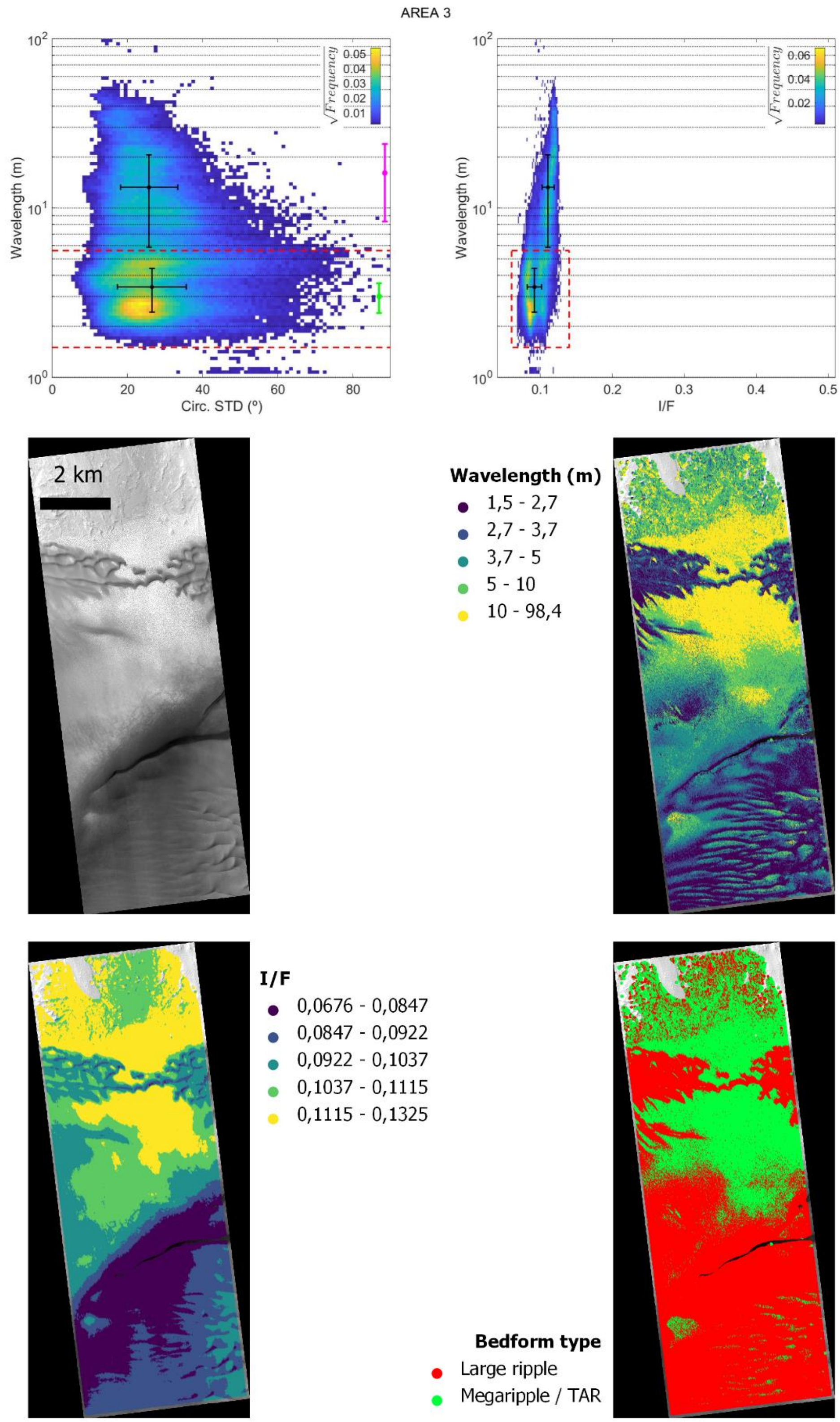
AREA 3
Wavelength (m)
Circ. STD (°)
√Frequency
Wavelength (m)
I/F
√Frequency
2 km
Wavelength (m)
1,5 - 2,7
2,7 - 3,7
3,7 - 5
5 - 10
10 - 98,4
I/F
0,0676 - 0,0847
0,0847 - 0,0922
0,0922 - 0,1037
0,1037 - 0,1115
0,1115 - 0,1325
Bedform type
Large ripple
Megaripple / TAR

Area 4

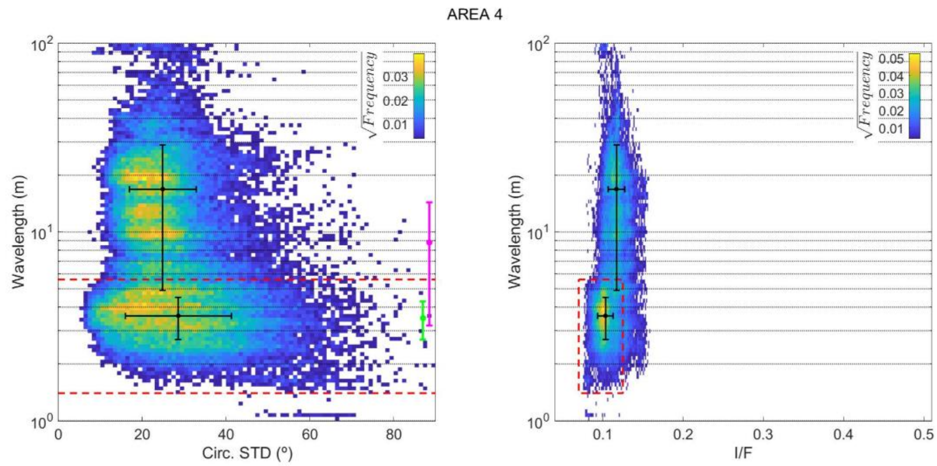
AREA 4
Wavelength (m)
Circ. STD (º)
I/F
√Frequency
0.01
0.02
0.03
0.04
0.05

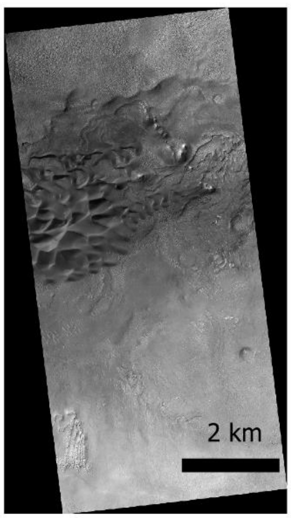
2 km

Wavelength (m)
1,4 - 3,4
3,4 - 4,7
4,7 - 9,5
9,5 - 17,6
17,6 - 115

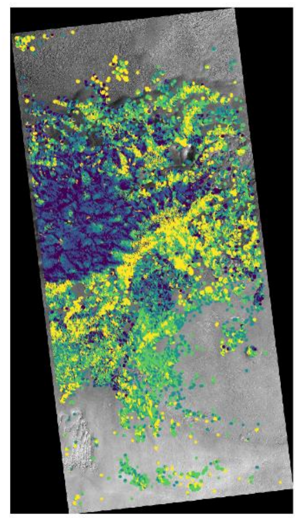

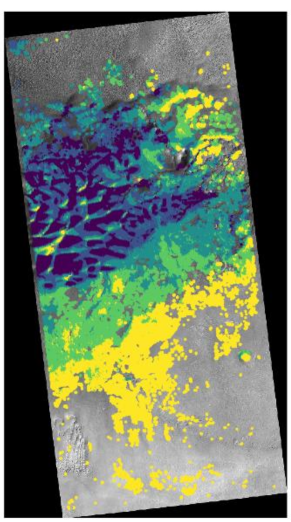

I/F
0,0762 - 0,1
0,1 - 0,1066
0,1066 - 0,1143
0,1143 - 0,1203
0,1203 - 0,1567

Bedform type
Large ripple
Megaripple / TAR

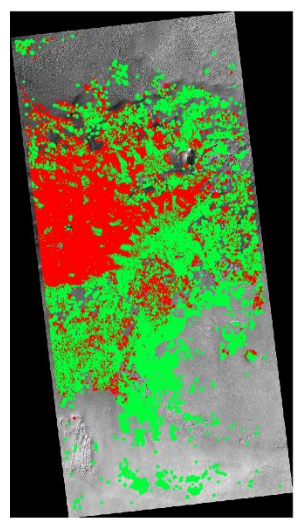

Area 5

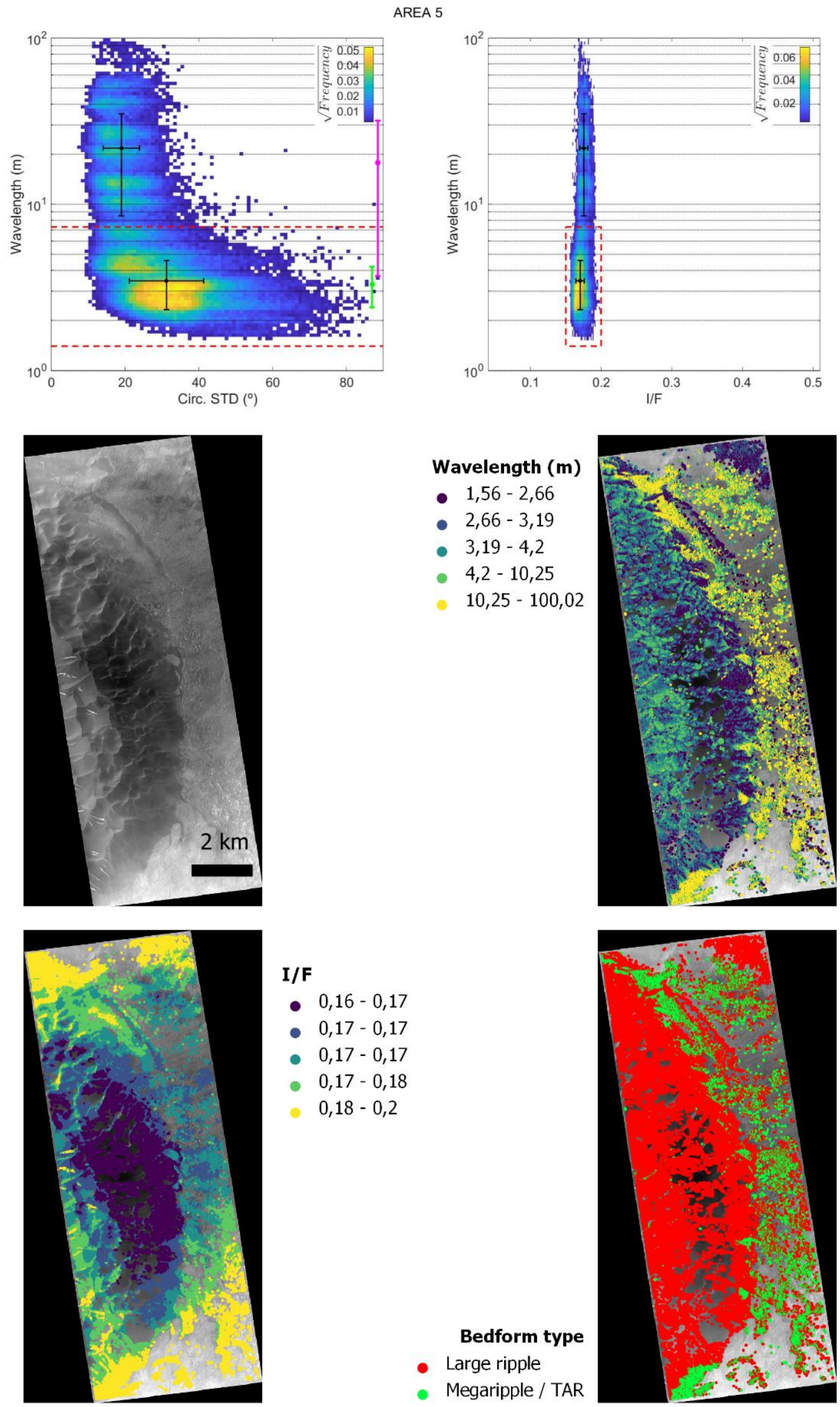
AREA 5
Wavelength (m)
Circ. STD (°)
√Frequency
Wavelength (m)
I/F
√Frequency
2 km
Wavelength (m)
1,56 - 2,66
2,66 - 3,19
3,19 - 4,2
4,2 - 10,25
10,25 - 100,02
I/F
0,16 - 0,17
0,17 - 0,17
0,17 - 0,17
0,17 - 0,18
0,18 - 0,2
Bedform type
Large ripple
Megaripple / TAR

Area 6

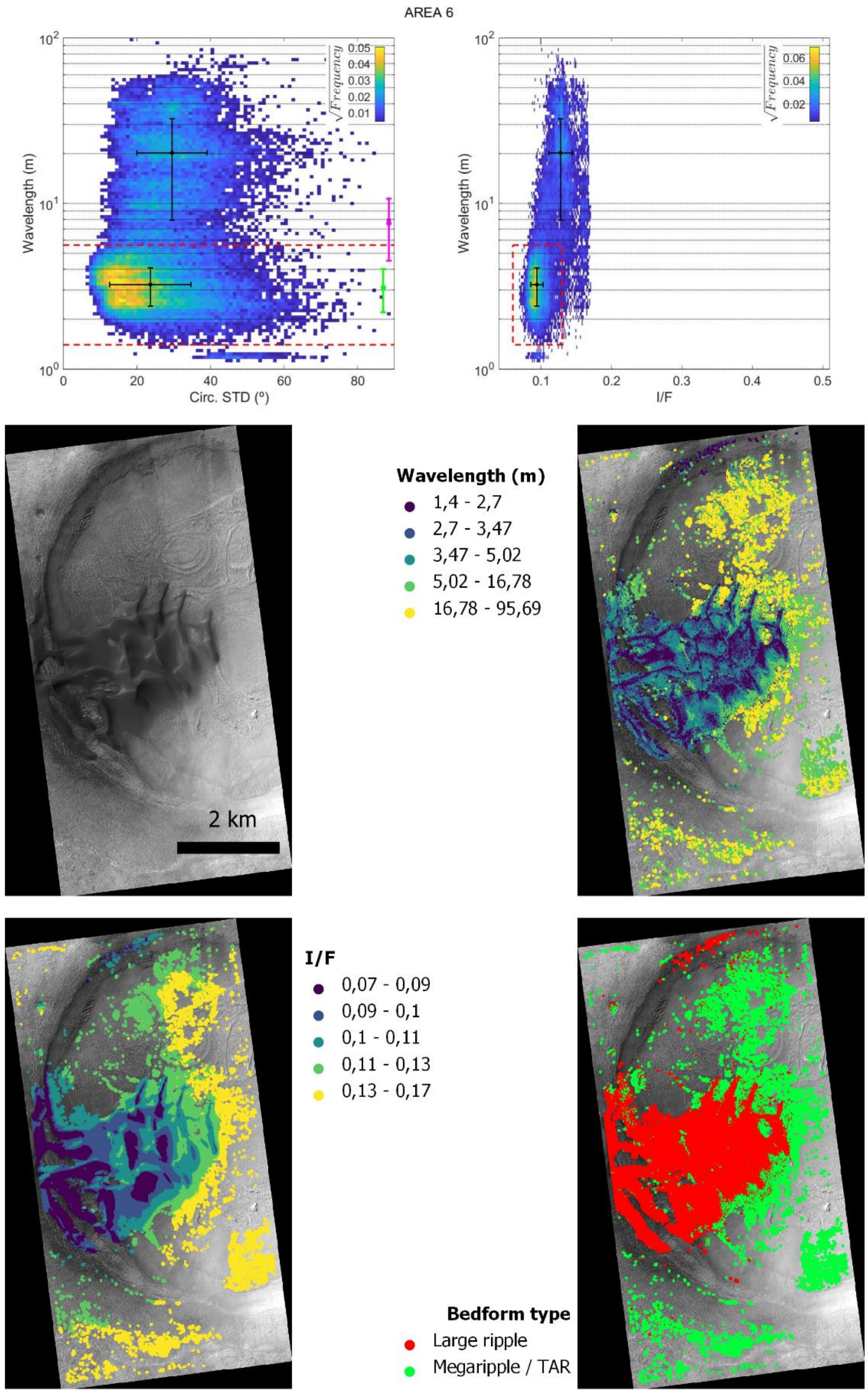
AREA 6
√Frequency
Wavelength (m)
Circ. STD (°)
I/F
2 km
Wavelength (m)
1,4 - 2,7
2,7 - 3,47
3,47 - 5,02
5,02 - 16,78
16,78 - 95,69
I/F
0,07 - 0,09
0,09 - 0,1
0,1 - 0,11
0,11 - 0,13
0,13 - 0,17
Bedform type
Large ripple
Megaripple / TAR

Area 7

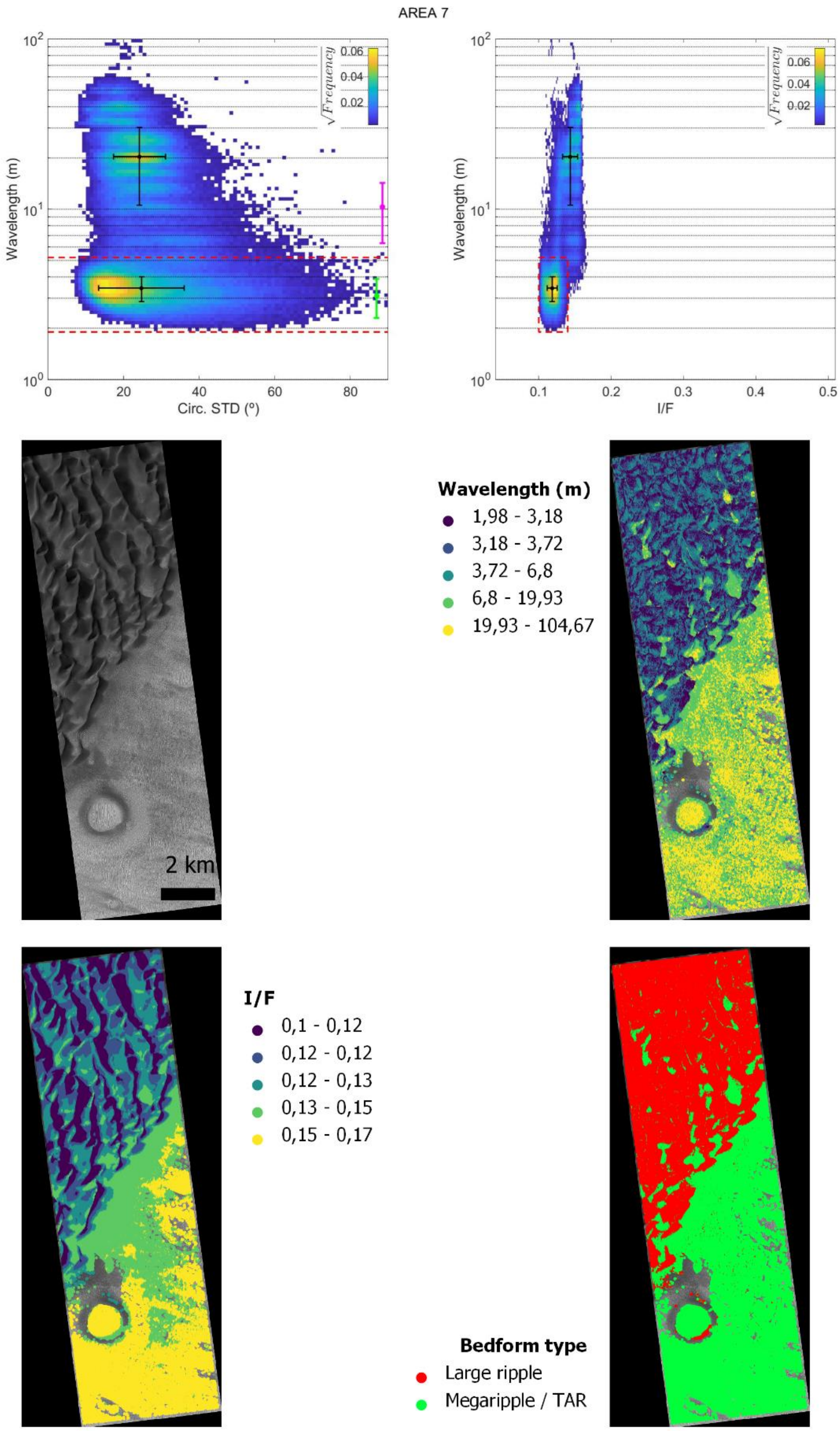
AREA 7
Wavelength (m)
Circ. STD (°)
I/F
√Frequency
2 km
Wavelength (m)
1,98 - 3,18
3,18 - 3,72
3,72 - 6,8
6,8 - 19,93
19,93 - 104,67
I/F
0,1 - 0,12
0,12 - 0,12
0,12 - 0,13
0,13 - 0,15
0,15 - 0,17
Bedform type
Large ripple
Megaripple / TAR

Area 8

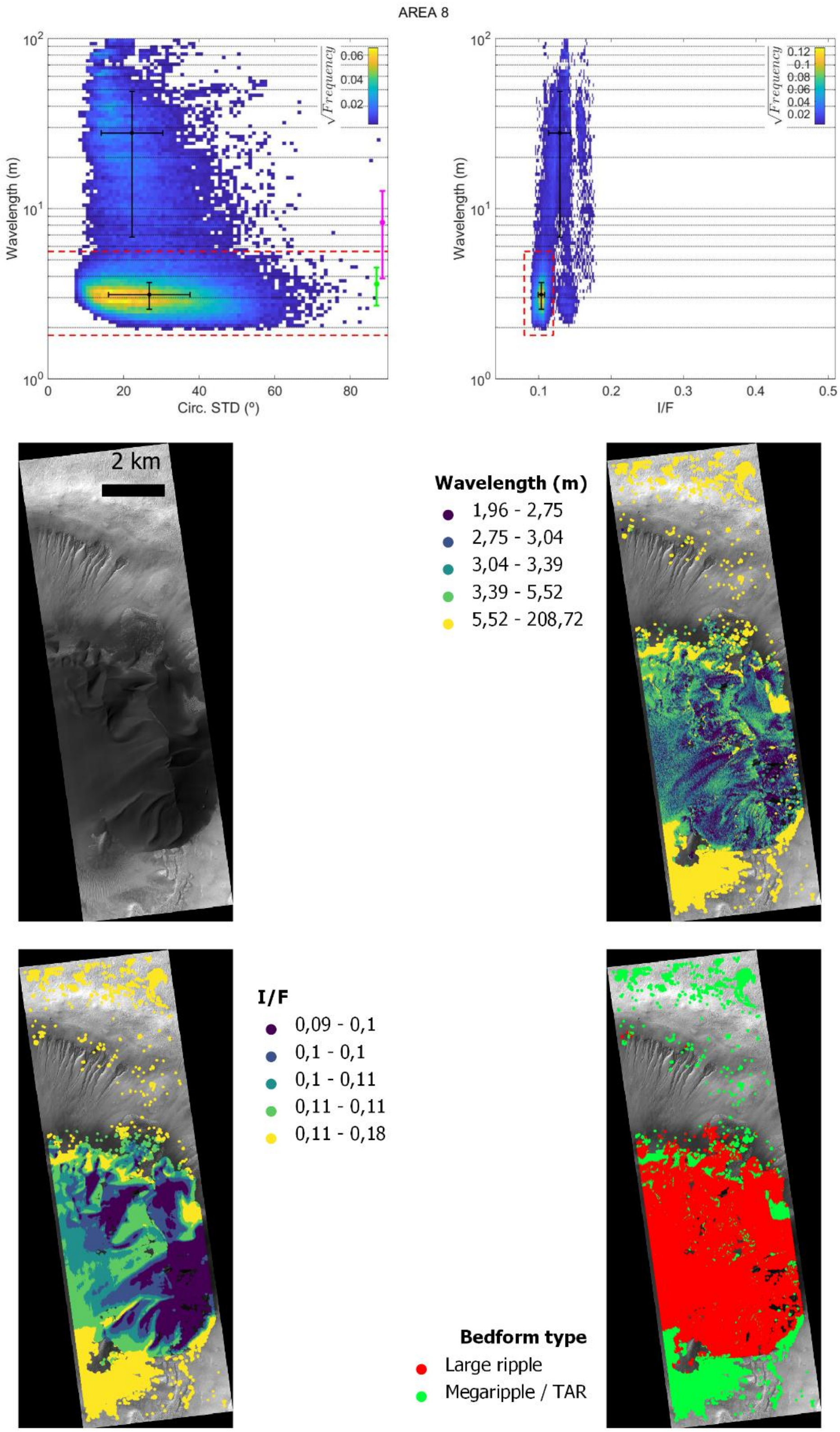
AREA 8
Wavelength (m)
Circ. STD (°)
I/F
√Frequency
2 km
Wavelength (m)
1,96 - 2,75
2,75 - 3,04
3,04 - 3,39
3,39 - 5,52
5,52 - 208,72
I/F
0,09 - 0,1
0,1 - 0,1
0,1 - 0,11
0,11 - 0,11
0,11 - 0,18
Bedform type
Large ripple
Megaripple / TAR

Area 9

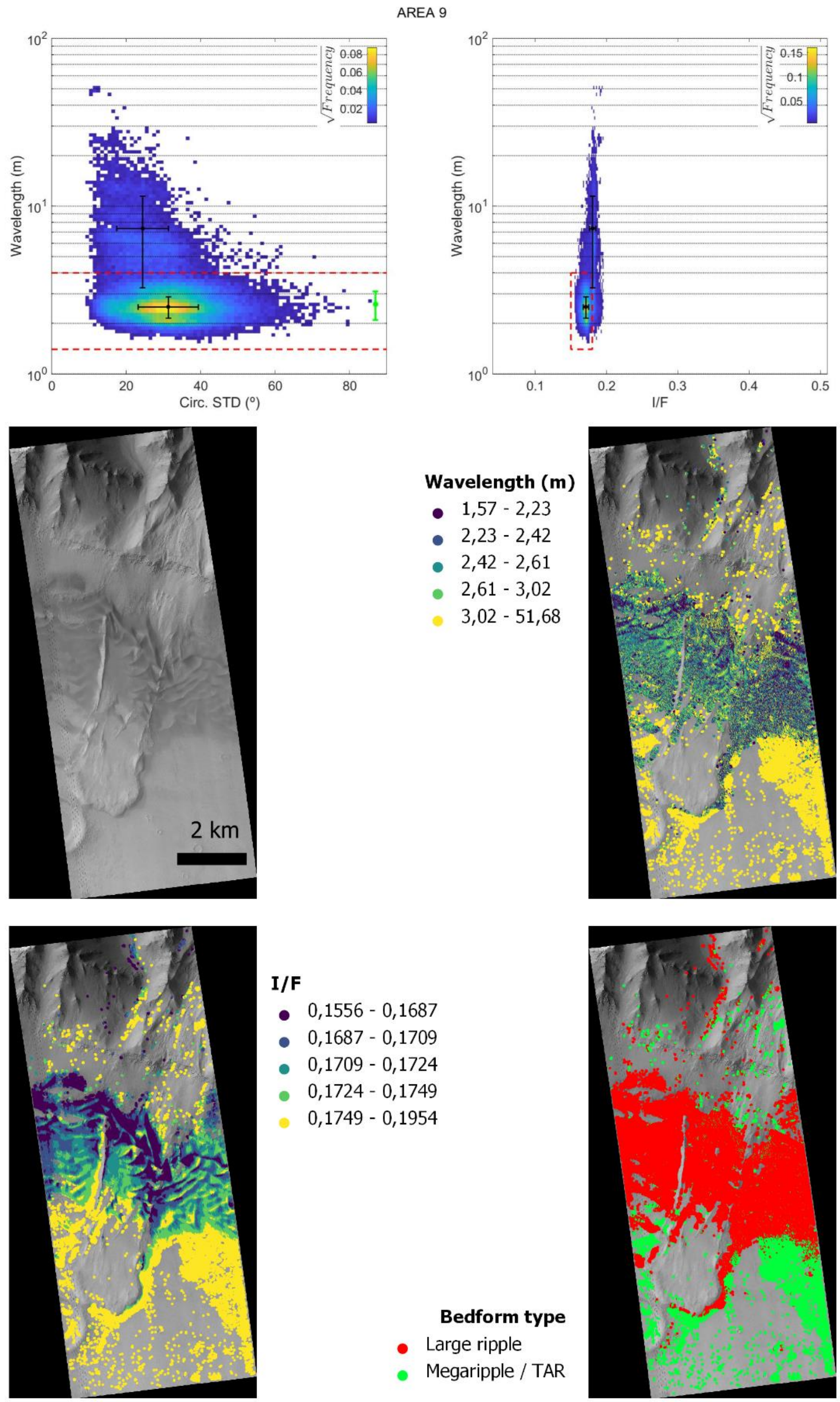
AREA 9
Wavelength (m)
Circ. STD (°)
I/F
√Frequency
2 km
Wavelength (m)
1,57 - 2,23
2,23 - 2,42
2,42 - 2,61
2,61 - 3,02
3,02 - 51,68
I/F
0,1556 - 0,1687
0,1687 - 0,1709
0,1709 - 0,1724
0,1724 - 0,1749
0,1749 - 0,1954
Bedform type
Large ripple
Megaripple / TAR

Area 10

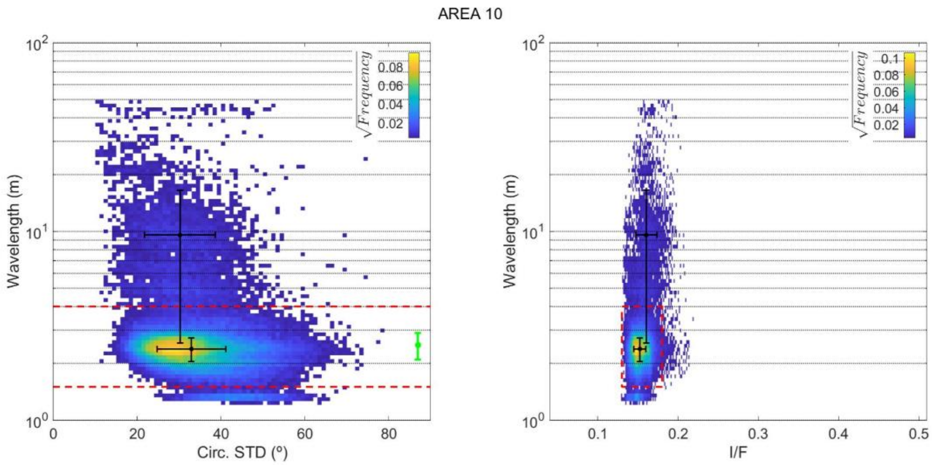
AREA 10
Wavelength (m)
Circ. STD (º)
I/F
√Frequency

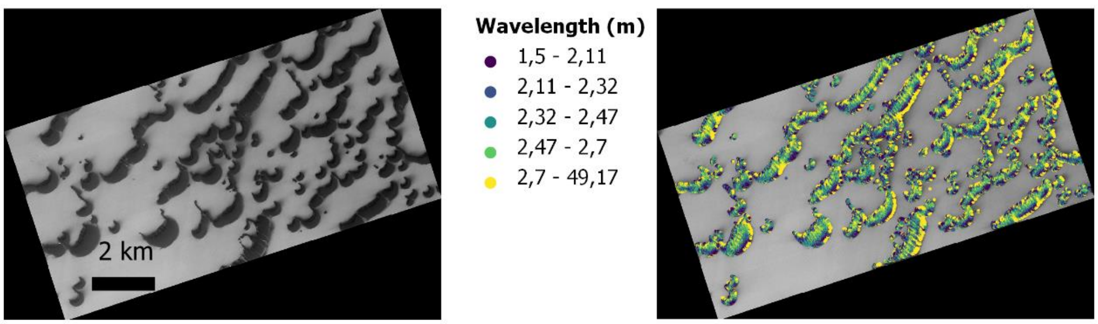
2 km
Wavelength (m)
1,5 - 2,11
2,11 - 2,32
2,32 - 2,47
2,47 - 2,7
2,7 - 49,17

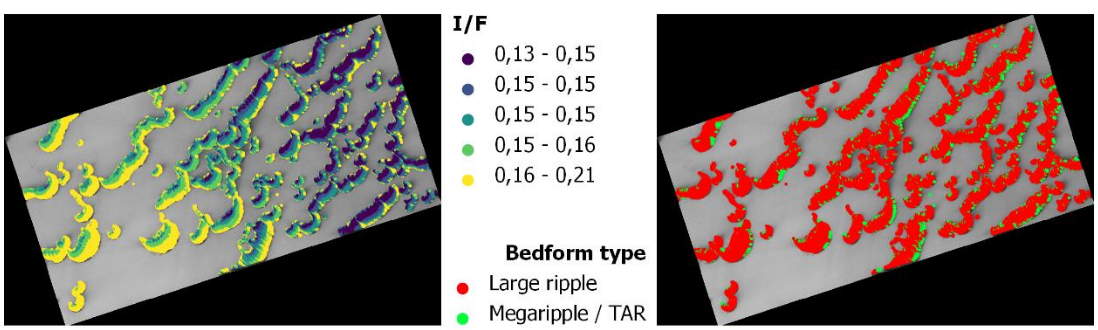
I/F
0,13 - 0,15
0,15 - 0,15
0,15 - 0,15
0,15 - 0,16
0,16 - 0,21
Bedform type
Large ripple
Megaripple / TAR

Area 11

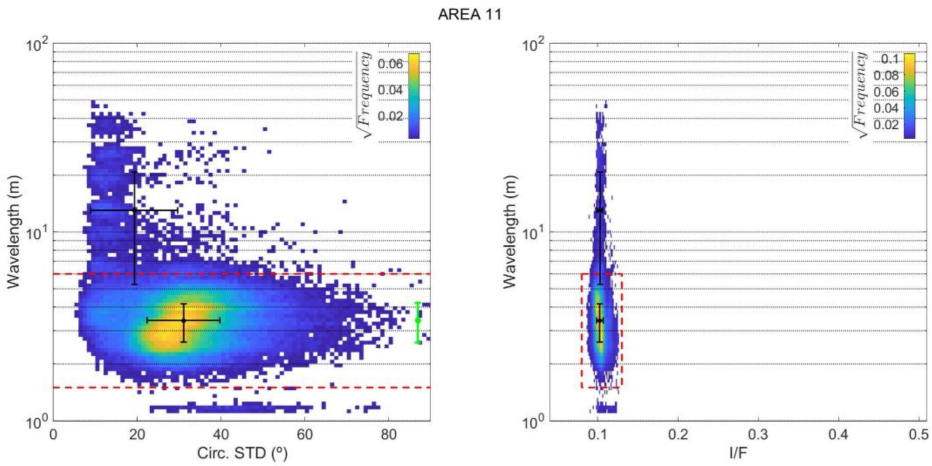
AREA 11
Wavelength (m)
Circ. STD (º)
√Frequency
0.06
0.04
0.02
I/F
0.1
0.08
0.06
0.04
0.02

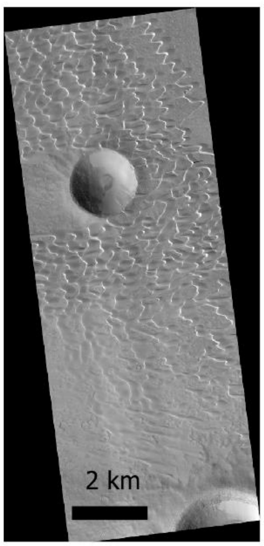
2 km

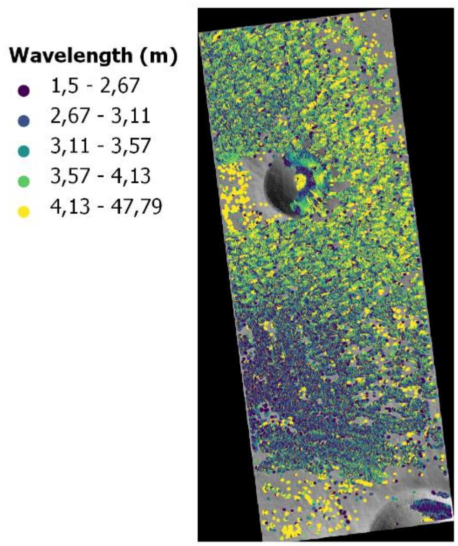
Wavelength (m)
1,5 - 2,67
2,67 - 3,11
3,11 - 3,57
3,57 - 4,13
4,13 - 47,79

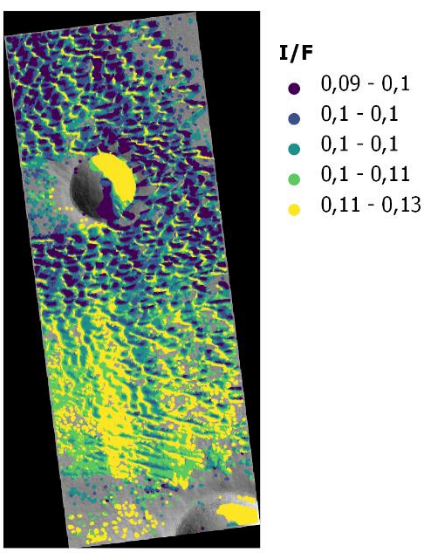
I/F
0,09 - 0,1
0,1 - 0,1
0,1 - 0,1
0,1 - 0,11
0,11 - 0,13

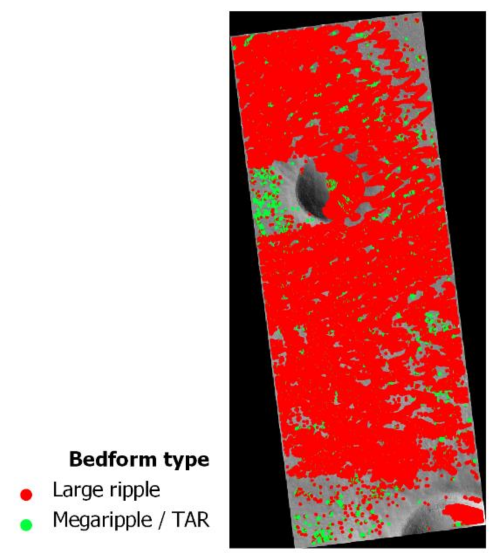
Bedform type
Large ripple
Megaripple / TAR

Area 12

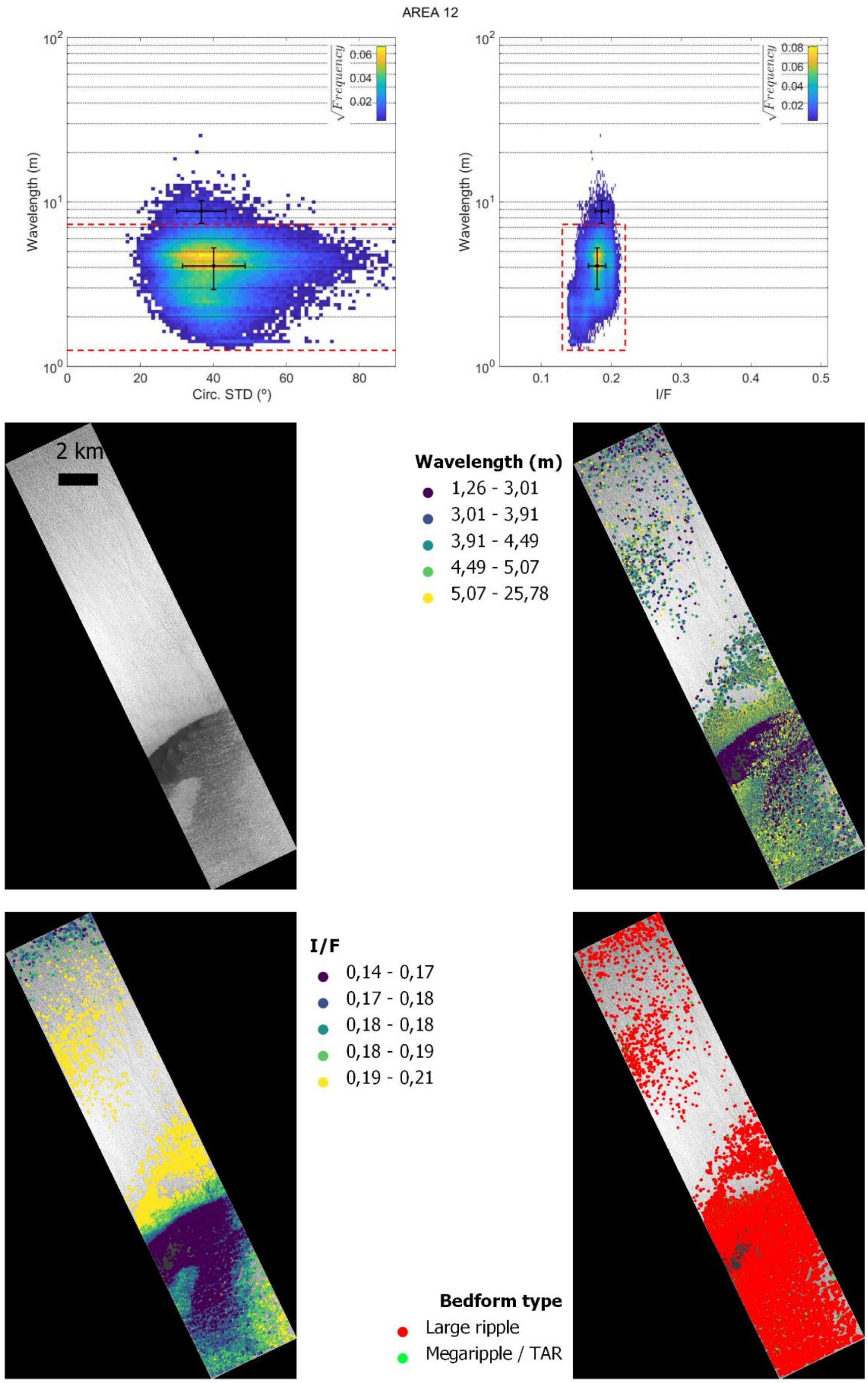
AREA 12
Wavelength (m)
Circ. STD (º)
I/F
√Frequency
2 km
Wavelength (m)
1,26 - 3,01
3,01 - 3,91
3,91 - 4,49
4,49 - 5,07
5,07 - 25,78
I/F
0,14 - 0,17
0,17 - 0,18
0,18 - 0,18
0,18 - 0,19
0,19 - 0,21
Bedform type
Large ripple
Megaripple / TAR

Area 13

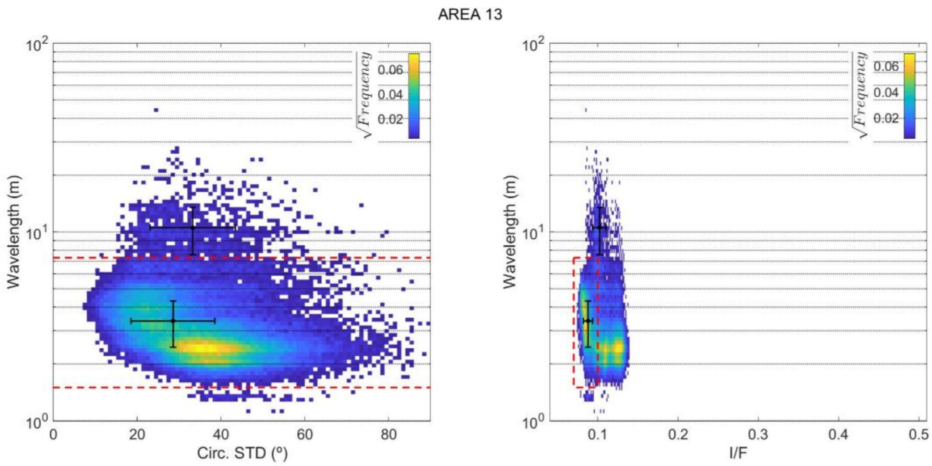
AREA 13
Wavelength (m)
Circ. STD (º)
I/F
√Frequency
0.06
0.04
0.02

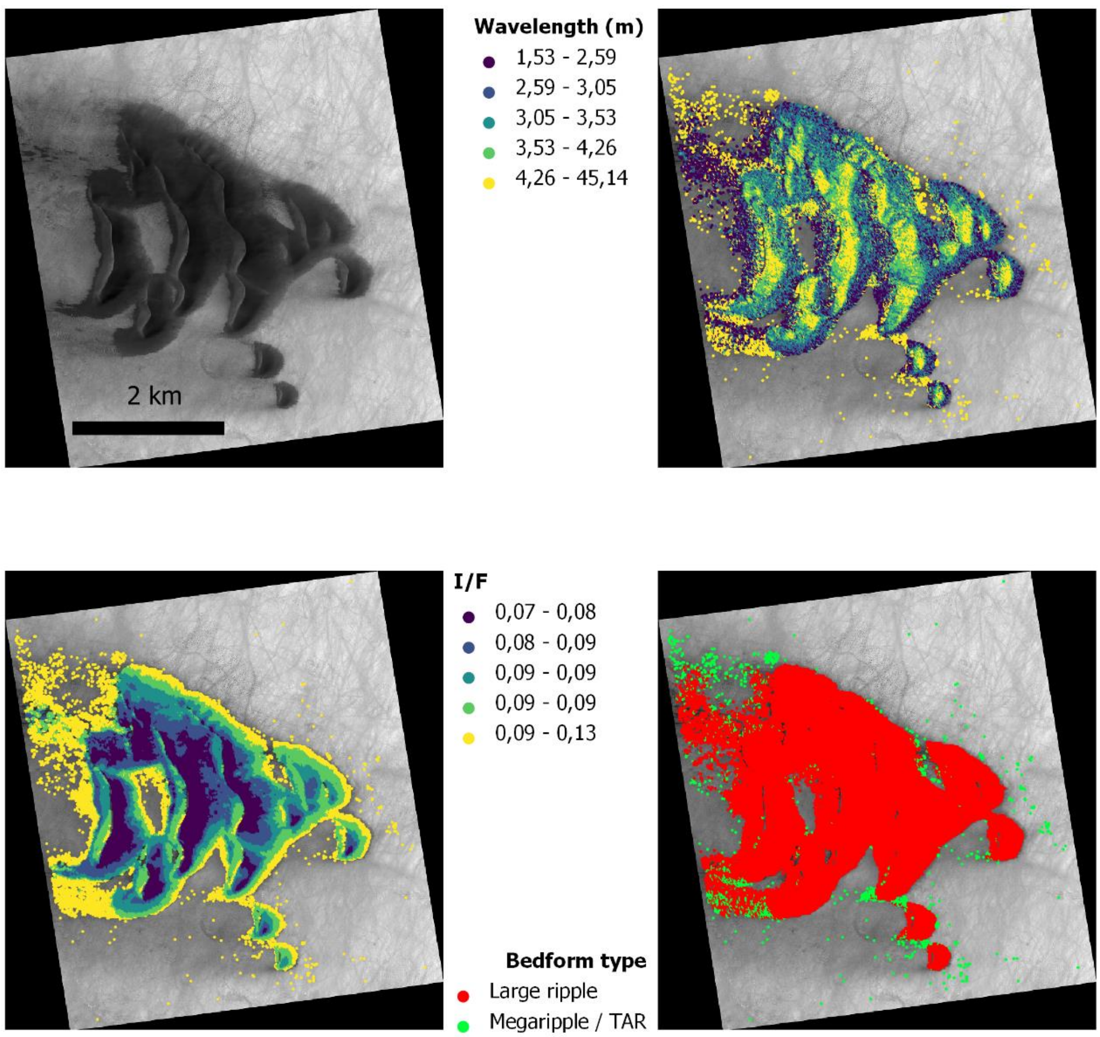
2 km
Wavelength (m)
1,53 - 2,59
2,59 - 3,05
3,05 - 3,53
3,53 - 4,26
4,26 - 45,14
I/F
0,07 - 0,08
0,08 - 0,09
0,09 - 0,09
0,09 - 0,09
0,09 - 0,13
Bedform type
Large ripple
Megaripple / TAR

Area 14

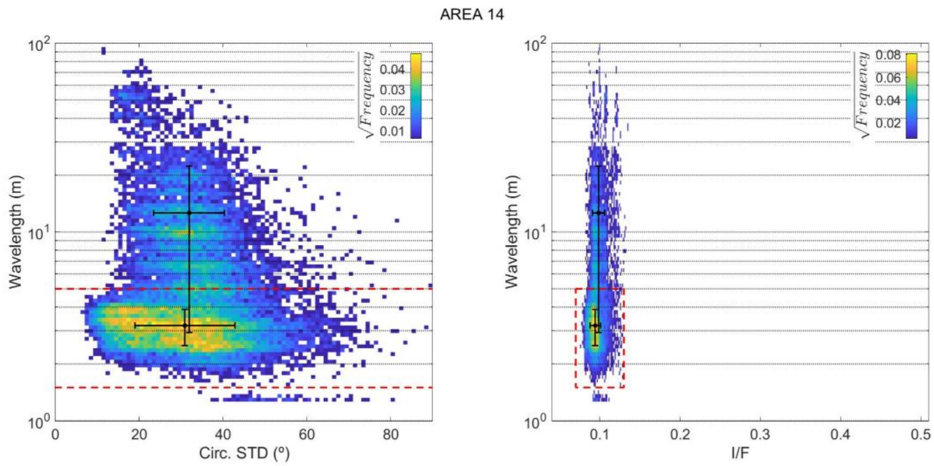
AREA 14
Wavelength (m)
Circ. STD (°)
I/F
√Frequency

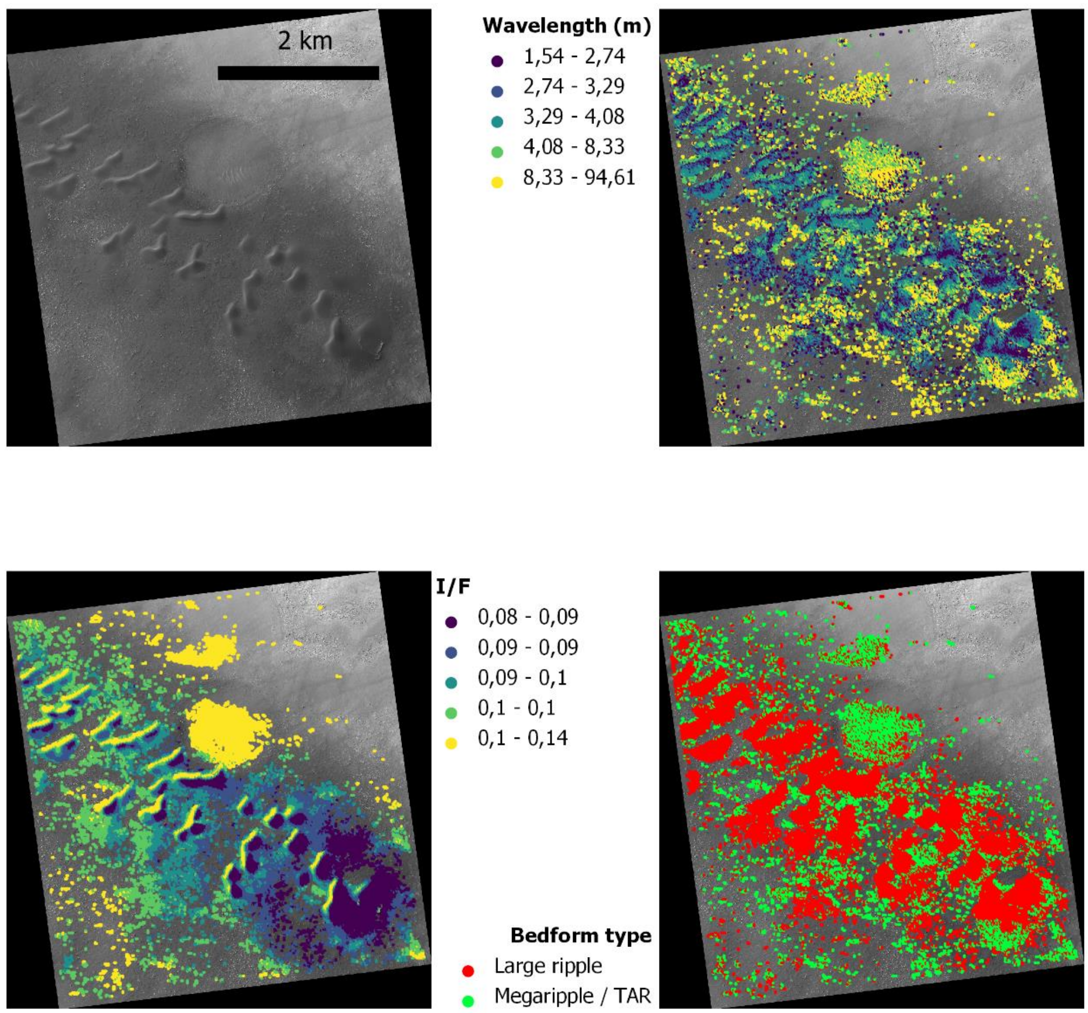
2 km
Wavelength (m)
1,54 - 2,74
2,74 - 3,29
3,29 - 4,08
4,08 - 8,33
8,33 - 94,61
I/F
0,08 - 0,09
0,09 - 0,09
0,09 - 0,1
0,1 - 0,1
0,1 - 0,14
Bedform type
Large ripple
Megaripple / TAR

Area 15

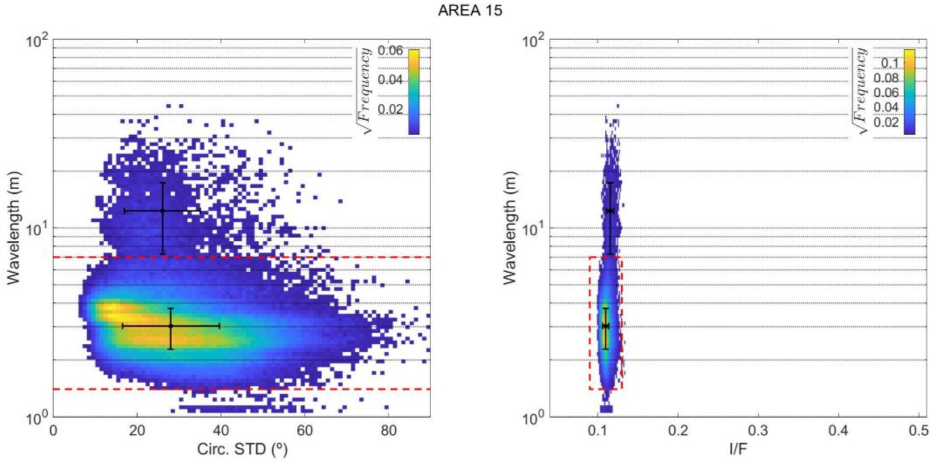
AREA 15
Wavelength (m)
Circ. STD (º)
I/F
$\sqrt{Frequency}$

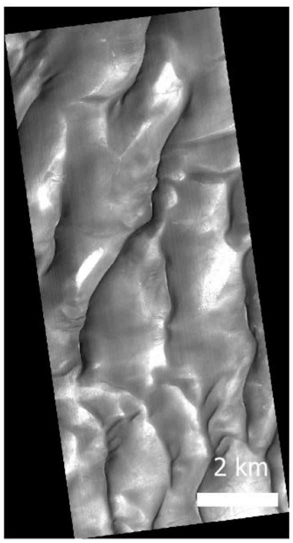
2 km

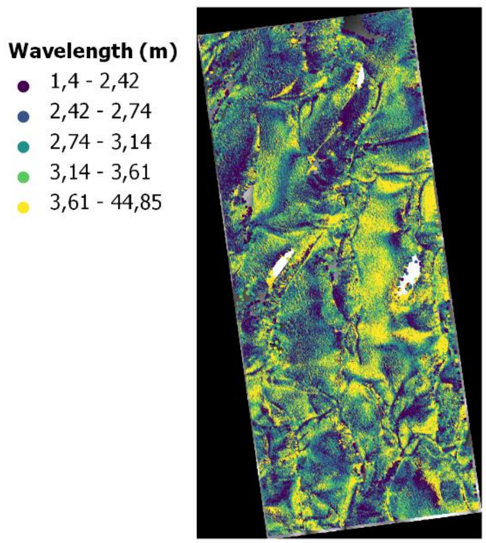
Wavelength (m)
1,4 - 2,42
2,42 - 2,74
2,74 - 3,14
3,14 - 3,61
3,61 - 44,85

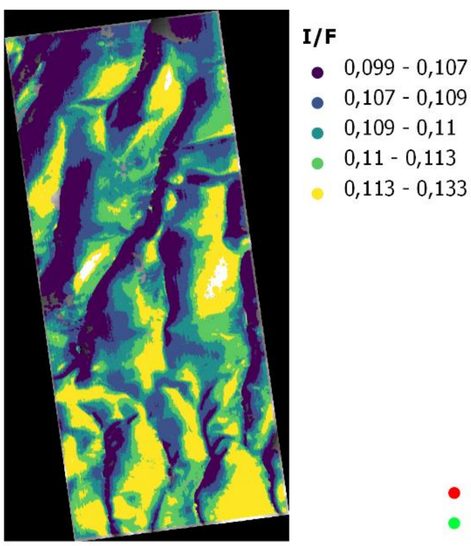
I/F
0,099 - 0,107
0,107 - 0,109
0,109 - 0,11
0,11 - 0,113
0,113 - 0,133

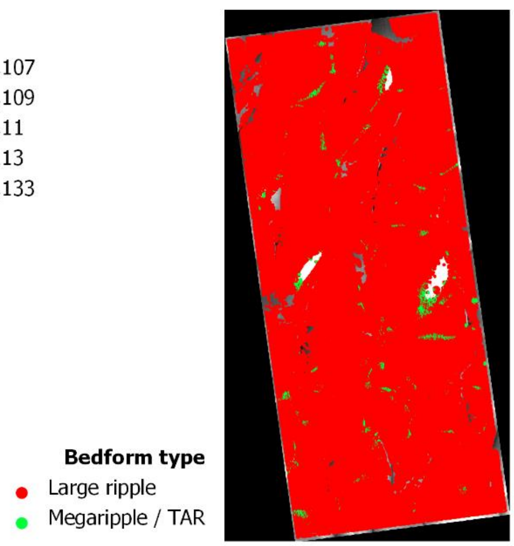
Bedform type
Large ripple
Megaripple / TAR

Area 16

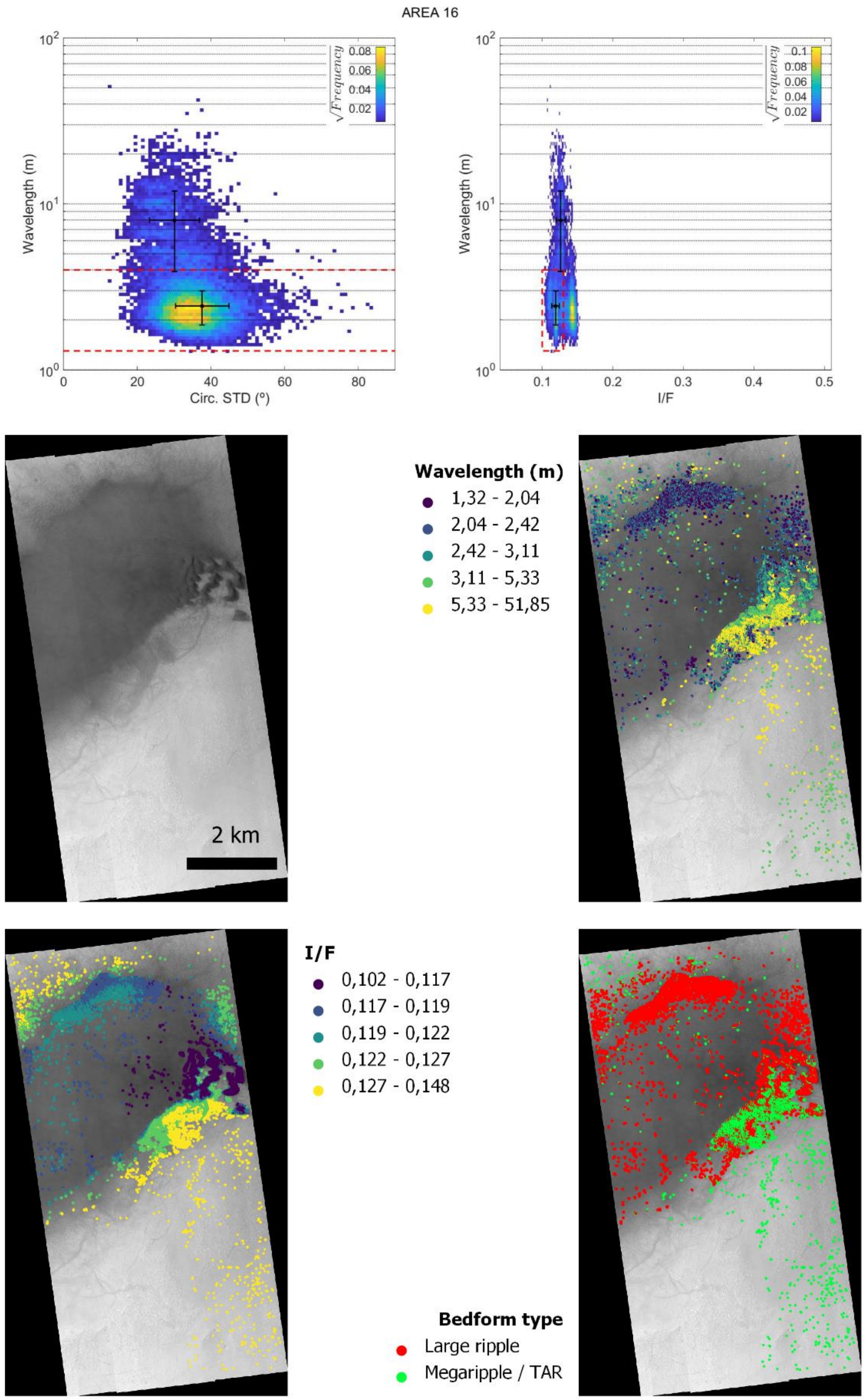
AREA 16
Wavelength (m)
Circ. STD (°)
√Frequency
Wavelength (m)
I/F
2 km
Wavelength (m)
1,32 - 2,04
2,04 - 2,42
2,42 - 3,11
3,11 - 5,33
5,33 - 51,85
I/F
0,102 - 0,117
0,117 - 0,119
0,119 - 0,122
0,122 - 0,127
0,127 - 0,148
Bedform type
Large ripple
Megaripple / TAR

Area 17

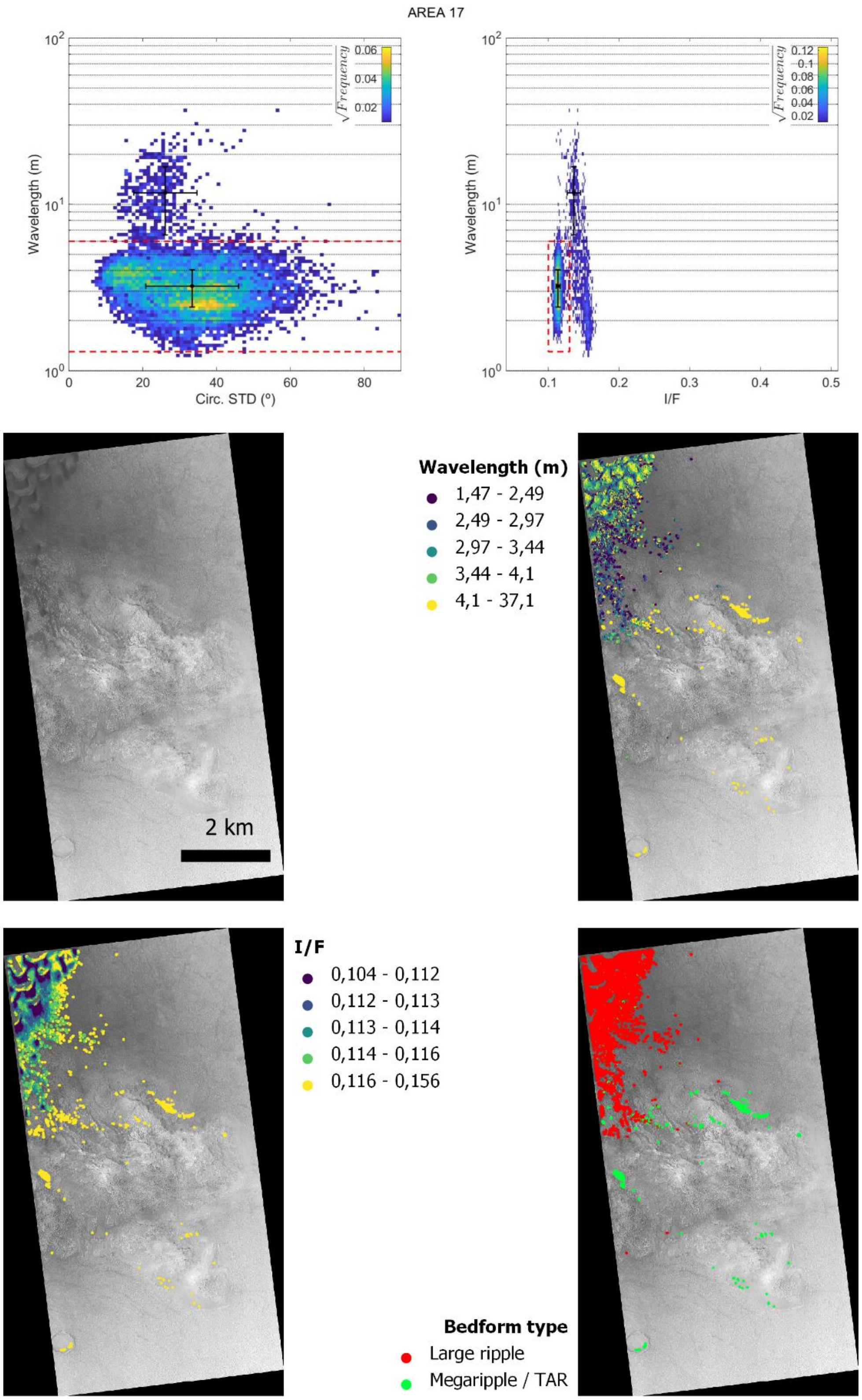
AREA 17
Wavelength (m)
Circ. STD (°)
I/F
√Frequency
2 km
Wavelength (m)
1,47 - 2,49
2,49 - 2,97
2,97 - 3,44
3,44 - 4,1
4,1 - 37,1
I/F
0,104 - 0,112
0,112 - 0,113
0,113 - 0,114
0,114 - 0,116
0,116 - 0,156
Bedform type
Large ripple
Megaripple / TAR

Area 18

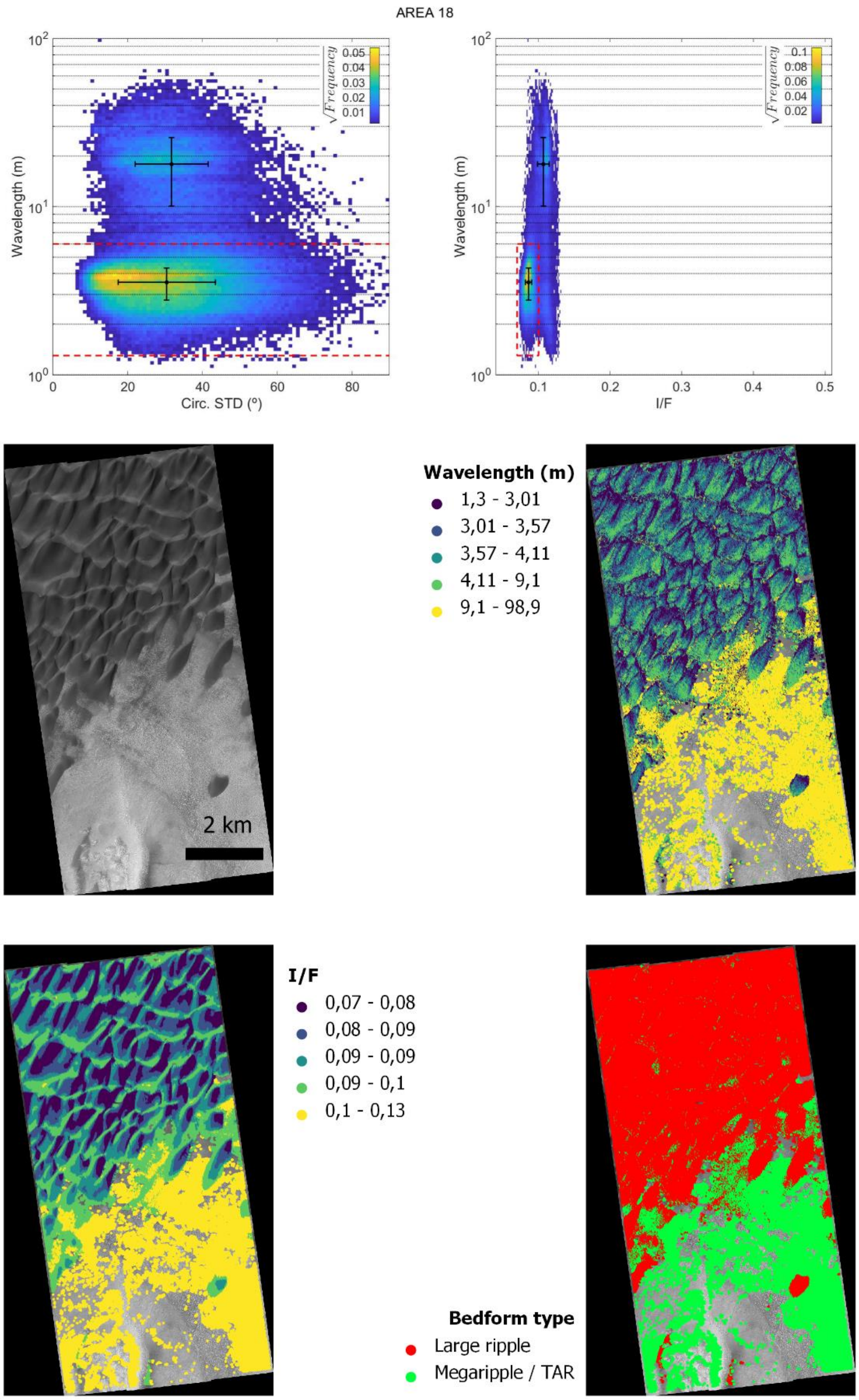

AREA 18
Wavelength (m)
Circ. STD (°)
I/F
√Frequency
2 km
Wavelength (m)
1,3 - 3,01
3,01 - 3,57
3,57 - 4,11
4,11 - 9,1
9,1 - 98,9
I/F
0,07 - 0,08
0,08 - 0,09
0,09 - 0,09
0,09 - 0,1
0,1 - 0,13
Bedform type
Large ripple
Megaripple / TAR

Area 19

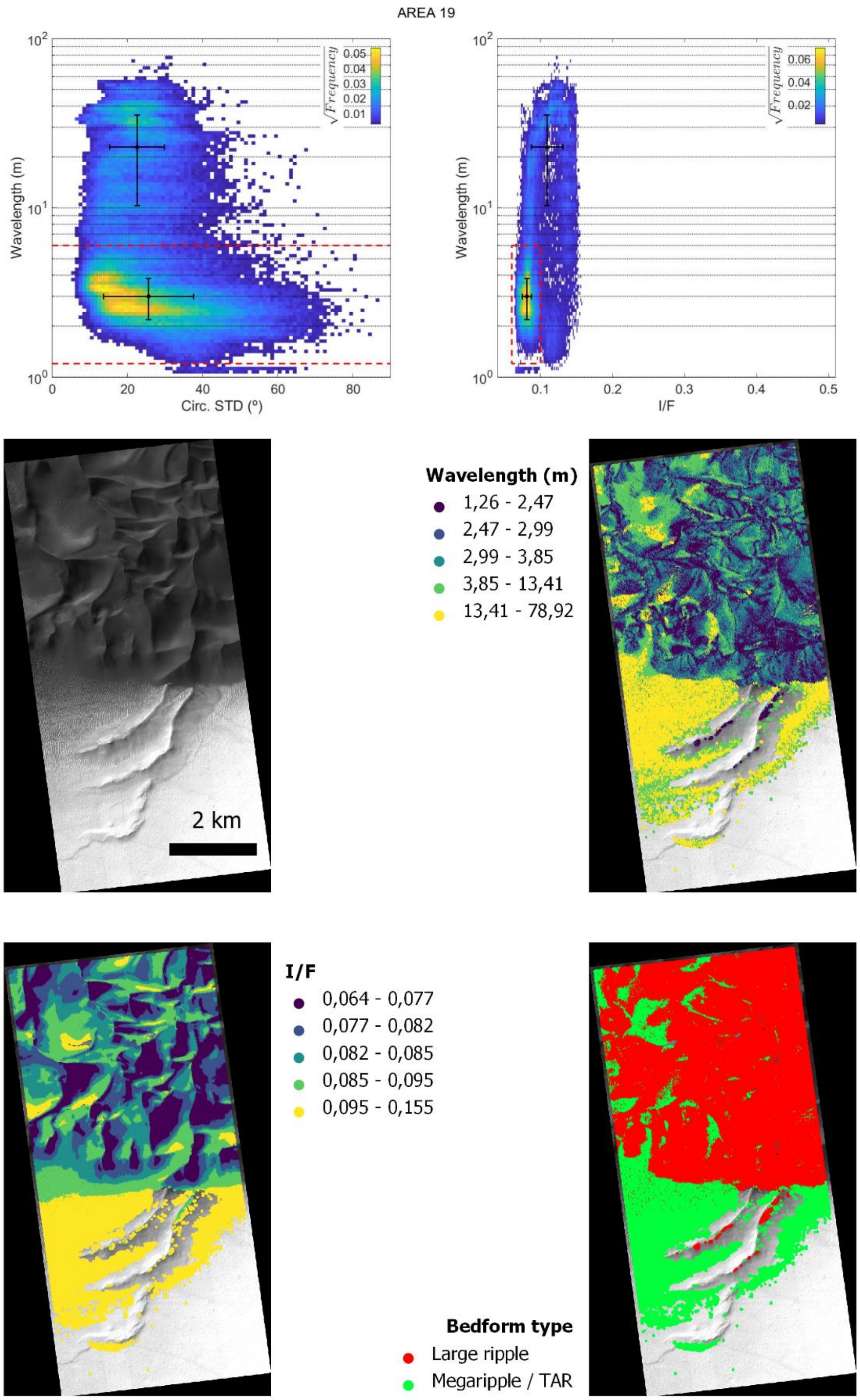

AREA 19
Wavelength (m)
Circ. STD (º)
I/F
√Frequency
2 km
Wavelength (m)
1,26 - 2,47
2,47 - 2,99
2,99 - 3,85
3,85 - 13,41
13,41 - 78,92
I/F
0,064 - 0,077
0,077 - 0,082
0,082 - 0,085
0,085 - 0,095
0,095 - 0,155
Bedform type
Large ripple
Megaripple / TAR

Area 20

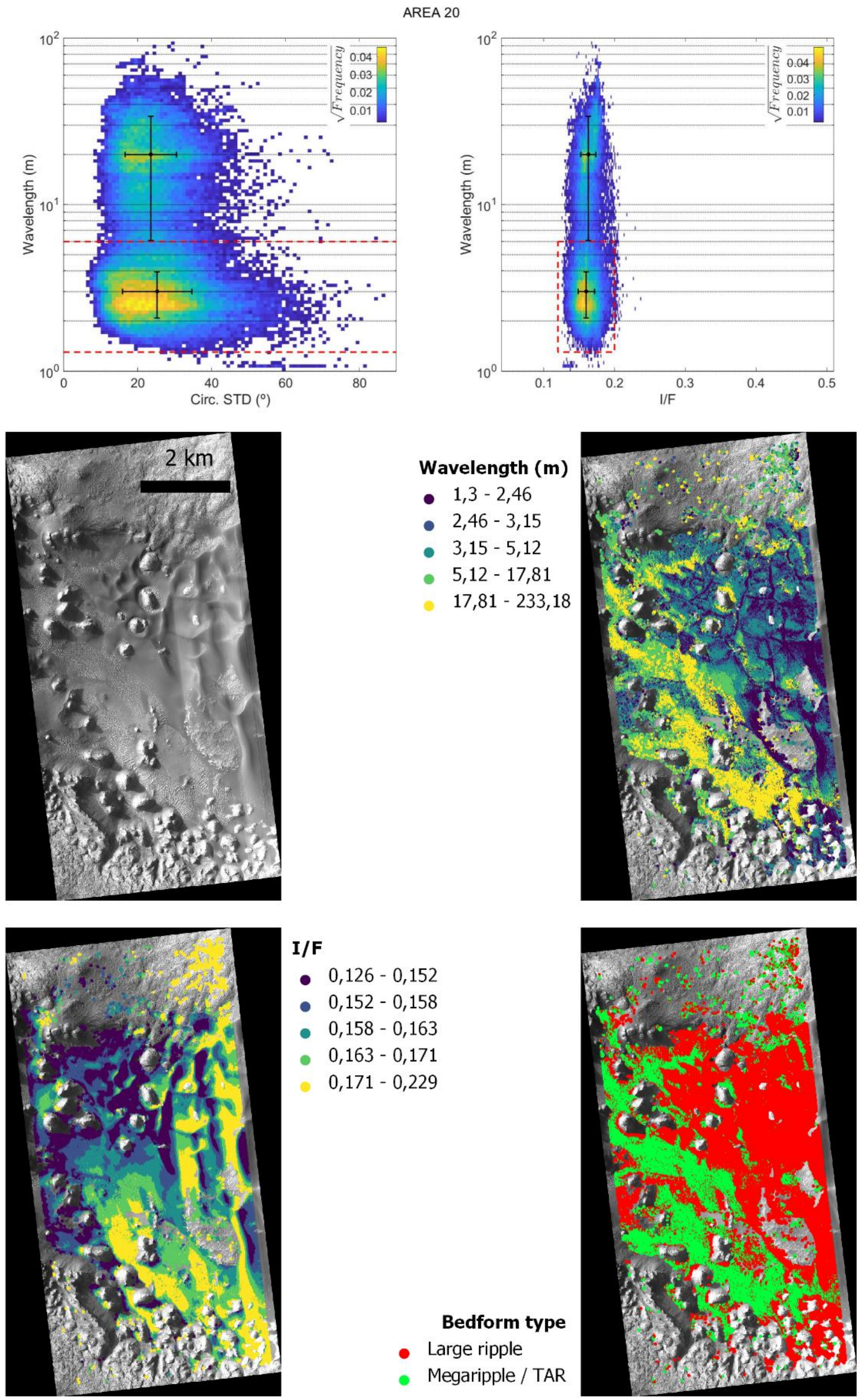
AREA 20
Wavelength (m)
Circ. STD (º)
√Frequency
0.04
0.03
0.02
0.01
I/F
2 km
Wavelength (m)
1,3 - 2,46
2,46 - 3,15
3,15 - 5,12
5,12 - 17,81
17,81 - 233,18
I/F
0,126 - 0,152
0,152 - 0,158
0,158 - 0,163
0,163 - 0,171
0,171 - 0,229
Bedform type
Large ripple
Megaripple / TAR

Area 21

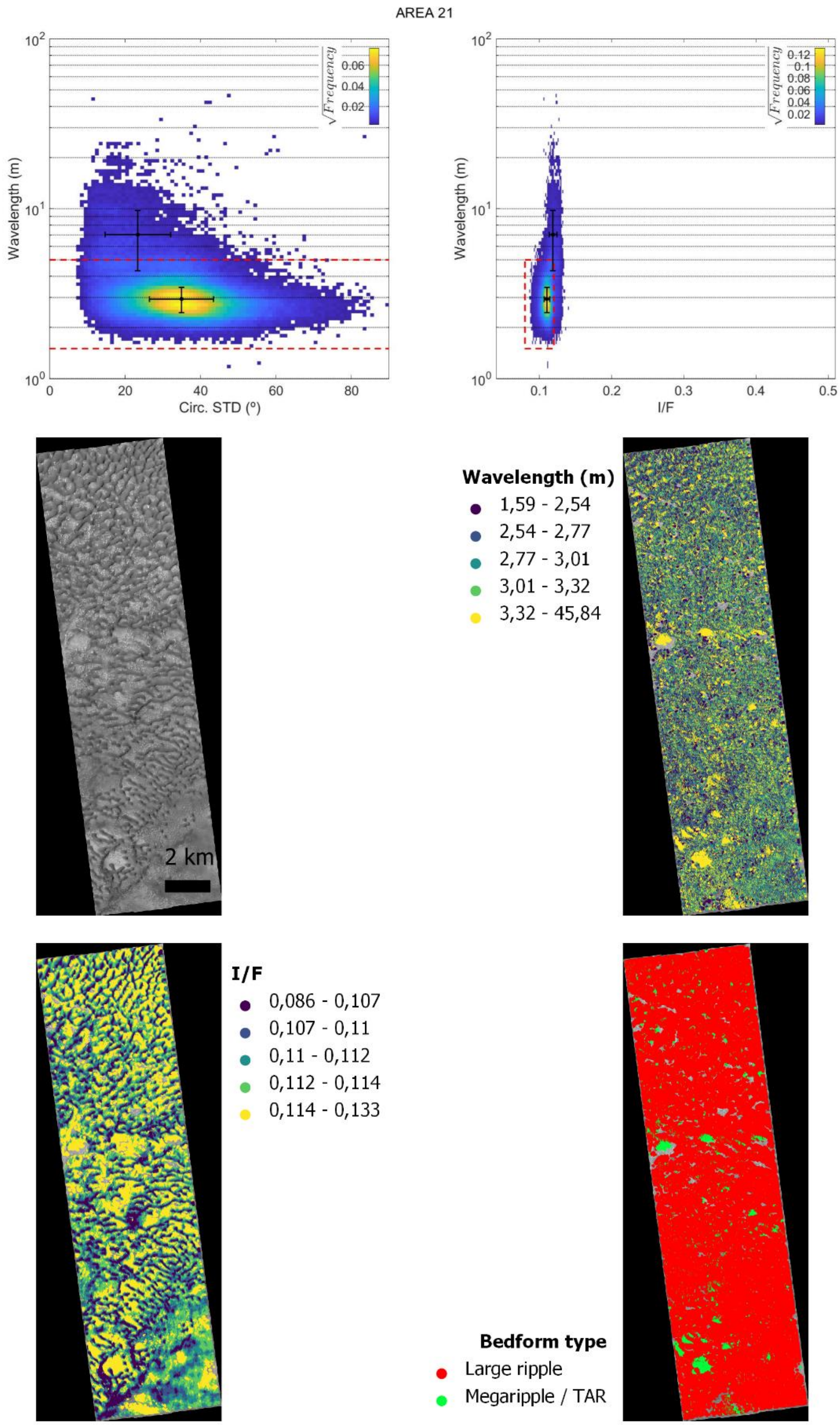
AREA 21
Wavelength (m)
Circ. STD (º)
√Frequency
I/F
2 km
Wavelength (m)
1,59 - 2,54
2,54 - 2,77
2,77 - 3,01
3,01 - 3,32
3,32 - 45,84
I/F
0,086 - 0,107
0,107 - 0,11
0,11 - 0,112
0,112 - 0,114
0,114 - 0,133
Bedform type
Large ripple
Megaripple / TAR

Area 22

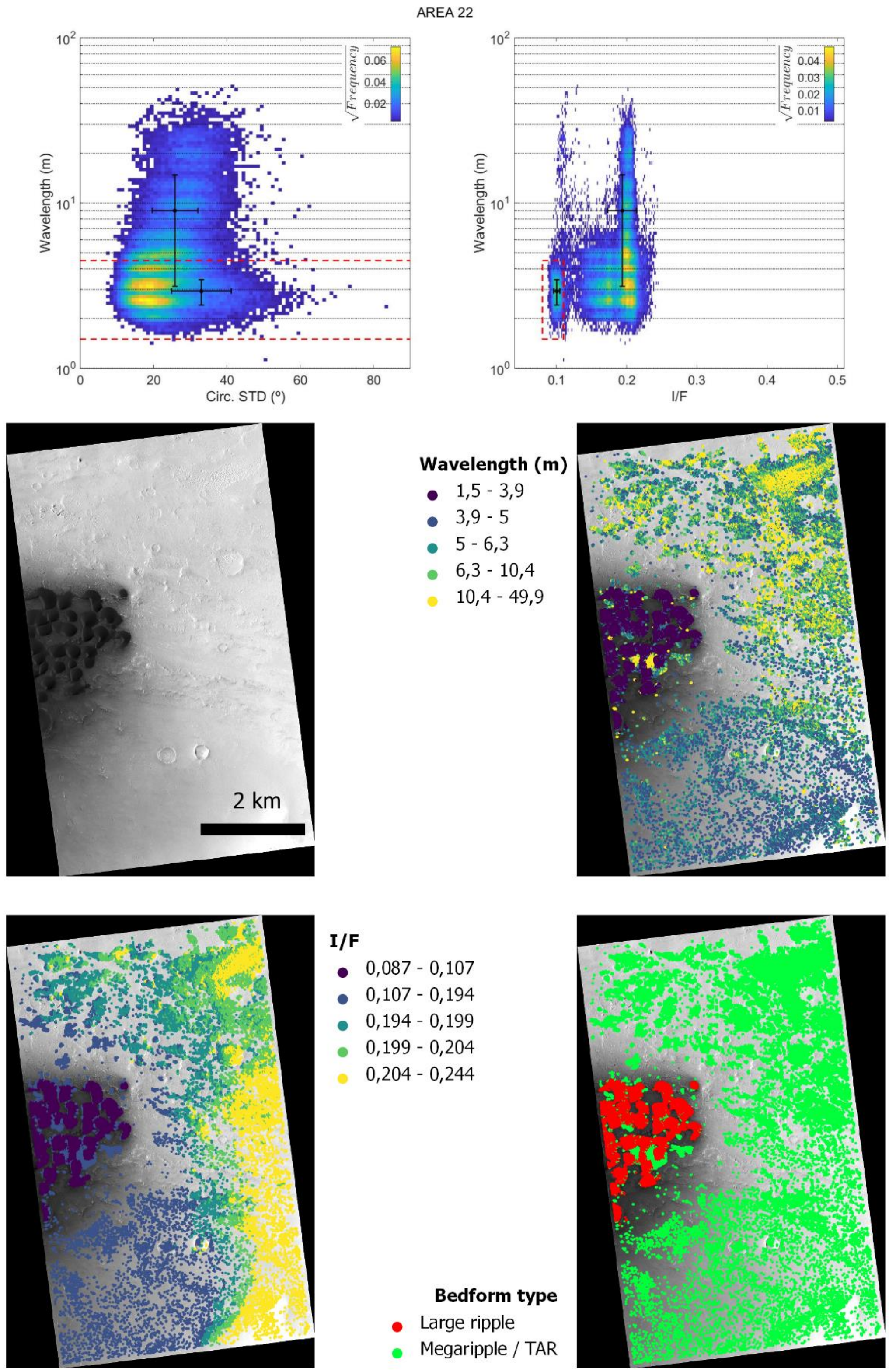
AREA 22
Wavelength (m)
Circ. STD (º)
√Frequency
0.06
0.04
0.02
I/F
0.04
0.03
0.02
0.01
2 km
Wavelength (m)
1,5 - 3,9
3,9 - 5
5 - 6,3
6,3 - 10,4
10,4 - 49,9
I/F
0,087 - 0,107
0,107 - 0,194
0,194 - 0,199
0,199 - 0,204
0,204 - 0,244
Bedform type
Large ripple
Megaripple / TAR

Area 23

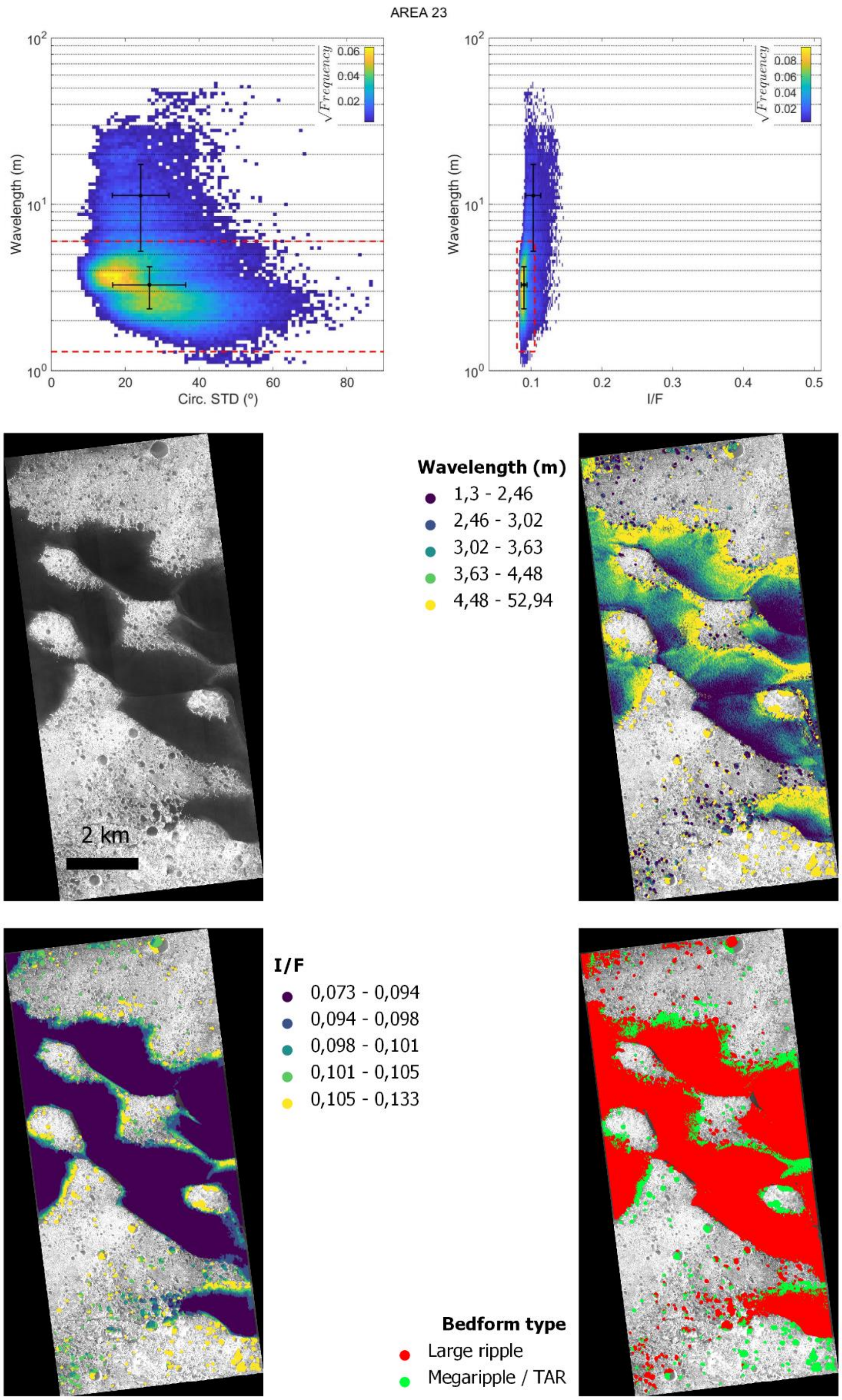

AREA 23
Wavelength (m)
Circ. STD (°)
I/F
√Frequency
2 km
Wavelength (m)
1,3 - 2,46
2,46 - 3,02
3,02 - 3,63
3,63 - 4,48
4,48 - 52,94
I/F
0,073 - 0,094
0,094 - 0,098
0,098 - 0,101
0,101 - 0,105
0,105 - 0,133
Bedform type
Large ripple
Megaripple / TAR

Area 24

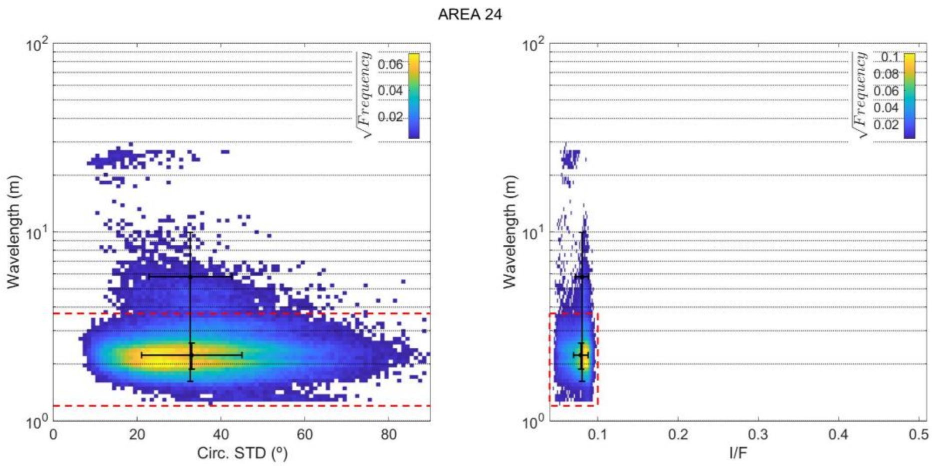
AREA 24
Wavelength (m)
Circ. STD (°)
I/F
$\sqrt{Frequency}$

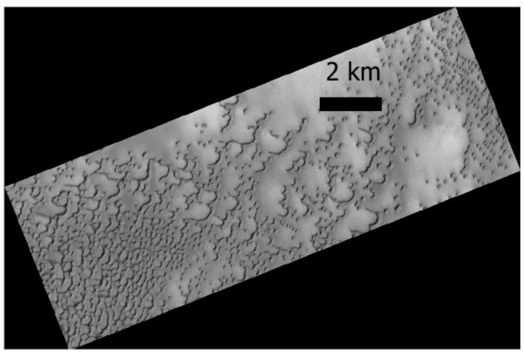
2 km

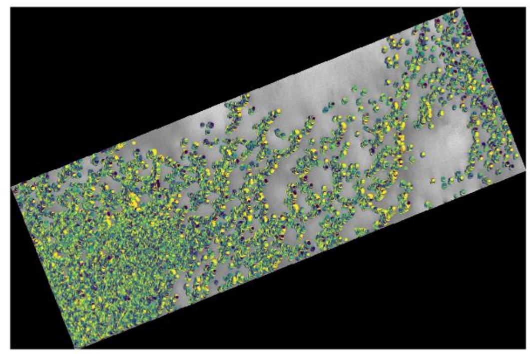
Wavelength (m)
1,23 - 1,95
1,95 - 2,1
2,1 - 2,29
2,29 - 2,49
2,49 - 28,54

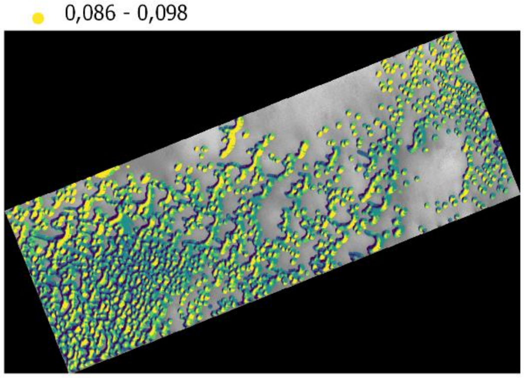
I/F
0,045 - 0,072
0,072 - 0,079
0,079 - 0,083
0,083 - 0,086
0,086 - 0,098

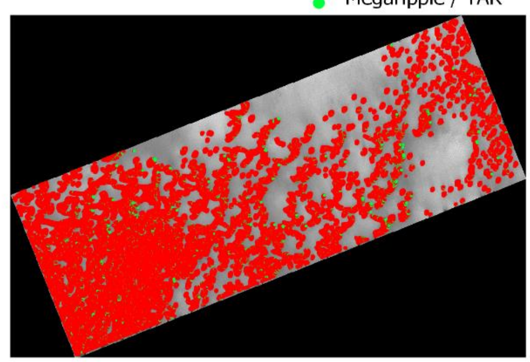
Bedform type
Large ripple
Megaripple / TAR

Area 25

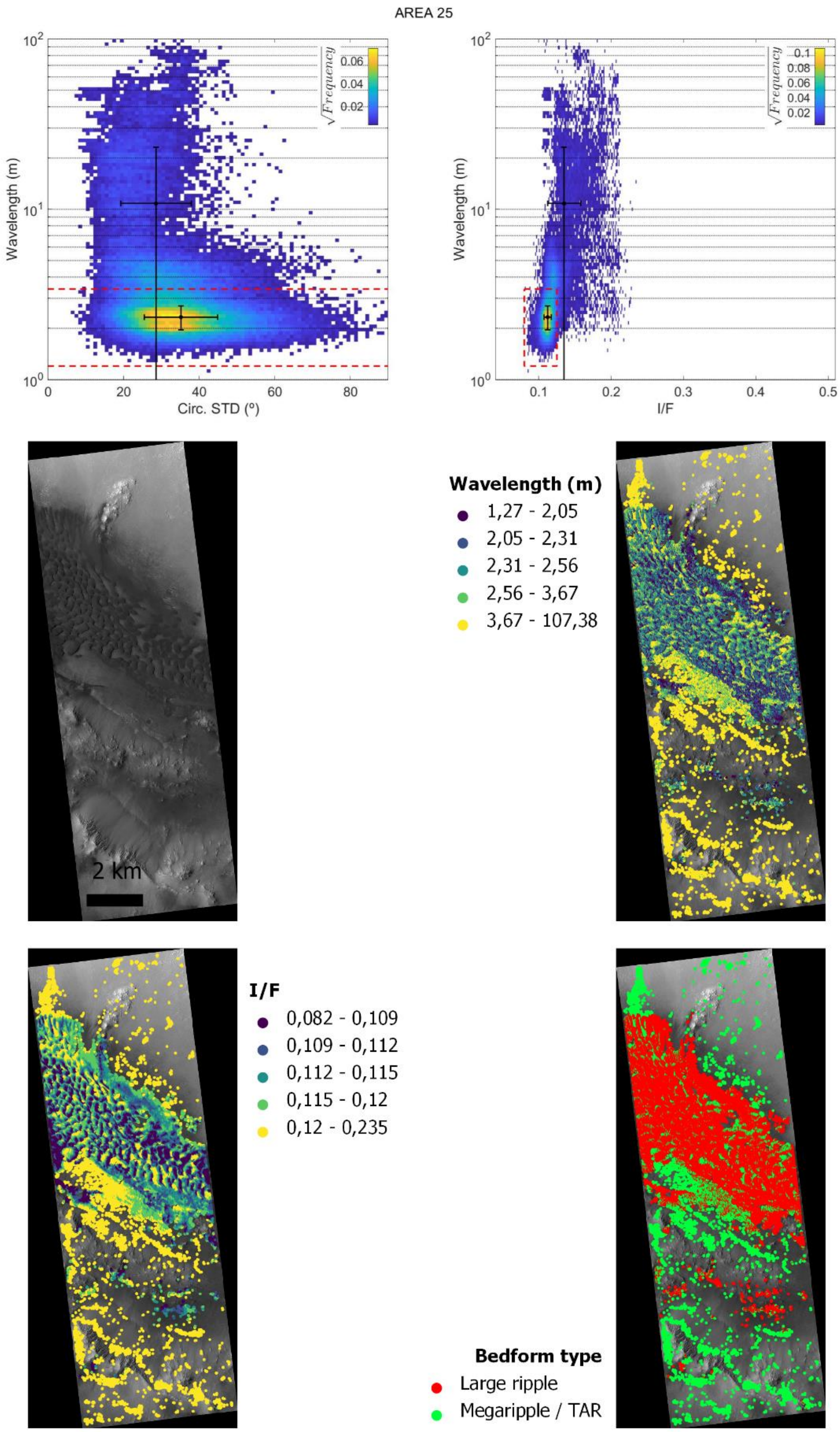
AREA 25
Wavelength (m)
Circ. STD (º)
$\sqrt{Frequency}$
I/F
2 km
Wavelength (m)
1,27 - 2,05
2,05 - 2,31
2,31 - 2,56
2,56 - 3,67
3,67 - 107,38
I/F
0,082 - 0,109
0,109 - 0,112
0,112 - 0,115
0,115 - 0,12
0,12 - 0,235
Bedform type
Large ripple
Megaripple / TAR

Area 26

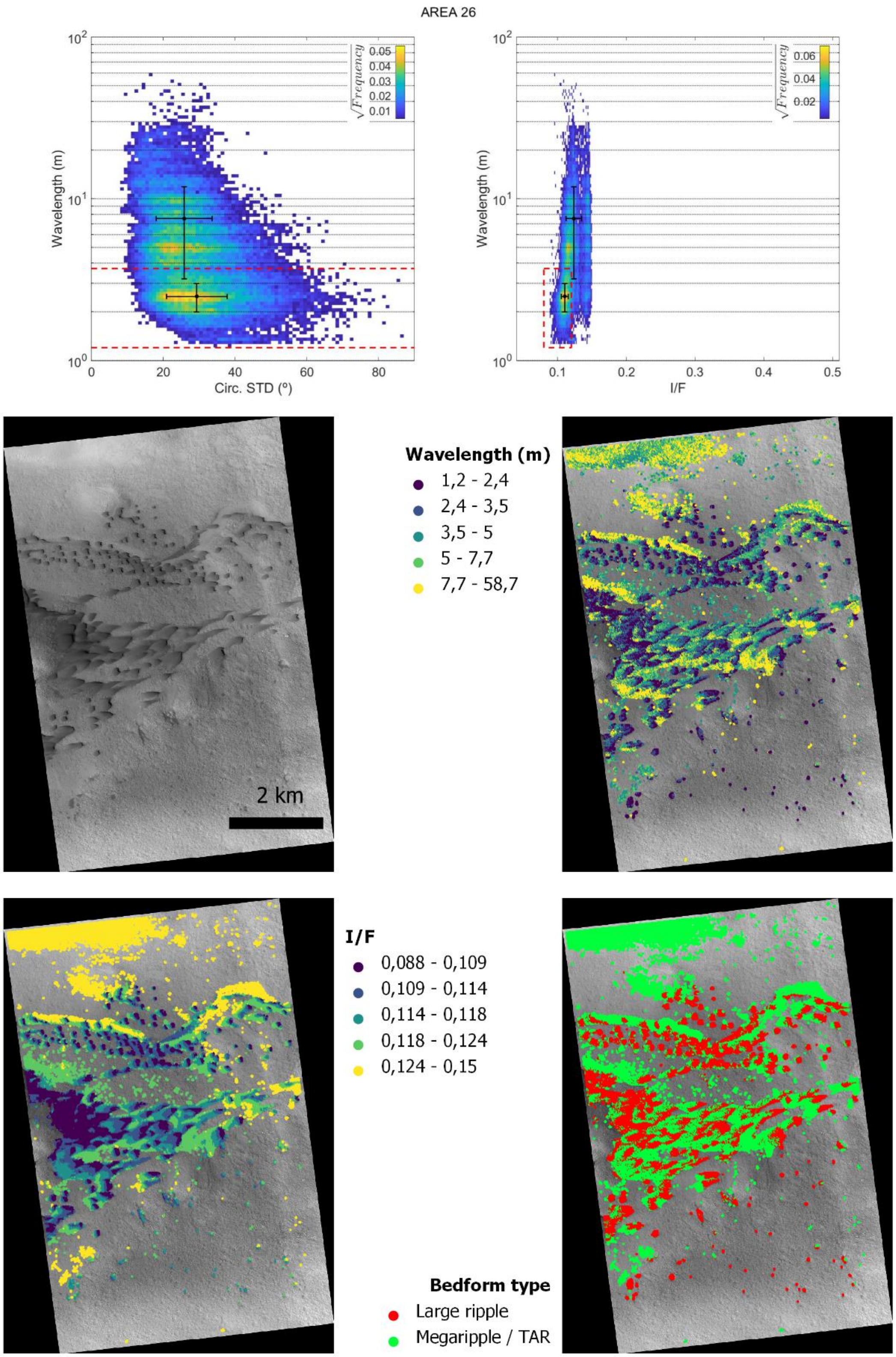
AREA 26
Wavelength (m)
Circ. STD (º)
I/F
√Frequency
2 km
Wavelength (m)
1,2 - 2,4
2,4 - 3,5
3,5 - 5
5 - 7,7
7,7 - 58,7
I/F
0,088 - 0,109
0,109 - 0,114
0,114 - 0,118
0,118 - 0,124
0,124 - 0,15
Bedform type
Large ripple
Megaripple / TAR

Area 27

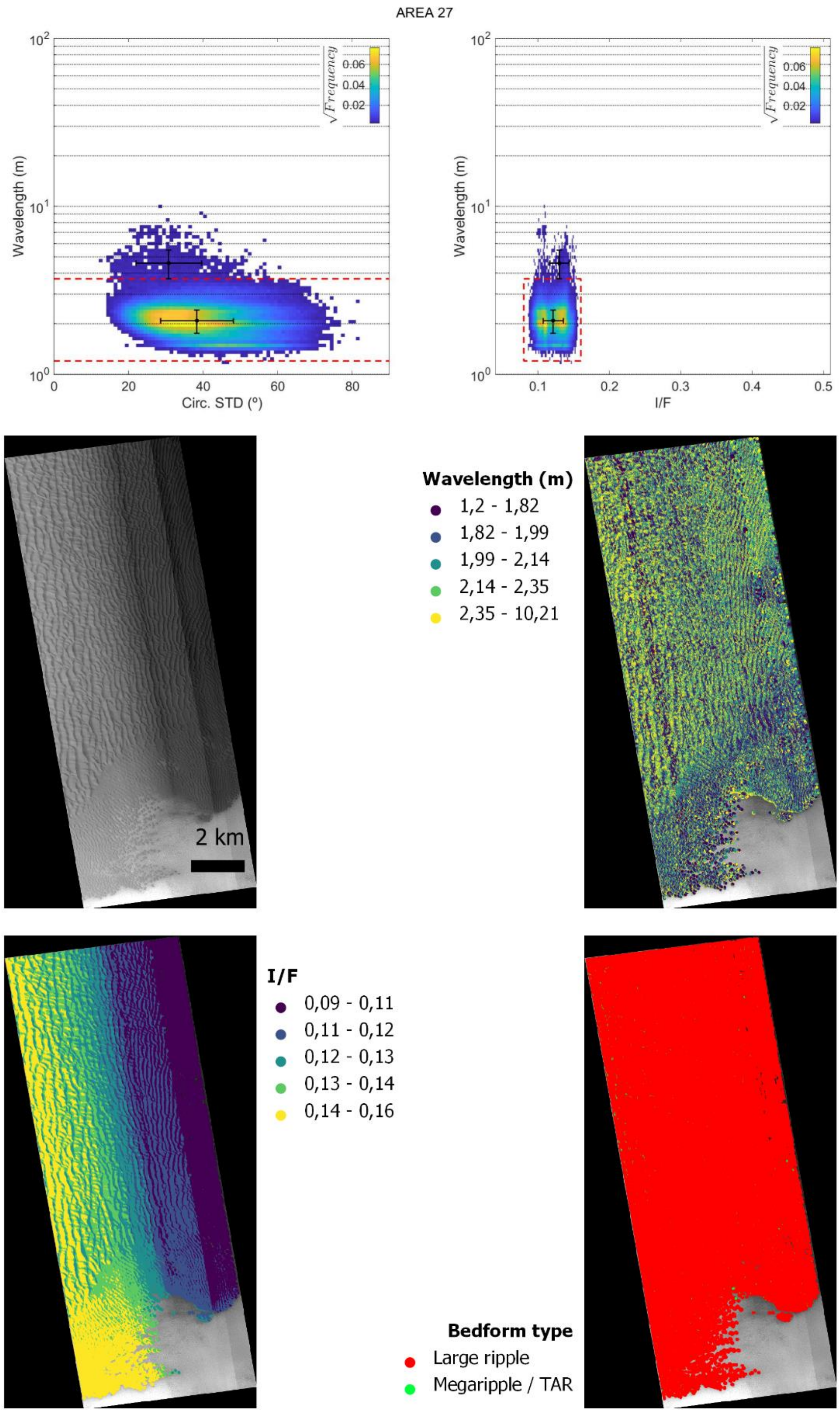
AREA 27
Wavelength (m)
Circ. STD (°)
I/F
√Frequency
0.06
0.04
0.02
2 km
Wavelength (m)
1,2 - 1,82
1,82 - 1,99
1,99 - 2,14
2,14 - 2,35
2,35 - 10,21
I/F
0,09 - 0,11
0,11 - 0,12
0,12 - 0,13
0,13 - 0,14
0,14 - 0,16
Bedform type
Large ripple
Megaripple / TAR

Area 28

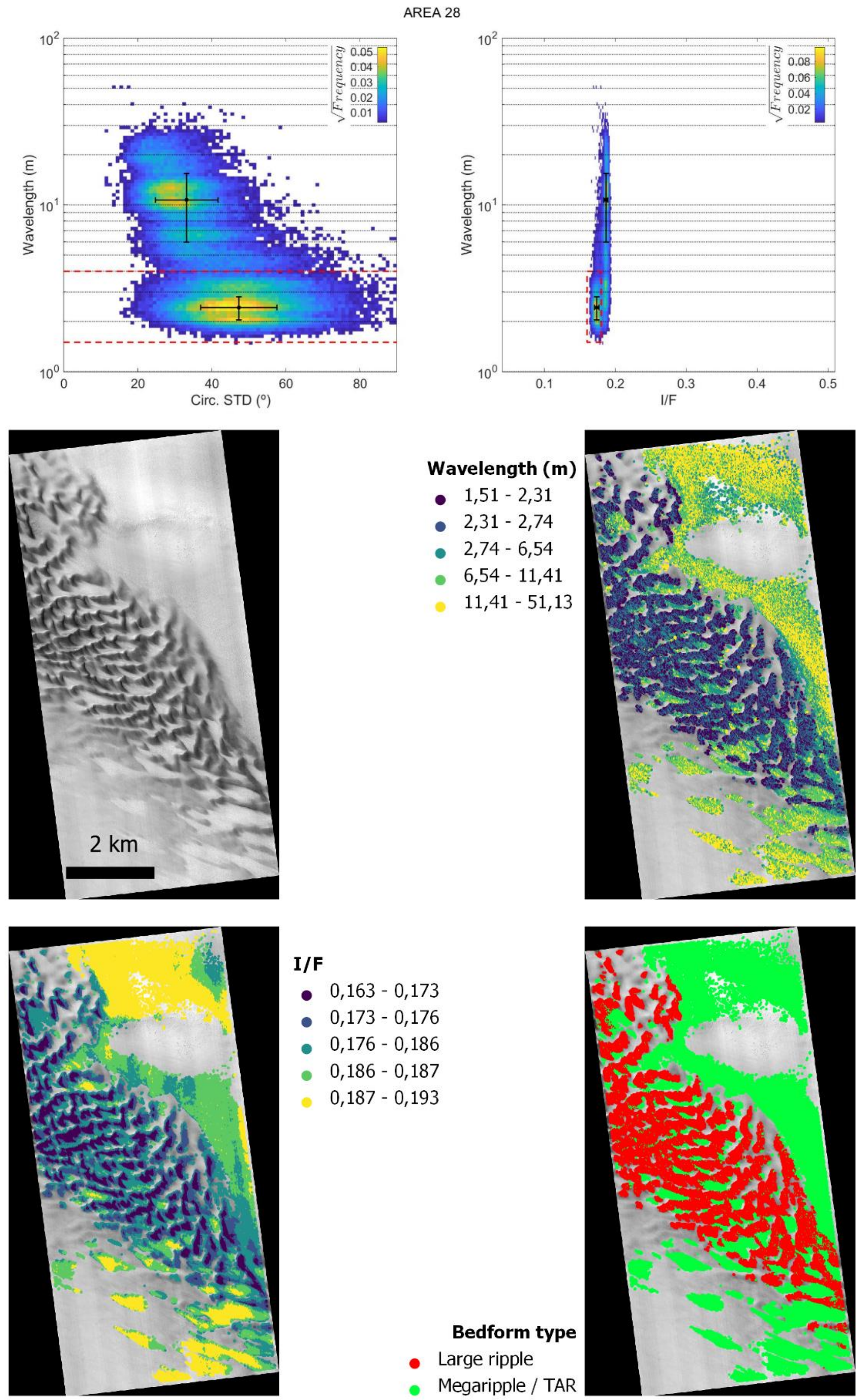
AREA 28
Wavelength (m)
Circ. STD (º)
I/F
√Frequency
2 km
Wavelength (m)
1,51 - 2,31
2,31 - 2,74
2,74 - 6,54
6,54 - 11,41
11,41 - 51,13
I/F
0,163 - 0,173
0,173 - 0,176
0,176 - 0,186
0,186 - 0,187
0,187 - 0,193
Bedform type
Large ripple
Megaripple / TAR

Area 29

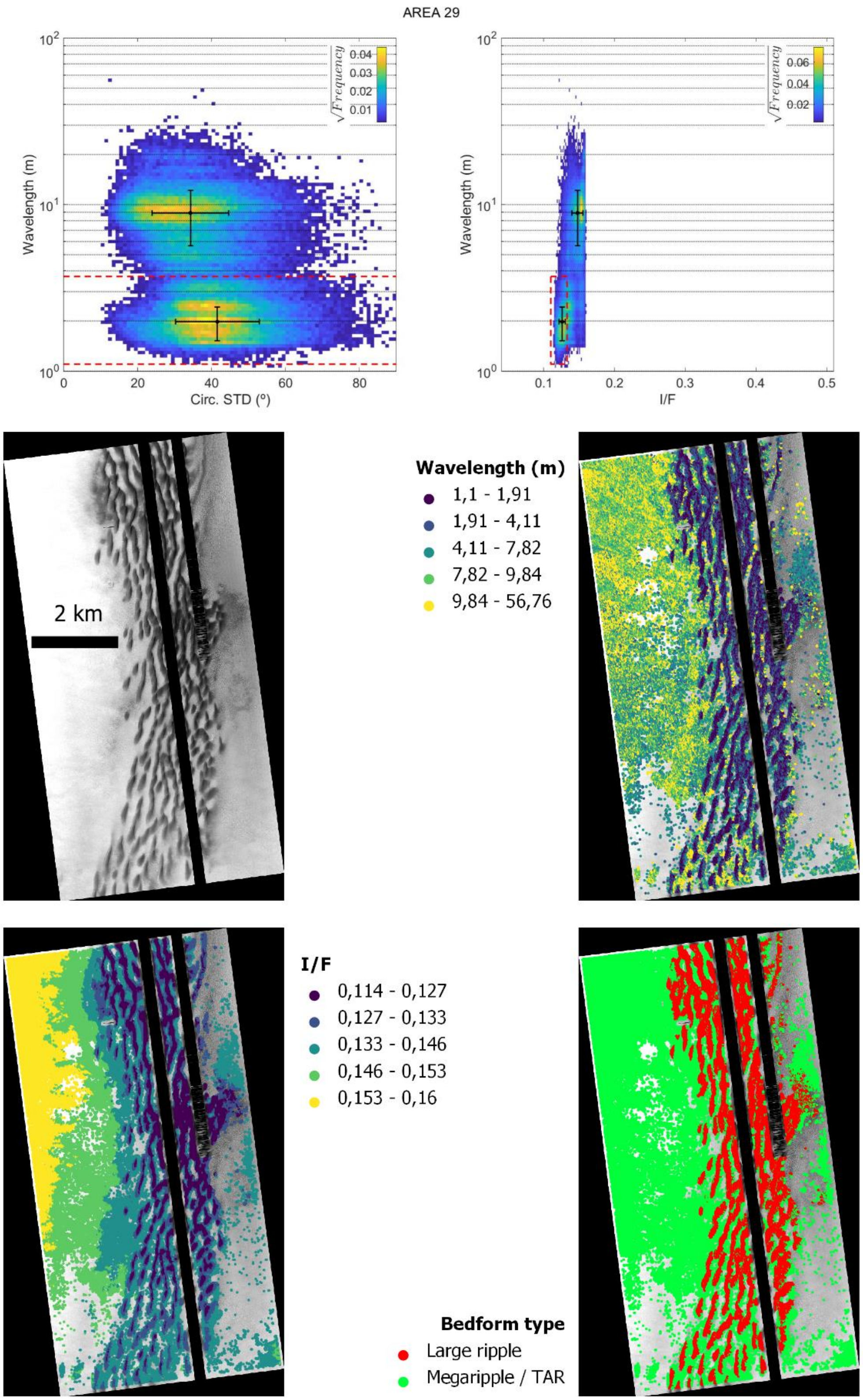
AREA 29
Wavelength (m)
Circ. STD (º)
I/F
√Frequency
2 km
Wavelength (m)
1,1 - 1,91
1,91 - 4,11
4,11 - 7,82
7,82 - 9,84
9,84 - 56,76
I/F
0,114 - 0,127
0,127 - 0,133
0,133 - 0,146
0,146 - 0,153
0,153 - 0,16
Bedform type
Large ripple
Megaripple / TAR

Area 30

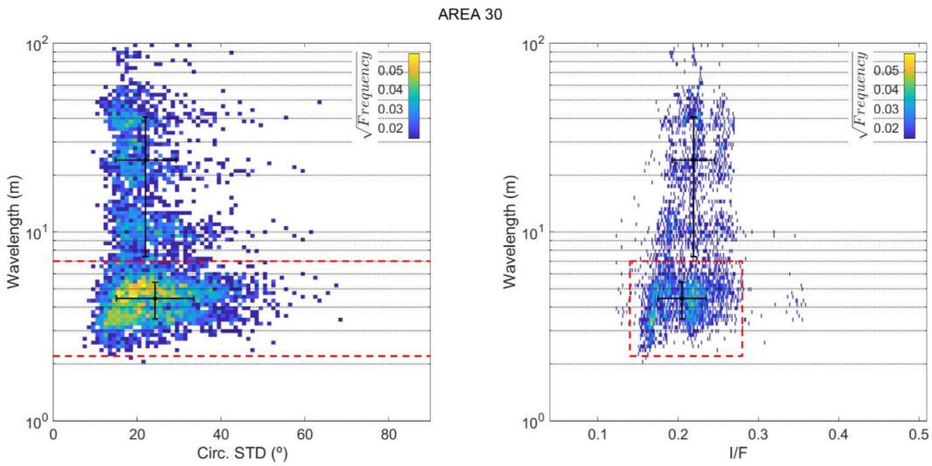
AREA 30
Wavelength (m)
Circ. STD (°)
I/F
$\sqrt{Frequency}$
0.05
0.04
0.03
0.02

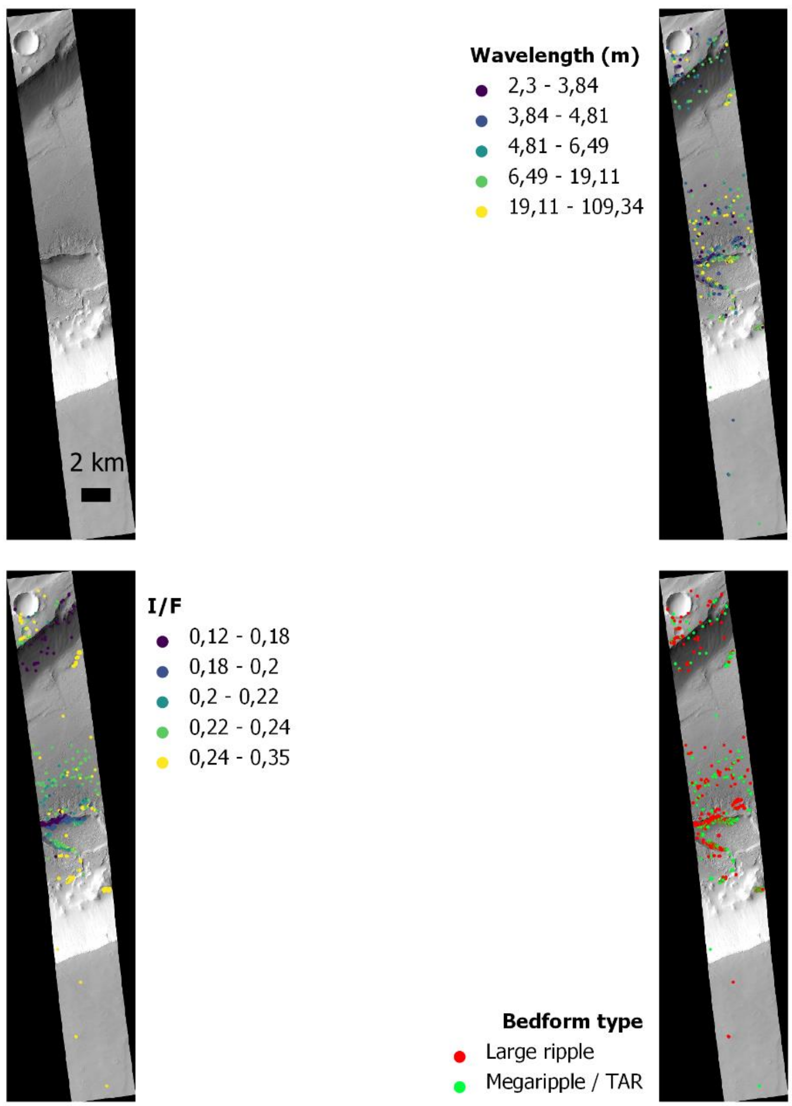
2 km
Wavelength (m)
2,3 - 3,84
3,84 - 4,81
4,81 - 6,49
6,49 - 19,11
19,11 - 109,34
I/F
0,12 - 0,18
0,18 - 0,2
0,2 - 0,22
0,22 - 0,24
0,24 - 0,35
Bedform type
Large ripple
Megaripple / TAR

Area 31

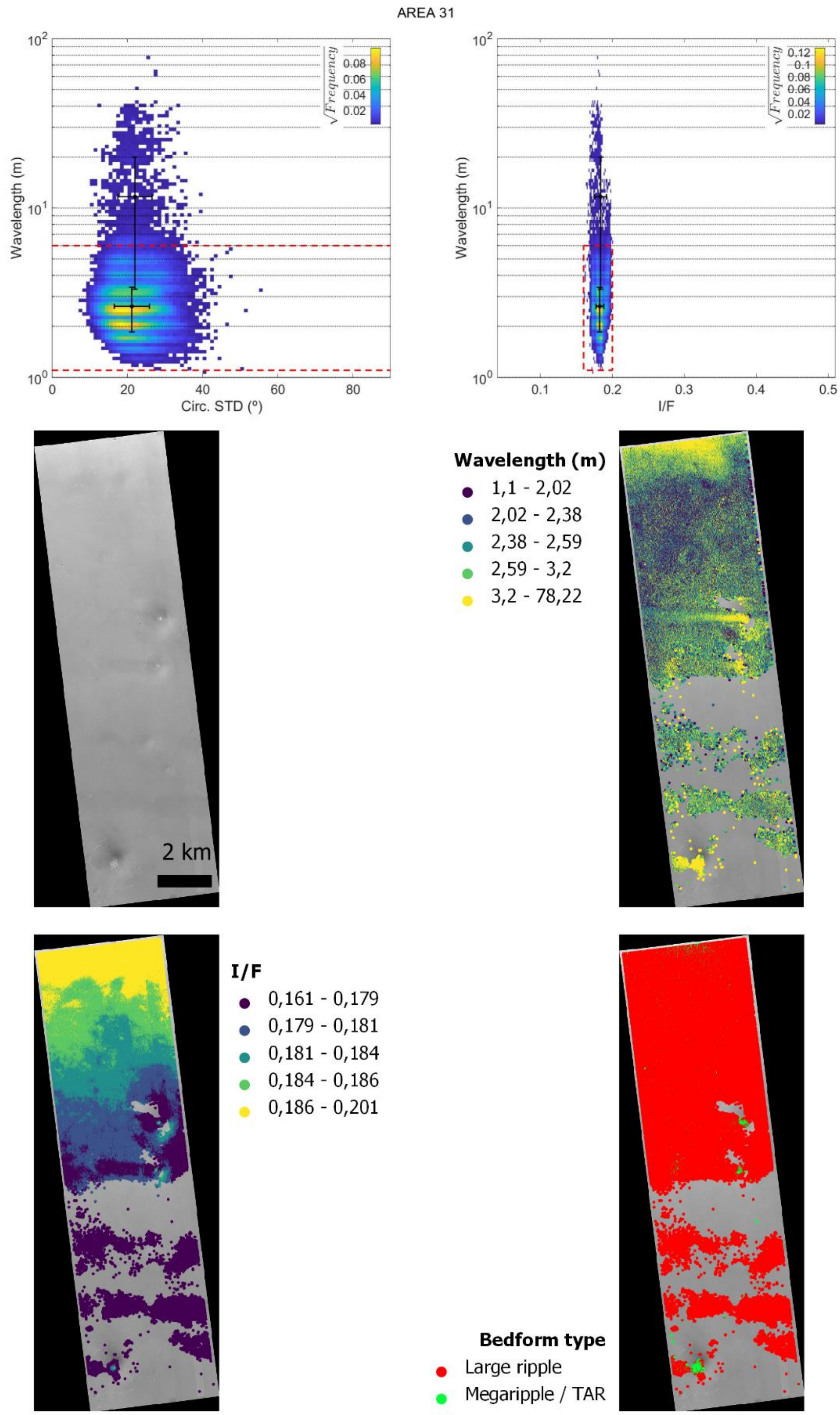
AREA 31
Wavelength (m)
Circ. STD (°)
I/F
√Frequency
2 km
Wavelength (m)
1,1 - 2,02
2,02 - 2,38
2,38 - 2,59
2,59 - 3,2
3,2 - 78,22
I/F
0,161 - 0,179
0,179 - 0,181
0,181 - 0,184
0,184 - 0,186
0,186 - 0,201
Bedform type
Large ripple
Megaripple / TAR

Area 32

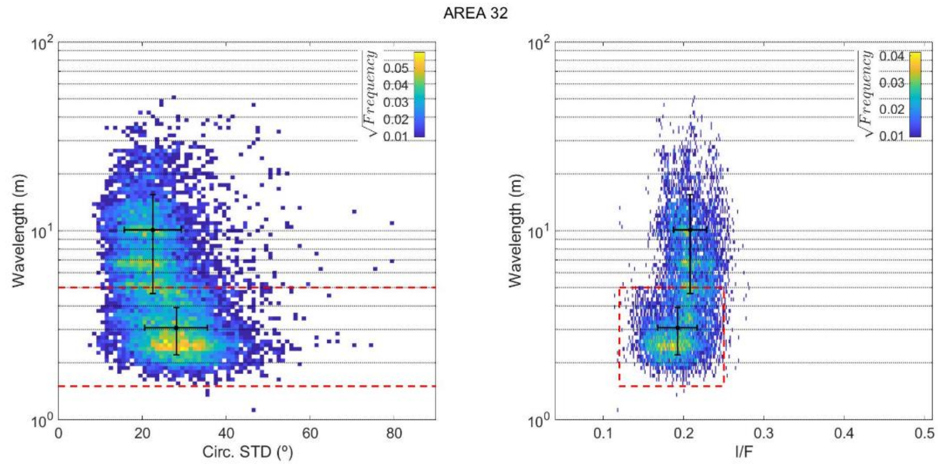
AREA 32
Wavelength (m)
Circ. STD (º)
√Frequency
Wavelength (m)
I/F
√Frequency

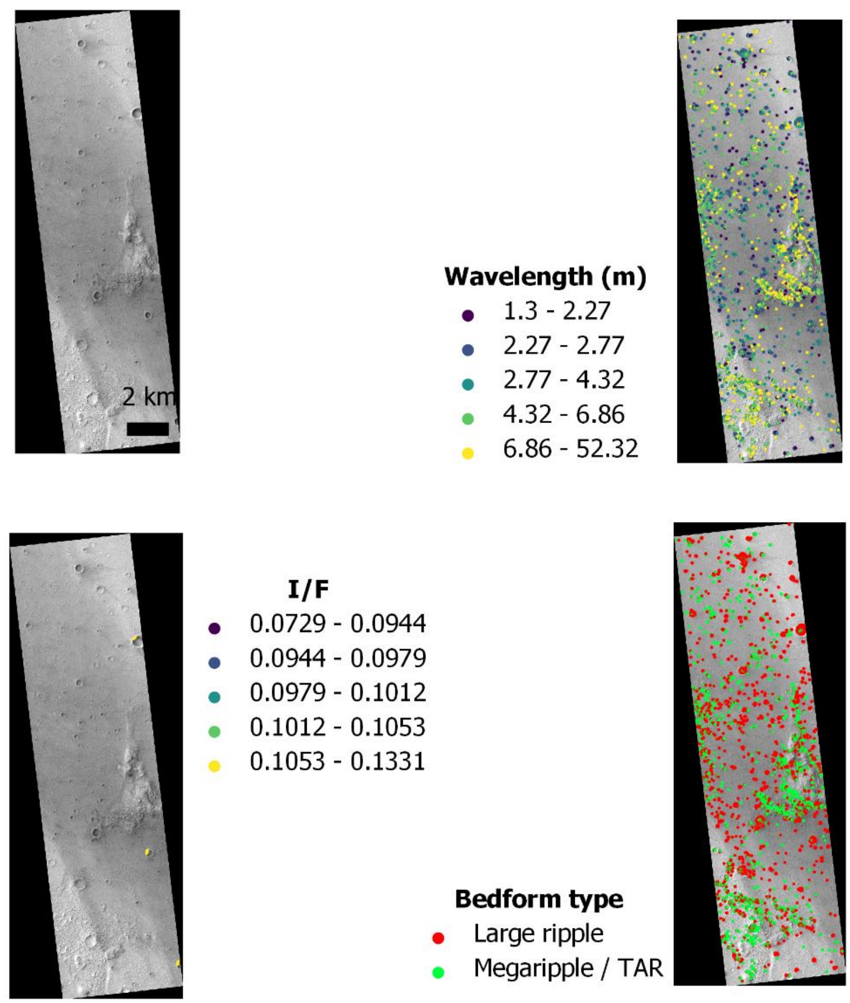
2 km
Wavelength (m)
1.3 - 2.27
2.27 - 2.77
2.77 - 4.32
4.32 - 6.86
6.86 - 52.32
I/F
0.0729 - 0.0944
0.0944 - 0.0979
0.0979 - 0.1012
0.1012 - 0.1053
0.1053 - 0.1331
Bedform type
Large ripple
Megaripple / TAR

Area 33

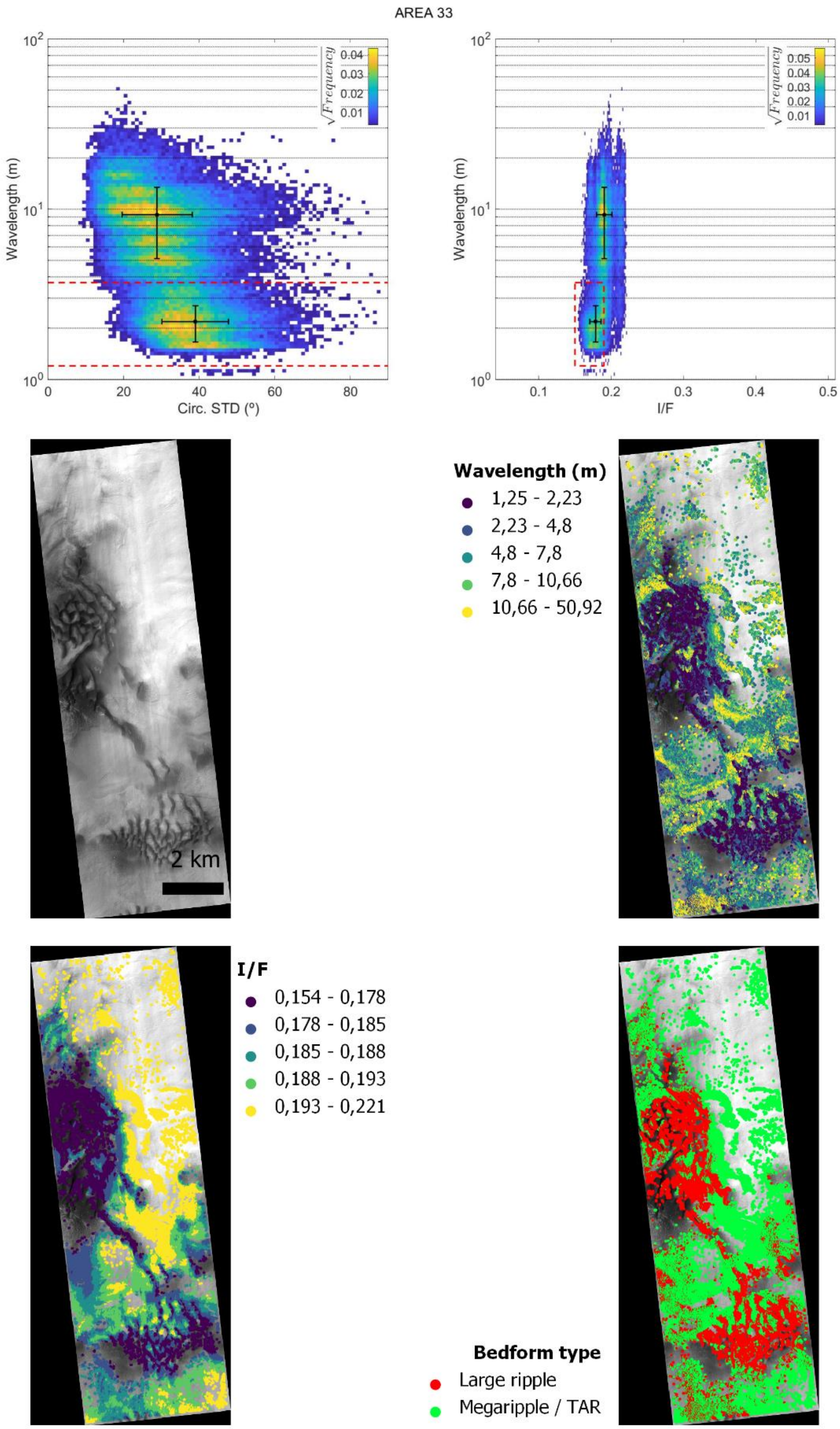
AREA 33
Wavelength (m)
Circ. STD (º)
I/F
√Frequency
2 km
Wavelength (m)
1,25 - 2,23
2,23 - 4,8
4,8 - 7,8
7,8 - 10,66
10,66 - 50,92
I/F
0,154 - 0,178
0,178 - 0,185
0,185 - 0,188
0,188 - 0,193
0,193 - 0,221
Bedform type
Large ripple
Megaripple / TAR

Area 34

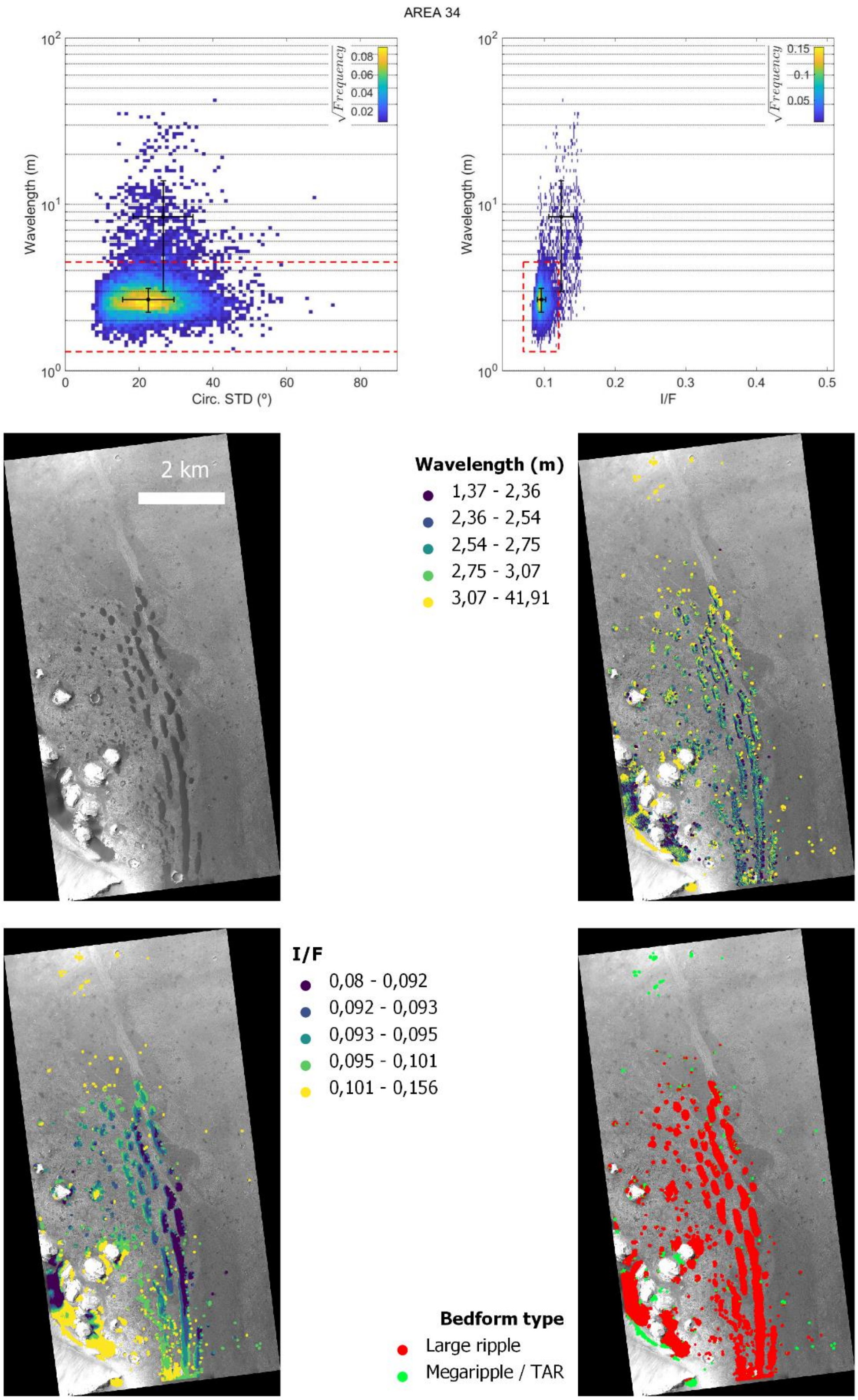

AREA 34
Wavelength (m)
Circ. STD (°)
I/F
√Frequency
2 km
Wavelength (m)
1,37 - 2,36
2,36 - 2,54
2,54 - 2,75
2,75 - 3,07
3,07 - 41,91
I/F
0,08 - 0,092
0,092 - 0,093
0,093 - 0,095
0,095 - 0,101
0,101 - 0,156
Bedform type
Large ripple
Megaripple / TAR

Area 35

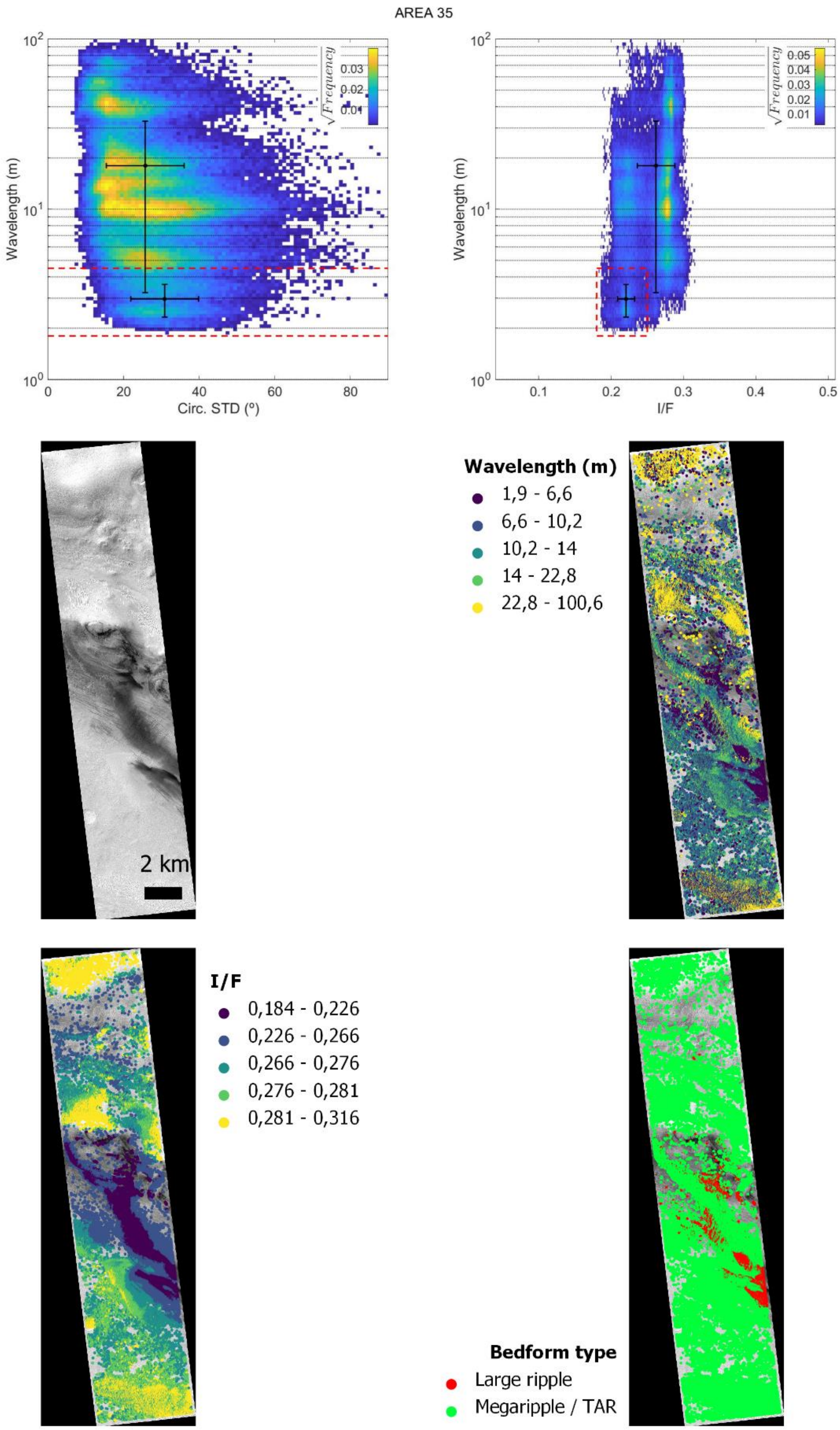
AREA 35
Wavelength (m)
Circ. STD (º)
√Frequency
0.01
0.02
0.03
Wavelength (m)
I/F
√Frequency
0.01
0.02
0.03
0.04
0.05
2 km
Wavelength (m)
1,9 - 6,6
6,6 - 10,2
10,2 - 14
14 - 22,8
22,8 - 100,6
I/F
0,184 - 0,226
0,226 - 0,266
0,266 - 0,276
0,276 - 0,281
0,281 - 0,316
Bedform type
Large ripple
Megaripple / TAR

Area 36

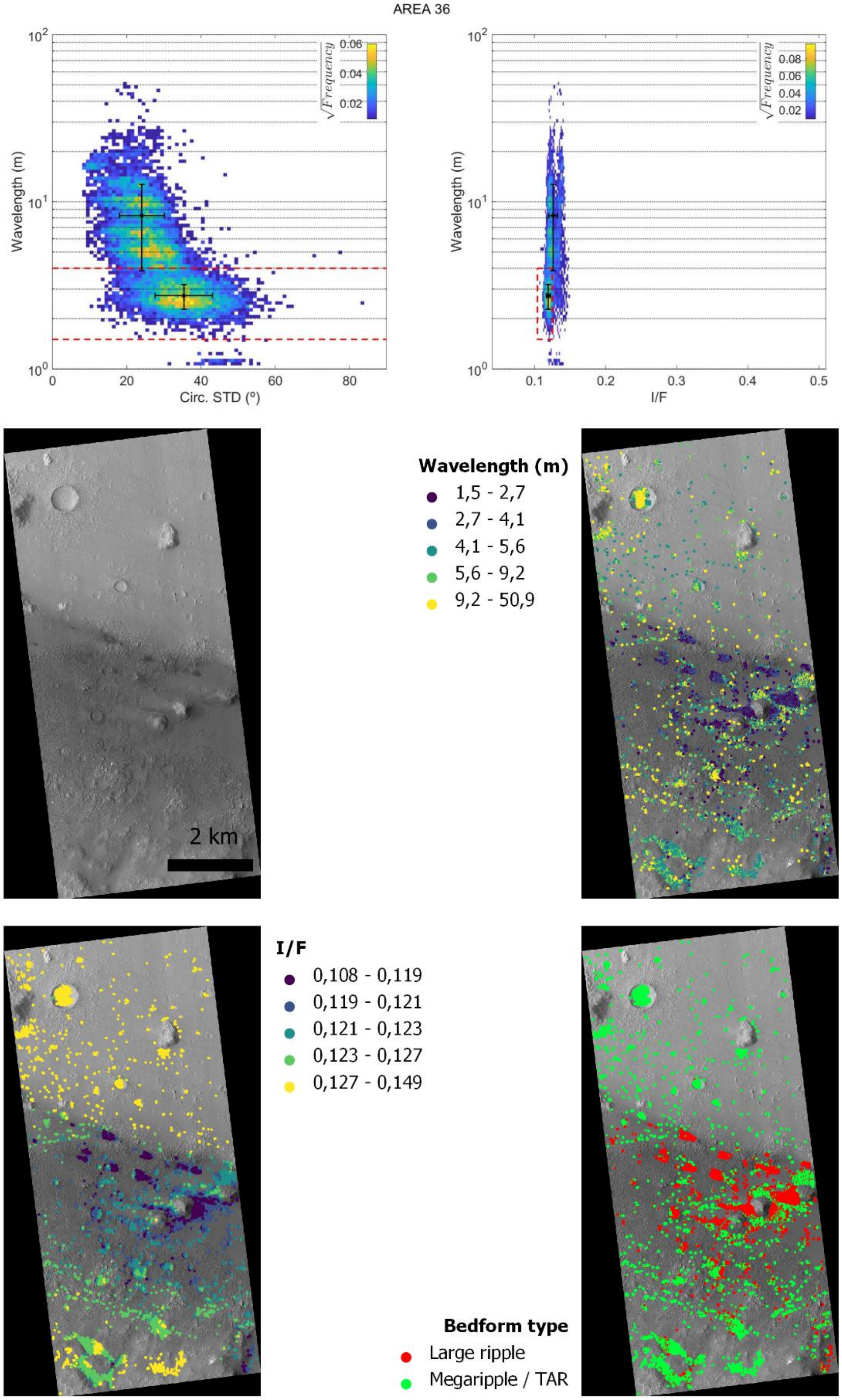
AREA 36
Wavelength (m)
Circ. STD (°)
I/F
√Frequency
Wavelength (m)
1,5 - 2,7
2,7 - 4,1
4,1 - 5,6
5,6 - 9,2
9,2 - 50,9
2 km
I/F
0,108 - 0,119
0,119 - 0,121
0,121 - 0,123
0,123 - 0,127
0,127 - 0,149
Bedform type
Large ripple
Megaripple / TAR

Area 37

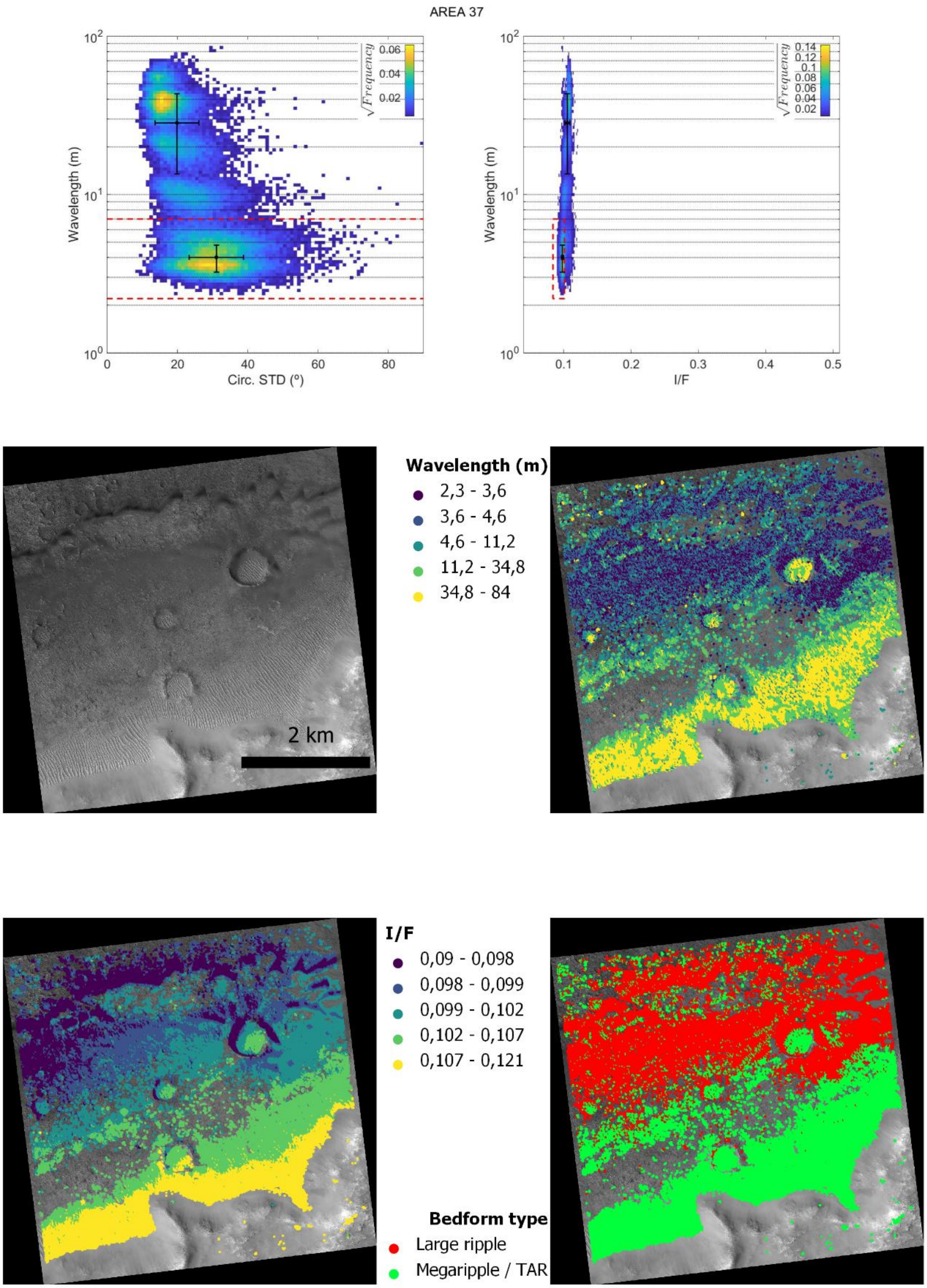

AREA 37
Wavelength (m)
Circ. STD (°)
I/F
$\sqrt{Frequency}$
2 km
Wavelength (m)
2,3 - 3,6
3,6 - 4,6
4,6 - 11,2
11,2 - 34,8
34,8 - 84
I/F
0,09 - 0,098
0,098 - 0,099
0,099 - 0,102
0,102 - 0,107
0,107 - 0,121
Bedform type
Large ripple
Megaripple / TAR

Area 38

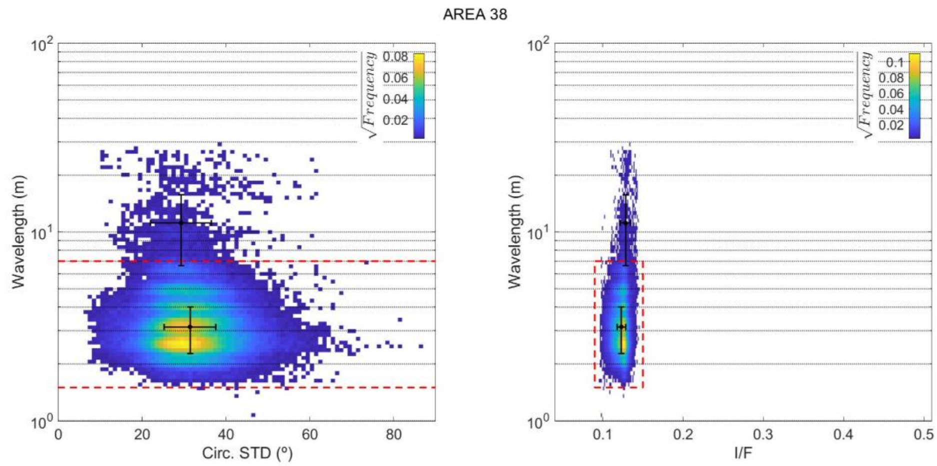

AREA 38
Wavelength (m)
Circ. STD (°)
√Frequency
Wavelength (m)
I/F
√Frequency

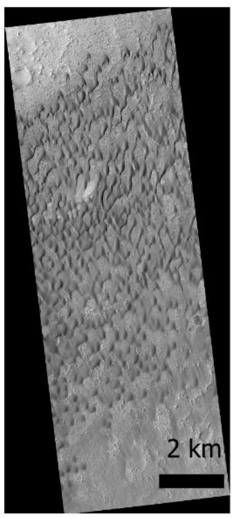

2 km

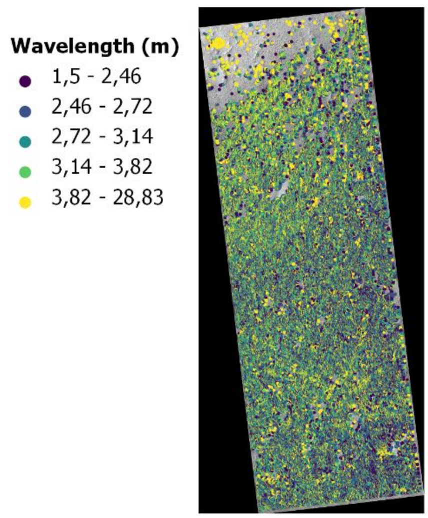

Wavelength (m)
1,5 - 2,46
2,46 - 2,72
2,72 - 3,14
3,14 - 3,82
3,82 - 28,83

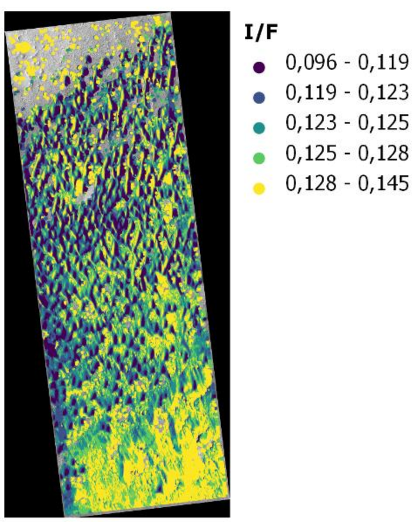

I/F
0,096 - 0,119
0,119 - 0,123
0,123 - 0,125
0,125 - 0,128
0,128 - 0,145

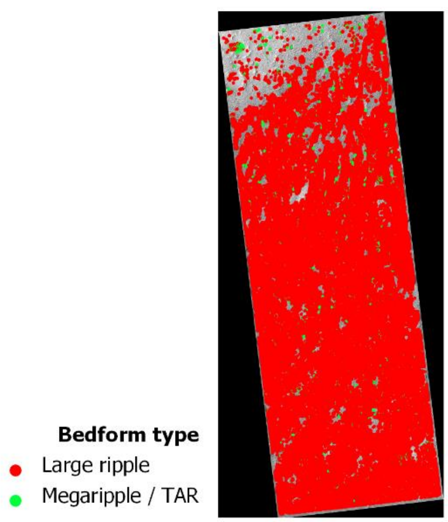

Bedform type
Large ripple
Megaripple / TAR

Area 39

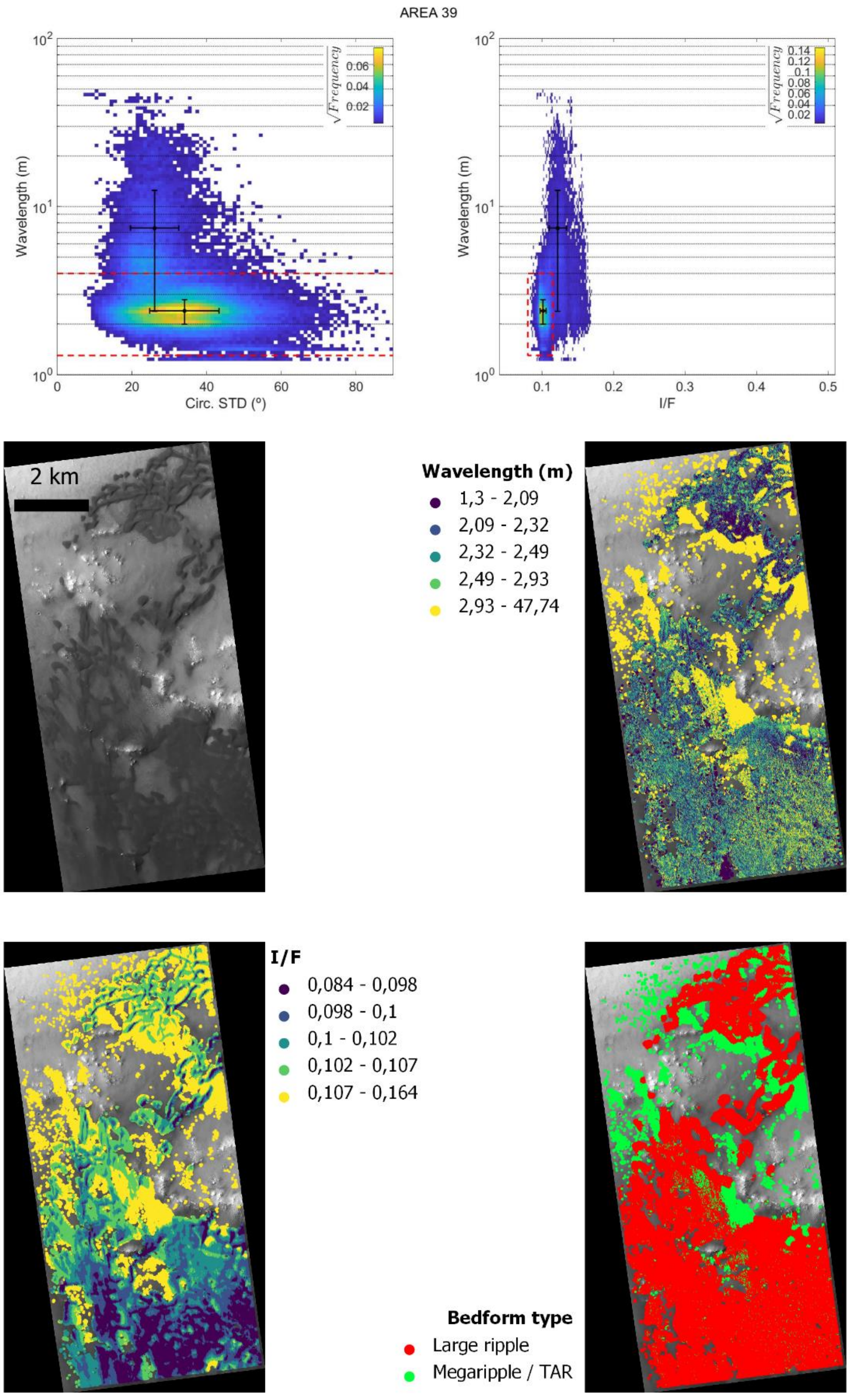
AREA 39
Wavelength (m)
Circ. STD (°)
I/F
√Frequency
2 km
Wavelength (m)
1,3 - 2,09
2,09 - 2,32
2,32 - 2,49
2,49 - 2,93
2,93 - 47,74
I/F
0,084 - 0,098
0,098 - 0,1
0,1 - 0,102
0,102 - 0,107
0,107 - 0,164
Bedform type
Large ripple
Megaripple / TAR

Area 40

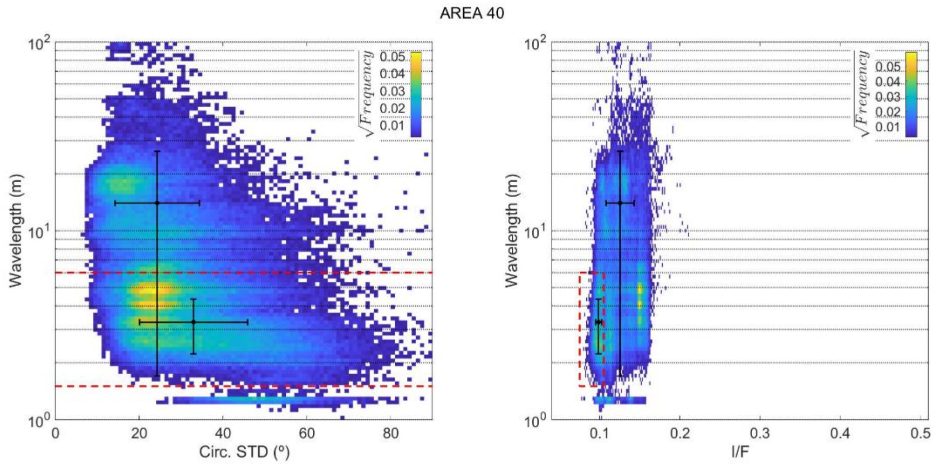
AREA 40
Wavelength (m)
Circ. STD (º)
I/F
$\sqrt{Frequency}$
0.05
0.04
0.03
0.02
0.01

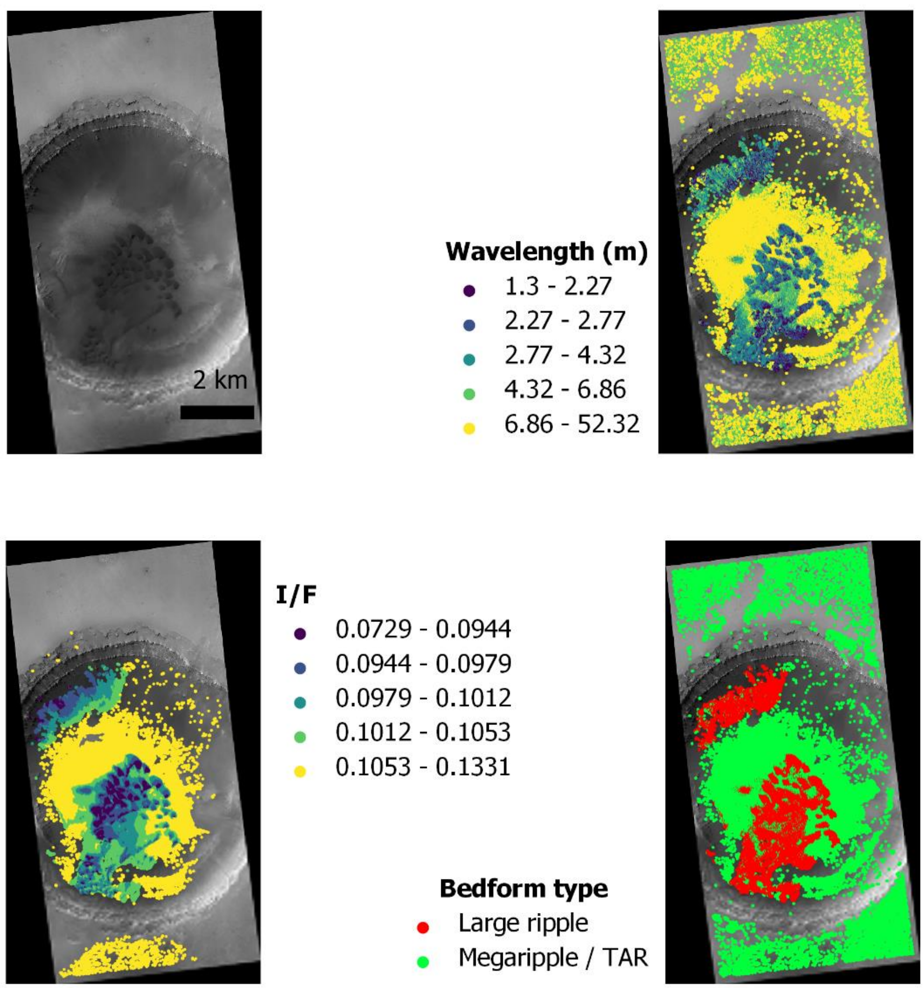
2 km
Wavelength (m)
1.3 - 2.27
2.27 - 2.77
2.77 - 4.32
4.32 - 6.86
6.86 - 52.32
I/F
0.0729 - 0.0944
0.0944 - 0.0979
0.0979 - 0.1012
0.1012 - 0.1053
0.1053 - 0.1331
Bedform type
Large ripple
Megaripple / TAR

Area 41

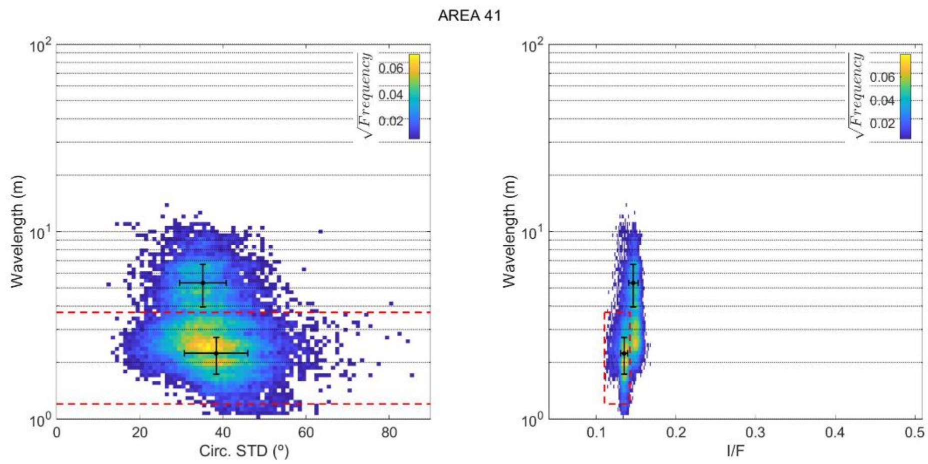
AREA 41
Wavelength (m)
Circ. STD (°)
I/F
√Frequency
0.06
0.04
0.02
10^2
10^1
10^0
0
20
40
60
80
0.1
0.2
0.3
0.4
0.5

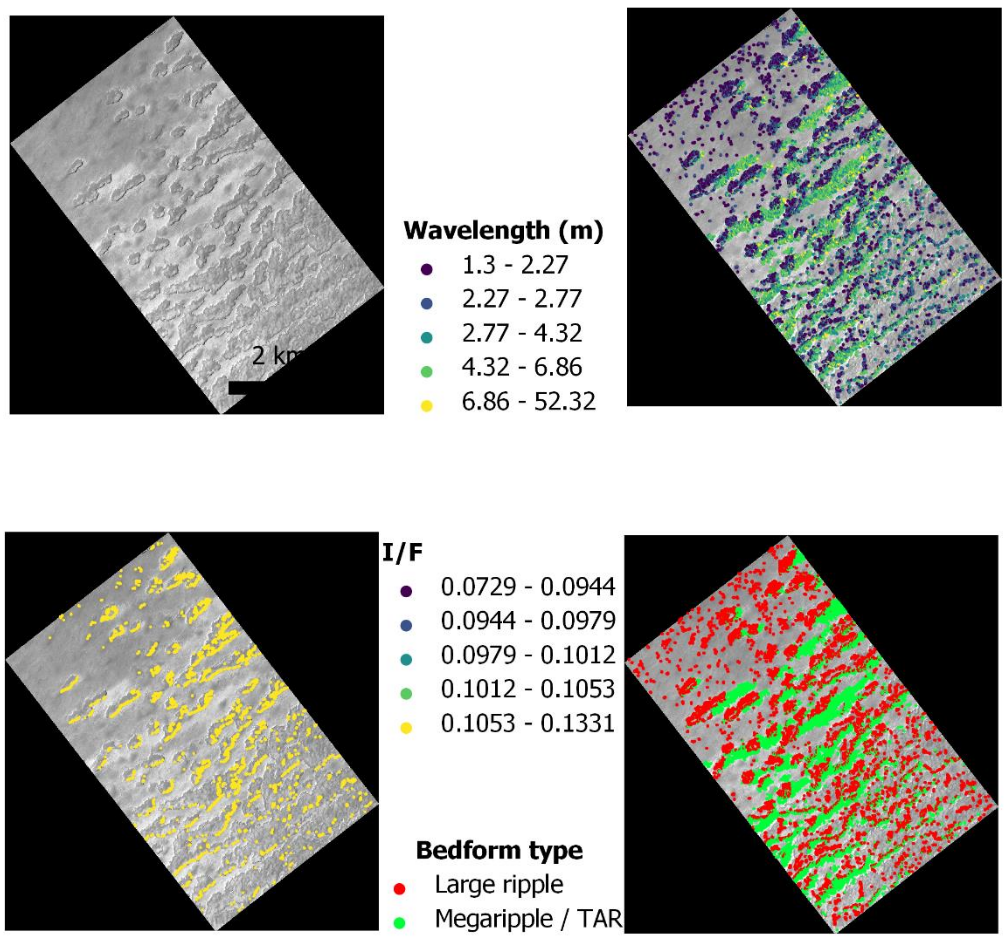
2 km
Wavelength (m)
1.3 - 2.27
2.27 - 2.77
2.77 - 4.32
4.32 - 6.86
6.86 - 52.32
I/F
0.0729 - 0.0944
0.0944 - 0.0979
0.0979 - 0.1012
0.1012 - 0.1053
0.1053 - 0.1331
Bedform type
Large ripple
Megaripple / TAR

Area 42

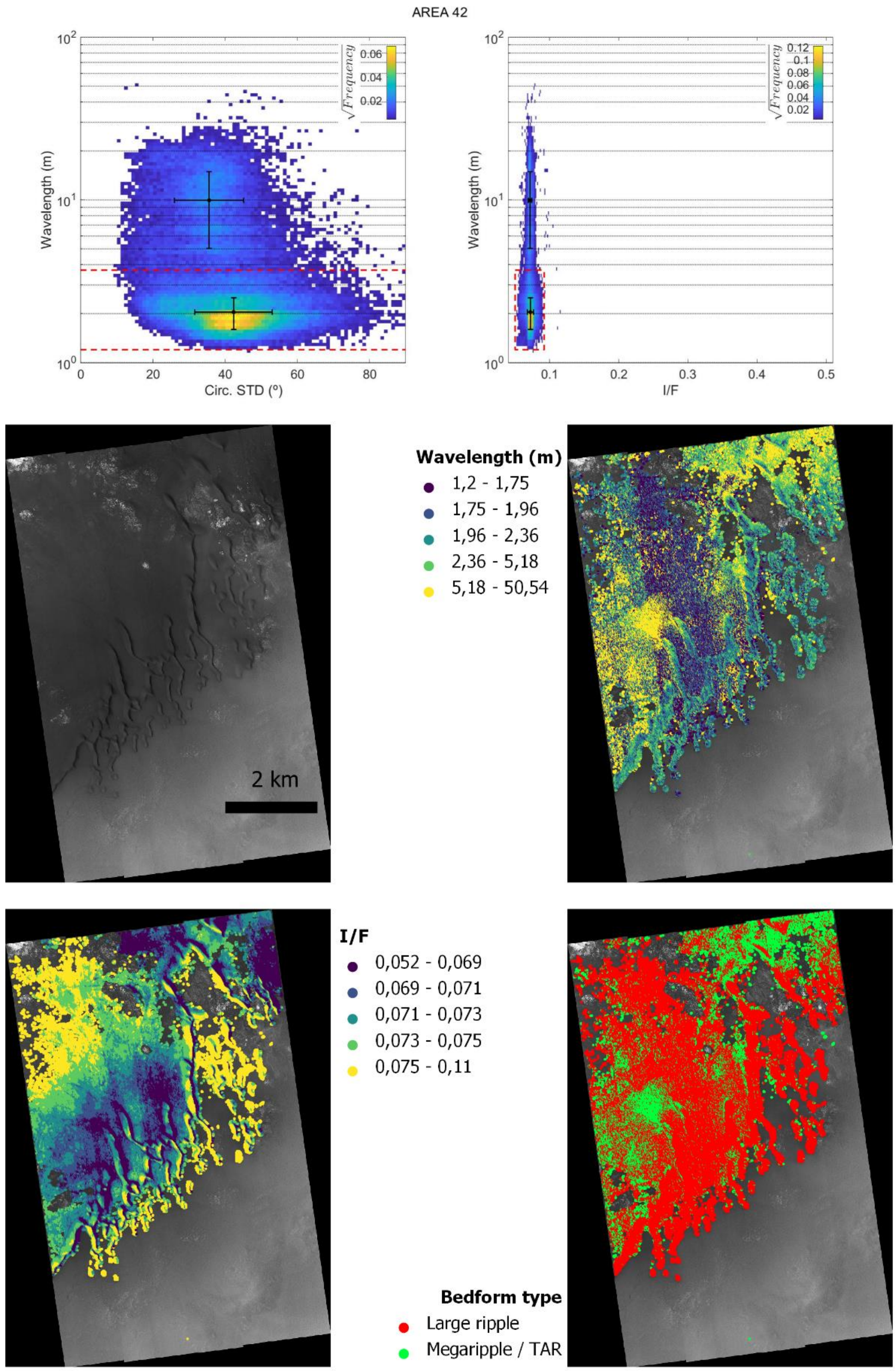

AREA 42
Wavelength (m)
Circ. STD (°)
I/F
√Frequency
2 km
Wavelength (m)
1,2 - 1,75
1,75 - 1,96
1,96 - 2,36
2,36 - 5,18
5,18 - 50,54
I/F
0,052 - 0,069
0,069 - 0,071
0,071 - 0,073
0,073 - 0,075
0,075 - 0,11
Bedform type
Large ripple
Megaripple / TAR

Area 43

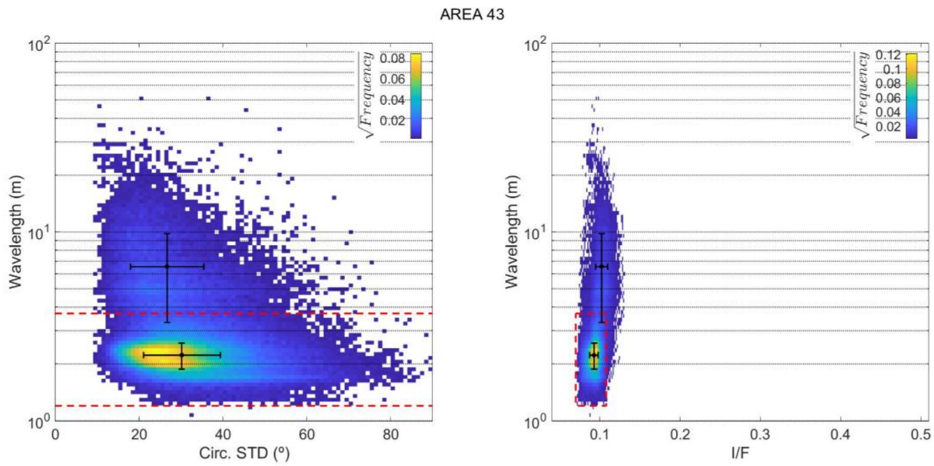

AREA 43
Wavelength (m)
Circ. STD (º)
Wavelength (m)
I/F

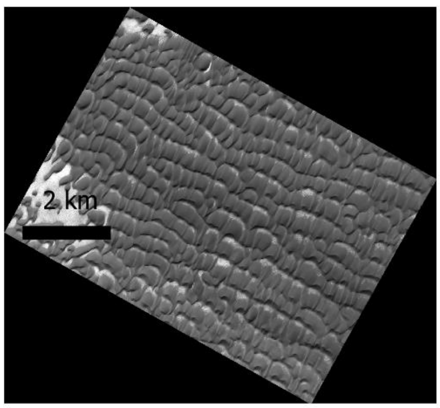

2 km

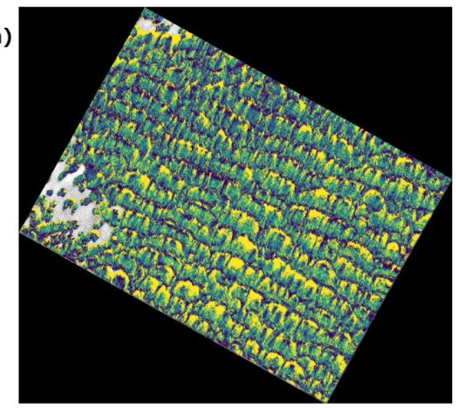

Wavelength (m)
1,21 - 1,97
1,97 - 2,15
2,15 - 2,33
2,33 - 2,6
2,6 - 51,78

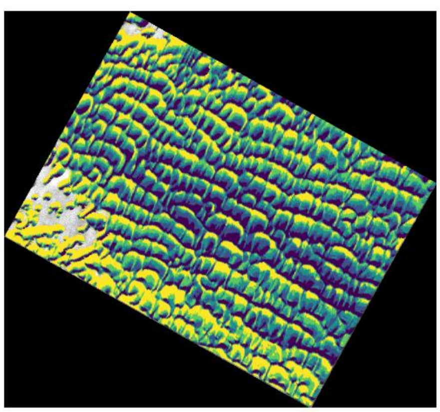

I/F
0,071 - 0,089
0,089 - 0,092
0,092 - 0,095
0,095 - 0,098
0,098 - 0,131

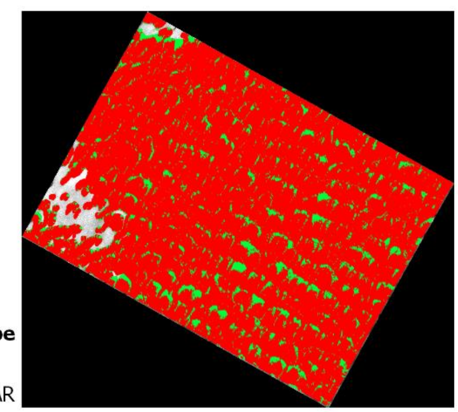

Bedform type
Large ripple
Megaripple / TAR

Area 44

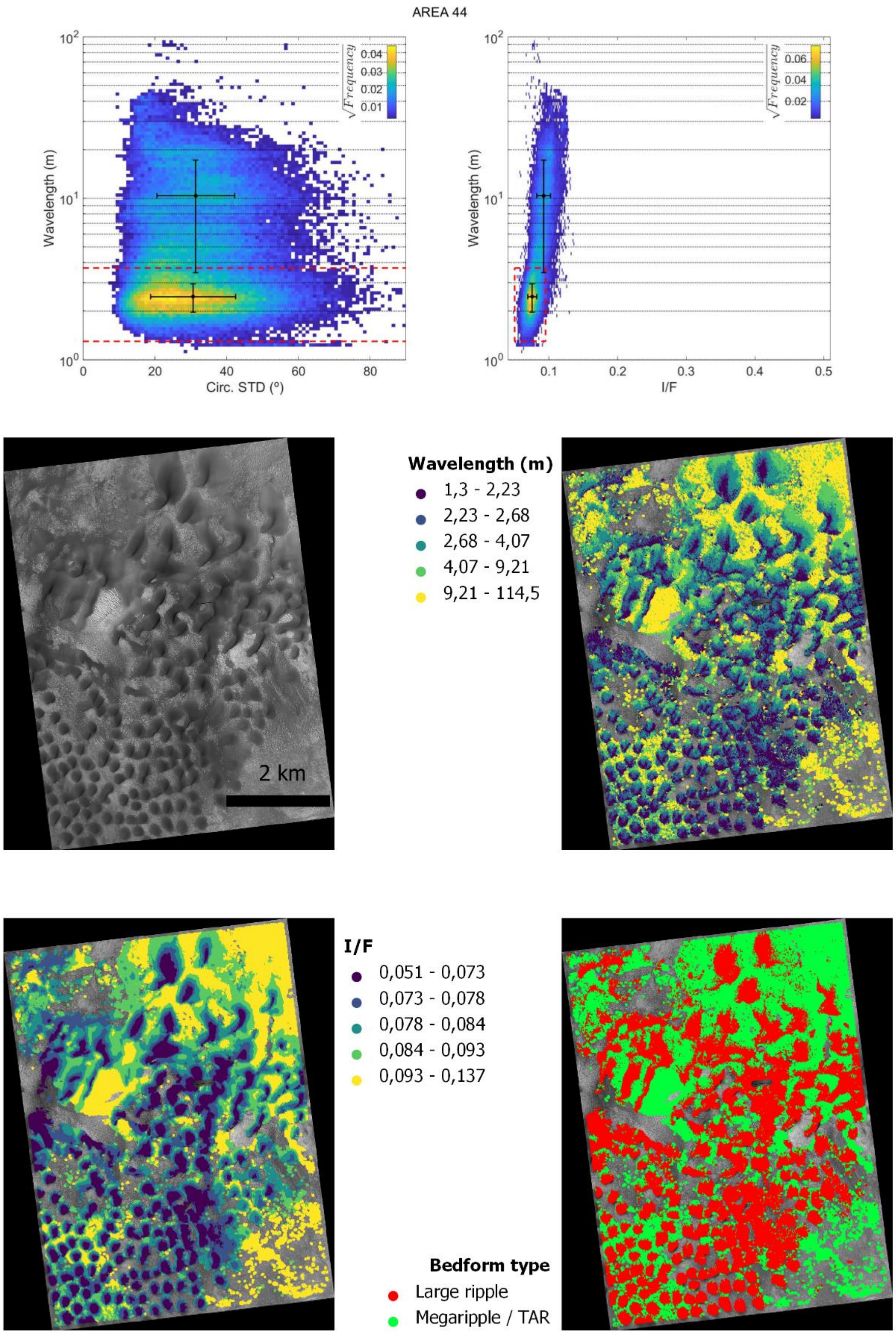

AREA 44
Wavelength (m)
Circ. STD (º)
I/F
$\sqrt{Frequency}$
2 km
Wavelength (m)
1,3 - 2,23
2,23 - 2,68
2,68 - 4,07
4,07 - 9,21
9,21 - 114,5
I/F
0,051 - 0,073
0,073 - 0,078
0,078 - 0,084
0,084 - 0,093
0,093 - 0,137
Bedform type
Large ripple
Megaripple / TAR

Area 45

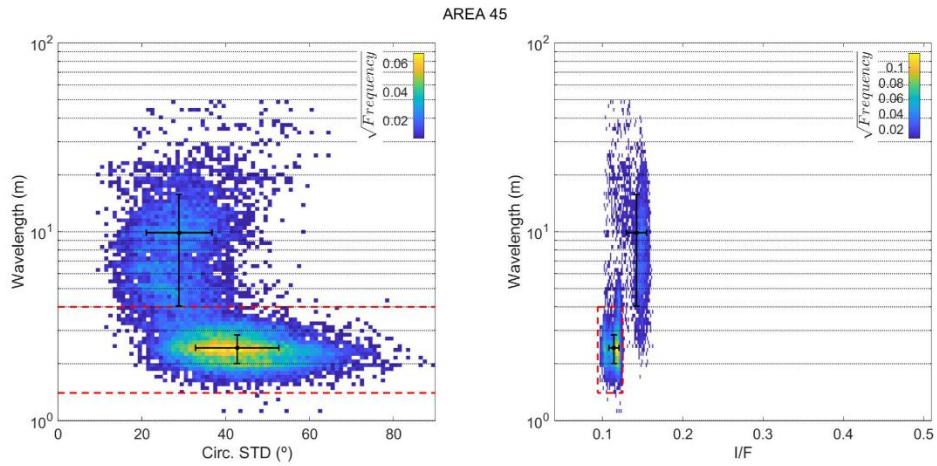

AREA 45
Wavelength (m)
Circ. STD (º)
I/F
$\sqrt{Frequency}$

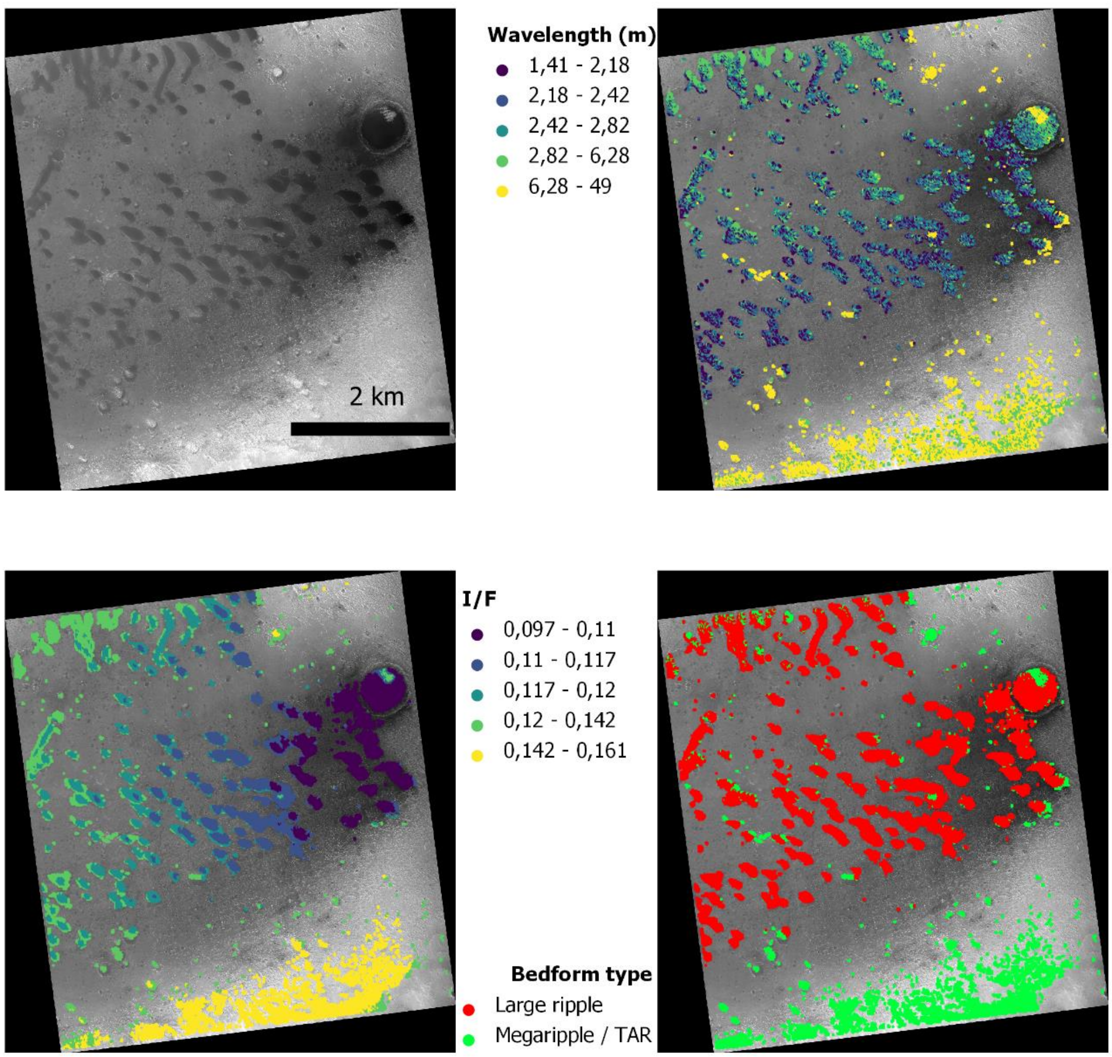

2 km
Wavelength (m)
1,41 - 2,18
2,18 - 2,42
2,42 - 2,82
2,82 - 6,28
6,28 - 49
I/F
0,097 - 0,11
0,11 - 0,117
0,117 - 0,12
0,12 - 0,142
0,142 - 0,161
Bedform type
Large ripple
Megaripple / TAR

Area 46

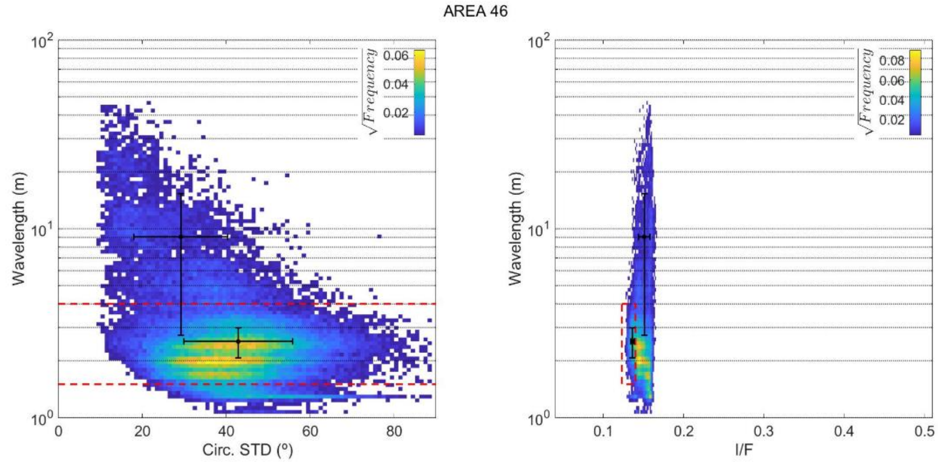
AREA 46
Wavelength (m)
Circ. STD (°)
$\sqrt{Frequency}$
0.06
0.04
0.02
Wavelength (m)
I/F
$\sqrt{Frequency}$
0.08
0.06
0.04
0.02

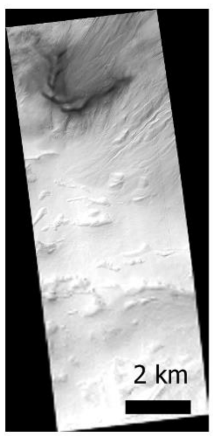
2 km

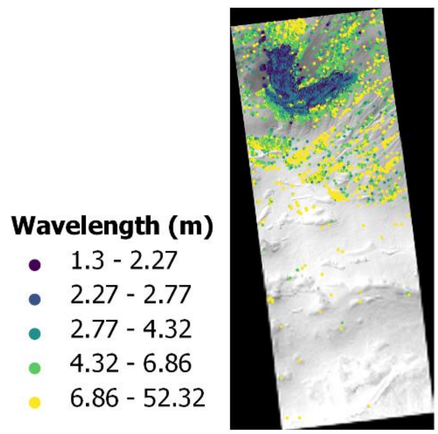
Wavelength (m)
1.3 - 2.27
2.27 - 2.77
2.77 - 4.32
4.32 - 6.86
6.86 - 52.32

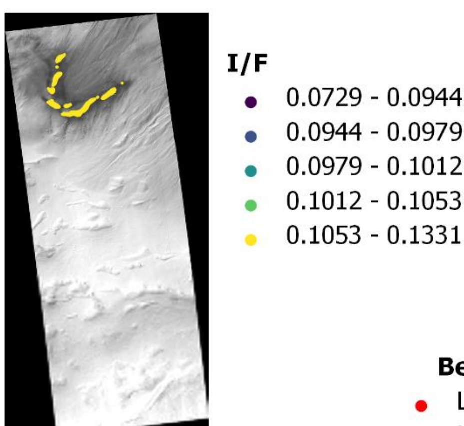
I/F
0.0729 - 0.0944
0.0944 - 0.0979
0.0979 - 0.1012
0.1012 - 0.1053
0.1053 - 0.1331

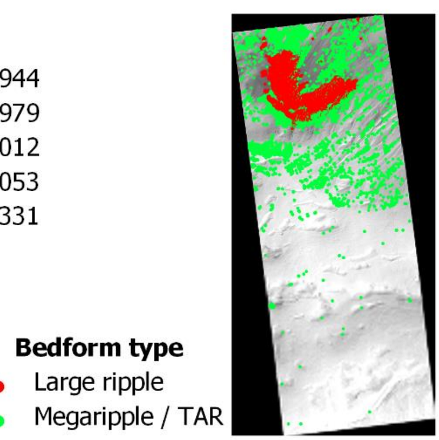
Bedform type
Large ripple
Megaripple / TAR

Area 47

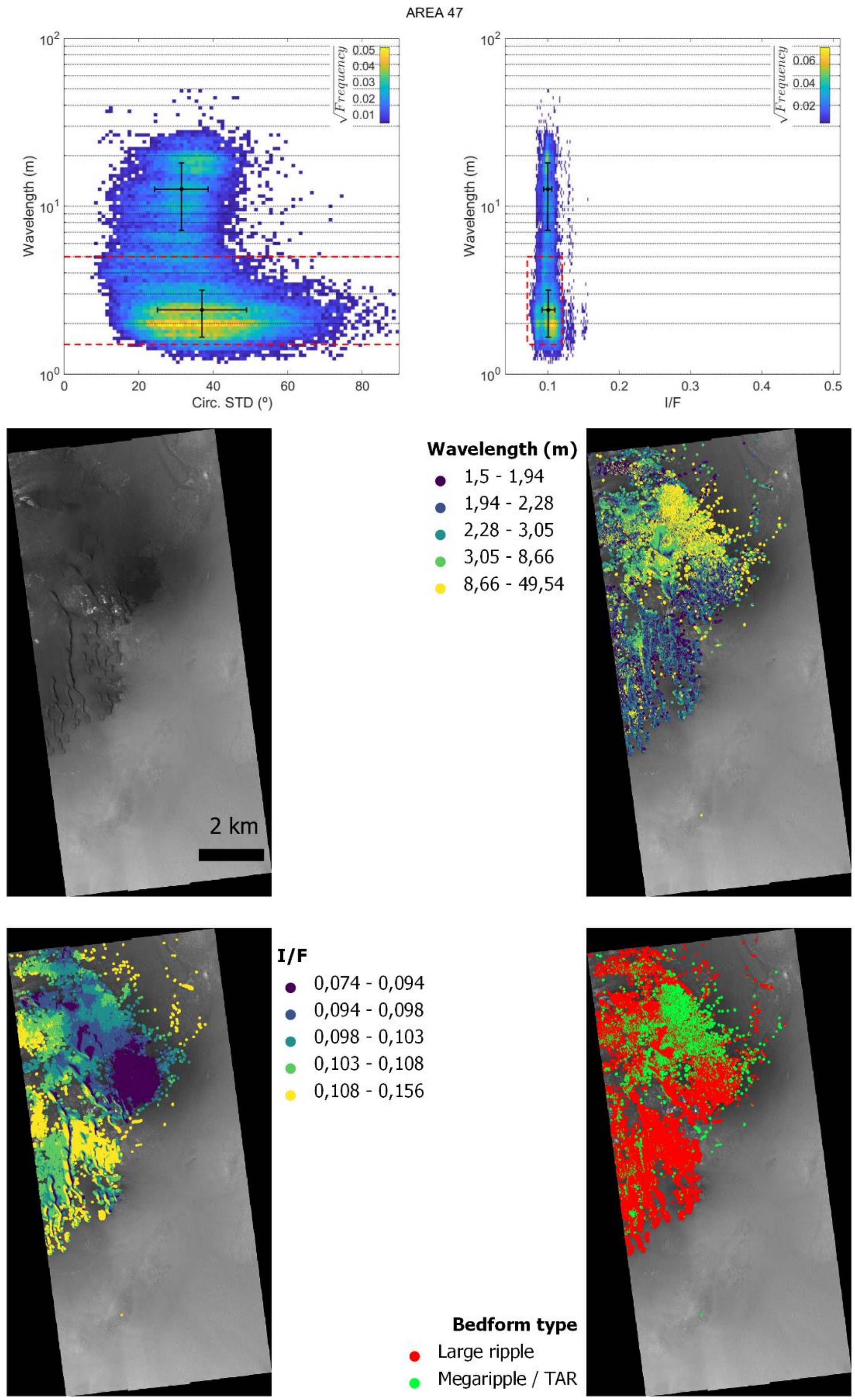
AREA 47
Wavelength (m)
Circ. STD (°)
I/F
√Frequency
2 km
Wavelength (m)
1,5 - 1,94
1,94 - 2,28
2,28 - 3,05
3,05 - 8,66
8,66 - 49,54
I/F
0,074 - 0,094
0,094 - 0,098
0,098 - 0,103
0,103 - 0,108
0,108 - 0,156
Bedform type
Large ripple
Megaripple / TAR

Area 48

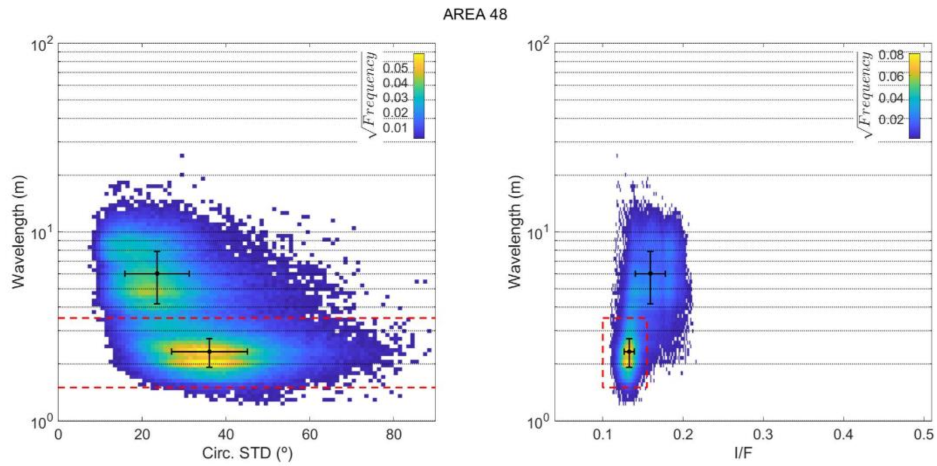

AREA 48
Wavelength (m)
Circ. STD (°)
I/F
√Frequency

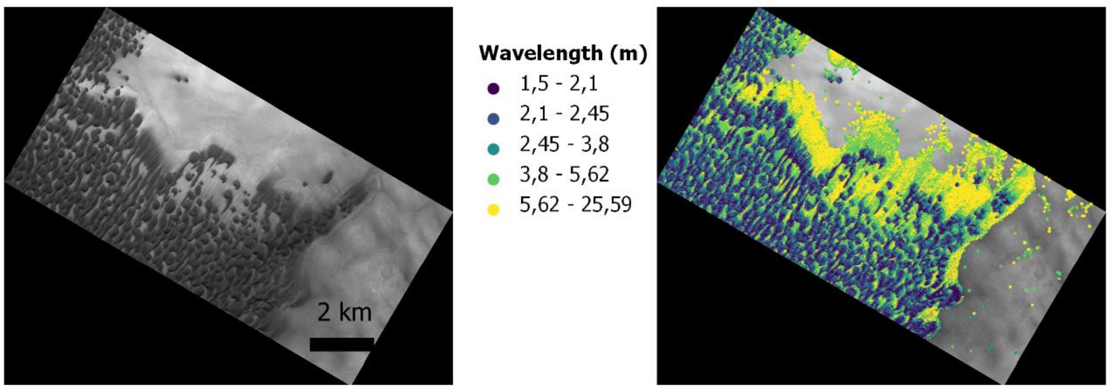

2 km
Wavelength (m)
1,5 - 2,1
2,1 - 2,45
2,45 - 3,8
3,8 - 5,62
5,62 - 25,59

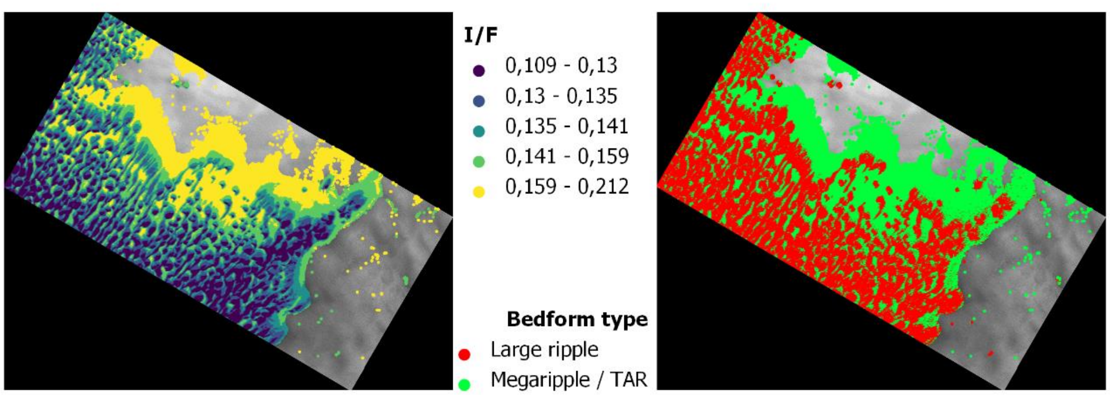

I/F
0,109 - 0,13
0,13 - 0,135
0,135 - 0,141
0,141 - 0,159
0,159 - 0,212
Bedform type
Large ripple
Megaripple / TAR

Area 49

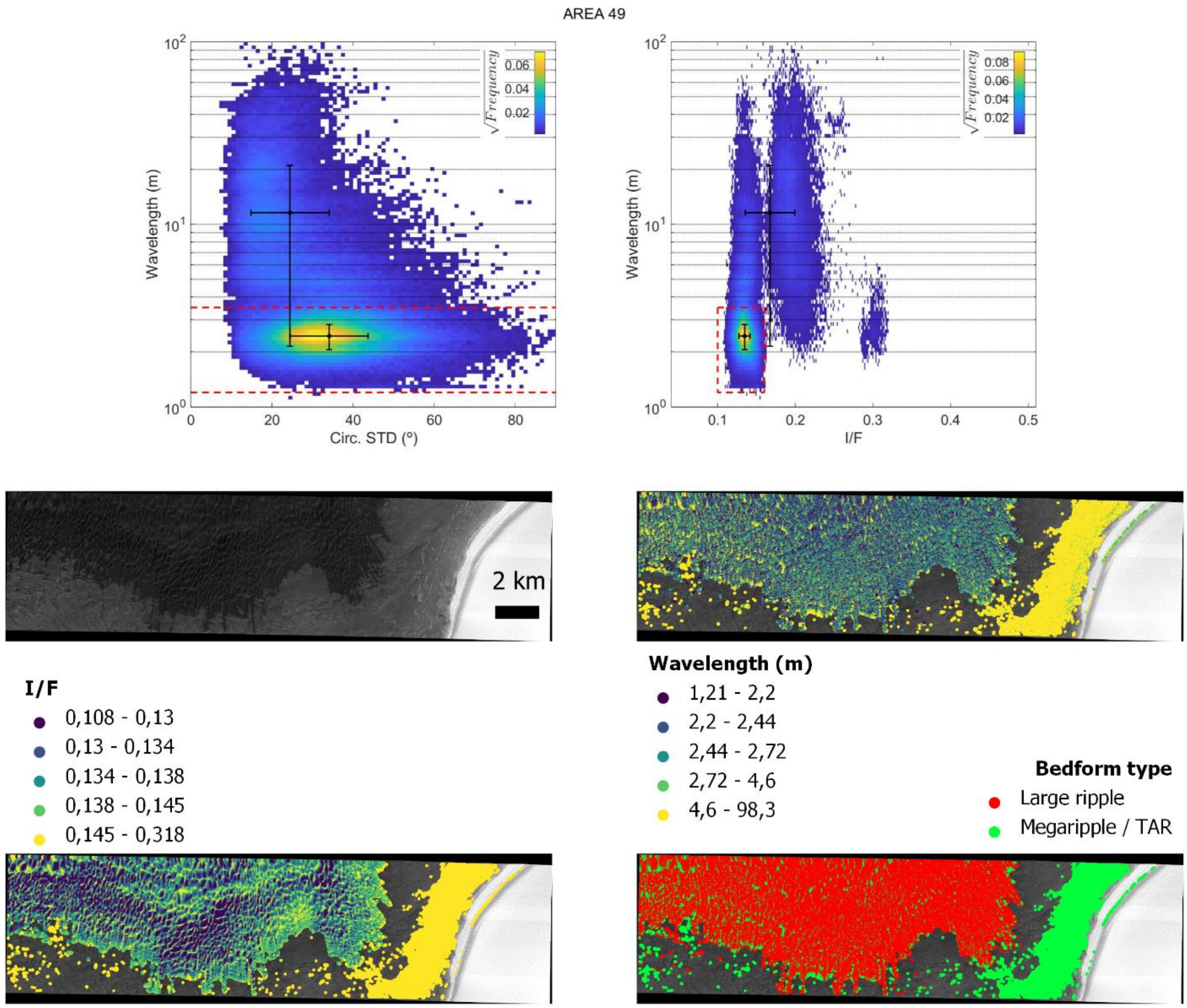
AREA 49
Wavelength (m)
Circ. STD (º)
I/F
√Frequency
2 km
I/F
0,108 - 0,13
0,13 - 0,134
0,134 - 0,138
0,138 - 0,145
0,145 - 0,318
Wavelength (m)
1,21 - 2,2
2,2 - 2,44
2,44 - 2,72
2,72 - 4,6
4,6 - 98,3
Bedform type
Large ripple
Megaripple / TAR

Area 50

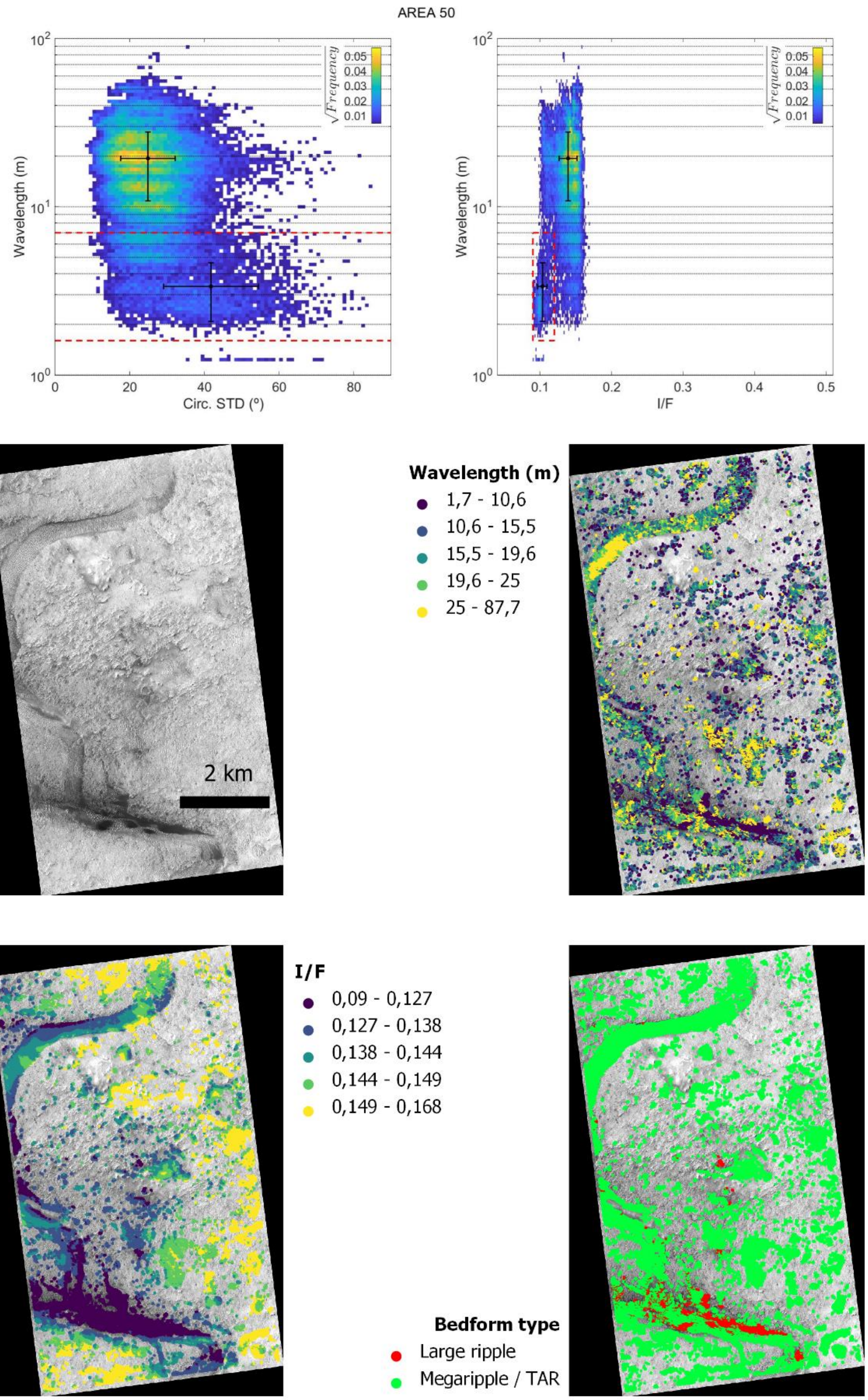
AREA 50
Wavelength (m)
Circ. STD (º)
I/F
√Frequency
2 km
Wavelength (m)
1,7 - 10,6
10,6 - 15,5
15,5 - 19,6
19,6 - 25
25 - 87,7
I/F
0,09 - 0,127
0,127 - 0,138
0,138 - 0,144
0,144 - 0,149
0,149 - 0,168
Bedform type
Large ripple
Megaripple / TAR

Area 51

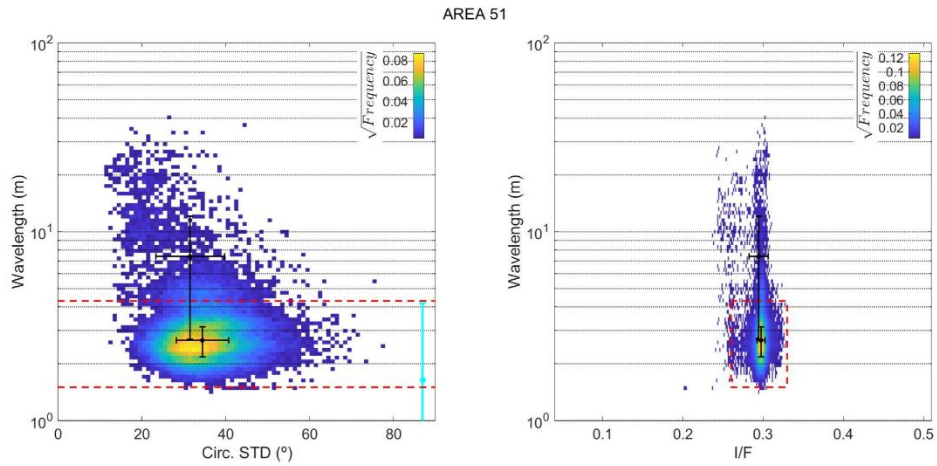
AREA 51
Wavelength (m)
Circ. STD (°)
I/F
√Frequency


2 km

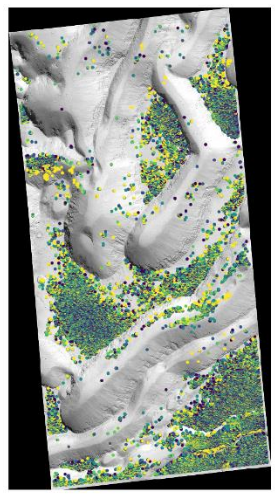
Wavelength (m)
1,54 - 2,28
2,28 - 2,49
2,49 - 2,75
2,75 - 3,17
3,17 - 39,95

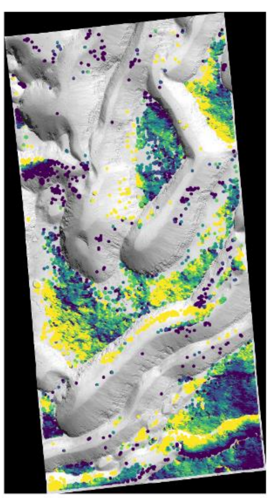
I/F
0,237 - 0,294
0,294 - 0,297
0,297 - 0,298
0,298 - 0,3
0,3 - 0,328

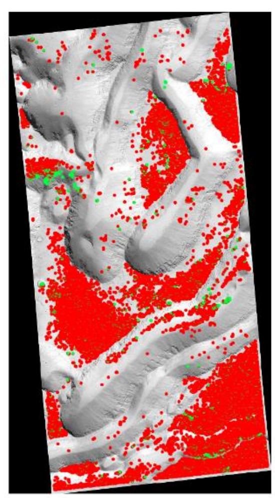
Bedform type
Large ripple
Megaripple / TAR

Area 52

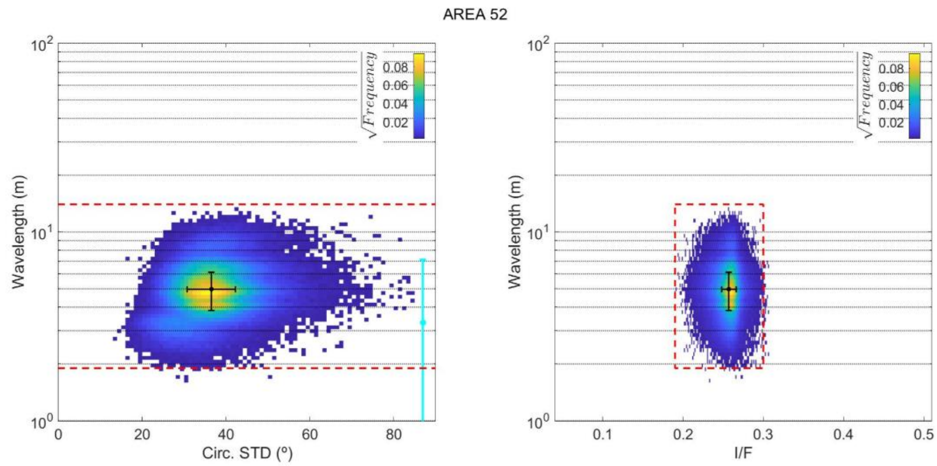
AREA 52
Wavelength (m)
Circ. STD (º)
I/F
√Frequency
0.08
0.06
0.04
0.02

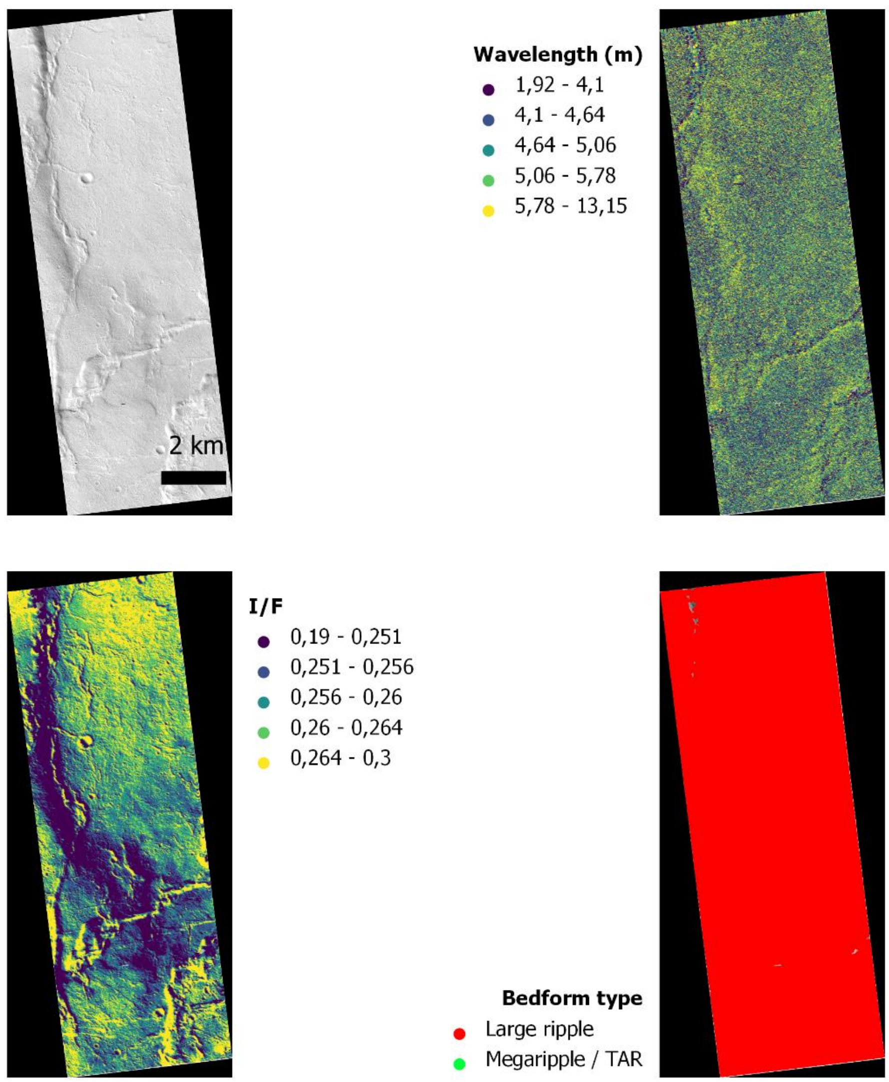
2 km
Wavelength (m)
1,92 - 4,1
4,1 - 4,64
4,64 - 5,06
5,06 - 5,78
5,78 - 13,15
I/F
0,19 - 0,251
0,251 - 0,256
0,256 - 0,26
0,26 - 0,264
0,264 - 0,3
Bedform type
Large ripple
Megaripple / TAR

Area 53

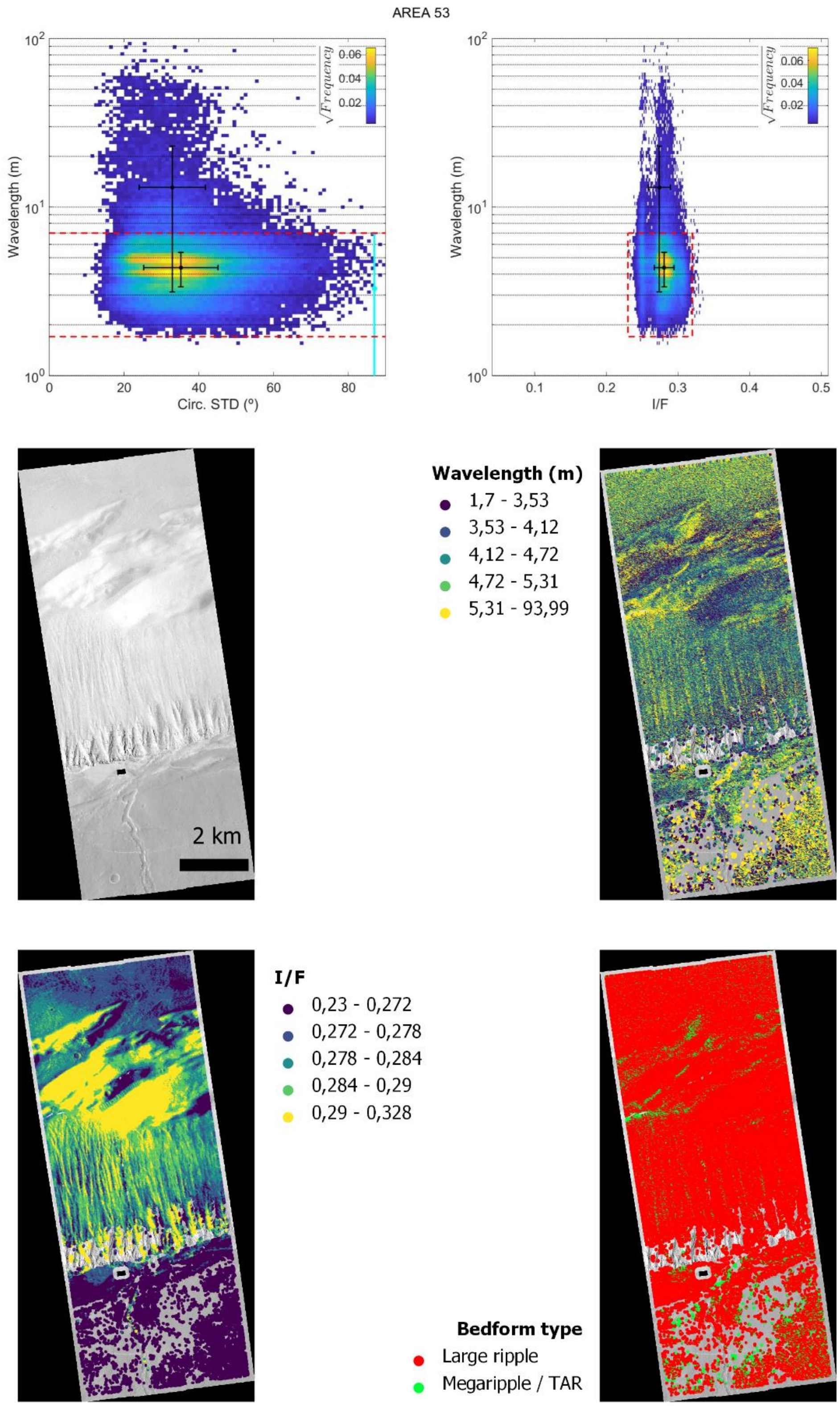
AREA 53
Wavelength (m)
Circ. STD (°)
I/F
√Frequency
Wavelength (m)
1,7 - 3,53
3,53 - 4,12
4,12 - 4,72
4,72 - 5,31
5,31 - 93,99
2 km
I/F
0,23 - 0,272
0,272 - 0,278
0,278 - 0,284
0,284 - 0,29
0,29 - 0,328
Bedform type
Large ripple
Megaripple / TAR

Area 54

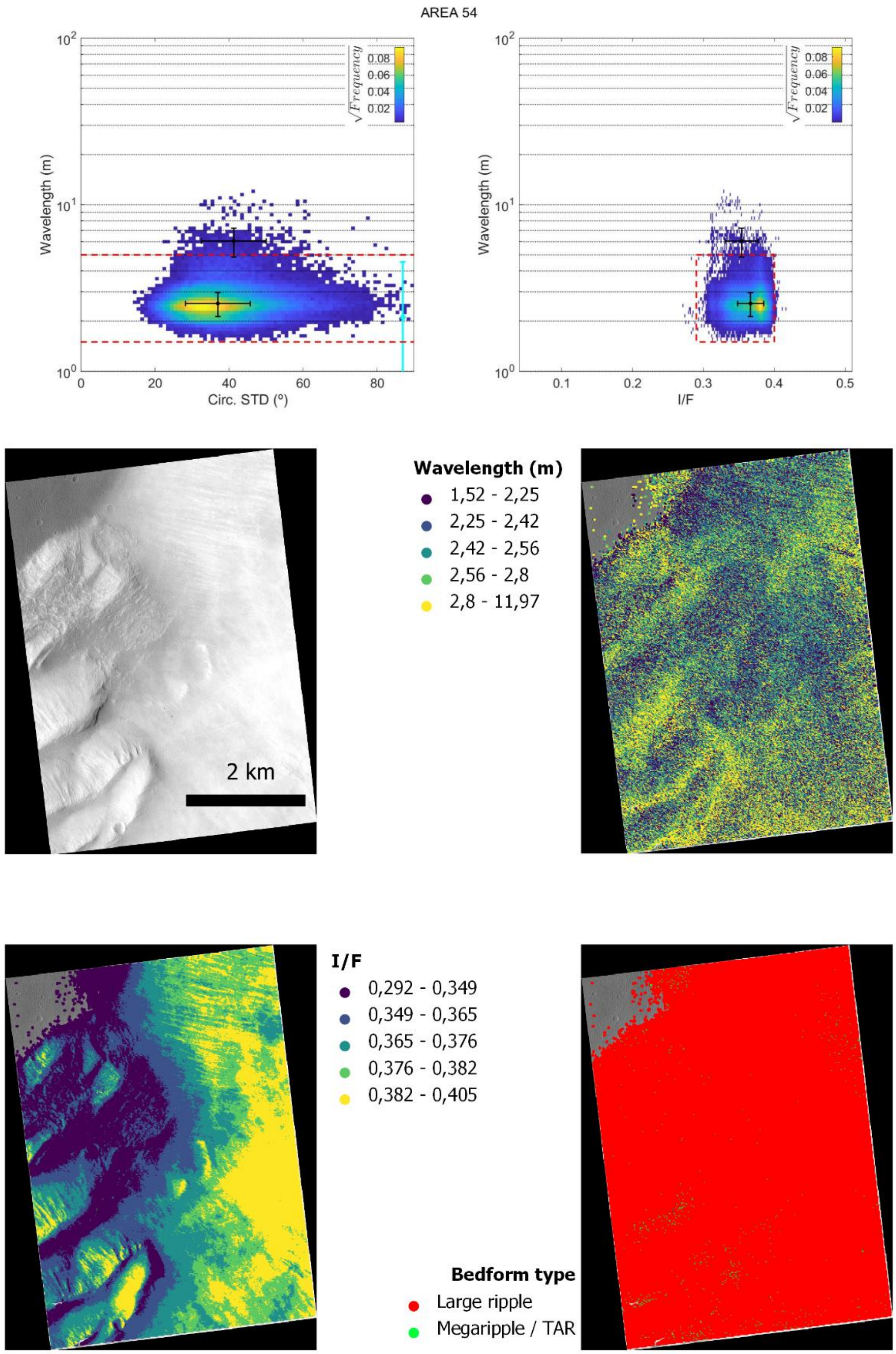

AREA 54
Wavelength (m)
Circ. STD (º)
I/F
√Frequency
0.08
0.06
0.04
0.02
Wavelength (m)
1,52 - 2,25
2,25 - 2,42
2,42 - 2,56
2,56 - 2,8
2,8 - 11,97
2 km
I/F
0,292 - 0,349
0,349 - 0,365
0,365 - 0,376
0,376 - 0,382
0,382 - 0,405
Bedform type
Large ripple
Megaripple / TAR

Area 55

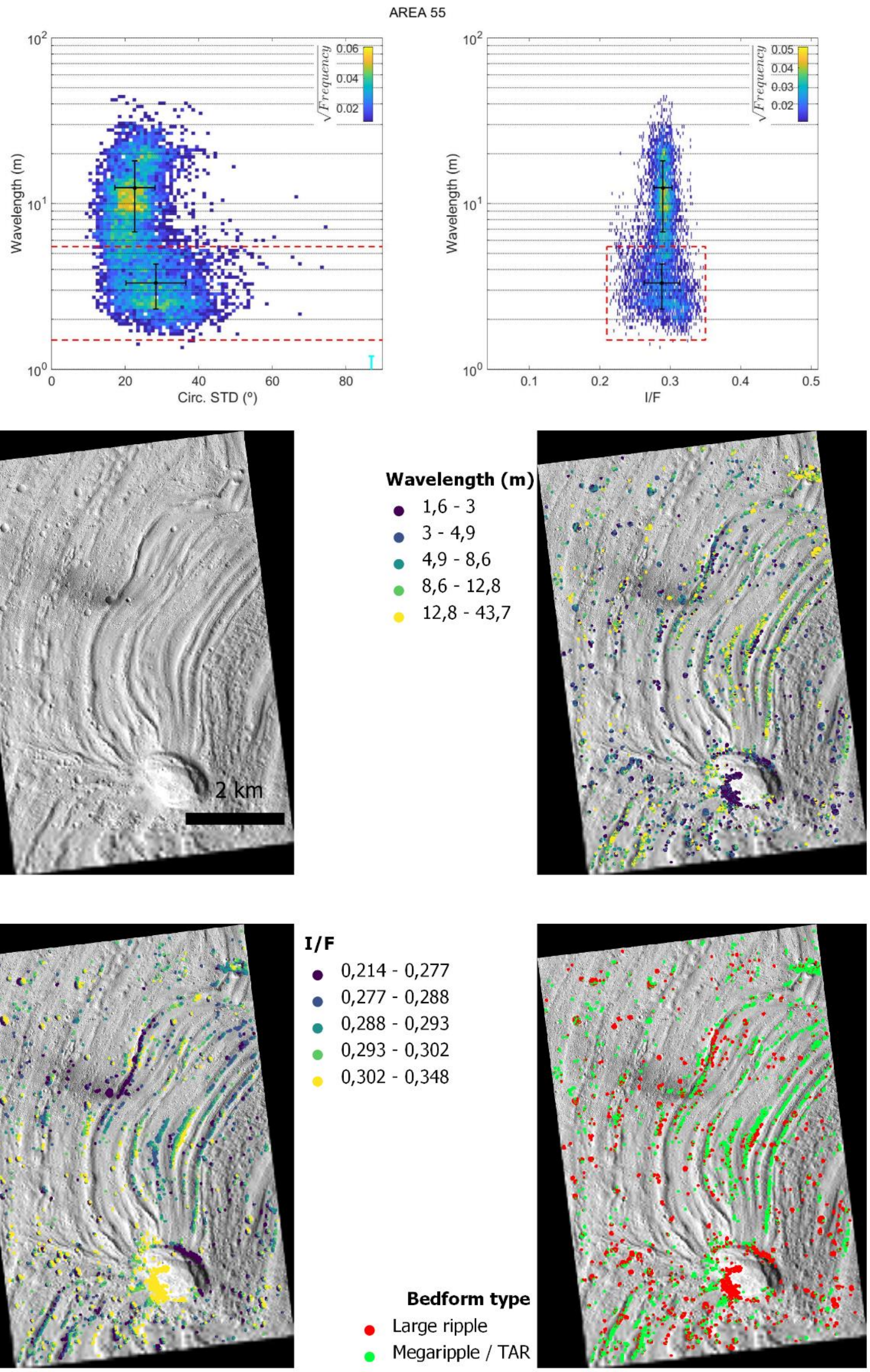

AREA 55
Wavelength (m)
Circ. STD (º)
I/F
√Frequency
2 km
Wavelength (m)
1,6 - 3
3 - 4,9
4,9 - 8,6
8,6 - 12,8
12,8 - 43,7
I/F
0,214 - 0,277
0,277 - 0,288
0,288 - 0,293
0,293 - 0,302
0,302 - 0,348
Bedform type
Large ripple
Megaripple / TAR

Area 56

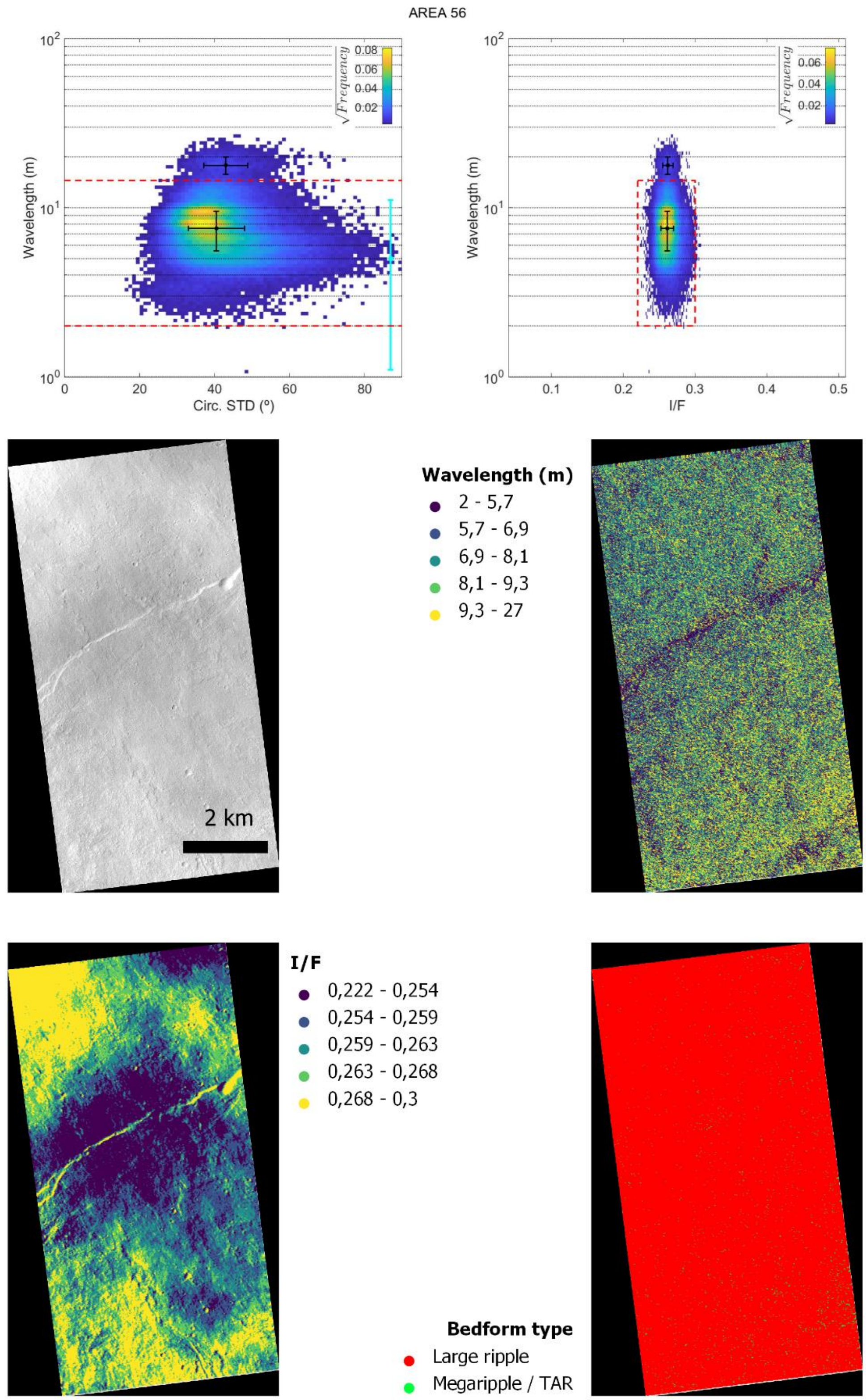
AREA 56
Wavelength (m)
Circ. STD (°)
√Frequency
0.08
0.06
0.04
0.02
I/F
10^2
10^1
10^0
0
20
40
60
80
0.1
0.2
0.3
0.4
0.5
2 km
Wavelength (m)
2 - 5,7
5,7 - 6,9
6,9 - 8,1
8,1 - 9,3
9,3 - 27
I/F
0,222 - 0,254
0,254 - 0,259
0,259 - 0,263
0,263 - 0,268
0,268 - 0,3
Bedform type
Large ripple
Megaripple / TAR

Area 57

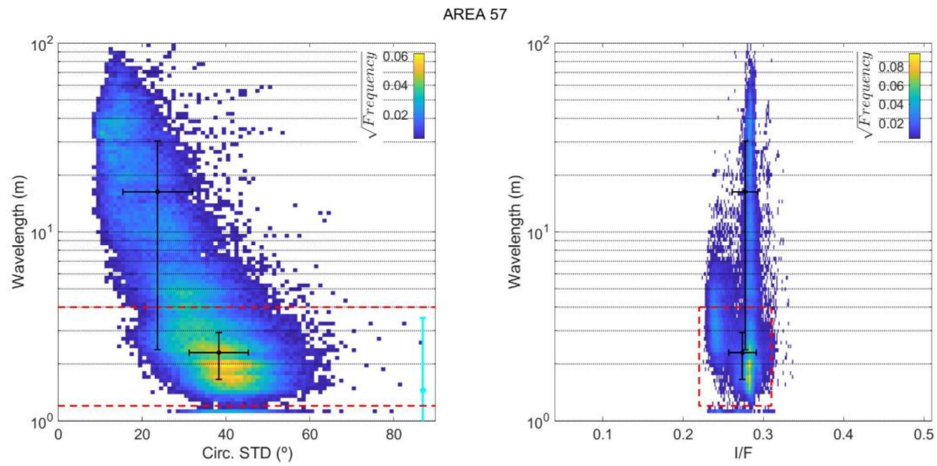
AREA 57
Wavelength (m)
Circ. STD (°)
√Frequency
Wavelength (m)
I/F
√Frequency

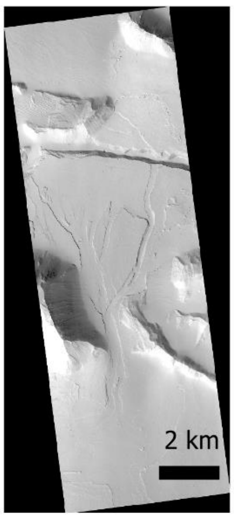
2 km

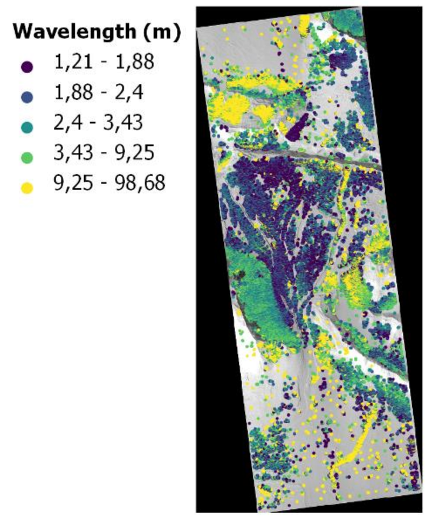
Wavelength (m)
1,21 - 1,88
1,88 - 2,4
2,4 - 3,43
3,43 - 9,25
9,25 - 98,68

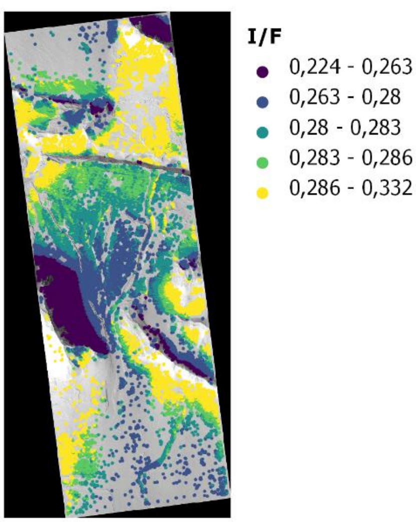
I/F
0,224 - 0,263
0,263 - 0,28
0,28 - 0,283
0,283 - 0,286
0,286 - 0,332

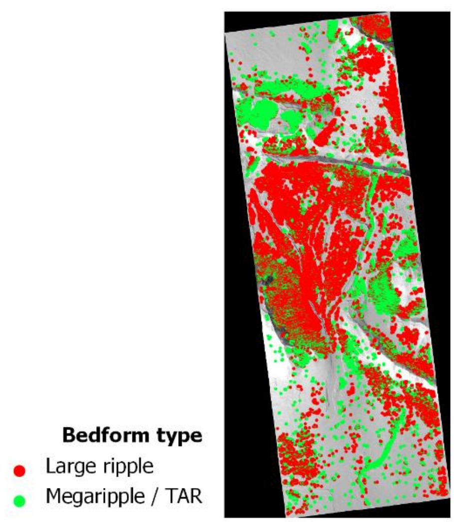
Bedform type
Large ripple
Megaripple / TAR

Area 58

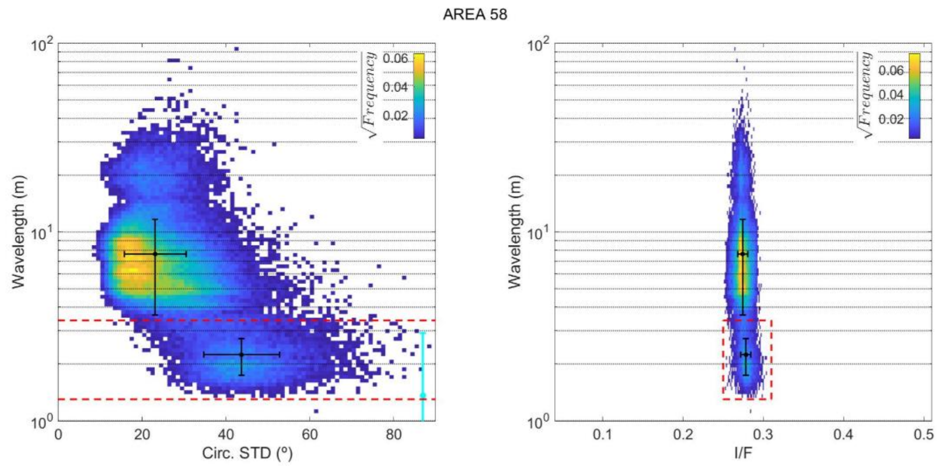

AREA 58
Wavelength (m)
Circ. STD (°)
I/F
√Frequency
0.06
0.04
0.02

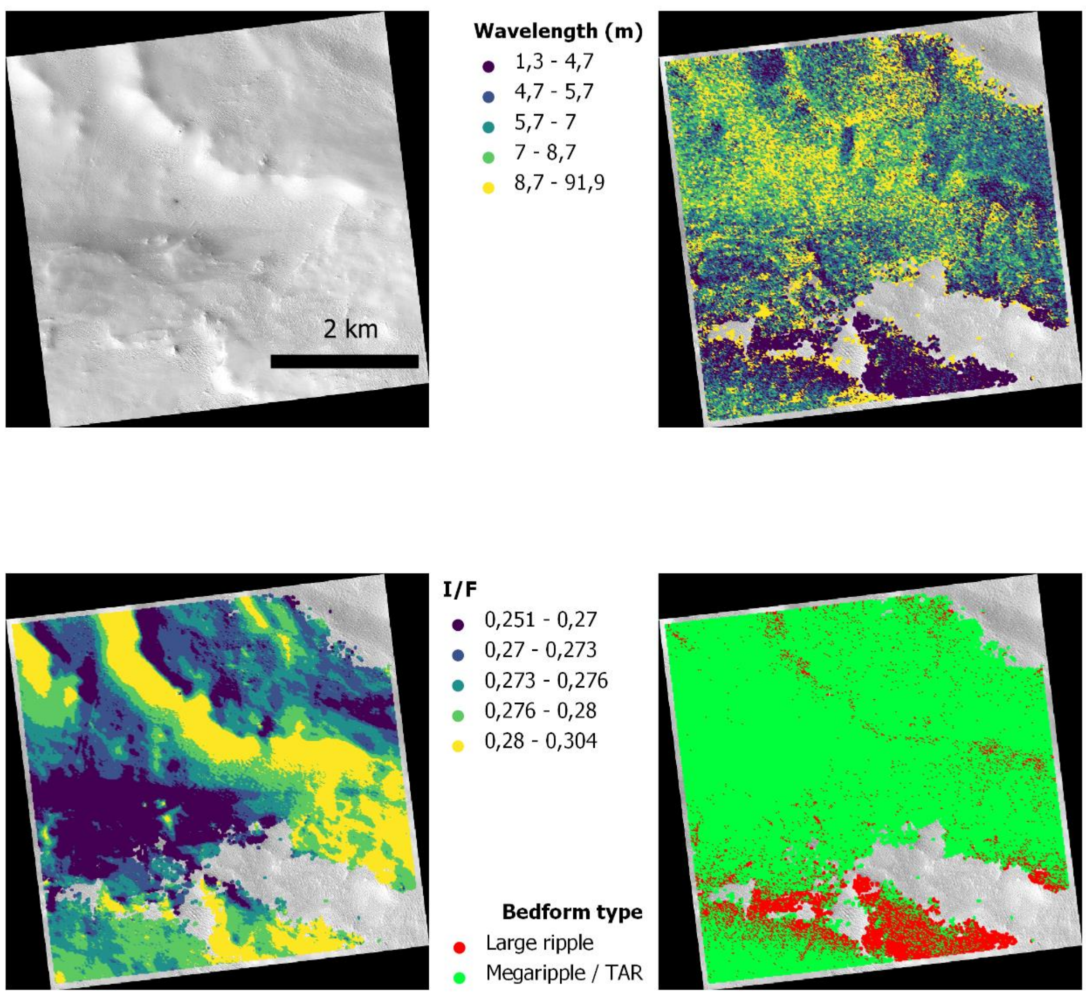

2 km
Wavelength (m)
1,3 - 4,7
4,7 - 5,7
5,7 - 7
7 - 8,7
8,7 - 91,9
I/F
0,251 - 0,27
0,27 - 0,273
0,273 - 0,276
0,276 - 0,28
0,28 - 0,304
Bedform type
Large ripple
Megaripple / TAR

Area 59

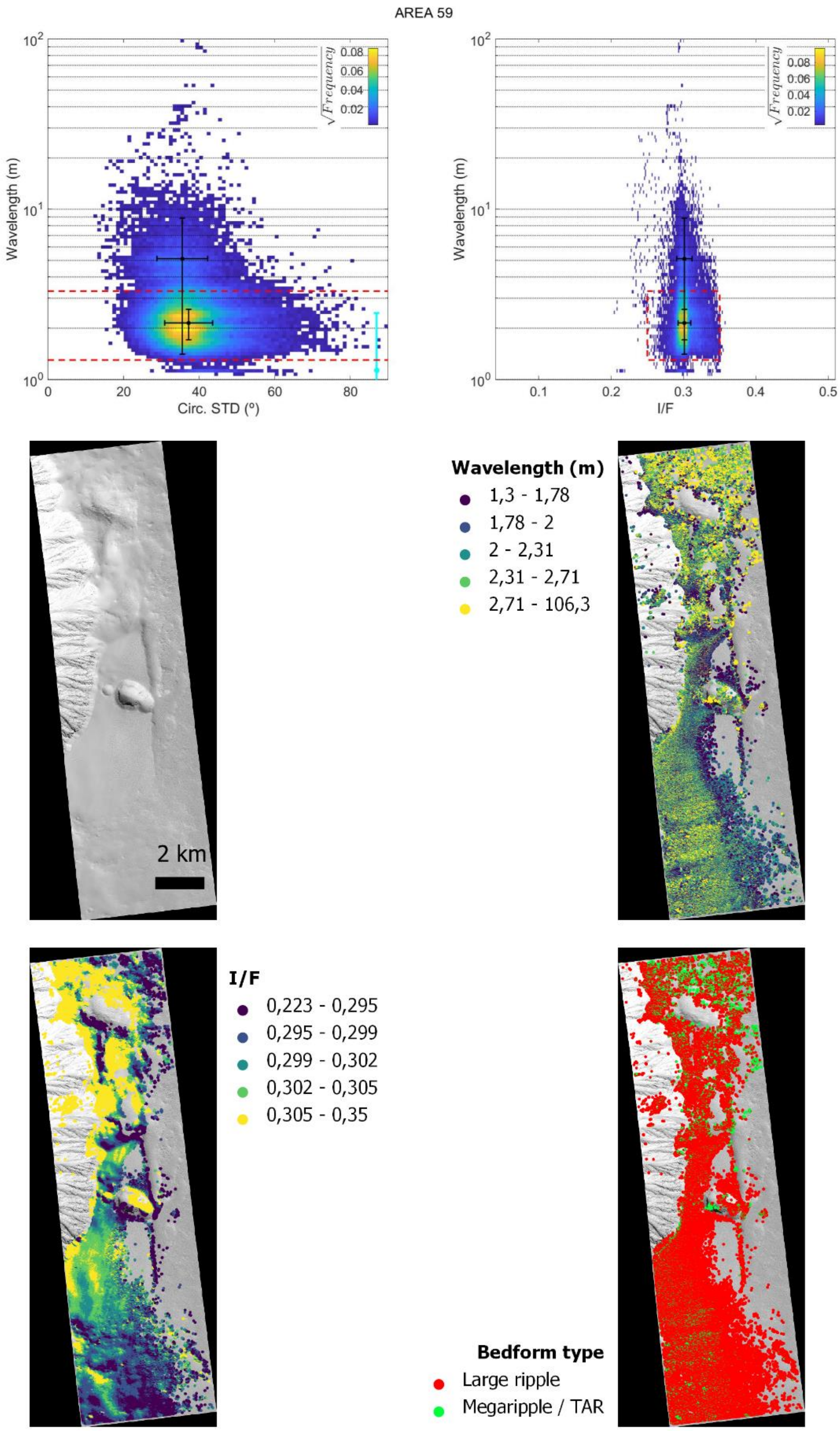

AREA 59
Wavelength (m)
Circ. STD (°)
I/F
√Frequency
2 km
Wavelength (m)
1,3 - 1,78
1,78 - 2
2 - 2,31
2,31 - 2,71
2,71 - 106,3
I/F
0,223 - 0,295
0,295 - 0,299
0,299 - 0,302
0,302 - 0,305
0,305 - 0,35
Bedform type
Large ripple
Megaripple / TAR

Area 60

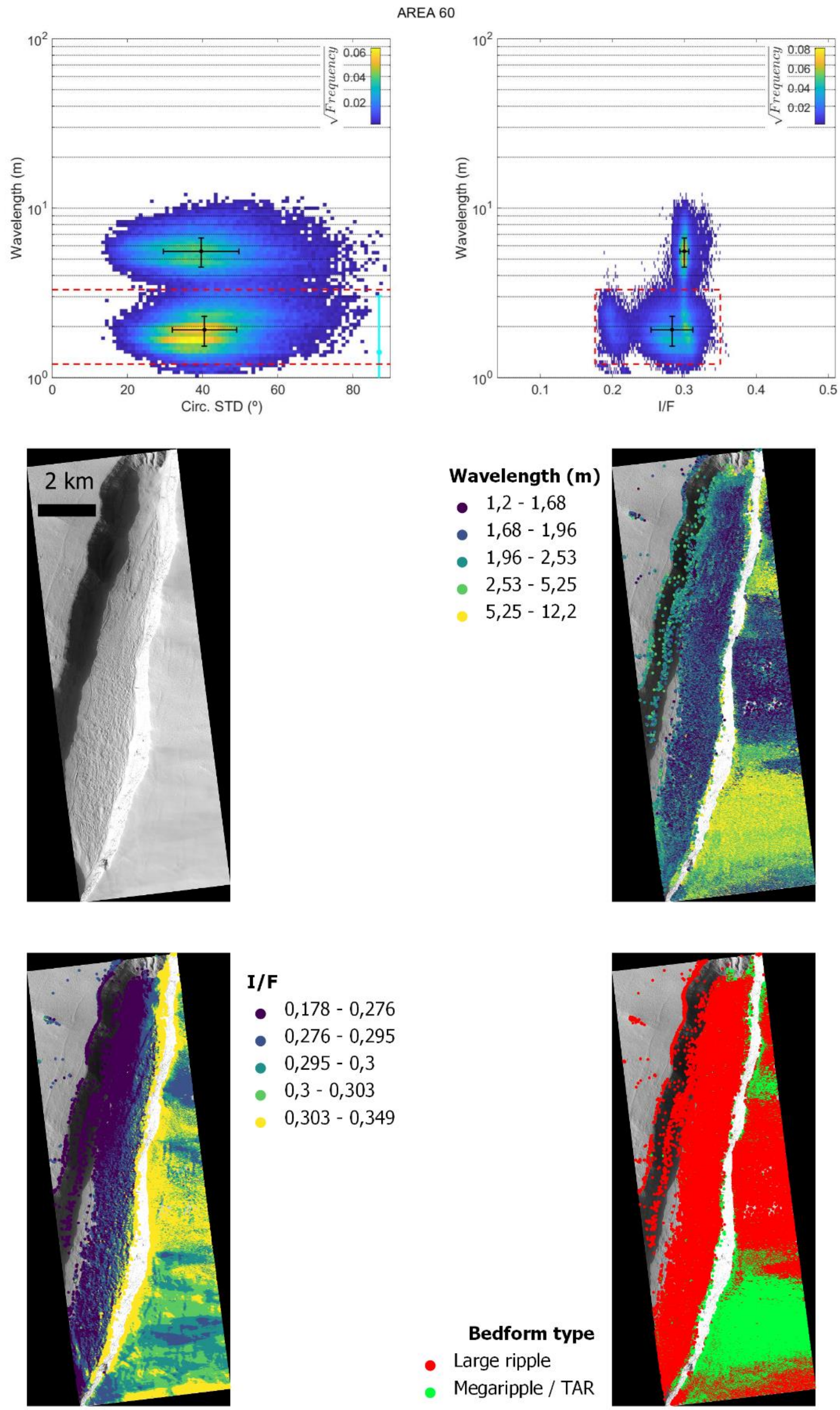

AREA 60
Wavelength (m)
Circ. STD (°)
I/F
√Frequency
2 km
Wavelength (m)
1,2 - 1,68
1,68 - 1,96
1,96 - 2,53
2,53 - 5,25
5,25 - 12,2
I/F
0,178 - 0,276
0,276 - 0,295
0,295 - 0,3
0,3 - 0,303
0,303 - 0,349
Bedform type
Large ripple
Megaripple / TAR

Area 61

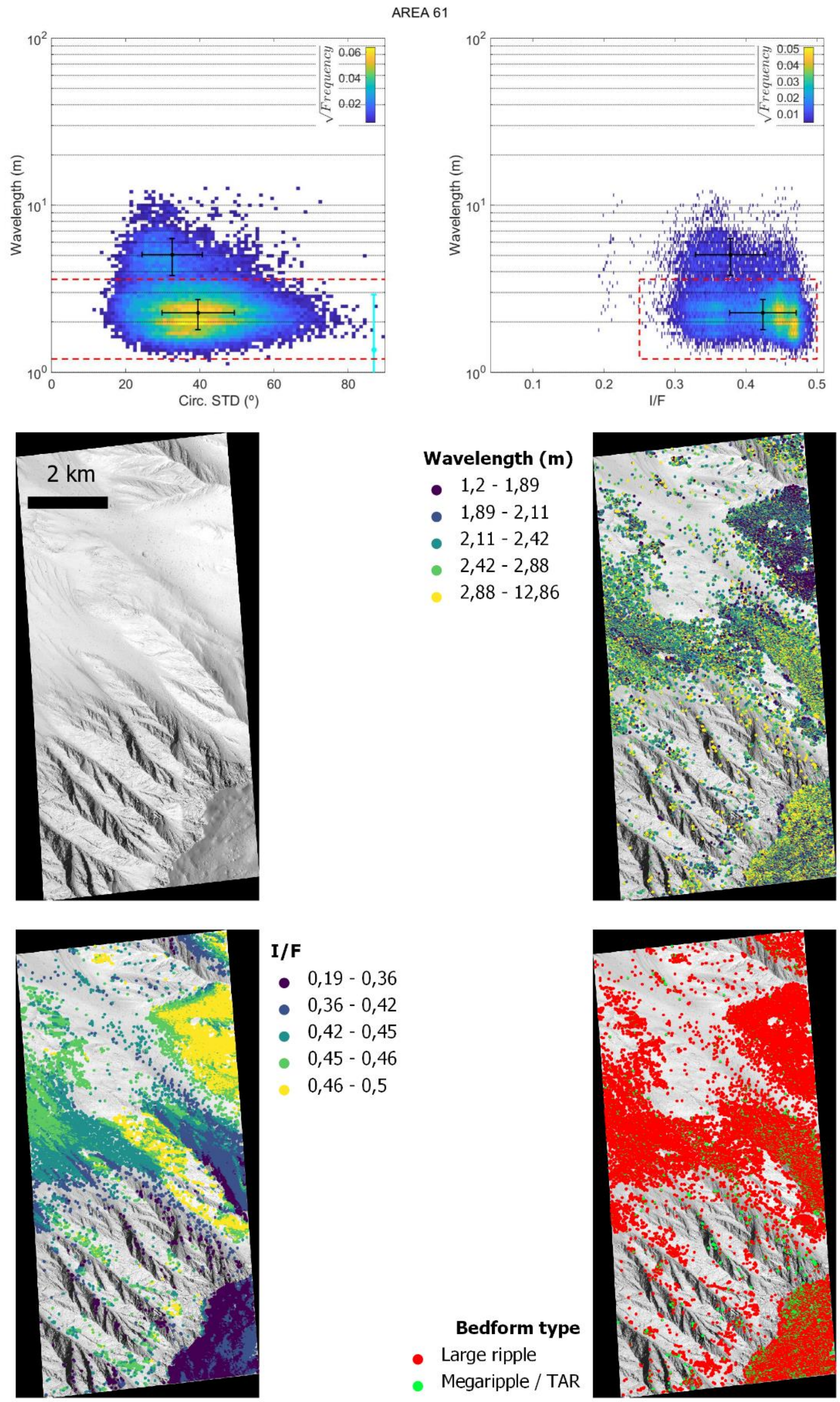
AREA 61
Wavelength (m)
Circ. STD (°)
I/F
√Frequency
Wavelength (m)
1,2 - 1,89
1,89 - 2,11
2,11 - 2,42
2,42 - 2,88
2,88 - 12,86
2 km
I/F
0,19 - 0,36
0,36 - 0,42
0,42 - 0,45
0,45 - 0,46
0,46 - 0,5
Bedform type
Large ripple
Megaripple / TAR

Area 62

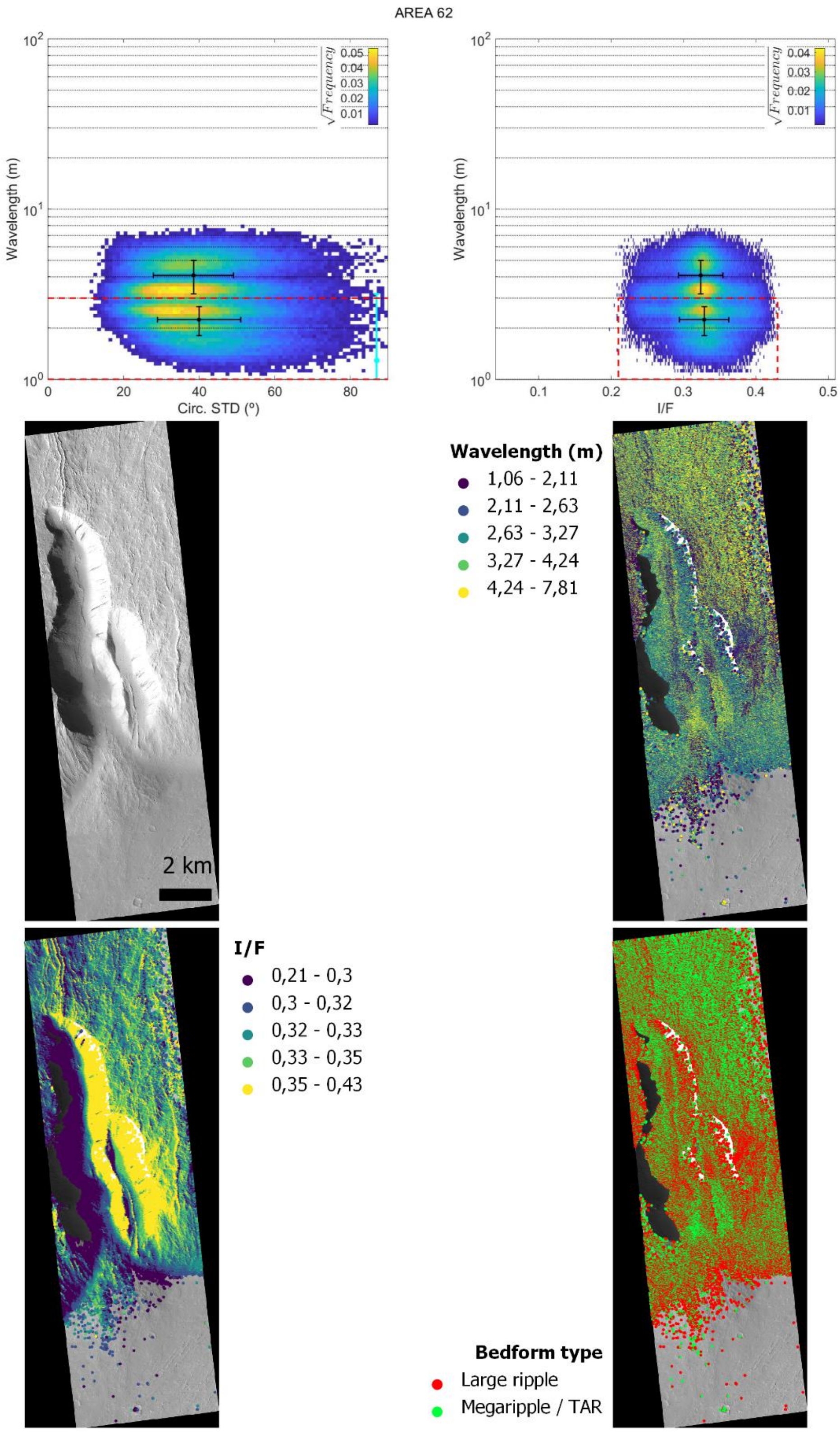
AREA 62
Wavelength (m)
Circ. STD (º)
I/F
√Frequency
Wavelength (m)
1,06 - 2,11
2,11 - 2,63
2,63 - 3,27
3,27 - 4,24
4,24 - 7,81
2 km
I/F
0,21 - 0,3
0,3 - 0,32
0,32 - 0,33
0,33 - 0,35
0,35 - 0,43
Bedform type
Large ripple
Megaripple / TAR

Area 63

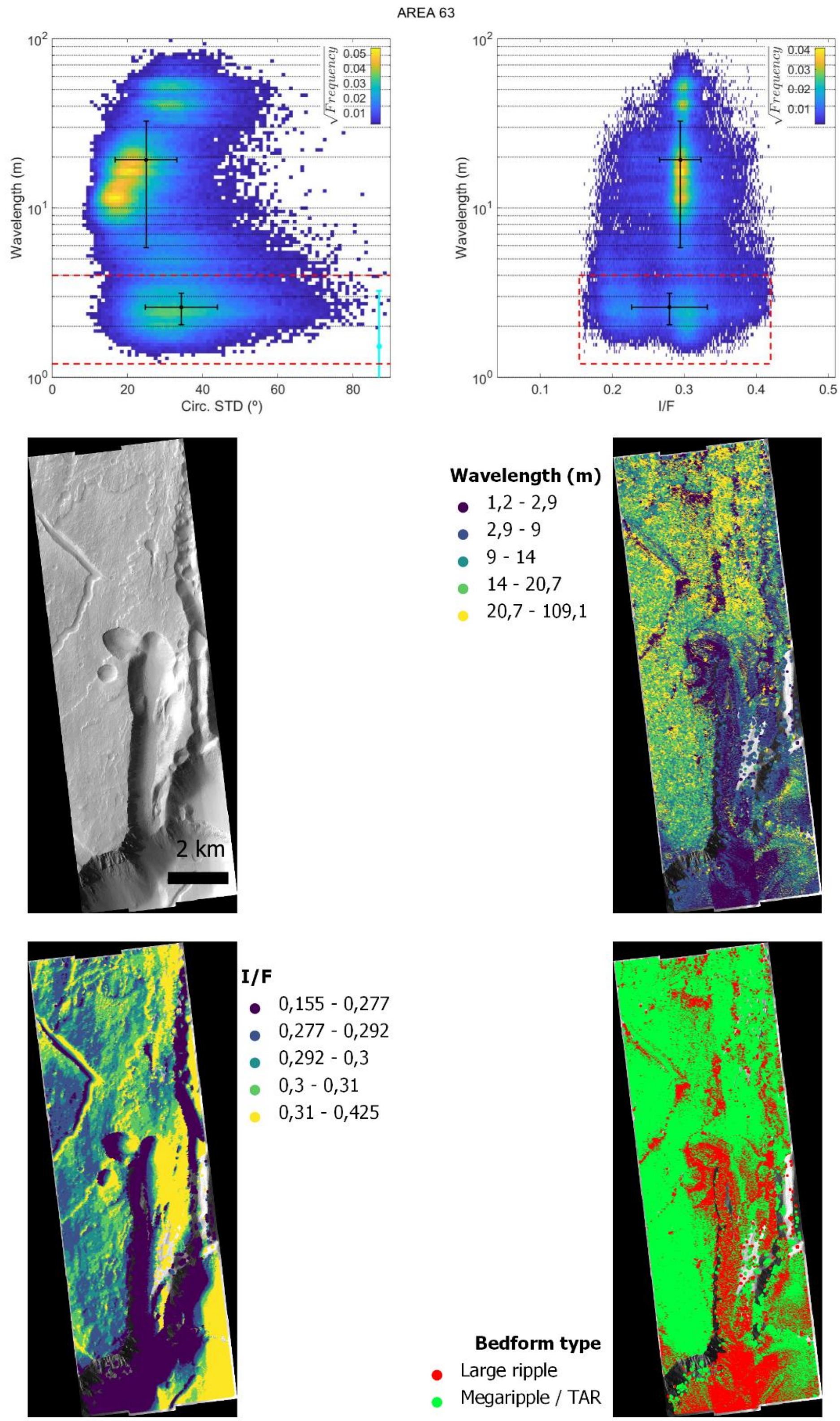
AREA 63
Wavelength (m)
Circ. STD (°)
I/F
√Frequency
2 km
Wavelength (m)
1,2 - 2,9
2,9 - 9
9 - 14
14 - 20,7
20,7 - 109,1
I/F
0,155 - 0,277
0,277 - 0,292
0,292 - 0,3
0,3 - 0,31
0,31 - 0,425
Bedform type
Large ripple
Megaripple / TAR

Area 64

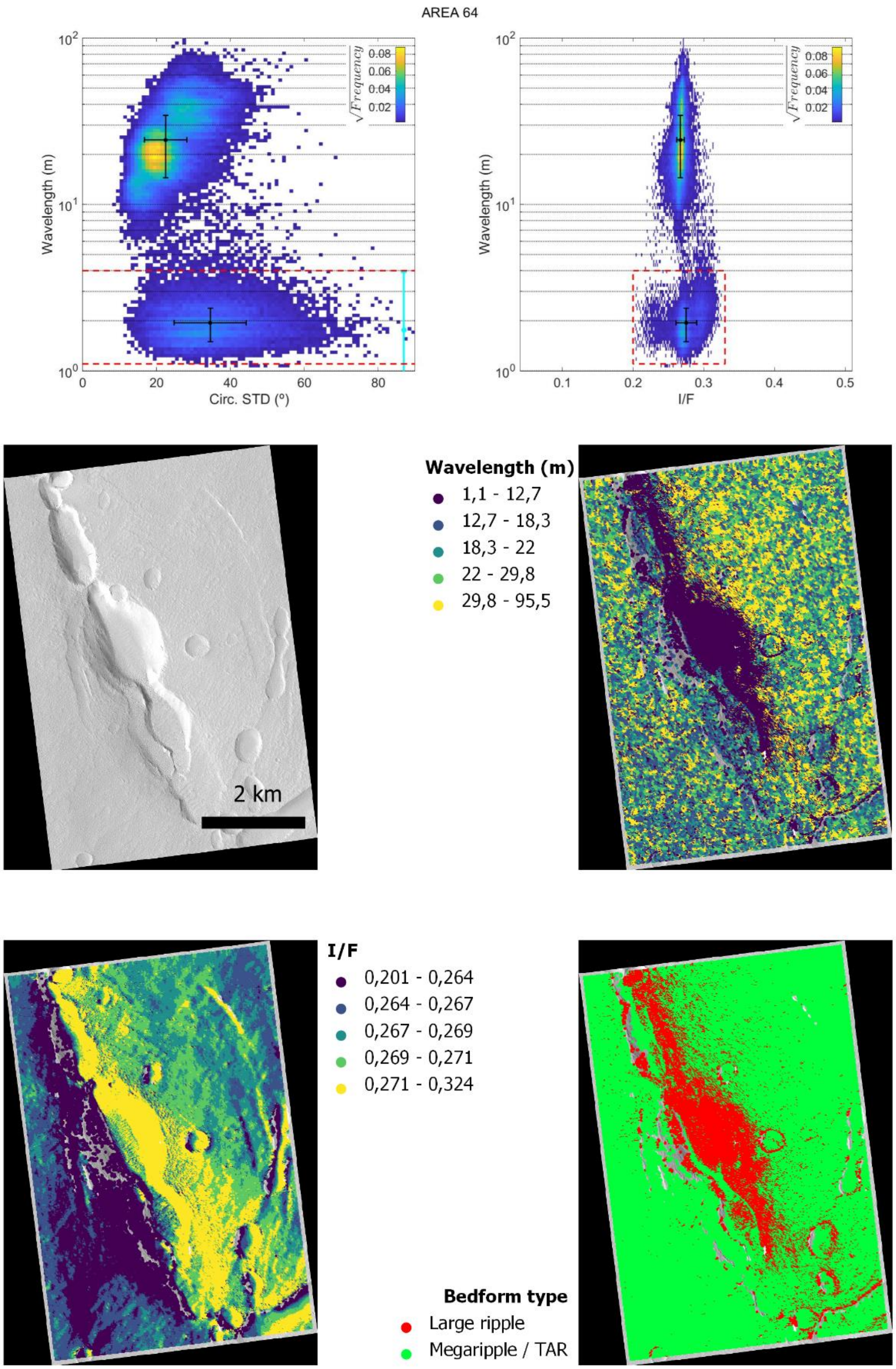
AREA 64
Wavelength (m)
Circ. STD (°)
I/F
√Frequency
2 km
Wavelength (m)
1,1 - 12,7
12,7 - 18,3
18,3 - 22
22 - 29,8
29,8 - 95,5
I/F
0,201 - 0,264
0,264 - 0,267
0,267 - 0,269
0,269 - 0,271
0,271 - 0,324
Bedform type
Large ripple
Megaripple / TAR

Area 65

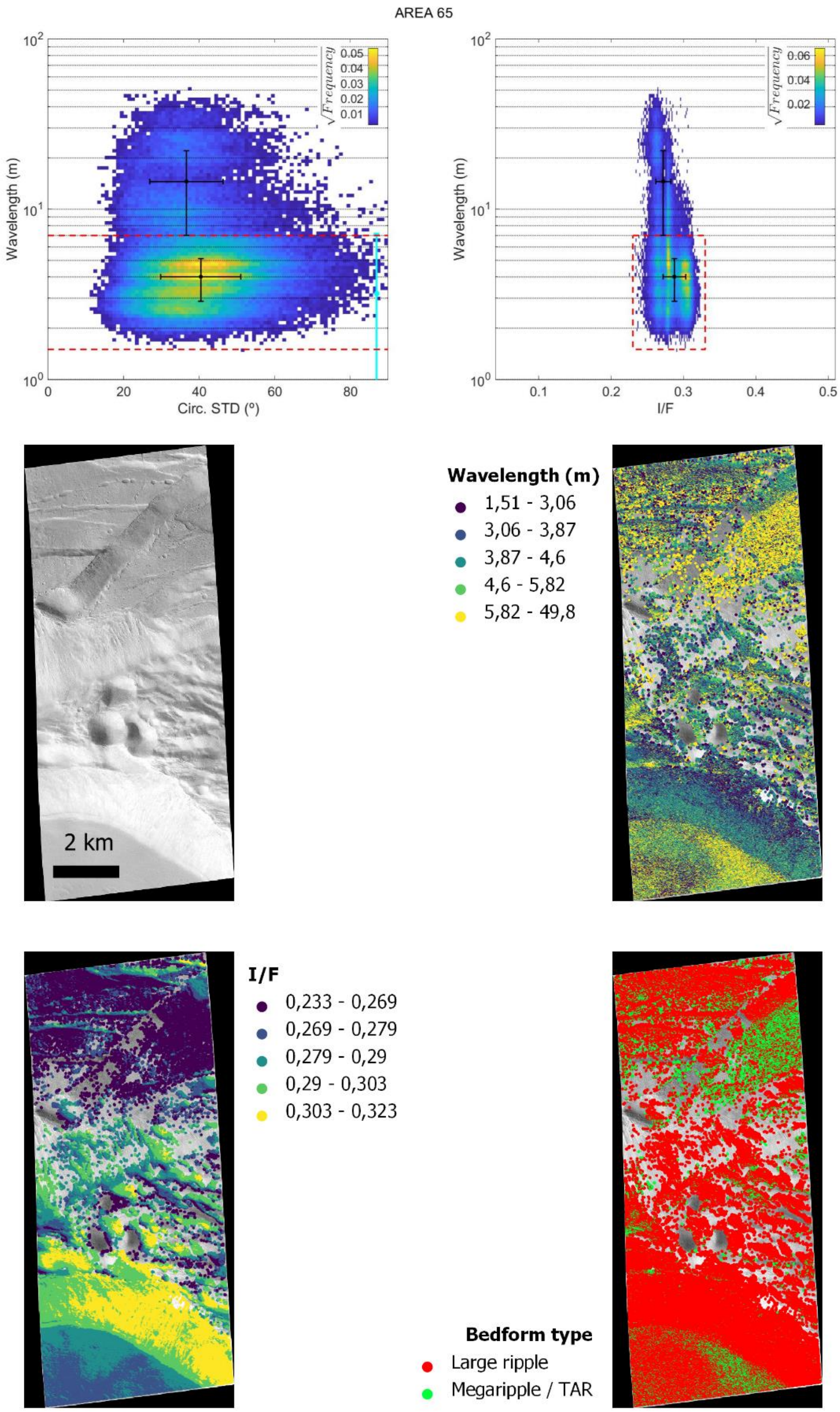
AREA 65
Wavelength (m)
Circ. STD (°)
I/F
√Frequency
2 km
Wavelength (m)
1,51 - 3,06
3,06 - 3,87
3,87 - 4,6
4,6 - 5,82
5,82 - 49,8
I/F
0,233 - 0,269
0,269 - 0,279
0,279 - 0,29
0,29 - 0,303
0,303 - 0,323
Bedform type
Large ripple
Megaripple / TAR

Area 66

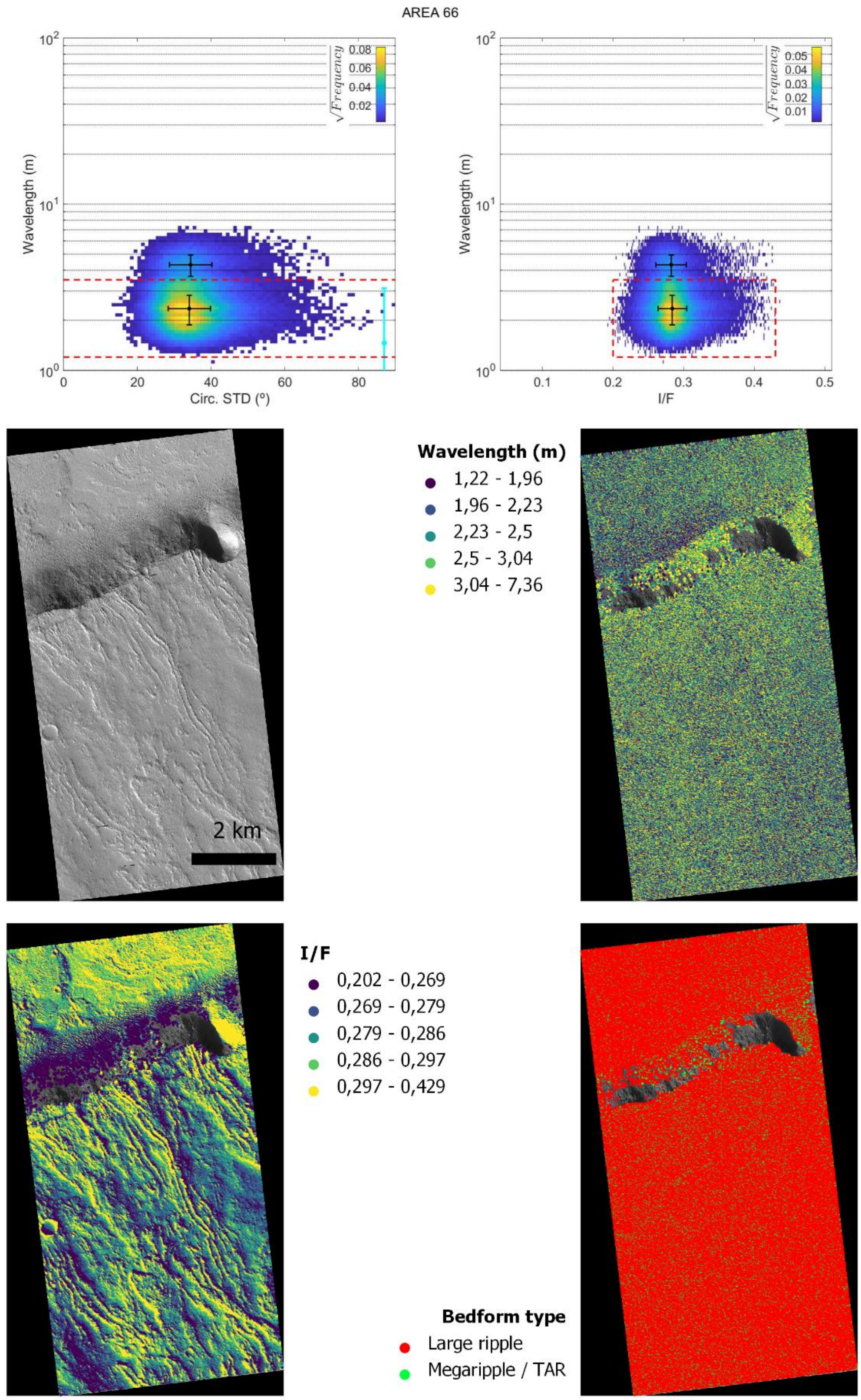

AREA 66
Wavelength (m)
Circ. STD (°)
I/F
√Frequency
2 km
Wavelength (m)
1,22 - 1,96
1,96 - 2,23
2,23 - 2,5
2,5 - 3,04
3,04 - 7,36
I/F
0,202 - 0,269
0,269 - 0,279
0,279 - 0,286
0,286 - 0,297
0,297 - 0,429
Bedform type
Large ripple
Megaripple / TAR

Area 67

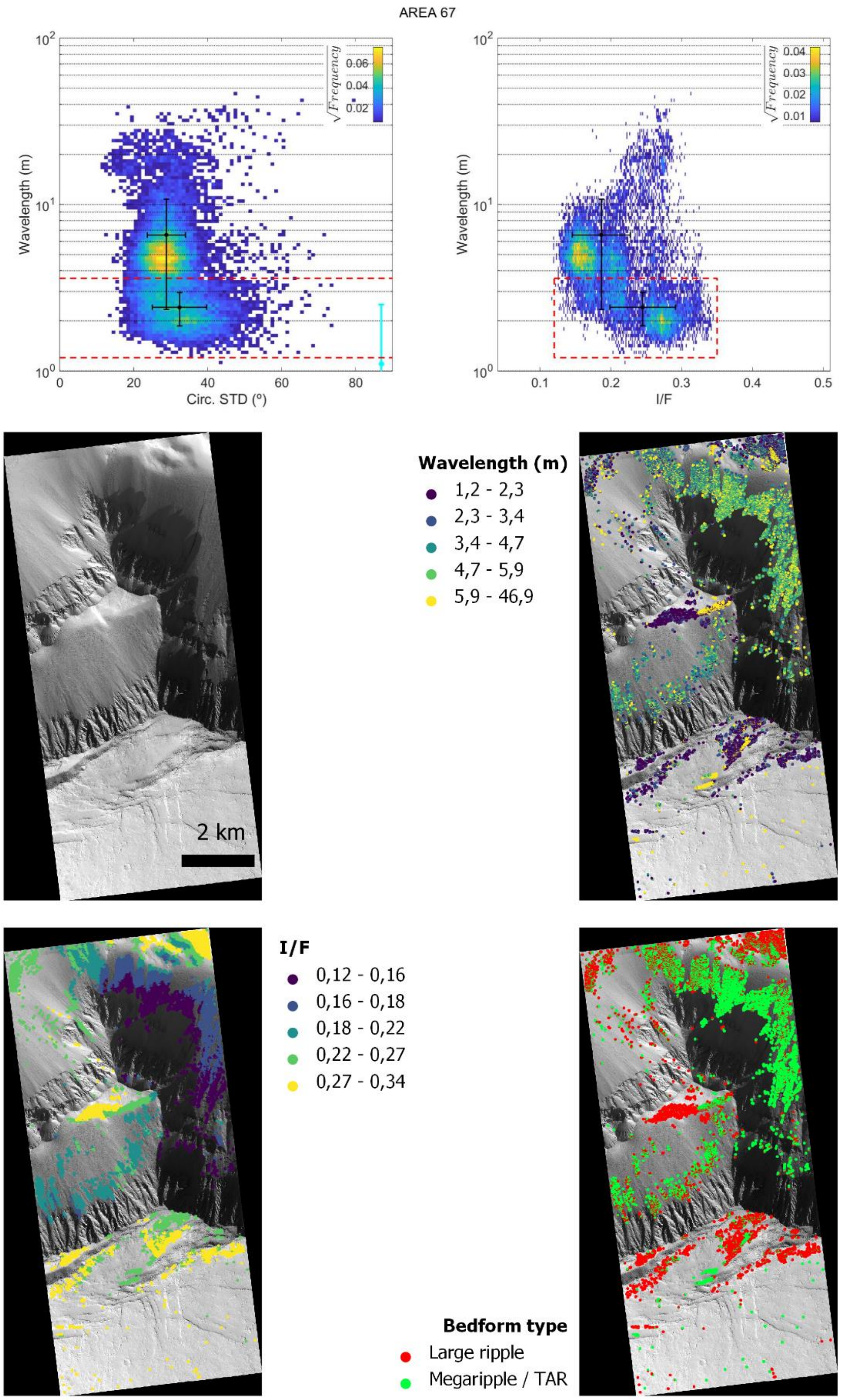
AREA 67
Wavelength (m)
Circ. STD (º)
√Frequency
I/F
2 km
Wavelength (m)
1,2 - 2,3
2,3 - 3,4
3,4 - 4,7
4,7 - 5,9
5,9 - 46,9
I/F
0,12 - 0,16
0,16 - 0,18
0,18 - 0,22
0,22 - 0,27
0,27 - 0,34
Bedform type
Large ripple
Megaripple / TAR

Area 68

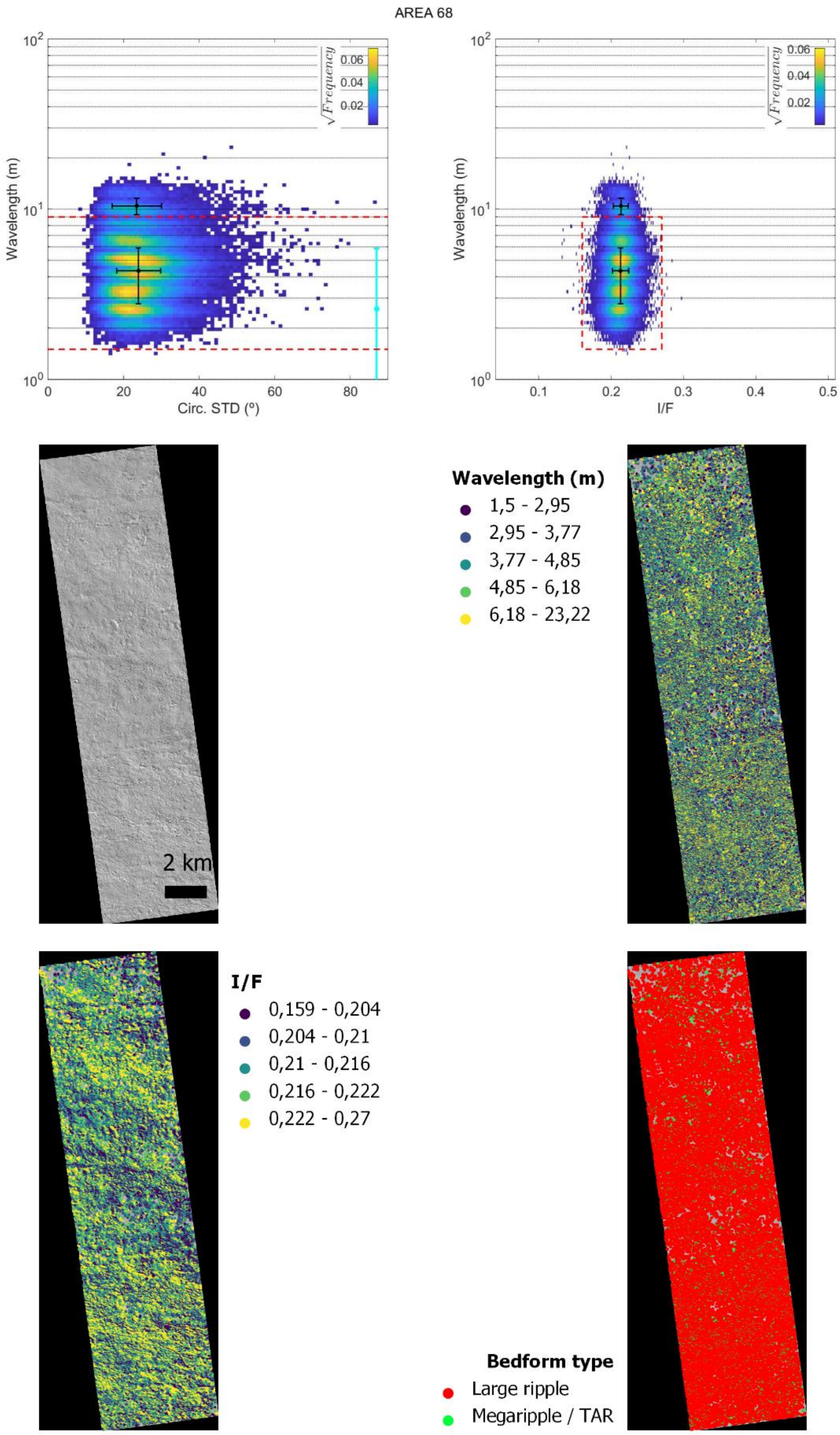
AREA 68
Wavelength (m)
Circ. STD (°)
I/F
√Frequency
2 km
Wavelength (m)
1,5 - 2,95
2,95 - 3,77
3,77 - 4,85
4,85 - 6,18
6,18 - 23,22
I/F
0,159 - 0,204
0,204 - 0,21
0,21 - 0,216
0,216 - 0,222
0,222 - 0,27
Bedform type
Large ripple
Megaripple / TAR

Area 69

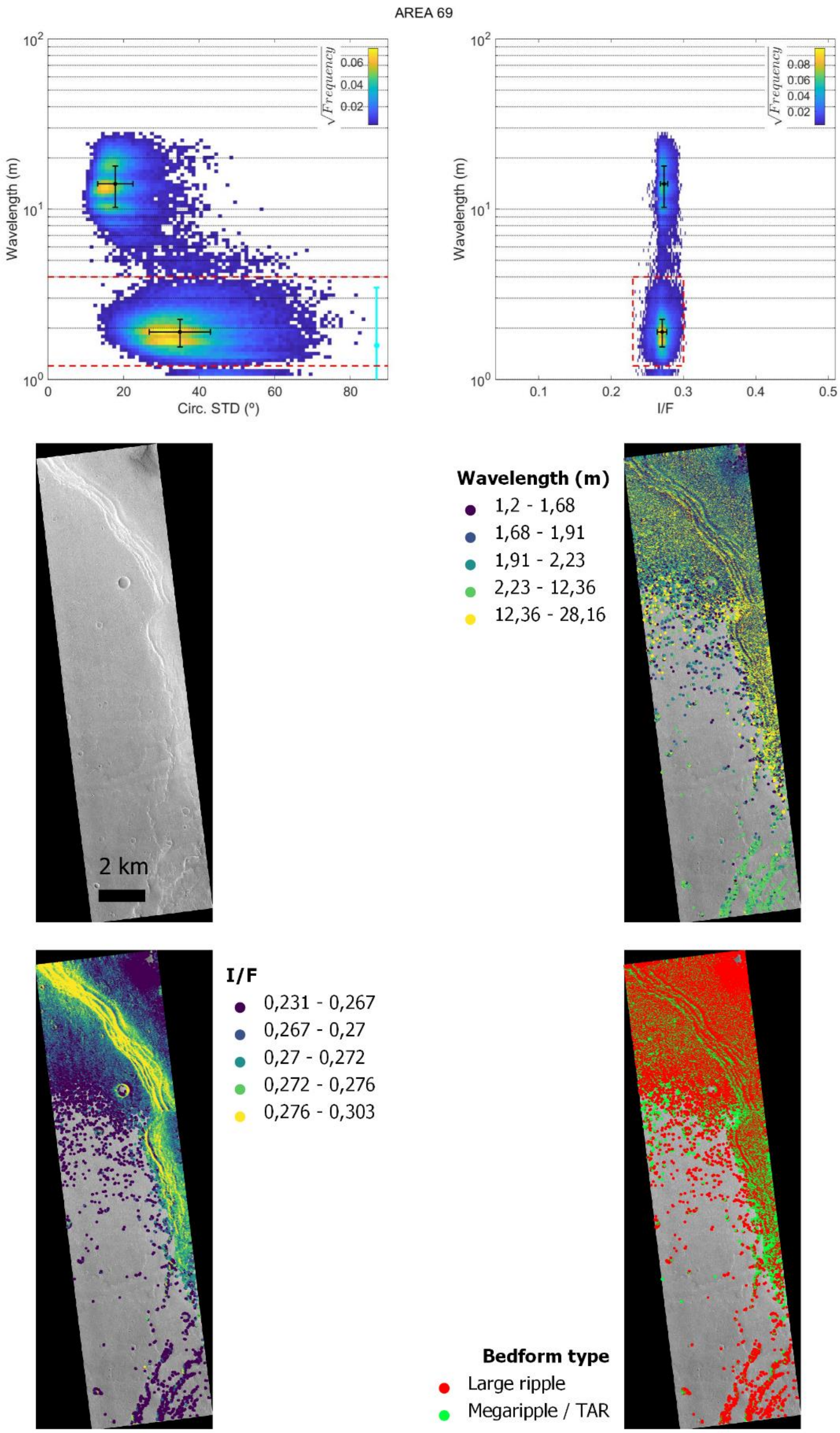
AREA 69
Wavelength (m)
Circ. STD (°)
√Frequency
I/F
2 km
Wavelength (m)
1,2 - 1,68
1,68 - 1,91
1,91 - 2,23
2,23 - 12,36
12,36 - 28,16
I/F
0,231 - 0,267
0,267 - 0,27
0,27 - 0,272
0,272 - 0,276
0,276 - 0,303
Bedform type
Large ripple
Megaripple / TAR

Area 70

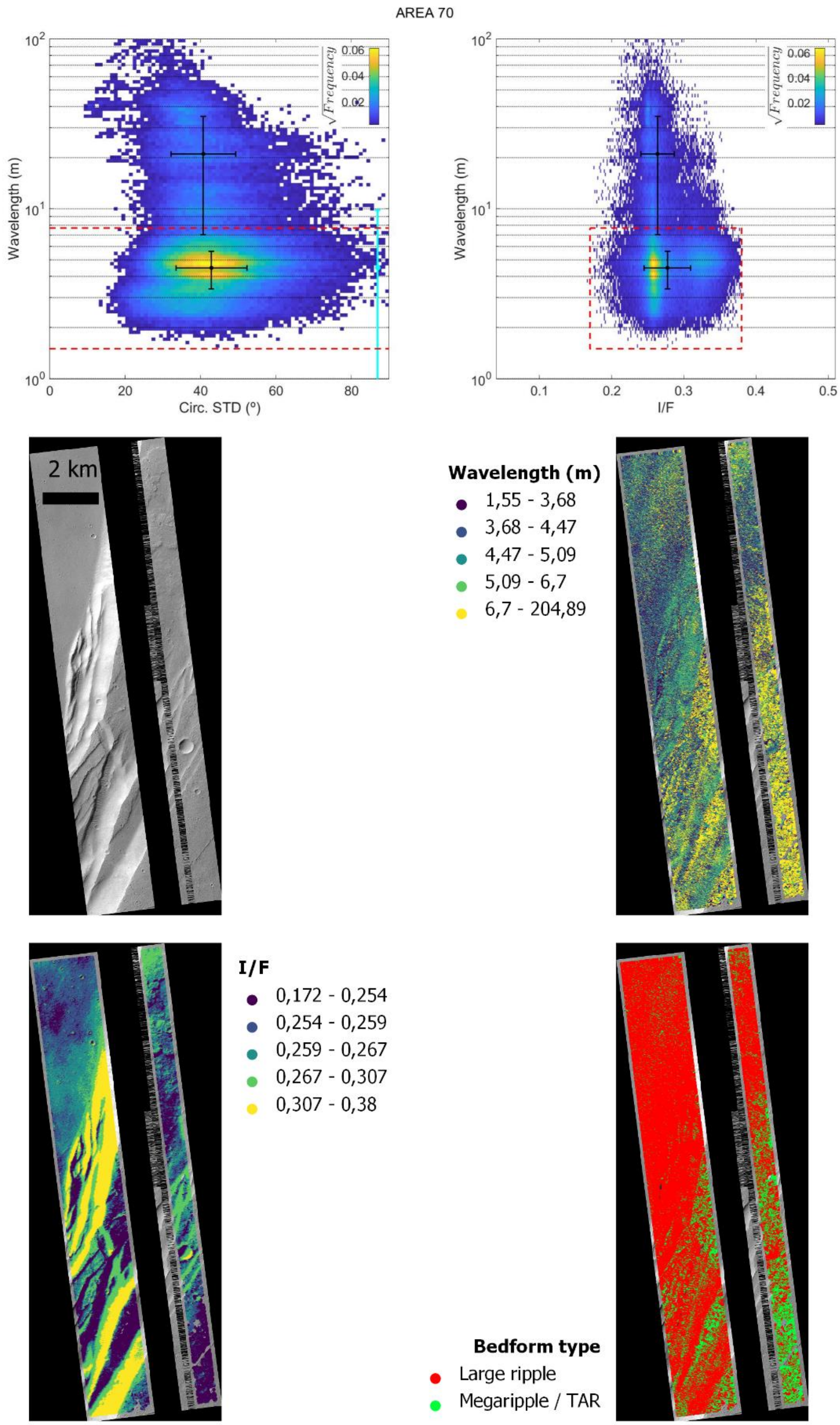
AREA 70
Wavelength (m)
Circ. STD (°)
√Frequency
I/F
2 km
Wavelength (m)
1,55 - 3,68
3,68 - 4,47
4,47 - 5,09
5,09 - 6,7
6,7 - 204,89
I/F
0,172 - 0,254
0,254 - 0,259
0,259 - 0,267
0,267 - 0,307
0,307 - 0,38
Bedform type
Large ripple
Megaripple / TAR

Area 71

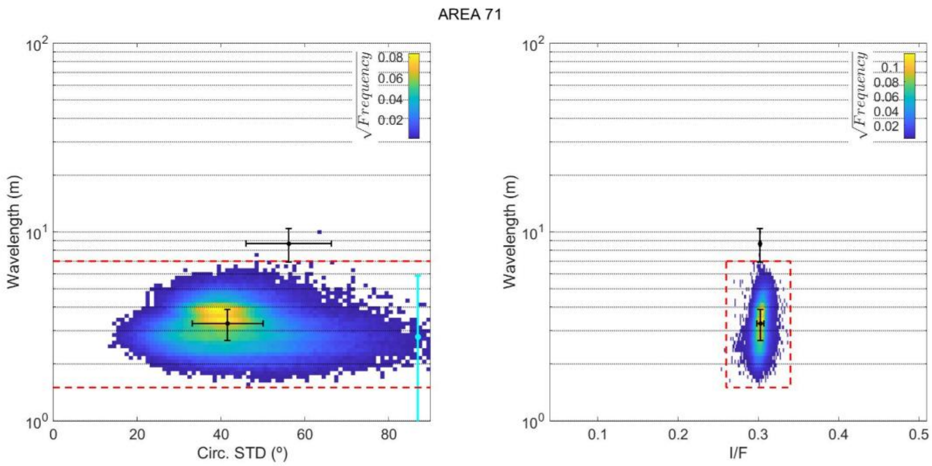
AREA 71
Wavelength (m)
Circ. STD (º)
I/F
√Frequency


2 km

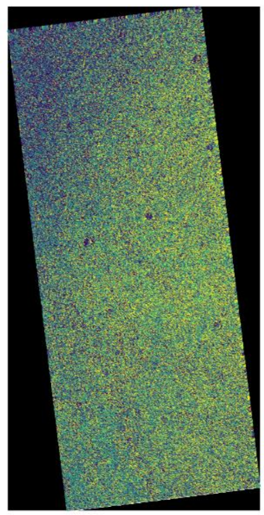
Wavelength (m)
1,58 - 2,71
2,71 - 3,08
3,08 - 3,43
3,43 - 3,84
3,84 - 9,9

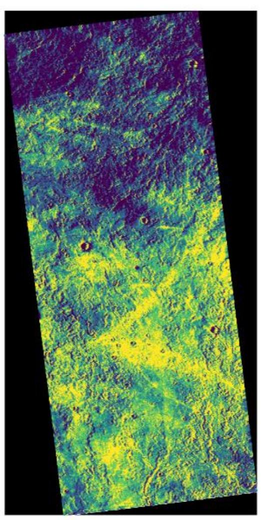
I/F
0,265 - 0,299
0,299 - 0,302
0,302 - 0,304
0,304 - 0,306
0,306 - 0,336

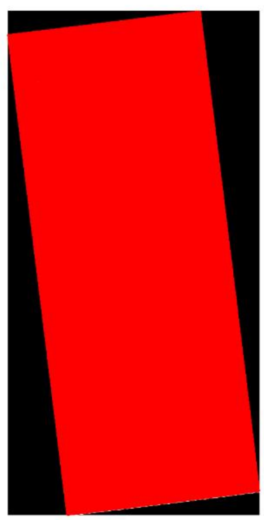
Bedform type
Large ripple
Megaripple / TAR

Area 72

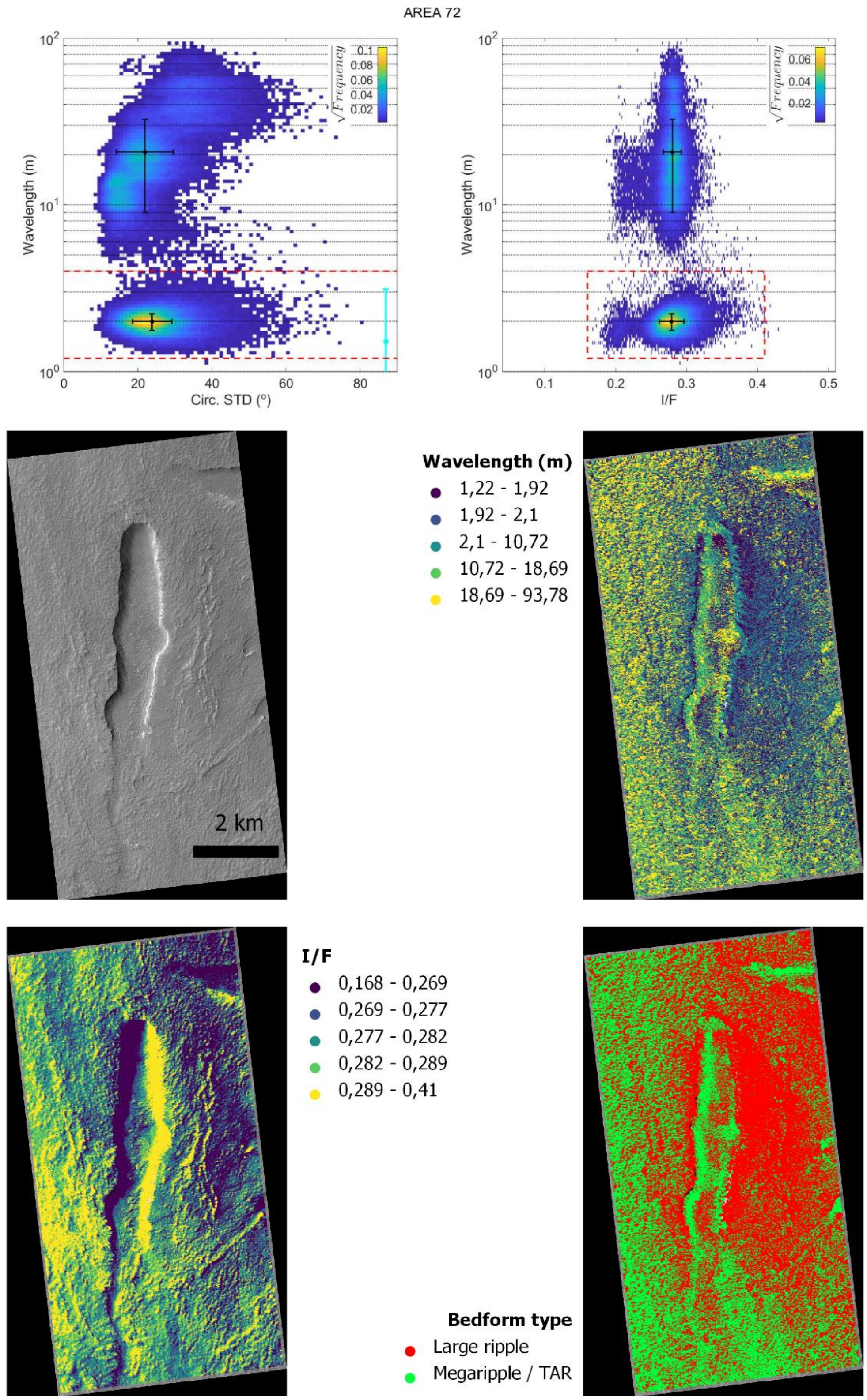
AREA 72
Wavelength (m)
Circ. STD (º)
I/F
√Frequency
2 km
Wavelength (m)
1,22 - 1,92
1,92 - 2,1
2,1 - 10,72
10,72 - 18,69
18,69 - 93,78
I/F
0,168 - 0,269
0,269 - 0,277
0,277 - 0,282
0,282 - 0,289
0,289 - 0,41
Bedform type
Large ripple
Megaripple / TAR

Area 73

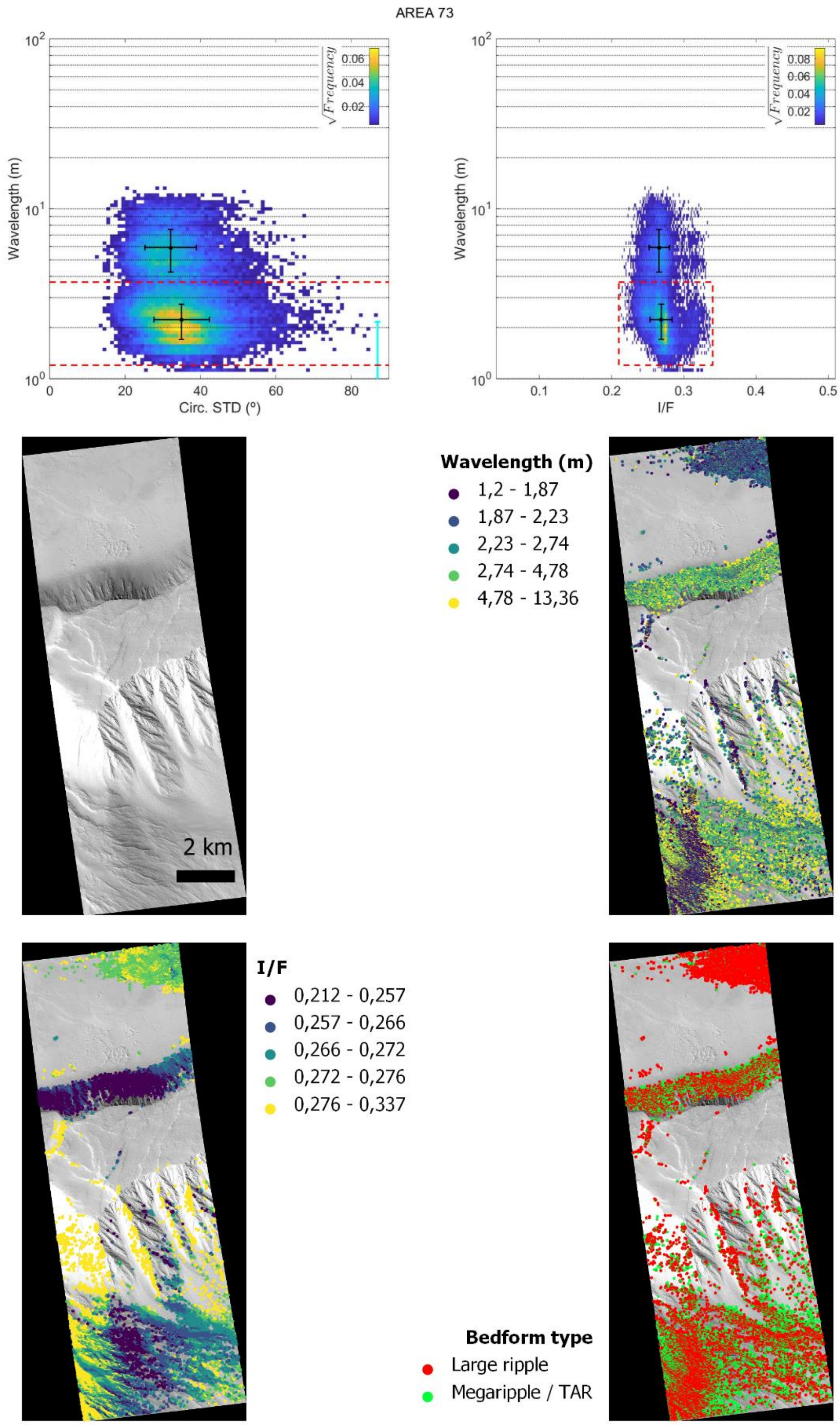
AREA 73
Wavelength (m)
Circ. STD (º)
I/F
√Frequency
2 km
Wavelength (m)
1,2 - 1,87
1,87 - 2,23
2,23 - 2,74
2,74 - 4,78
4,78 - 13,36
I/F
0,212 - 0,257
0,257 - 0,266
0,266 - 0,272
0,272 - 0,276
0,276 - 0,337
Bedform type
Large ripple
Megaripple / TAR

Area 74

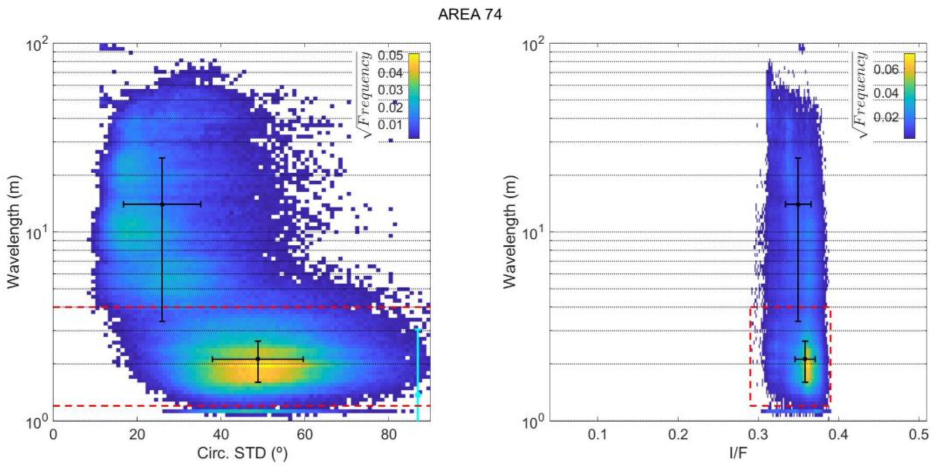
AREA 74
Wavelength (m)
Circ. STD (°)
√Frequency
0.05
0.04
0.03
0.02
0.01
Wavelength (m)
I/F
√Frequency
0.06
0.04
0.02

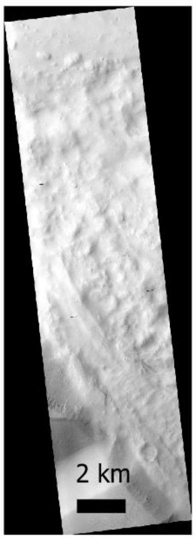
2 km

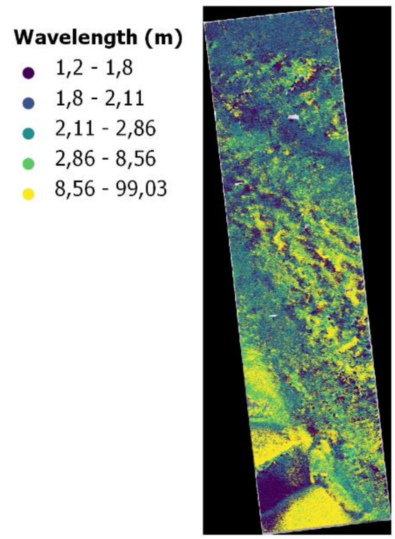
Wavelength (m)
1,2 - 1,8
1,8 - 2,11
2,11 - 2,86
2,86 - 8,56
8,56 - 99,03

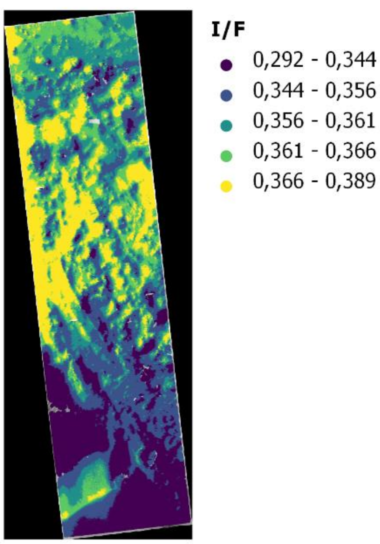
I/F
0,292 - 0,344
0,344 - 0,356
0,356 - 0,361
0,361 - 0,366
0,366 - 0,389

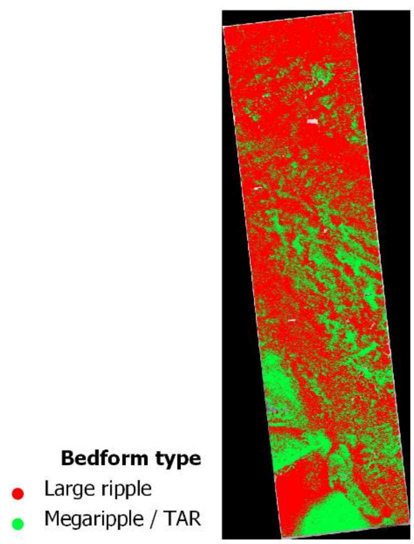
Bedform type
Large ripple
Megaripple / TAR

Area 75

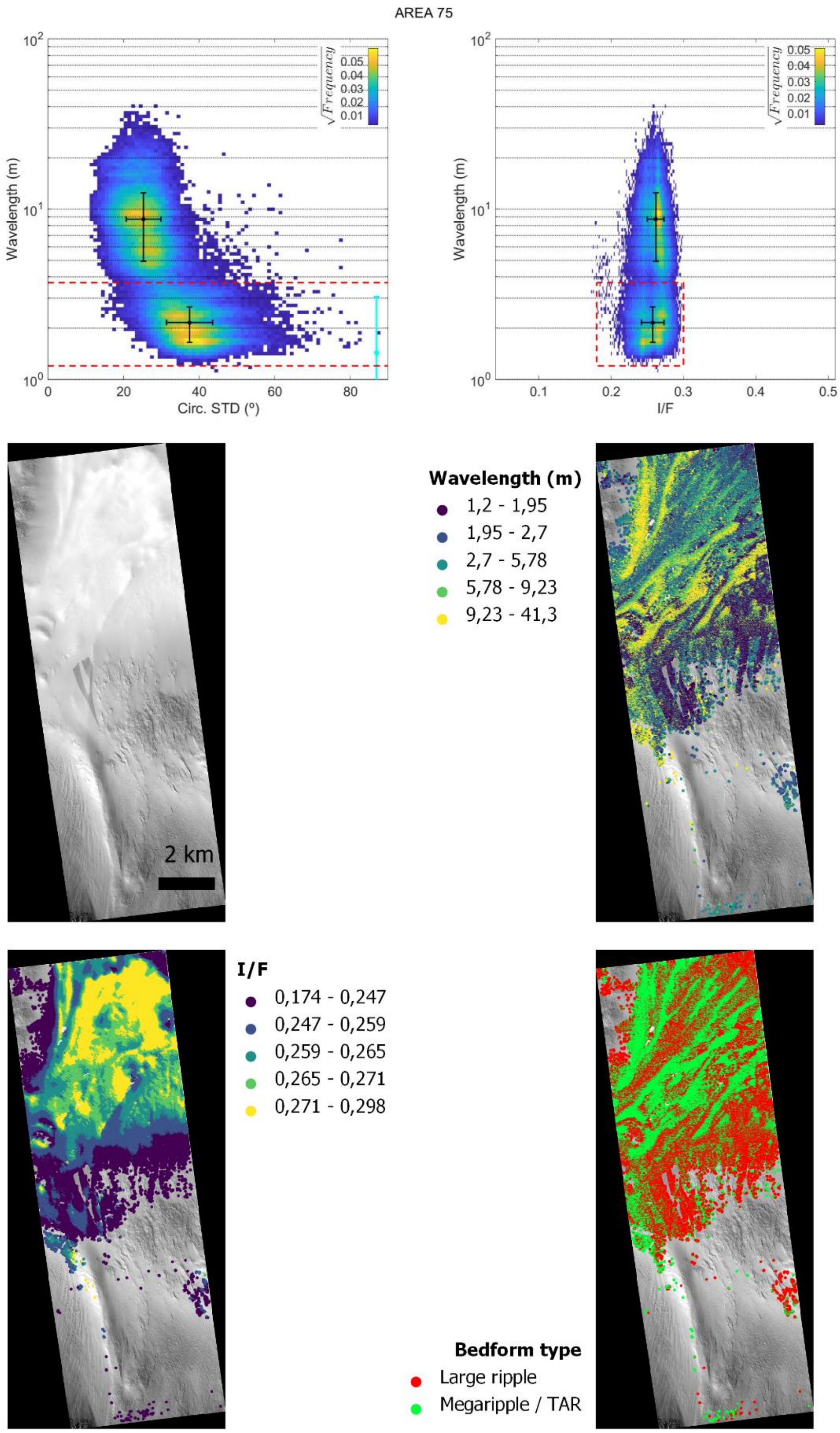
AREA 75
Wavelength (m)
Circ. STD (°)
√Frequency
Wavelength (m)
I/F
2 km
Wavelength (m)
1,2 - 1,95
1,95 - 2,7
2,7 - 5,78
5,78 - 9,23
9,23 - 41,3
I/F
0,174 - 0,247
0,247 - 0,259
0,259 - 0,265
0,265 - 0,271
0,271 - 0,298
Bedform type
Large ripple
Megaripple / TAR